The growth of mass in star-forming galaxies at high redshift

DUDZEVICIUTE, UGNE

The growth of mass in star-forming galaxies at high redshift

Ugnė Dudzevičiūtė

A thesis presented for the degree of

Doctor of Philosophy

Centre for Extragalactic Astronomy

Durham University

United Kingdom

September 2021

The growth of mass in star-forming galaxies at high redshift

Ugnė Dudzevičiūtė

This thesis presents an analysis of star-forming galaxies across the cosmic noon ($z \sim$1–4) spanning a wide range in physical properties, from strongly dust-obscured systems, to more typical 'main-sequence' galaxies. Consistent analysis and methodology, together with the large sample sizes, allow us to compare and contrast populations of different stellar, gas and dark matter masses to assess their evolutionary trends and probe the mass build up across the 'main-sequence'.

For consistent analysis throughout the thesis, we test and check the reliability of using an SED fitting code MAGPHYS (da Cunha et al., 2015) to derive photometric redshifts as well as key physical properties (such as stellar mass, far-infrared luminosity, star-formation rate) for high redshift star-forming galaxies in Chapter 2. Knowing the capabilities and shortcomings of the modelling code, in Chapters 3, 4 and 5, we model multi-wavelength photometric data to derive physical properties of galaxies across the 'main-sequence'.

In Chapter 3, we analyse the physical properties of a large, homogeneously selected sample of ALMA-located sub-millimetre galaxies (SMGs) from the AS2UDS survey (Stach et al., 2019), which identified 707 SMGs across the $\sim 1\,\mathrm{deg}^2$ field. We determine a median redshift of $z = 2.61 \pm 0.08$, and the redshift distribution is well fit by a model combining evolution of the gas fraction in halos with the growth of halo mass past a critical threshold of $M_\mathrm{h} \sim 6 \times 10^{12}\,\mathrm{M}_\odot$, thus SMGs may represent the highly efficient collapse of gas-rich massive halos. We suggest that almost all galaxies with $M_* \gtrsim 3 \times 10^{11}\,\mathrm{M}_\odot$ have passed through an SMG-like phase. SMGs are broadly consistent with simple homologous systems in the far-infrared, such as a centrally illuminated starburst. Overall, this study provides strong support for an evolutionary link between the active, gas-rich SMG population at $z > 1$ and the formation of massive, bulge-dominated galaxies across the history of the Universe.

We analyse the physical properties of 121 sub-millimetre galaxies (SMGs) from the STUDIES 450-μm survey in Chapter 4, and compare the results to 850-μm-selected SMGs from Chapter 3 to understand the fundamental physical differences between the two populations at the observed depths. The 450-μm sample has a median redshift of $z = 1.85 \pm 0.12$. The fainter 450-μm-selected sources have higher space density than the brighter 850-μm sample at $z \lesssim 2$, and a lower space density at $z > 3$, suggesting LIRGs are the main obscured population at $z \sim 1$–2, while ULIRGs dominate at higher redshifts. Using a uniform $\lambda_{\rm rest} \sim 180\mu$m-selected sample at $z = 1$–2 and $z = 3$–4, we suggest that higher-redshift sources have higher dust densities due to smaller inferred dust continuum sizes at a given dust mass, leading to higher dust attenuation. We suggest that the dust content of galaxies is governed by a combination of both the variation of gas content and dust destruction timescale.

Finally, in Chapter 5 we present an on-going analysis of a sample of star-forming galaxies at $z \sim 1.5$ from the KMOS Ultra-deep Rotational Velocity Survey (KURVS). We construct spatially-resolved 2D stellar mass maps from deep *HST* observations and use them to constrain the baryonic mass profile of the sample galaxies. Using these, together with the dynamical mass profiles from the deep Hα observations, we derive the dark matter profiles, which reveal high dark matter fractions ($\sim$0.8), even at effective radius.

Acknowledgements

Firstly, my heartfelt thanks to my fantastic supervisors Mark Swinbank and Ian Smail, for their guidance, support and encouragement. Your assistance and dedicated involvement throughout my PhD has made me a better researcher, so thank you for all those (very) long discussions, endless emails and red comments, and numerous opportunities throughout the years. You constantly pushed me to achieve my best, and for that I am truly grateful.

I had the pleasure to work with a wonderful group of people. In particular, thanks to Stuart S., Julie W., Bitten G., Lizzie C., and Soh I. for a motivating and inspiring work environment. I am very grateful to Anna P., for all the help and support, especially this past year. I would like to express my gratitude to Alastair E., Dave A. and Carlton B. for their useful advice and assistance, and Lydia H. for computer support. I am also grateful to Kristen C., for her assistance with job applications. Thanks to John Lucey, for his enthusiasm and guidance during my masters which helped me to continue in academia. Also, special thanks to my teacher Chris Brown who encouraged me to believe in myself and pursue my dreams.

I would like to thank my fellow students, who made my time at Durham such a great experience. To my officemates, FangXia A., Steve G., Will C., Sut-Ieng T., Duncan M., Cameron G. and Alice E. To all the people in my year group, in particular Louise W., Aidan S., Tom R., Josh B., Calvin S., Chris D., and shout out to Tom C. for the motivation during the thesis write-up. I would also like to thank Jack B., for being a great colleague and friend throughout the years.

Finally, and most importantly, my biggest thanks is to my family, without whom I would not be where I am today. To my mum and dad, Daiva and Vytis, for their love, support and encouragement throughout my whole life. Thanks to my brother Gustas, whose chilled attitude always reminds me to enjoy the little things in life. I am very thankful to my sister, Austė, for her limitless enthusiasm and positivity. And, of course, to Dean, who undoubtedly has been the most caring and supportive person throughout. Thank you for being there for me every day, through all the ups and downs, for motivating me and helping me reach my goals.

Ačiū, jums, už viską.

Contents

Declaration

The research in this thesis was carried out at the Centre for Extragalactic Astronomy, Durham University between October 2017 and September 2021 while the author was a research student under supervision of Prof Mark Swinbank and Prof Ian Smail. No part of this thesis has been submitted elsewhere for any other degree or qualification, and it is the sole work of the author unless referenced to the contrary in the text.

The following sections of this thesis have been published in a peer-reviewed journal:

- *Chapter 2 & 3*: Dudzevičiūtė, U.; Smail, I.; Swinbank, A. M.; Stach, S. M.; Almaini, O.; da Cunha, E.; An, Fang Xia; Arumugam, V.; Birkin, J.; Blain, A. W.; Chapman, S. C.; Chen, C. -C.; Conselice, C. J.; Coppin, K. E. K.; Dunlop, J. S.; Farrah, D.; Geach, J. E.; Gullberg, B.; Hartley, W. G.; Hodge, J. A.; Ivison, R. J.; Maltby, D. T.; Scott, D.; Simpson, C. J.; Simpson, J. M.; Thomson, A. P.; Walter, F.; Wardlow, J. L.; Weiss, A.; van der Werf, P; 2020/03 MNRAS 494 3828: *An ALMA survey of the SCUBA-2 CLS UDS field: physical properties of 707 sub-millimetre galaxies*

- *Chapter 4*: Dudzevičiūtė, U.; Smail, I.; A. M. Swinbank; C.-F. Lim; W.-H. Wang; J. M. Simpson; Y. Ao; S. C. Chapman; C.-C. Chen; D. Clements; H. Dannerbauer; L. C. Ho; H. S. Hwang; M. Koprowski; C.-H. Lee; D. Scott; H. Shim; R. Shirley; and Y. Toba; 2021/01 MNRAS 500 942: *Tracing the evolution of dust-obscured activity using sub-millimetre galaxy populations from STUDIES and AS2UDS*

The author carried out the work in this thesis with the following exceptions: (1) Mark Swinbank has carried out the deblending of the *Herschel* photometry in Chapters 2 & 4; (2) the growth rate of dark matter halos as a function of redshift from Millennium Simulation in Chapter 3 was provided by John Helly; (3) The $YJHK_s$ photometry extraction and $u*$–8μm photometry correction for Galactic

extinction in Chapter 4 was carried out by James Simpson; (4) In Chapter 5, the pixel-by-pixel photometry was extracted from the *HST* images by Mark Swinbank; (5) The KURVS $H\alpha$ data reduction and rotation curve extraction in Chapter 5 was carried out by Annagrazia Puglisi. In addition to the work presented in this thesis, the author also contributed to the following published work during their PhD:

1. Tiley, A. L.; Gillman, S.; Cortese, L. Swinbank, A. M.; **Dudzevičiūtė, U.**; Harrison, C. M.; Smail, I.; Obreschkow, D.; Croom, S. M.; Sharples, R. M.; Puglisi, A.; 2021/09 MNRAS 506 323: *The KMOS galaxy evolution survey (KGES): the angular momentum of star-forming galaxies over the last ∼10 Gyr*

2. Stach, S. M. ; Smail, I.; Amvrosiadis, A.; Swinbank, A. M.; **Dudzevičiūtė, U.**; Geach, J. E.; Almaini, O.; Birkin, J. E.; Chen, C. -C; Conselice, C. J. ; Cooke, E. A.; Coppin, K. E. K. ; Dunlop, J. S.; Farrah, D.; Ikarashi, S.; Ivison, R. J.; Wardlow, J. L; 2021/06 MNRAS 504 172: *An ALMA survey of the SCUBA-2 Cosmology Legacy Survey UKIDSS/UDS field: halo masses for submillimetre galaxies*

3. Cochrane, R. K.; Best, P. N.; Smail, I.; Ibar, E.; Cheng, C.; Swinbank, A. M.; Molina, J.; Sobral, D.; **Dudzevičiūtė, U.**; 2021/05 MNRAS 503 2262: *Resolving a dusty, star-forming SHiZELS galaxy at z=2.2 with HST, ALMA and SINFONI on kiloparsec scales*

4. Smail, I.; **Dudzevičiūtė, U.**; Stach, S. M.; Almaini, O.; Birkin, J. E.; Chapman, S. C.; Chen, C.-C ; Geach, J. E.; Gullberg, B.; Hodge, J. A.; Ikarashi, S.; Ivison, R. J.; Scott, D.; Simpson, C.; Swinbank, A. M.; Thomson, A. P.; Walter, F.; Wardlow, J. L.; van der Werf, P.; 2021/04 MNRAS 502 3426: *An ALMA survey of the S2CLS UDS field: Optically invisible submillimetre galaxies*

5. Birkin, J. E.; Weiss, A.; Wardlow, J. L.; Smail, I.; Swinbank, A. M.; **Dudzevičiūtė, U.**; An, Fang Xia; Ao, Y.; Chapman, S. C.; Chen, C. -C; da Cunha, E.; Dannerbauer, H.; Gullberg, B.; Hodge, J. A.; Ikarashi, S.; Ivison, R. J.; Matsuda, Y.; Stach, S. M.; Walter, F.; Wang, W. -H van der Werf, P; 2021/03 MNRAS 501 3926: *An ALMA/NOEMA survey of the molecular gas properties of high-redshift star-forming galaxies*

6. Mitsuhashi, I.; Matsuda, Y.; Smail, I.; Hayatsu, N.; Simpson, J.; Swinbank, M.; Umahata, H.; **Dudzevičiūtė, U.**; Birkin, J.; Ikarashi, S.; Chen, C. -C; Tadaki, K.; Yajima, H.; Harikane, Y.; Inami, H.; Chapman, S.; Hatsukade, B.; Iono, D.; Bunker, A.; Ao, Y.; Saito, T.; Ueda, J.; Sakamoto, S.; 2021/02

ApJ 907 122: *FIR-luminous [CII] emitters in the ALMA-SCUBA-2 COSMOS survey (AS2COSMOS): The nature of submillimeter galaxies in a 10 comoving Mpc-scale structure at z∼4.6*

7. Gillman, S.; Tiley, A. L.; Swinbank, A. M.; **Dudzevičiūtė, U.**; Sharples, R. M.; Smail, I.; Harrison, C. M.; Bunker, A. J.; Bureau, M.; Cirasuolo, M.; Magdis, G. E.; Mendel, T.; Stott, J. P.; 2021/01 MNRAS 500 4229: *The Evolution of Gas-Phase Metallicity and Resolved Abundances in Star-forming Galaxies at $z \approx 0.6 - 1.8$*

8. Algera, H. S. B.; Smail, I.; **Dudzevičiūtė, U.**; Swinbank, A. M.; Stach, S.; Hodge, J. A.; Thomson, A. P.; Almaini, O.; Arumugam, V.; Blain, A. W.; Calistro-Rivera, G.; Chapman, S. C.; Chen, C. -C; da Cunha, E.; Farrah, D.; Leslie, S.; Scott, D.; Van der Vlugt, D.; Wardlow, J. L.; Van der Werf, P; 2020/11 ApJ 903 138: *An ALMA Survey of the SCUBA-2 Cosmology Legacy Survey UKIDSS/UDS Field: The Far-infrared/Radio correlation for High-redshift Dusty Star-forming Galaxies*

9. Bouwens, R.; Gonzalez-Lopez, J.; Aravena, M.; Decarli, R.; Novak, M.; Stefanon, M.; Walter, F.; Boogaard, L.; Carilli, C.; **Dudzeviciute, U.**; Smail, I.; Daddi, E.; da Cunha, E.; Ivison, R.; Nanayakkara, T.; Cortes, P.; Cox, P.; Inami, H.; Oesch, P.; Popping, G.; Riechers, D.; van der Werf, P.; Weiss, A.; Fudamoto, Y.; Wagg, J.; 2020/10 ApJ 902 112: *The ALMA Spectroscopic Survey Large Program: The Infrared Excess of z=1.5-10 UV-selected Galaxies and the Implied High-Redshift Star Formation History*

10. Simpson, J. M.; Smail, I.; **Dudzevičiūtė, U.**; Matsuda, Y.; Hsieh, B. -C.; Wang, W. -H.; Swinbank, A. M.; Stach, S. M.; An, Fang Xia; Birkin, J. E.; Ao, Y.; Bunker, A. J.; Chapman, S. C.; Chen, C. -C; Coppin, K. E. K.; Ikarashi, S.; Ivison, R. J.; Mitsuhashi, I.; Saito, T.; Umehata, H. Wang, R.; Zhao, Y; 2020/07 MNRAS 495 3409: *An ALMA survey of the brightest sub-millimetre sources in the SCUBA-2-COSMOS field*

11. Koprowski, M. P.; Coppin, K. E. K.; Geach, J. E.; **Dudzevičiūtė, U.**; Smail, I.; Almaini, O.; An, Fangxia; Blain, A. W.; Chapman, S. C.; Chen, C. -C; Conselice, C. J.; Dunlop, J. S.; Farrah, D.; Gullberg, B.; Hartley, W.; Ivison, R. J.; Karska, A.; Maltby, D.; Malek, K.; Michałowski, M. J.; Pope, A.; Salim, S.; Scott, D.; Simpson, C. J.; Simpson, J. M.; Swinbank, A. M.; Thomson, A. P.; Wardlow, J. L.; van der Werf, P. P.; Whitaker, K. E; 2020/03 MNRAS 492 4927: *An ALMA survey of the SCUBA-2 cosmology legacy survey UKIDSS/UDS field: Dust attenuation in high-redshift Lyman-break galaxies*

12. Gillman, S.; Tiley, A. L.; Swinbank, A. M.; Harrison, C. M.; Smail, I.; **Dudzevičiūtė, U.**; Sharples, R. M.; Cortese, L.; Obreschkow, D.; Bower, R. G.; Theuns, T.; Cirasuolo, M.; Fisher, D. B.; Glazebrook, K.; Ibar, E.; Mendel, J. T.; Sweet, S. M.; 2020/02 MNRAS 492 1492: *From peculiar morphologies to Hubble-type spirals: the relation between galaxy dynamics and morphology in star-forming galaxies at z∼1.5*

13. Lim, C.-F; Wang, W.-H; Smail, I.; Scott, D.; Chen, C.-C; Chang, Y.-Y; Simpson, J. M.; Toba, Y.; Shu, X.; Clements, D.; Greenslade, J.; Ao, Y.; Babul, A.; Birkin, J.; Chapman, S. C.; Cheng, T.-A; Cho, B. S.; Dannerbauer, H.; **Dudzevičiūtė, U.**; Dunlop, J.; Gao, Y.; Goto, T.; Ho, L. C.; Hsu, L.-T.; Hwang, H. S.; Jeong, W.-S.; Koprowski, M.; Lee, C.-H.; Lin, M.-Y.; Lin, W.-C.; Michałowski, M. J.; Parsons, H.; Sawicki, M.; Shirley, R.; Shim, H.; Urquhart, S.; Wang, J.; Wang, T.; 2020/02 ApJ 889 80: *SCUBA-2 Ultra Deep Imaging EAO Survey (Studies). III. Multiwavelength Properties, Luminosity Functions, and Preliminary Source Catalog of 450 μm Selected Galaxies*

14. Gullberg, B.; Smail, I.; Swinbank, A. M.; **Dudzevičiūtė, U.**; Stach, S. M.; Thomson, A. P.; Almaini, O.; Chen, C.-C; Conselice, C.; Cooke, E. A.; Farrah, D.; Ivison, R. J.; Maltby, D.; Michałowski, M. J.; Simpson, J. M.; Scott, D.; Wardlow, J. L.; Weiss, A; 2019/12 MNRAS 490 4956: *An ALMA survey of the SCUBA-2 Cosmology Legacy Survey UKIDSS/UDS field: high-resolution dust continuum morphologies and the link between sub-millimetre galaxies and spheroid formation*

15. Ivison, R. J.; Page, M. J.; Cirasuolo, M.; Harrison, C. M.; Mainieri, V.; Arumugam, V.; **Dudzevičiūtė, U.**; 2019/10 MNRAS 489 427: *Hyperluminous starburst gives up its secrets*

16. Thomson, A. P.; Smail, I.; Swinbank, A. M.; Simpson, J. M.; Arumugam, V.; Stach, S.; Murphy, E. J.; Rujopakarn, W.; Almaini, O.; An, F.; Blain, A. W.; Chen, C. C.; Cooke, E. A.; **Dudzevičiūtė, U.**; Edge, A. C.; Farrah, D.; Gullberg, B.; Hartley, W.; Ibar, E.; Maltby, D.; Michałowski, M. J.; Simpson, C.; van der Werf, P.; Wardlow, J. L; 2019/10 ApJ 883 204: *Radio Spectra and Sizes of Atacama Large Millimeter/submillimeter Array-identified Submillimeter Galaxies: Evidence of Age-related Spectral Curvature and Cosmic-Ray Diffusion?*

17. Stach, S. M.; **Dudzevičiūtė, U.**; Smail, I.; Swinbank, A. M.; Geach, J. E.; Simpson, J. M.; An, F. X.; Almaini, O.; Arumugam, V.; Blain, A. W.; Chapman, S. C.; Chen, C.-C; Conselice, C. J.; Cooke, E. A.; Coppin, K. E. K.; da Cunha, E.; Dunlop, J. S.; Farrah, D.; Gullberg, B.; Hodge, J. A.; Ivison,

R. J.; Kocevski, D. D.; Michałowski, M. J.; Miyaji, T.; Scott, D.; Thomson, A. P.; Wardlow, J. L.; Weiss, A.; van der Werf, P; 2019/08 MNRAS 487 4648: *An ALMA survey of the SCUBA-2 Cosmology Legacy Survey UKIDSS/UDS field: source catalogue and properties*

18. Lang, P.; Schinnerer, E.; Smail, I.; **Dudzevičiūtė, U.**; Swinbank, A. M.; Liu, D.; Leslie, S. K.; Almaini, O.; An, F. X.; Bertoldi, F.; Blain, A. W.; Chapman, S. C.; Chen, C. -C; Conselice, C.; Cooke, E. A.; Coppin, K. E. K.; Dunlop, J. S.; Farrah, D.; Fudamoto, Y.; Geach, J. E.; Gullberg, B.; Harrington, K. C.; Hodge, J. A.; Ivison, R. J.; Jiménez-Andrade, E. F.; Magnelli, B.; Michałowski, M. J.; Oesch, P.; Scott, D.; Simpson, J. M.; Smolčić, V.; Stach, S. M.; Thomson, A. P.; Toft, S.; Vardoulaki, E.; Wardlow, J. L.; Weiss, A.; van der Werf, P; 2019/07 ApJ 879 54: *Revealing the Stellar Mass and Dust Distributions of Submillimeter Galaxies at Redshift 2*

19. Gillman, S.; Swinbank, A. M.; Tiley, A. L.; Harrison, C. M.; Smail, I.; **Dudzevičiūtė, U.**; Sharples, R. M.; Best, P. N.; Bower, R. G.; Cochrane, R.; Fisher, D.; Geach, J. E.; Glazebrook, K.; Ibar, E.; Molina, J.; Obreschkow, D.; Schaller, M.; Sobral, D.; Sweet, S.; Trayford, J. W.; Theuns, T; 2019/06 MNRAS 486 175: *The dynamics and distribution of angular momentum in HiZELS star-forming galaxies at z = 0.8-3.3*

List of Figures

List of Tables

Chapter 1

Introduction

1.1 Galaxies

Research into extragalactic astronomy started relatively recently, since it is only a century ago that the existence of galaxies outside our own Milky Way was proven. In the 18th century, first catalogues of large numbers of 'nebulae' were published by Messier (1781) and Herschel (1786). These were speculated to possibly be galaxies outside of the Milky Way (Wright, 1750; Kant, 1755), however there was no widely accepted consensus until much later. Follow-up studies by William Parsons, the third Earl of Rosse, identified spiral structures in some of these 'nebulae' and early spectroscopic studies showed that they represent collections of stars (Huggins & Miller, 1864; Scheiner, 1899) with radial velocities exceeding that of any know astronomical object (Slipher, 1914). However, it wasn't until 1926 that it was widely accepted that these spiral 'nebulae' are external galaxies that lie far beyond the extent of our Milky Way. This was achieved by studying pulsating Cepheid variables by Hubble (1925). In the same decade, Hubble (1929) observed a relation between the distance and recession velocity among 'extragalactic nebulae', which unveiled the expansion of the Universe, forever changing the way we view the Cosmos. These discoveries provided the foundations for extragalactic astronomy, indicating that our own Milky Way is just one of the many galaxies in the Universe. Indeed, the deepest *Hubble Space Telescope* (*HST*) observations suggest that there

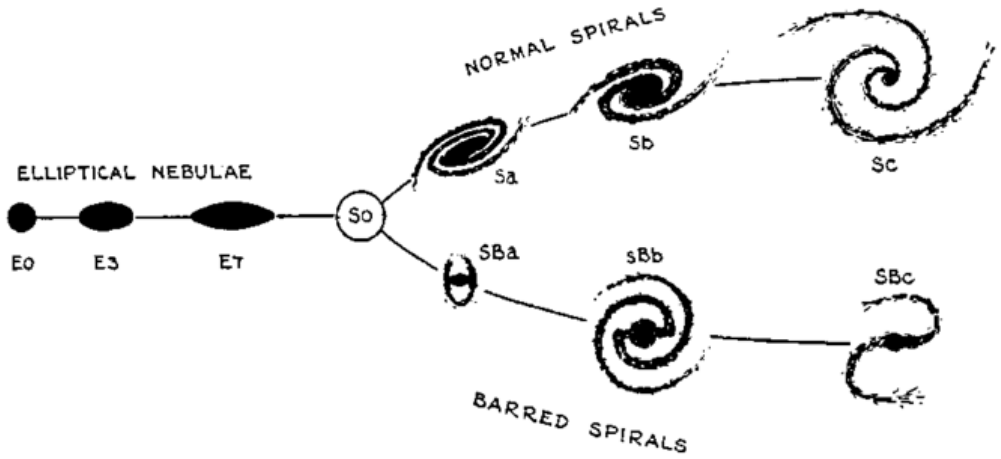

Figure 1.1: Hubble's classification system of galaxies from Hubble (1936). This selection highlights the sequence of morphological complexity in the systems in terms of their optical appearance, such as prominence of the central bulge and existence (as well as prominence) of the spiral arms.

are over a 100 billion of galaxies (e.g. Beckwith et al., 2006) with a wide-range of photometric, physical and morphological properties in the observable Universe. Thus, one of the main aims of astronomy is to try and understand how these galaxies form and evolve into the populations we observe today.

The range of morphologies of galaxies was first assessed by Hubble (1926, 1936), who constructed a classification system based on the optical appearance of galaxy images on photographic plates, known as Hubble sequence or Hubble 'tuning fork' shown in Fig. 1.1. This sequence highlights the morphological complexity in the systems and is generally divided into three main classes: ellipticals (E), lenticulars (S0) and spirals (S), shown in Fig. 1.1. In this sequence, galaxies are organised from elliptical, which are pure bulge systems with increasing ellipticity, $e = 1 - b/a$ (where b/a is the axial ratio), through galaxies with increasing contribution from the disk component but no spiral arms (S0), to those with both bulge and spiral arms in the disk (Sa-Sc). The spiral galaxies are further split into those with (S) and without (SB) a prominent bar structure. Hubble noted elliptical and lenticular galaxies as "early-type" and spiral galaxies as "late-type", referring to the increased complexity of their structures (rather than the misconception that it denotes an evolutionary sequence). In addition, Hubble (1926) classified three per cent of

galaxies as having irregular structure, with more recent studies showing $\lesssim$10 per cent of local galaxies to have irregular or peculiar morphologies (e.g. Delgado-Serrano et al., 2010), which escape this simple classification.

Since the identification of different types of galaxies, our understanding of galaxy populations has advanced significantly. Spectroscopic studies have revealed that elliptical galaxies are typically gas-poor systems dominated by old stellar populations, with little or no on-going star formation. Therefore, they are commonly called 'red and dead'. Elliptical galaxies are pressure-supported, meaning their structure is supported by the random motions of stars and they follow a relation between the range in orbital velocities (velocity dispersion) and the total luminosity (Faber & Jackson, 1976). In contrast, spiral galaxies are gas-rich systems with typically much younger stellar populations and are actively star forming. They host young, hot O- and B-type stars, thus are photometrically classified as 'blue galaxies'. These galaxies have disks of stars and gas which are rotationally-supported. In addition, early-type spirals may host a spherical bulge component consisting of older stars on pressure-supported random orbits. The rotational velocity of the disk of the late-type galaxies is correlated with the total luminosity of the galaxy (Tully & Fisher, 1977).

1.1.1 Dark matter

Advances in technology in the early 20th century allowed us to study galaxies in more detail using spectroscopy. Studies of the Milky Way revealed that velocity of some stars should be sufficient for them to escape the gravitational effect of the Galaxy estimated from the visible stellar mass in the disk, meaning that there must be some undetected matter, such as unseen interstellar dust, holding them in orbit (Oort, 1927, 1932). Carrying on from this, measurements of motions of galaxies in the Coma Cluster by Zwicky (1933) revealed large velocities, suggesting that there must be "invisible matter" keeping the cluster stable. Similar results were found for the rotation speeds of stars (flat rotation curves) in individual galaxies (e.g. Babcock, 1939; Oort, 1940). Early radio observations of the rotation curve

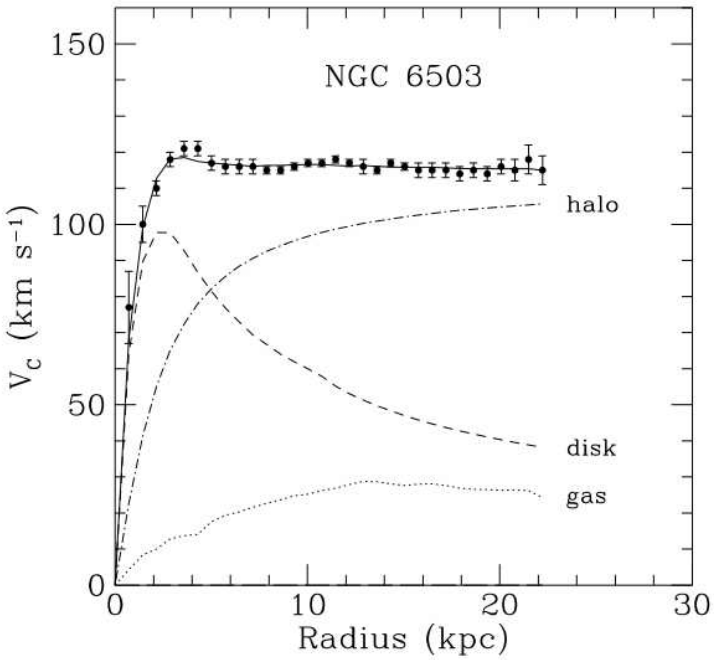

Figure 1.2: The rotational velocity as a function of galactocentric radius, also know as velocity rotation curve, of the local spiral galaxy NGC 6503 from Begeman et al. (1991). The inferred stellar (dashed) and gaseous (dotted) components cannot explain the large and flat observed rotational velocity traced by HI, suggesting that there must be large amount of dark matter (halo; dot-dashed) to account for this difference.

of M31 using the HI 21 cm emission line showed that the rotation of the galaxy remains approximately flat far beyond the optical radius (≈ 25 kpc; van de Hulst et al., 1957). This was contrary to the expected Keplerian decline, whereby the orbital speed of stars in the disk should decrease with increasing distance from the galaxy's centre (see the velocity implied by the stellar disk component in Fig. 1.2).

This indicated that there could be large amounts of this 'invisible' mass that has a much larger extent than the visible matter (Schmidt, 1957), assuming that the Newtonian physics applies on large scales. The existence of dark matter was later comprehensively acknowledged in early 1970-80s with more statistically robust measurements of galaxy rotation curves. The velocities of 67 HII regions in the disk of M31 were measured by Rubin & Ford (1970), showing that the enclosed dynamical mass of the galaxy continues to rise out to at least 24 kpc, again outside the optical radius. By the mid-80s, flat rotation curves (at radii up to 50kpc) were found to be ubiquitous in high luminosity spiral galaxies (Bosma, 1978; Rubin et al., 1978,

1980, 1982, 1985). During this period, the work of observers and theorists converged, culminating in a general assertion that galaxies are immersed in extended dark matter halos (Ostriker & Peebles, 1973; Ostriker et al., 1974; Davis et al., 1985; Frenk et al., 1985). Many subsequent studies of rotation curves of galaxies have confirmed these early results (for a review see Sofue & Rubin, 2001, and references therein). The shapes of the rotation curves remain one of the fundamental pillars of the dark matter paradigm, together with evidence from mass distribution in cluster galaxies (Zwicky, 1933), and strong and weak gravitational lensing (Walsh et al., 1979).

1.1.2 Galaxy baryonic and dark matter components

Detailed studies of local galaxies have revealed the typical ratios of baryonic to dark matter, as well as the total dynamical masses for both 'late-type' and 'early-type' galaxies. For example, the Milky Way has a median stellar mass of $M_* \sim 5\times10^{10}\mathrm{M}_\odot$ and has an extended dark matter halo, with a centrally concentrated baryonic component that dominates in the central few kpc. The inferred dark matter fraction of the Milky Way from dynamical mass analysis varies in the range of $f_{\mathrm{DM}} = 0.3$–0.6 at $R = 6$–$10\,\mathrm{kpc}$ (for a review, see Bland-Hawthorn & Gerhard, 2016). This is typical for star-forming late-type galaxies at low redshift, which are found to have $\gtrsim$50 per cent dark matter fractions at $\sim$3 times the effective radius (Persic et al., 1996; Martinsson et al., 2013; Courteau & Dutton, 2015). In contrast, low dark matter fractions ($\lesssim$30 per cent) across a wide range of mass has been suggested for massive local 'early-type' galaxies (for a review, see Cappellari, 2016). The differences in the dark matter fraction possibly indicates different evolutionary paths in these morphologically different galaxies. This highlights the importance for detailed studies of statistically robust samples of galaxies at high redshift, to address whether the differences in their dark matter fractions are already set in their star-forming ancestors at earlier times, and thus gain a better understanding of galaxy formation and evolution processes.

1.2 Galaxy formation and evolution

In our current understanding of cosmology, the Universe started from a much denser and hotter, nearly homogeneous state. In this scenario, the quantum fluctuations in the very early Universe were amplified during the epoch of very rapid expansion (10^{-36} s after the Big Bang), called inflation, creating small inhomogeneities. These irregularities continued growing as the Universe expanded and are now detectable as temperature fluctuations in the cosmic microwave background (e.g. Planck Collaboration et al., 2011). Current constraints from multiple independent measurements (e.g. Type Ia SNe, Cepheid stars, galaxy clusters) suggest a geometrically flat universe that is dominated by dark matter and dark energy. These two, still currently unknown, components are expected to account for ∼95 per cent of all energy density of the Universe, with only ∼5 per cent in the form of baryonic matter (Freedman & Turner, 2003). In the most widely accepted framework for structure formation and evolution in the Universe, ∼25 per cent of the cosmic energy density is in the form of cold dark matter and 70 per cent is dark energy in the form of cosmological constant, Λ. This makes up the ΛCDM model (e.g. Peebles, 1982; Blumenthal et al., 1984; Spergel et al., 2003).

In this cold dark matter and dark energy filled Universe, the fluctuations in the dark matter density cause instabilities and inevitably collapse due to gravity, forming dark matter haloes (e.g. Davis et al., 1985). These haloes grow through 'hierarchical assembly', where larger haloes are formed by the merging of smaller haloes (Blumenthal et al., 1984; Davis et al., 1985).

When an overdense region of dark matter and gas (primarily hydrogen and helium) collapses, the entropy of gas is increased due to strong shocks. The subsequent evolution of this gas is determined by the efficiency of cooling. If the cooling is inefficient, a gaseous pressure-supported halo may form. This gas eventually cools, loses pressure support and collapses onto a forming protogalaxy, which is known as the hot mode of accretion. If the gas cools in a short timescale compared to the dynamical time (time for the gas to collapse under gravity), gas accretes directly

onto a forming protogalaxy (White & Frenk, 1991; Birnboim & Dekel, 2003) along dense and relatively cold filaments (Kereš et al., 2005; Dekel et al., 2009; Ceverino et al., 2010). The gravity of the collapsed gas in the central regions of the halo may become dominant over the gravity of dark matter allowing further rapid cooling to form giant molecular clouds (GMCs). Some regions within these dense clouds then become dense enough to collapse and ignite nuclear fusion starting to form stars, and eventually galaxies (White & Rees, 1978).

Star and, subsequently, galaxy formation is surprisingly inefficient, with only ∼5–10 per cent of the total baryonic mass in the Universe in the form of stars and cold gas (Bell et al., 2003; Shull et al., 2012). This indicates that there must be significant feedback or suppression of gas cooling (and hence, star formation), preventing from transforming most of the gas to stars by the present day. Studies have shown that there are many processes which can potentially contribute to making star formation inefficient. These include feedback from massive stars and supernovae that are able to inject energy into the interstellar medium and, eventually, drive large-scale winds (Hopkins et al., 2012). Moreover, the majority of massive galaxies are expected to have a super-massive black hole (e.g. Kormendy & Richstone, 1995; Magorrian et al., 1998), which can produce high-velocity winds that might be able to eject material required for star formation from galaxies, as well as heat the halo gas preventing it from cooling and collapsing. Thus, the feedback activity from stars and active galactic nucleus (AGN) can have a significant impact on the ability of gas to cool and hence, galaxy formation and evolution (e.g. Bower et al., 2006).

1.3 Tracing galaxy properties

The evolution of a given galaxy is a complex interplay of many different factors and processes. Hence, a careful characterisation of the observed galaxy properties is required to gain an insight into the on-going processes across galaxies in the Hubble sequence, and hence understand how these morphologically different galaxies relate to each other.

Galaxies can be characterised by their spectral properties across the electromagnetic spectrum, so called spectral energy distributions (SEDs). SEDs of galaxies are a complex combination of the star-formation history (and AGN activity) and the amount and arrangement of stars, gas and dust in galaxies, and hence provide important clues on their formation and evolution. To study galaxy physical properties in detail, this information needs to be extracted through modelling of the observed SEDs.

To extract intrinsic galaxy properties, such as the stellar mass, star-formation history and age, recent models use an evolutionary synthesis technique (Bruzual A. & Charlot, 1993; Vazdekis, 1999; Bruzual & Charlot, 2003; Maraston, 2005) as shown in Fig. 1.3. Briefly, these models assume that a galaxy is a combination of Simple Stellar Populations (SSPs), which are groups of stars of the same age, in the same volume of space and formed from gas with a homogeneous chemical composition. The evolution of a given star depends on its initial mass and metallicity, hence stellar evolution models provide complete sets of stellar evolutionary tracks for stars of different mass and metallicity (e.g. Bertelli et al., 2008). To obtain an SED for a simple stellar population, three main parameters are required as shown in the top panels of Fig. 1.3. First, an initial mass function (IMF), which defines the total number of stars that are born in with initial masses in a given mass range, has to be adopted. Commonly used IMFs include Salpeter (1955), Kroupa (2001) and Chabrier (2003). Second, the stellar evolution theory in terms of isochrones, which gives the luminosity and effective temperature of a given population of stars of the same age and metallicity. Finally, theoretical and empirical spectral libraries are needed to convert such theoretical predicted quantities into observables (e.g. Rodríguez-Merino et al., 2005; Coelho et al., 2007). Using these three inputs, a grid of predicted SEDs for different age/metallicity SSPs are produced (see Fig. 1.3).

To obtain a galaxy integrated spectrum, SSPs have to be combined taking into account the star formation history (SFH), which describes the evolution of star-formation rate with time, and metallicity evolution. Since its real shape is unknown and is likely complex, the SFH of a given galaxy is usually parametrised by an

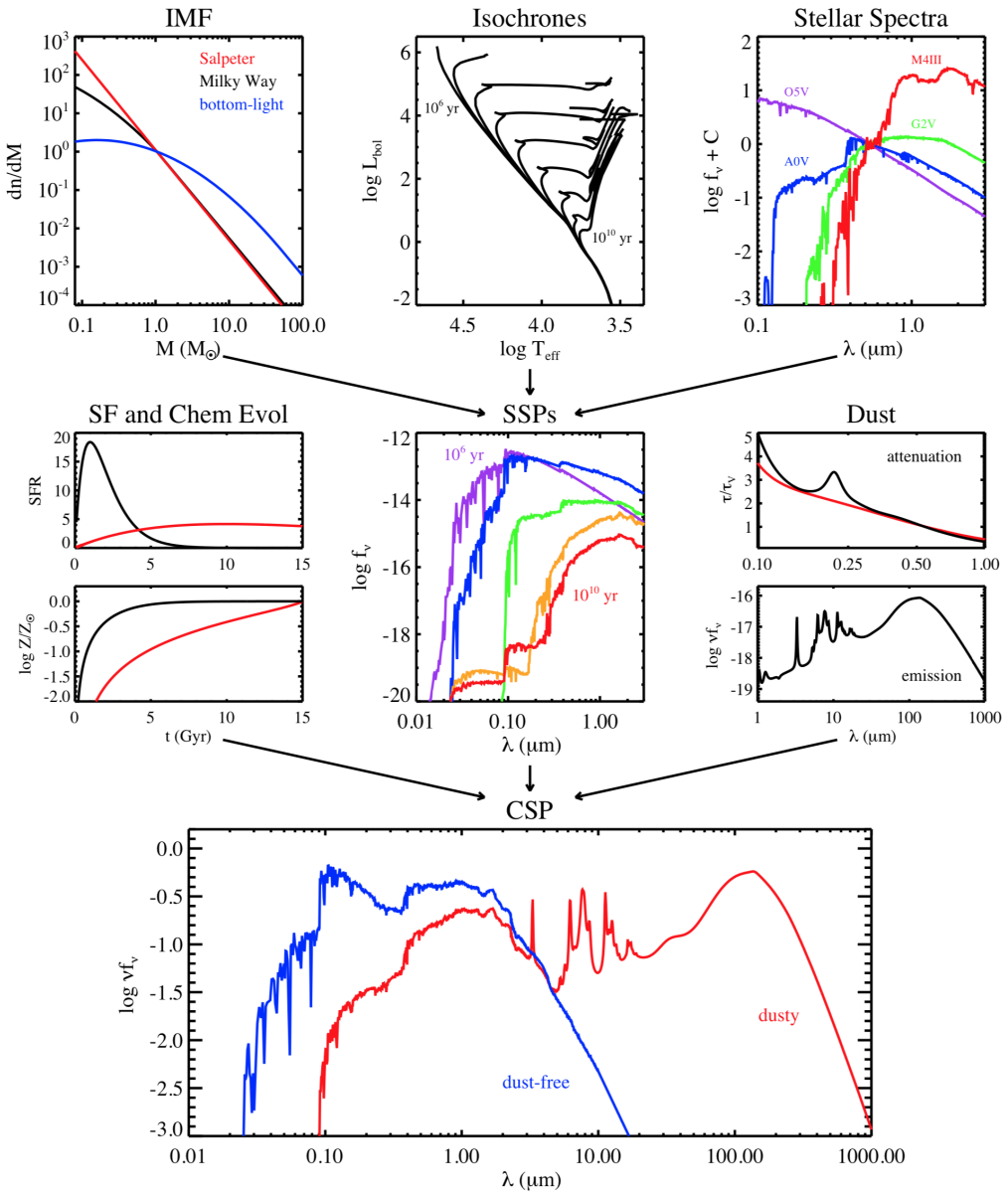

Figure 1.3: A schematic of a stellar population synthesis technique to model spectral energy distributions of galaxies from Conroy (2013). Simple stellar populations are constructed using isochrones for a range of ages/metallicities and spectral libraries, with an assumed IMF. The composite model SED is then constructed using an SFH and a chemical evolution model, together with a model for dust attenuation and emission. The bottom panel shows the unattenuated composite SED (blue) and attenuated SED (red), highlighting the effect of dust attenuation on the galaxy's SED.

analytic function that can take a range of assumed shapes: exponentially declining, constant, single burst component, or multiple component. The resulting galaxy SED is shown in blue in the bottom panel of Fig. 1.3.

One very important aspect to include when modelling the SED of a star-forming galaxy is attenuation by dust, which alters the shape of the integrated stellar emission, especially at UV/optical wavelengths, as well as the the reprocessed emission in the infrared (see § 1.3.3). For example, in the dusty (star-forming) SED in Fig. 1.3, three distinct components are visible: the stellar emission bump in the optical regime that is dimmer that that of a dust-free SED (due to dust attenuation), emission features in the mid-infrared and a peak of emission in the far-infrared (resulting from reprocessed emission from the UV/optical). For a detailed review on SED modelling, see Conroy (2013). In the rest of this section, we give a brief overview of some of the physical processes and their effect on the emission observed from a given galaxy, such as the one shown in Fig. 1.3.

1.3.1 Estimating stellar mass

The combined stellar spectra of individual stars in a galaxy are one of the main components of the UV/optical/near-infrared galaxy SED. As the star formation history of galaxies is imprinted in the integrated emitted light, photometric observations can be used to infer the stellar mass content of galaxies, with the use of stellar evolutionary models as described above. From the predicted composite SED, the best fit parameters, such as the age of the galaxy, dust attenuation and mass-to-light ratio can be extracted. Stellar mass is then estimated by combining the predicted mass-to-light ratio and the observed luminosity.

Of course this is a simplified view and a number of uncertainties and systematics have to be taken into account when estimating the stellar mass of a galaxy. Firstly, the uncertainties and different choices of model parameters in stellar population synthesis models, such as Bruzual & Charlot (2003) versus Maraston (2005), can lead to 50 per cent difference in the derived stellar mass, as highlighted by Hainline et al. (2011). Moreover the uncertainty in the IMF can result in significant

differences in the inferred stellar mass. Even minor differences in the IMF, such as using Chabrier (2003) IMF, instead of a Salpeter (1955) IMF, would result in ∼1.8 times higher derived stellar mass. As mentioned above, the SFH can be modelled analytically with a range of assumed shapes and these differences in the assumed model can lead to systematically-different inferred stellar masses. Finally, interpreting the UV/optical spectrum of a galaxy is a highly degenerate problem, with dust attenuation introducing another source of uncertainty in the derived stellar masses. Due to these systematics, the stellar mass estimates have a 0.2–0.3 dex uncertainty, therefore care must be taken when comparing samples from different studies.

1.3.2 Tracers of star formation

To quantify the rate at which a galaxy is converting the available gas to form stars, the emission from recently formed young stellar populations has to be identified. This can be achieved using several methods, depending on the available photometric and/or spectroscopic coverage (for a review, see Kennicutt & Evans, 2012).

In the absence of an unobscured AGN, the unattenuated galaxy spectrum at λ ∼1250-2500Å is dominated by the emission from young stars, and therefore provides a good tracer of the star-formation rate. For local studies, this wavelength range can only be probed reliably using space based observations (such as *GALEX*), however this emission shifts to the optical regime with increasing redshift making it accessible with ground based telescopes. Though this method is one of the most direct ways to measure the star-formation rate, it becomes increasingly uncertain for star-forming galaxies as UV emission is strongly attenuated by dust (see § 1.3.3), by typically 0.5–3 magnitudes for 'main-sequence' star-forming galaxies, but can be much higher for strongly dust-obscured galaxies, such as those usually selected in the far-infrared waveband (see § 1.5.2). Another source of uncertainty comes from the dependence of the derived star-formation rate on the assumed form of the IMF, as the integrated UV spectrum is dominated by stars with masses above $\sim 5\,M_{\odot}$ so there is a large extrapolation to lower stellar masses. AGN contamination is also

a concern for UV continuum measurements.

The high-energy UV radiation from the young, hot stars (OB type) is able to ionise the interstellar birth clouds of hydrogen gas that they reside in, forming HII regions. As the electrons recombine with ions and drops down the energy levels, emission is released at specific wavelengths (Osterbrock & Ferland, 2006). Hence, the flux of hydrogen recombination lines provides another tracer of the star-formation rate. Most studies of this method use the Hα (3→2 transition; $\lambda = 6562.8$Å) as star-formation indicator, as it is the brightest of the Balmer series, however other hydrogen recombination lines, such as Hβ (4→2 transition; $\lambda = 4861.4$Å), are also indicative of the ongoing star formation. Hydrogen recombination lines are the closest to a measurement of the instantaneous star formation because of the short lifetime (∼10 Myr) of the massive OB-type stars that dominate the UV continuum. Other spectral features, such as forbidden lines arising from electron decays from metastable states, are also indicative of rate of star formation, including [OII] doublet and [OIII]. These methods mainly suffer from the same uncertainties as the UV continuum method, mainly due to dust attenuation.

Since a significant fraction of stellar light in the UV/optical wavelengths is affected by dust attenuation (see § 1.3.3), the aforementioned methods become increasingly difficult and uncertain for dust-obscured star-forming galaxies (especially at high redshift, where the emission is even fainter due to cosmological dimming). The emission at wavelengths comparable to the dust grain size (∼0.001-1μm) is attenuated most effectively. As the dust grains cool, this radiation is re-emitted in the mid-/far-infrared wavelengths ($\lambda \sim$ 8-1000μm). Dust emission is thus a direct tracer of star formation for the dust-obscured star-forming systems (Kennicutt, 1998). The calibration from the far-infrared luminosity to star-formation rate has to assume not only an IMF and an SFH, but also a dust optical depth, which is hard to constrain at high redshift and thus assumptions have to be made, such as an optically thick dust component illuminated by young stars with a lifetime of ∼100 Myr, as in Kennicutt (1998). While the range of $\lambda \sim$ 8–1000μm is inclusive of all dust emission, such a wide wavelength range captures not only the cold diffuse

dust, but also the hot-dust and polycyclic aromatic hydrocarbon (PAH) emission in the mid-infrared. This mid-infrared emission is sensitive to non-star-formation driven processes, such as AGN heating. In fact, taking the whole infrared range, AGN can contribute up to ∼25 per cent to the far-infrared luminosity for star-forming sources (e.g. Kirkpatrick et al., 2015). Other ranges such as 40–120μm or 40–1000μm have also been used (e.g. Younger et al., 2009), however most of the literature still largely uses the whole infrared range.

If the wavelength coverage allows, the obscured (far-infrared) and un-obscured (UV or Hα) star formation indicators can be combined to infer the total star-formation rate of a galaxy (e.g. Kennicutt et al., 2009; Hao et al., 2011).

1.3.3 Dust attenuation and emission

Dust, while a small component of the overall baryonic mass of a galaxy, is a useful tracer of the ISM and has significant effects on the observed emission from galaxies as shown in Fig. 1.3. As galaxies form and evolve, their chemical composition evolves as well, with the interstellar medium becoming increasingly enriched with heavy metals. Thus, to obtain reliable measurements of stellar mass, star-formation rate and age of a given galaxy, the effect of dust on the UV/optical SED has to be taken into account.

Dust is primarily produced in low/intermediate mass asymptotic giant branch (AGB) stars (Gehrz, 1989; Sargent et al., 2010) and massive stars at the end of their lives when they explode as supernovae (SNe) (Rho et al., 2008; Dunne et al., 2009). Though dust includes a large range of complex molecules of different composition and sizes, the most commonly used model is that these dust grains primarily consist of amorphous silicates and carbonaceous material (e.g. Draine & Li, 2007). The presence of silicates and carbon was inferred from absorption features in the interstellar regions. The smallest carbon based grains are PAHs, which create the multiple absorption features in the mid-infrared of the SED of a galaxy (see Fig. 1.3). Dust grain sizes usually range between ∼0.001–1μm and size is very important as incident radiation is affected most strongly by grains of comparable

size to the wavelength of the radiation. Dust grains can scatter the radiation out of line of sight, as well as absorb it, reddening the spectrum (e.g. Calzetti, 2001). In addition, absorbed radiation causes the heating of the dust. Note that the geometry of the stars and dust has a significant effect on the observed SED, as the light can be scattered in as well as out of light of sight, and the net effect on the SED is then termed 'attenuation'.

The heated dust grain cool via thermal emission, emitting in the infrared wavelengths and this emission can be approximated by a modified blackbody:

$$S_\nu \propto (1 - e^{-\tau}) \times B_\nu(T), \tag{1.1}$$

where $B_\nu(T)$ is the Planck function, τ is the frequency-dependent optical depth of the dust of the form $\tau = \left(\frac{\nu}{\nu_0}\right)^\beta$, ν_0 is the frequency at which optical depth is equal to one and β is the dust emissivity index. This index is a function of frequency, and depends on the properties of the ISM (e.g. chemical composition, size and shape of dust grains). Small carbonaceous grains have $\beta \simeq 1$, and amorphous silicate grains have $\beta \simeq 2$ or higher, based on theoretical models and laboratory studies (e.g. Draine & Lee, 1984; Agladze et al., 1996), with some dependence on temperature. The temperature of the dust can be estimated using the peak wavelength of the infrared emission, which is at $\sim$100μm for T_d $\sim$30 K. Note though, that the peak of the dust SED is also affected by the optical depth. To measure the total dust mass, dust grain size and density must be assumed, together with a mass absorption coefficient, k_ν. For a simple optically thin case, if the rest-frame luminosity at a given far-infrared wavelength is known:

$$M_d = \frac{L_\nu}{4\pi k_\nu B_\nu(T)} \tag{1.2}$$

for emission that is isotropic over a spherical surface.

The derivation of dust mass not only provides information about the ISM of galaxies, but can also be used to derive gas mass via an assumed constant gas-to-dust

ratio (e.g. Eales et al., 2012; Magdis et al., 2012). Though molecular gas is generally probed using measurements of the intensity of the rotational transitions of CO, together with a CO-to-H_2 ratio (for a review, see Bolatto et al., 2013), detections of star-forming galaxies at high redshift are still limited to modest statistics and mostly to luminous galaxies (see Carilli & Walter, 2013, for a review). Therefore, a faster way to gain information about the gas content of galaxies, given they have far-infrared photometric coverage, is to adopt a gas-to-dust ratio. However, gas-to-dust ratios are only reliably constrained in the Milky Way molecular clouds, where reliable measures for both, dust mass and molecular gas masses from millimeter lines are available. A gas-to-dust ratio of 100 is considered to be the average value for most local, metal-rich galaxies (e.g Draine et al., 2007; Rémy-Ruyer et al., 2014). Studies of local galaxies have shown that the gas-to-dust ratio is a function of metallicity, increasing as the metallicity decreases (Leroy et al., 2011), which has possible implications for high-redshift studies where the mass-metallicity relations are not well constrained.

1.3.4 General types of observed galaxy SEDs

The combined effects of the processes discussed above are apparent in the galaxy SEDs, as shown in Fig. 1.4. Elliptical galaxies are gas-poor, have no on-going star formation and are composed mainly of old stellar populations. They have little to no dust and have prominent stellar emission leading to a very high UV-to-infrared luminosity ratio ($L_{0.2-1\mu\mathrm{m}}/L_{8-1000\mu\mathrm{m}}$), shown in Fig. 1.4. The variation of the $L_{0.2-1\mu\mathrm{m}}/L_{8-1000\mu\mathrm{m}}$ ratio is clearly visible as star-formation activity increases. A typical star-forming galaxy SED (M 101) has a lower $L_{0.2-1\mu\mathrm{m}}/L_{8-1000\mu\mathrm{m}}$ ratio than an elliptical galaxy. This ratio is approximately equal to one for a starburst (M 82), indicating that this type of galaxy has higher dust attenuation and emits a similar fraction of the total luminosity in the infrared. Ultra-luminous infra-red galaxies (ULIRGs) have the lowest $L_{0.2-1\mu m}/L_{8-1000\mu m}$ ratio due to their highly obscured nature and strong star formation. The figure highlights that multi-wavelength observations allows us to distinguish between different galaxy populations and probe

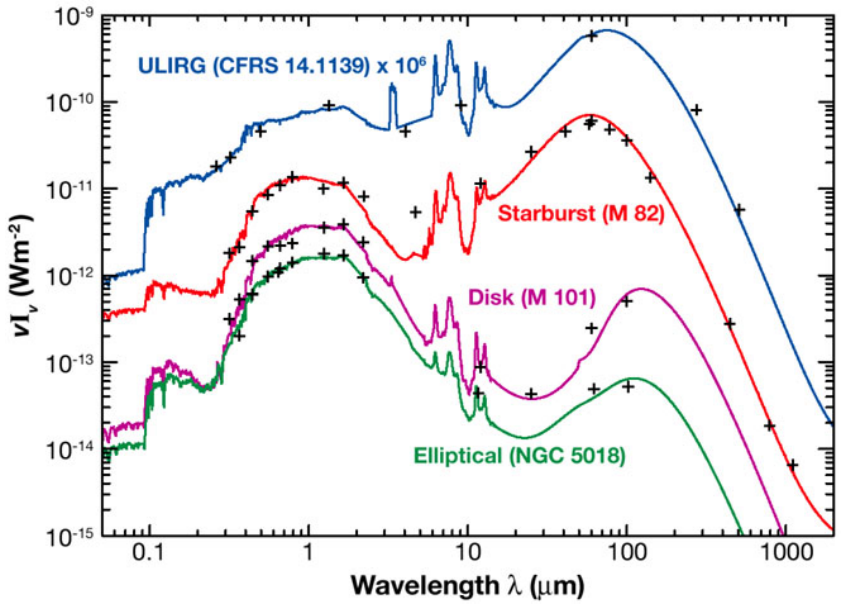

Figure 1.4: Comparison of rest-frame spectral energy distributions of typical elliptical, spiral, starburst and ULIRG galaxies in the local Universe from Lagache et al. (2005). The SEDs show that UV-to-infrared luminosity ratio decreases with increasing star formation (elliptical to ULIRG). Moreover, the stellar emission region in the optical wavelengths is less pronounced as the dust attenuation increases with star formation.

their physical properties to understand their evolution.

1.4 Redshift evolution of galaxy properties

To gain a better understanding of how galaxies evolve over time and form the well-defined Hubble sequence in the present day, it is crucial to study galaxies locally as well as in the distant Universe. Our understanding of high-redshift galaxies and their properties has advanced significantly in the past few decades, owing largely to the technological advances. For example, major advances in understanding galaxy morphologies at higher redshifts came from *HST*, allowing detailed studies, e.g. on 200 pc scales at $z \sim 1$, to trace how morphologies evolve with cosmic time. These studies allowed to identify a transformation from single (either bulge or disc) to two component (bulge and disc) systems at $z \sim 2$ (e.g. Sachdeva et al., 2019). Moreover, dynamical studies have shown that high-redshift star-forming galaxies are, on average, more turbulent and gas rich (Bouché et al., 2007; Genzel et al.,

2011; Wisnioski et al., 2015; Johnson et al., 2018) than comparable galaxies at low redshift. Therefore, there appears to be a transition from irregular morphologies to smooth, rotation-dominted galaxies at around $z \sim 1.5$, which is suggested to be the epoch when the Hubble Sequence emerged (Cowie et al., 1995; Conselice et al., 2011; Gillman et al., 2020), with the diversity of galaxy morphologies seen today reflecting the sum of the multiple evolutionary paths. This transition is also reflected in the physical properties of galaxies, such as star-formation rate, stellar mass and gas fractions. In this section, we give a brief overview of each of these key galaxy properties.

1.4.1 Star-formation rate density

An effective way to trace the stellar evolution through cosmic time is through the evolution of cosmic star-formation rate. In the past 20+ years, various studies have allowed to constrain the total star-formation rate density over a wide redshift range (summarised in Madau & Dickinson, 2014). Early studies were based on observations in the rest-frame UV (Lilly et al., 1996; Madau et al., 1996; Bouwens et al., 2012), indicating a peak around $z \sim$1. More recent studies in the infrared (Magnelli et al., 2011; Gruppioni et al., 2013; Bouwens et al., 2016; Novak et al., 2017), placed further constraints and the combined data shows that the cosmic star-formation rate density peaked at $z \sim$1.5–2, around 3.5 Gyr after the Big Bang (see Fig. 1.5). Fig. 1.5 shows that the total star-formation rate has declined by a factor of $\sim$10 to the present day, implying that as much as half of the stellar mass observed in local galaxies, was built up in a short timescale of around $\sim$3.5 Gyr, between $z \sim$1–3. This highlights the importance of studying star-forming galaxies across the cosmic noon, during the peak of cosmic star formation, to better understand the processes leading to the galaxies we observe today.

1.4.2 Evolution of gas fraction and total gas density

To better understand the driving mechanisms of the elevated star formation in the distant past, many recent studies have focused on molecular gas studies of galaxies

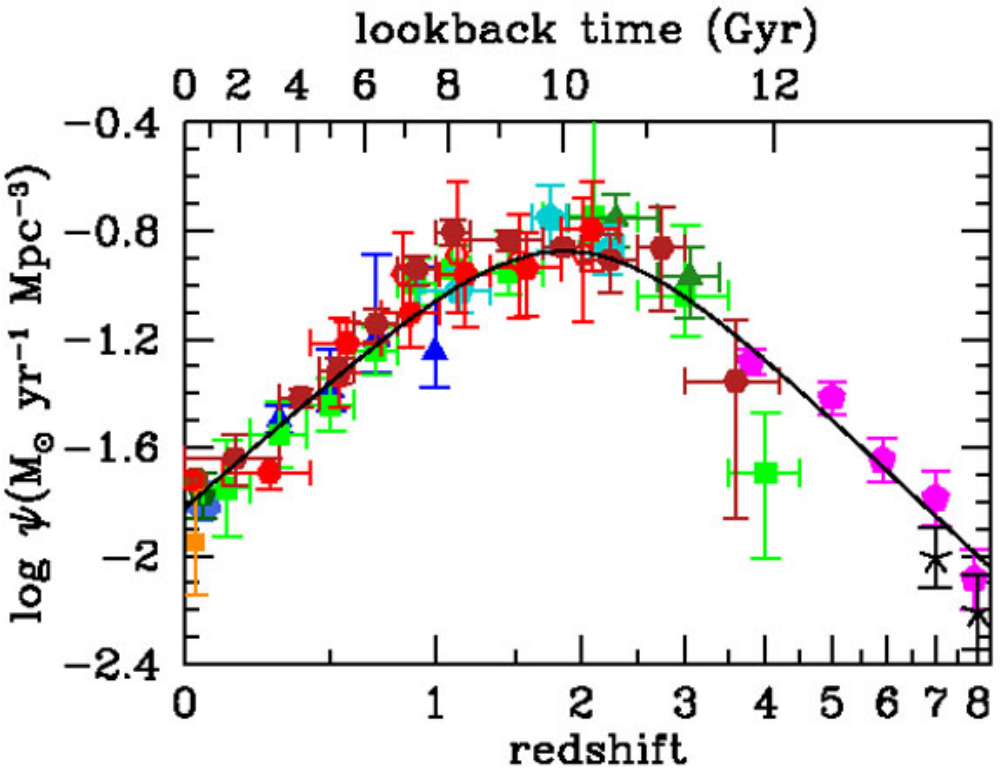

Figure 1.5: The redshift evolution of star-formation rate density from Madau & Dickinson (2014). The measurements are a combination of UV and infrared studies, showing that star formation activity in the Universe peaked around 10 Gyr ago, when the Universe was ∼25 percent its current age, at z ∼2. This epoch is commonly defined as the “cosmic noon".

at different redshifts (Genzel et al., 2010; Lagos et al., 2011, 2015; Tacconi et al., 2018; Scoville et al., 2017; Decarli et al., 2019). Investigating the cold gas and its evolution with redshift gives an indication of how efficiently stars are formed from the available gas reservoir and allows us to better understand how star formation proceeds across cosmic epochs. These studies have shown that galaxies in the distant Universe have larger gas-to-stellar mass ratio ($\mu_{\rm gas} = M_{\rm gas}/M_*$; see Fig. 1.6) than comparably massive galaxies today. Another important quantity to characterise star formation in galaxies is the ratio of the molecular gas mass to the star-formation rate, termed gas depletion timescale ($t_{\rm dep} = M_{\rm gas}/SFR$). This ratio expresses the time in which a molecular gas reservoir would be depleted by current star-formation activity (assuming no mass loss to the ISM). As shown in

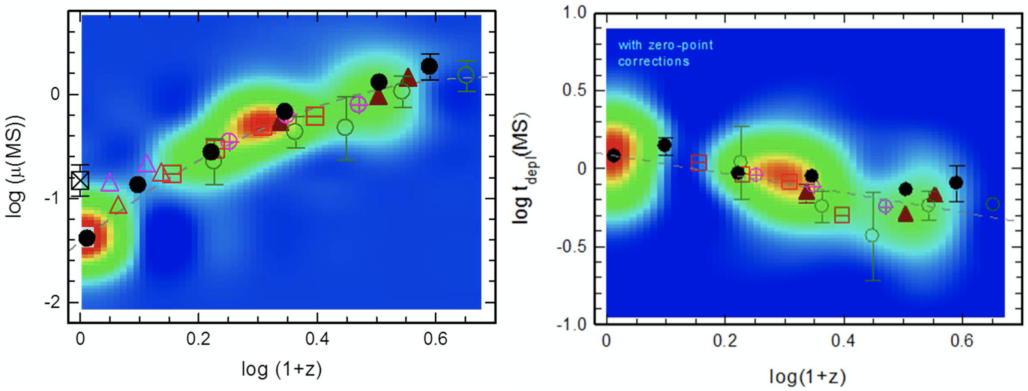

Figure 1.6: The gas-to-stellar mass ratio (left) and gas depletion timescale (right) as a function of redshift from (Tacconi et al., 2018).

Fig. 1.6, the decrease in the gas depletion timescale (indicative of star-formation efficiency of a galaxy) with redshift appears to be relatively small. These results suggest that star formation processes might be similar at low and high redshift, but galaxies in the distant Universe have more massive gas reservoirs leading to elevated star formation. Similarly, analysis of simulated galaxies observe higher gas fractions and decreasing depletion timescales with increasing redshift (e.g. Lagos et al., 2015).

The global evolution of the gas reservoirs in galaxies can be assesed through the cosmic atomic and molecular gas densities. Atomic gas is traced by HI 21 cm emission, which becomes increasingly faint at higher redshift and therefore can only be reliably assessed up to $z \sim 0.5$ (or $z \lesssim 1$ through stacking analysis) (Braun, 2012; Kanekar et al., 2016; Jones et al., 2018; Bera et al., 2019). At higher redshifts, damped Lyα systems (DLAs) can yield estimates of atomic gas density, though the systematic biases in this are still poorly understood (Jorgenson et al., 2006; Krogager et al., 2019). Fig. 1.7 shows that the atomic gas density is approximately constant with redshift, with a slight decrease below $z \sim 2$. Note though that HI emission arises from a more extended reservoir compared to the star formation (Walter et al., 2008; Leroy et al., 2009). Molecular gas (H_2) is more centrally-concentrated, thus its density is expected to trace the total star-formation rate density better. Fig. 1.7 shows the combined results from dust-continuum and CO-based measurements of the molecular gas component (summarised in Walter et al.,

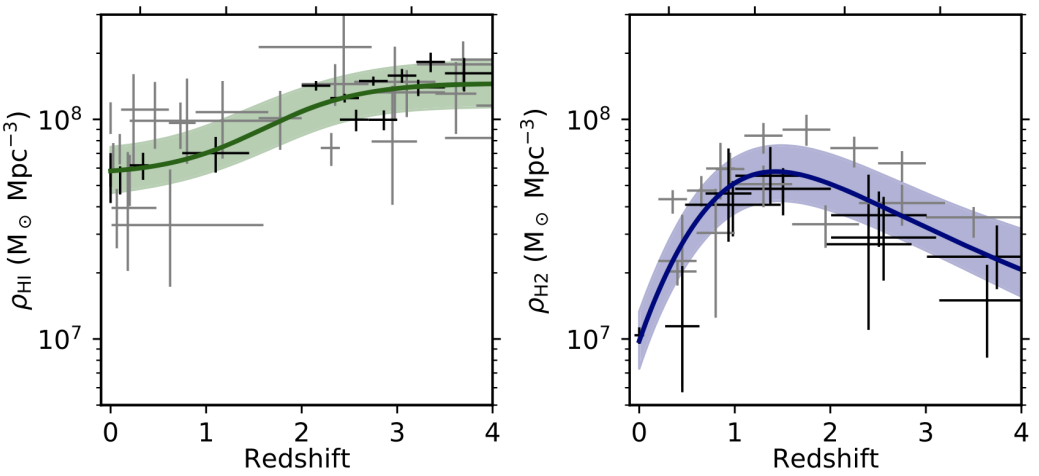

Figure 1.7: Redshift evolution of atomic (left) and molecular (right) gas density compiled by (Walter et al., 2020). The cosmic density of neutral atomic gas remains approximately constant at high redshift, and declines only slightly (a factor of ∼2) from z ∼3 to present day. Molecular gas density decreases by a factor of ∼6 from the peak at z ∼2. The overall shape of the molecular gas density follows the star-formation rate density well.

2020). The cosmic molecular gas density is lower than the atomic gas density at all redshifts, approaching equality at z ∼1.5. Currently, results suggest that the cosmic density of molecular gas decreases significantly (a factor of ∼6) from the peak at z ∼2 to the present day (for a review, see Tacconi et al., 2020).

Taken together, high redshift galaxies have higher star-formation rates (Fig. 1.5), higher molecular gas fractions (Fig 1.6) and higher total gas density (Fig 1.7), highlighting the critical importance of studies of distant galaxies and their ISM in order to better understand the evolution of galaxies.

1.4.3 The main-sequence of star-forming galaxies

As well as addressing the properties of galaxies integrated over cosmic time, studies have been able to investigate scaling relations for galaxies at increasingly high redshifts, such as the apparently nearly linear relation between star-formation rate and stellar mass followed by the the vast majority of star-forming galaxies, known as the 'main-sequence' (see Fig. 1.8). This relation was first claimed for local galaxies by the Sloan Digital Sky Survey (SDSS; Brinchmann et al., 2004) and later studies suggested that this relation is visible out to at least z ∼ 5 (Daddi

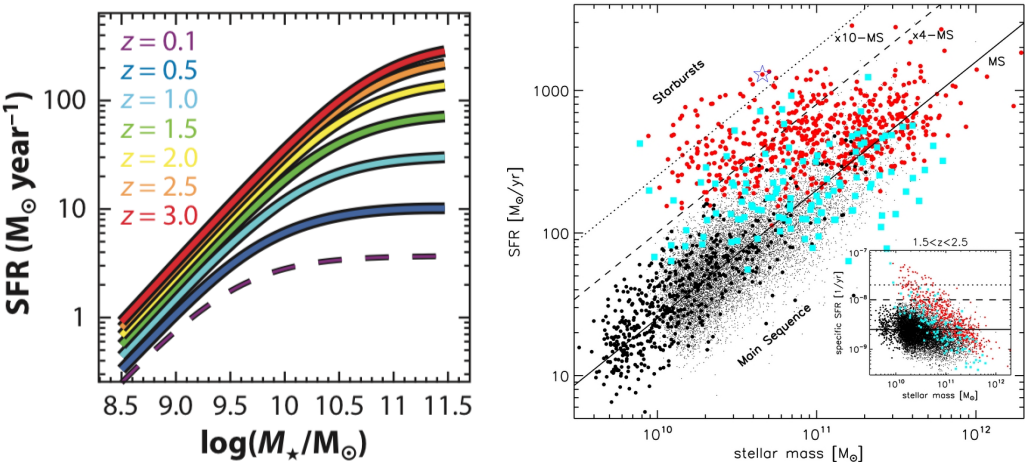

Figure 1.8: **Left:** Star-formation rate as a function of stellar mass for 'main-sequence' galaxies at different cosmic epochs from Förster Schreiber & Wuyts (2020). This highlights the evolution in the normalisation and shape with increasing redshift. **Right:** Star-formation rate versus stellar mass at $z = 1.5$–2.5 from Rodighiero et al. (2011). BzK-selected (see § 1.5.1) galaxies are shown in black and are representative of the 'main-sequence'. The cyan and red shows data with *Herschel* PACS far-infrared detections. The dashed line shows the empirical boundary (sSFR 4 times above the 'main-sequence') which is used to classify the star-burst mode galaxies.

et al., 2007; Rodighiero et al., 2011; Speagle et al., 2014; Rodighiero et al., 2014; Renzini & Peng, 2015; Schreiber et al., 2017). The main characteristics claimed for this relation is a tight scatter of ∼0.2-0.3 dex across a wide range of stellar masses and redshifts, flattening of the slope at the high mass end (especially at lower redshifts) and an evolution in the normalisation with redshift (see Fig. 1.8; Whitaker et al., 2014; Förster Schreiber & Wuyts, 2020).

However, it is important to note that the scatter, slope and normalisation of the derived 'main-sequence' can be affected by the choice of the wavelength that the galaxy is selected in and/or star-formation tracers adopted, as well as uncertainties in the derived star-formation rates and stellar masses. For example, the inferred slope may vary between 0.8–1 due to different colour cuts in star-forming population selection (Whitaker et al., 2012; Rodighiero et al., 2014; Johnston et al., 2015). However, the more the dynamic range in stellar mass is constrained (and is complete), the more consistent relation can be derived for a variety of star-forming tracers (Rodighiero et al., 2011).

The existence of 'main-sequence' for star-forming galaxies with a tight scatter has been interpreted as the indication that star formation in the majority of star-forming galaxies is a fairly ordered process occurring over long timescales, with not many galaxies experiencing bursts of star formation that might be expected from stochastic processes such as merger events, unless the duty cycles are very short (Rodighiero et al., 2011; Schreiber et al., 2015). Moreover, the claimed evolution in the normalisation indicates that star-forming galaxies in the distant Universe have higher specific star-formation rate ($sSFR = SFR/M_*$) reflecting the evolution of the star-formation rate density shown in Fig. 1.5 (Renzini, 2016).

1.5 Selection of galaxies across the 'main-sequence'

The wealth of multi-wavelength data covering multiple extragalactic fields, due to technological advances across the whole observable wavelength range, has allowed us to achieve major advances in our knowledge about galaxies across cosmic time. This includes fields targeted by the UKIDSS Ultra-Deep Survey (UDS; Lawrence et al., 2007); the Cosmic Evolution Survey (COSMOS; Scoville et al., 2007); Great Observatories Origins Deep Survey (GOODS; Dickinson et al., 2003); and All-Wavelength Extended Groth Strip International Survey (AEGIS; Davis et al., 2007). Our understanding of galaxies has advanced from just the identification of galaxies from photometric samples to spectroscopic confirmation and detailed follow-up with spatially or spectroscopically resolved measurements. The increased photometric coverage of the targets has allowed efficient methods for galaxy classifications over a wide range of redshift based on their physical properties. In this section, we briefly review the effects and biases in selecting star-forming galaxies in the optical and infrared wavelengths.

1.5.1 Selection of galaxies in the optical/near-infrared wavelengths

Observations in the optical/near-infrared with ground-based instruments, such as VISTA , Subaru, CFHT, as well as space-based *HST* and *Spitzer*, have allowed wide coverage of the rest-frame UV to near-infrared emission from galaxies, which is sensitive to the shape of the stellar continuum as well as the attenuation by dust in the interstellar medium (ISM). Selection in the optical wavelengths samples the stellar emission of galaxies and thus can be used to construct mass-selected samples (though note that is only applicable for galaxies with low dust attenuation, Fig. 1.4). For example, a galaxy population selected with K_s =25 mag corresponds to (90 per cent completeness) limit of M_*=$10^{8.5}$, $10^{9.5}$, $10^{10}\,\mathrm{M}_\odot$ at $z\sim$1, 2, 3, respectively (Tomczak et al., 2016).

The availability of multi-color information allows for diagnostic methods to identify high-redshift star-forming galaxies, such as criteria based on $(B-z)$ and $(z-K)$ (BzK; Daddi et al., 2004), $(U-V)$ and $(V-J)$ (UVJ; Whitaker et al., 2012), or (8μm-4.5μm) and (5.8μm-3.6μm) (Donley et al., 2012) colours. The first two criteria are widely used to distinguish between star-forming and quiescent galaxies, while the latter helps identify AGN from star-forming galaxies. Star-forming galaxies selected from optical samples using these colour criteria typically have star-formation rates in range of SFR$\sim$ 10–100 $\mathrm{M}_\odot\mathrm{yr}^{-1}$, corresponding to far-infrared luminosities of $L_{\mathrm{FIR}}\sim5\times10^{10-11}\,\mathrm{L}_\odot$.

Many studies have investigated the 'main-sequence' of star-forming galaxies using optically selected samples, to determine their physical properties and evolution across cosmic time (see Förster Schreiber & Wuyts, 2020, for a review). These studies have revealed that the properties of galaxies within the 'main-sequence' appears to evolve with redshift, with galaxies at higher redshift having a higher fraction of irregular morphologies and higher turbulence than the local galaxies (Wisnioski et al., 2015; Harrison et al., 2017), which is likely due to the higher gas fraction in these systems (see § 1.4; Fig. 1.6).

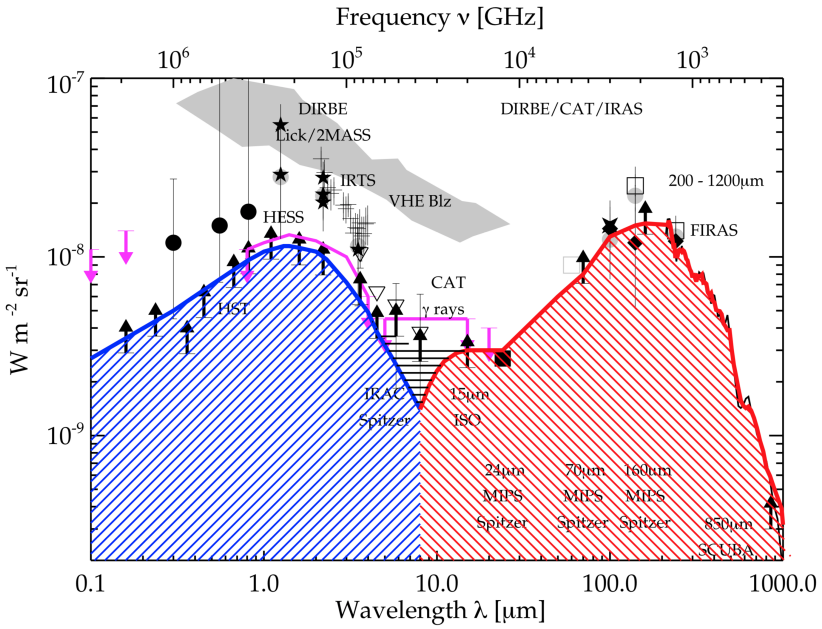

Figure 1.9: The total extragalactic energy density as a function of wavelength from Dole et al. (2006). The blue region indicates the optical background, while the red region shows the infra-red background. Results indicate that the Universe is emitting a comparable energy density in the far-infrared as it does in the optical, highlighting the importance of studying both optically-selected populations as well as dust-obscured systems to get a complete view of star formation across cosmic time.

1.5.2 Selection of galaxies in the far-infrared

Analysis of the relative brightness of the extragalactic background in the UV/optical and far-infrared/sub-millimetre suggests that around half of all of the star formation that has occurred over the history of the Universe was obscured by dust (e.g. Puget et al., 1996), as shown in Fig. 1.9. This far-infrared/sub-millimetre emission is expected to primarily comprise the reprocessing of UV emission from young, massive stars by dust grains in the interstellar medium of distant galaxies, which is re-emitted in the form of far-infrared/sub-millimetre photons as the grains cool. The importance of accounting for this dust-obscured component of star formation is amplified at higher redshift, across the cosmic noon $z \sim 1$–3 (see Fig. 1.5). Therefore, understanding the nature, origin, and evolution of this dust-obscured activity in galaxies is crucial for obtaining a complete understanding of the star formation activity in the distant Universe (see Casey et al. 2014 for a review).

1.5.2. Selection of galaxies in the far-infrared

In the mid-1990s, the first surveys at sub-millimetre wavelengths (450 μm and 850 μm) using the Sub-millimeter Common User Bolometric Array (SCUBA) on James Clerk Maxwell Telescope (JCMT) began to resolve this far-infrared/sub-millimetre background into its constituent galaxies and identified the first statistical samples of high-redshift, sub-millimetre bright galaxies (SMGs – Smail et al. 1997; Hughes et al. 1998; Barger et al. 1998; Eales et al. 1999).

As a result of strong dust-obscuration of their star-forming regions, these galaxies radiate a significant amount of their bolometric luminosity in the mid-/far-infrared. Due to their relative faintness in UV/optical wavebands they are most easily identified through surveys in the far-infrared waveband. Ground-based observations in the infrared are only possible in certain 'atmospheric windows', which is a range of wavelengths over which there is relatively little absorption of radiation by molecules in the atmosphere, such as H_2O. Thus, studies of high-redshift dust-obscured sources have been undertaken around ∼350-450μm (e.g. Eales et al., 2010; Oliver et al., 2012; Wang et al., 2014; Valiante et al., 2016; Casey et al., 2013; Geach et al., 2013; Roseboom et al., 2013; Zavala et al., 2014, 2017; Bourne et al., 2017; Lim et al., 2020). As the transmission improves in the sub-millimetre/radio wavelengths, 850μm-1.3 mm wavebands are also used to select these dusty strongly star-forming sources (e.g. Coppin et al., 2006; Scott et al., 2008; Weiß et al., 2009; Hatsukade et al., 2011; Mocanu et al., 2013; Umehata et al., 2014; Geach et al., 2017; Miettinen et al., 2017; Cowie et al., 2018; Stach et al., 2019; Simpson et al., 2020).

These studies have shown that SMGs represent a population of particularly dusty, high-infrared luminosity systems ($> 10^{11-12}\,L_\odot$) that are typically found at high redshift ($z \sim 1$–4). These galaxies have large gas reservoirs (Frayer et al., 1998; Greve et al., 2005; Bothwell et al., 2013), stellar masses of the order of $10^{10-11}\,M_\odot$ and can reach very high star-formation rates up to (and in some cases in excess of) $\sim 1{,}000\,M_\odot\,yr^{-1}$. SMGs have some observational properties that appear similar to those of local ULIRGs, such as high far-infrared luminosities and star-formation rates; however, their space densities are a factor of $\sim 1{,}000\times$ higher than the com-

parably luminous local population (e.g. Smail et al., 1997; Chapman et al., 2005; Simpson et al., 2014). This highlights the cosmological significance of far-infrared-luminous galaxies, in particular their potentially significant contribution to the star-formation rate density at high redshifts (see Madau & Dickinson, 2014). With such high star formation rates, and perhaps merger induced activity, some studies have suggested that SMGs lie above the main sequence, although the relatively small sample sizes mean that firm conclusions are limited, and we will address this in the subsequent chapters of this thesis.

1.6 Thesis overview

The aim of this thesis is to probe the formation and evolution of galaxies by analysing samples of high-redshift galaxies with a range of physical properties, from typical star-forming 'main-sequence' sources to dust-obscured strongly star-forming galaxies. We aim to address how the properties of galaxies vary as a function of star-formation rate, especially for the most intense star-forming galaxies and those at high redshifts ($z > 2$), to probe whether such intense star-formation is due to a distinct staburst mode of star-formation, or whether it could be driven by the same processes as in the less active systems. We wish to test if dust-selected samples could be used to trace gas reservoirs and build-up of dust mass in star-forming galaxies across cosmic time, as well as when and why this dust-obscured activity begins to dominate galaxy evolution. Finally, we also aim to examine spatially resolved physical properties of galaxies to probe the growth, activity and evolution of star-forming galaxies at high redshift.

Chapters 2, 3, and 4 are comprised of published work, while Chapter 5 is an ongoing study. A brief overview of each science chapter is given below.

Chapter 2 presents the testing and calibration of a spectral energy distribution (SED) fitting code, to understand the capabilities and shortcomings of such codes and test the robustness of the derived physical properties of high redshift galaxies. Analysis includes a comparison with simulations to test for any systematics,

applying SED modelling to ∼9,000 galaxies from the EAGLE hydrodynamical simulation. We then apply the code to 707 ALMA-detected dust-obscured strongly star-forming galaxies, as well as ∼300,000 K-selected star-forming 'main-sequence' galaxies in the UDS field, to compare the derived physical properties to the observed photometry to confirm the reliability of the code for high-redshift galaxies.

Chapter 3 comprises of a detailed study of the physical properties of the 707 sub-millimetre galaxies from the AS2UDS survey (Stach et al., 2019), which were derived using the SED fitting-code in Chapter 2. Since the 870μm-selected population includes some of the most strongly star-forming galaxies in the history of the Universe, in this chapter we aim to gain a better understanding of the physical properties and the evolution of these systems and the role of the sub-millimetre bright phase in the wider context of galaxy formation and evolution.

Chapter 4 combines and compares 450μm- and 850μm-selected surveys to provide a more complete view of luminous far-infrared activity in the Universe over a wider redshift range than possible with either individual sample. The relationship between samples selected at 450- and 850-μm is examined by comparing the physical properties of the galaxies, that were analysed in a consistent manner using the same methodology. Construction of a wavelength- and dust-mass-matched sample at $z = 1$–2 and $z = 3$–4 made it possible to probe the evolution of a uniform sample of dusty star-forming galaxies spanning the cosmic noon era.

Chapter 5 presents the on-going study of the initial data from the KMOS Ultra-deep Rotational Velocity Survey (KURVS, PI: A.M. Swinbank). The studied sample consists of very deep (∼80 h on source integration) KMOS observations of 19 'main-sequence' star-forming galaxies at $z \sim 1.5$. This survey is ∼10 times deeper than previous studies at this redshift, allowing us to trace Hα emission in individual galaxies out to ∼15 kpc. The total dynamical mass profiles extracted from the Hα rotation curves are deconstructed into the baryonic and dark matter components with the use of spatially resolved 2D stellar mass maps of galaxies that are derived by fitting pixel level SEDs to the available HST photometry.

The main results and conclusions are presented in Chapter 6, where we also discuss

on-going studies and future follow-up projects to help gain a better understanding of the formation and evolution of star-forming galaxies in the distant Universe.

Chapter 2

Testing and calibration of an SED fitting code for high redshift galaxies

Preamble

In this chapter we test an SED fitting code, MAGPHYS (da Cunha et al., 2015), for use in modelling the photometric data of dusty star-forming galaxies at high redshift. We examine the code using $\sim$9,000 galaxies from the EAGLE simulations, $\sim$300,000 'main-sequence' star-forming galaxies and $\sim$700 dusty star-forming galaxies. We compare the derived properties to the observed photometry and confirm the reliability of the code to derive the photometric redshift and physical properties of dust-obscured star-forming galaxies at high redshift. This work has been published as part of a first author paper (Dudzevičiūtė et al., 2020).

2.1 Introduction

The spectral energy distributions (SEDs) of galaxies are essential for studying the properties of galaxies, and through that, their formation and evolution. They contain information about the stellar, gaseous and dust components, giving an

insight into the environment of the galaxies and the stage of their evolution. The stellar emission is probed by rest-frame UV, optical and near-infrared emission, which provides information on the past star formation history, chemical enrichment and attenuation of starlight by dust. The mid- and far-infrared emission reflects the heating of dust in the birth clouds and the diffuse interstellar medium (ISM) by stars of all ages as well as obscured AGN. The far-infrared/sub-millimetre emission reveals information about the cold dust and gas reservoirs. Large scale surveys at these wavelength ranges are becoming increasingly common. For example, Galaxy Evolution Explorer (GALEX; Martin et al., 2005) in UV; Sloan Digital Sky Survey (SDSS; Stoughton et al., 2002) in the optical; Two Micron All Sky Survey (2MASS; Skrutskie et al., 1997) in the near-IR; *Herschel* Astrophysical Terahertz Large Area Survey (H-ATLAS; Eales et al., 2010) and *Herschel* Multi-tiered Extragalactic Survey (HerMES; Oliver et al., 2012) in the far-infrared.

Modelling the SEDs requires consistency in combining the emission from stars and dust in galaxies, which can be approached in a few different ways. Detailed radiative transfer models of idealised spatial distributions of stars and dust model the complex stellar and dust emission from stars, molecular clouds and dust grains over a wide range of galaxy geometries and luminosities. These models include many features, such as spectral and chemical evolution of stellar population (eg. Silva et al., 1998), and also nebular emission modelling and dynamic evolution of HII regions (eg. Dopita et al., 2005). Though increasingly higher redshift galaxies have extensive multi-wavelength data, it is not possible to conduct intricate analysis that would disentangle effects such as geometry and optical depth. A simpler approach is to use empirical templates from various dust emission curves with an assumption about the dust mass distributions and dust temperatures (power-law, blackbody, modified blackbody, two-temperature modified blackbody) over a wide range of radiation fields (e.g. Dale et al., 2001; Draine & Li, 2007; Rieke et al., 2009; Casey et al., 2012).

In Chapters 3& 4 of this thesis, we analyse dusty star-forming galaxies at high redshift; systems where coupling between the stellar and dust emission is very im-

portant to take into account. Thus, to constrain the physical properties of these high redshift dust-obscured systems, we consider a model that uses an energy balance technique. An energy balance technique combines the attenuation of the stellar emission in the UV/optical and near-infrared by dust, and the re-radiation of this energy in the far-infrared. This approach provides several significant advances compared to modelling the optical and infrared wavelengths separately (e.g. Simpson et al., 2014; Swinbank et al., 2014), allowing more control of the covariance between parameters and generally providing more robust constraints on the photometric redshift and physical parameters (e.g. stellar masses, and star-formation rates). However, the modelling assumes that sub-millimetre and optical emission arises from a region of comparable size, which is likely to be a simplification. There are a few models that use an energy balance technique, for example MAGPHYS and CIGALE, which are largely empirical but physically motivated models that consistently fit rest-frame SEDs from the optical to radio wavelengths.

Throughout the thesis, we consistently use MAGPHYS for all of our analysis to avoid any systematic differences due to the SED modelling. In this chapter we test and calibrate MAGPHYS, for use in modelling high redshift galaxy samples, which we discuss in Chapter 3, 4 and 5, by constructing the UV-to-radio SEDs using the available multi-wavelength photometry. We use the updated MAGPHYS code from da Cunha et al. (2015) and Battisti et al. (2019) to model SEDs of these SMGs, as it is optimised to model the photometry of high redshift ($z > 1$) star-forming galaxies. This code includes modifications such as extended prior distributions of star-formation history and dust optical depth effects, as well as the inclusion of intergalactic medium absorption of UV photons. The Battisti et al. (2019) version also includes photometric redshift as a variable which we use in Chapters 3 and 4.

The chapter is structured as follows. In § 2.2 we describe the MAGPHYS model and the SED fitting procedure, and test the systematic uncertainties on the derived physical properties with ∼9000 galaxies from the EAGLE simulation. We describe the samples of SMGs and 'main-sequence' galaxies in § 2.3, before we test the robustness of the code in derived the physical properties of these high-redshift

sources in § 2.4. The conclusions are presented in § 2.5.

2.2 MAGPHYS: testing the systematics

Before we can apply MAGPHYS to samples of high-redshift star-forming galaxies, we briefly review the most important aspects of the model that are likely to affect our conclusions and check for any systematic uncertainties in the derived physical properties by fitting the SEDs of simulated galaxies.

The full description of the MAGPHYS SED fitting code is available in da Cunha et al. (2008, 2015) and Battisti et al. (2019). Briefly, MAGPHYS uses stellar population models from Bruzual & Charlot (2003), a Chabrier IMF (Chabrier, 2003) and metallicities that vary uniformly from 0.2 to 2 times solar. Star-formation histories are modelled as continuous delayed exponential functions (Lee et al., 2010) with the peak of star formation occurring in range of 0.7–13.3 Gyr after the onset of star formation. The age is drawn randomly in the range of 0.1–10 Gyrs. To model starbursts, MAGPHYS also superimposes bursts on top of the star-formation history. These bursts are added randomly, but with a 75 per cent probability that they occurred within the previous 2 Gyr. The duration of these bursts varies in range of 30 – 300 Myr with a total mass formed in stars varying from 0.1 to 100 × the mass formed by the underlying continuous model. In this way, starbursts, as well as more quiescent galaxies, can be modelled. We note that the star-formation rate returned from MAGPHYS for a given model is defined as the average of the star-formation history over the last 100 Myr.

The far-infrared emission from dust in MAGPHYS is determined self-consistently from the dust attenuated stellar emission. Dust attenuation is modelled using two components following Charlot & Fall (2000): a dust model for young stars that are still deeply embedded in their birth clouds; and a dust model for the intermediate/old stars in the diffuse ISM. The far-infrared luminosity we report is measured by integrating the SED between rest-frame 8–1000 μm and is calculated through the sum of the birth cloud and ISM luminosities, which also include contributions

from the PAHs, and mid-infrared continuum from hot, warm and cold dust in thermal equilibrium. The dust mass is calculated using the far-infrared radiation and a wavelength-dependent dust mass coefficient. For a full description of how each parameter is modelled see da Cunha et al. (2015) and Battisti et al. (2019).

To fit the photometry of a galaxy, MAGPHYS generates a library of SEDs for a grid of redshifts for each star-formation history considered. MAGPHYS identifies the models that best-fit the multi-wavelength photometry by matching the model SEDs to the data using a χ^2 test and returns the respective best-fit parameters. In this study, we focus on eight of the derived parameters: photometric redshift (z); star-formation rate (SFR); stellar mass (M_*); mass-weighted age (Age_m); dust temperature (T_d); dust attenuation (A_V); far-infrared luminosity (L_{IR}) and dust mass (M_d). For each parameter, MAGPHYS returns the probability distribution (PDF) from the best-fit model.

2.2.1 Comparison of simulated and MAGPHYS derived physical properties

Before we derive the physical properties of high redshift galaxies (which are then further analysed in Chapter 3) by modelling their SEDs, we test how well MAGPHYS-derived parameters are expected to track the corresponding physical quantities. This is challenging as we lack knowledge of the "true" quantities (e.g. stellar mass or star-formation rate) for observed galaxies. Therefore, we analyse simulated galaxies from the Evolution and Assembly of GaLaxies and their Environments (EAGLE, Schaye et al., 2015; Crain et al., 2015) galaxy formation model to test how well MAGPHYS recovers the intrinsic properties of realistic model galaxies.

The EAGLE model is a smoothed-particle hydrodynamical simulation that incorporates processes such as accretion, radiative cooling, photo-ionisation heating, star formation, stellar mass loss, stellar feedback, mergers and feedback from black holes. The full description of the simulation as a whole can be found in Schaye et al. (2015) and the calibration strategy is described in Crain et al. (2015). The most recent post-processing analysis of the model galaxies in EAGLE includes dust

reprocessing using the SKIRT radiative transfer code (Baes et al., 2011; Camps & Baes, 2015). This yields predicted SEDs of model galaxies covering the rest-frame UV-to-radio wavelengths (e.g. Camps et al., 2018; McAlpine et al., 2019), and is calibrated against far-infrared observations from the *Herschel* Reference Survey (Boselli et al., 2010). Our primary goal here is to run MAGPHYS on the model photometry of EAGLE galaxies and so test whether the uncertainties on the derived quantities from MAGPHYS encompass the known physical properties of the model galaxies. This will provide us with a threshold that we can use to test the significance of any trends we observe in our real data in Chapters 3 and 4. We stress that MAGPHYS makes very different assumptions about the star-formation histories and dust properties of galaxies than are assumed in EAGLE and SKIRT and so this should provide a fair test of the robustness of the derived parameters from MAGPHYS for galaxies with complex star-formation histories and mixes of dust and stars.

To select a sample of galaxies from the EAGLE model we use the largest volume in the simulation set – Ref-L0100N1504, which is a 100 cMpc on-a-side periodic box (total volume 10^6 cMpc^3). However, we note that the volume of even the largest published EAGLE simulation contains only a modest number of high-redshift galaxies with star-formation rates (or predicted 870-μm flux densities) comparable to those seen in 870μm-selected galaxies, which we analyse in Chapter 3 (McAlpine et al., 2019). As a result, to match the observations as closely as possible, but also provide a statistical sample for our comparison, we select all 9,431 galaxies from EAGLE with SFR $> 10\,\mathrm{M}_\odot\,\mathrm{yr}^{-1}$ and $z > 0.25$, but also isolate the 100 most strongly star-forming galaxies in the redshift range $z = 1.8$–3.4 (the 16–84th percentile redshift range of our 870μm-selected galaxies survey which we analyse in § 3.2 of Chapter 3. To be consistent with the observations, for each model galaxy we extract the predicted photometry in the same 22 photometric bands as our observations (which we fully describe in § 2.3) and run MAGPHYS to predict their physical properties.

We show the comparison of intrinsic EAGLE properties versus derived MAGPHYS properties for these 9,431 galaxies in Fig. 2.1. We concentrate our comparison

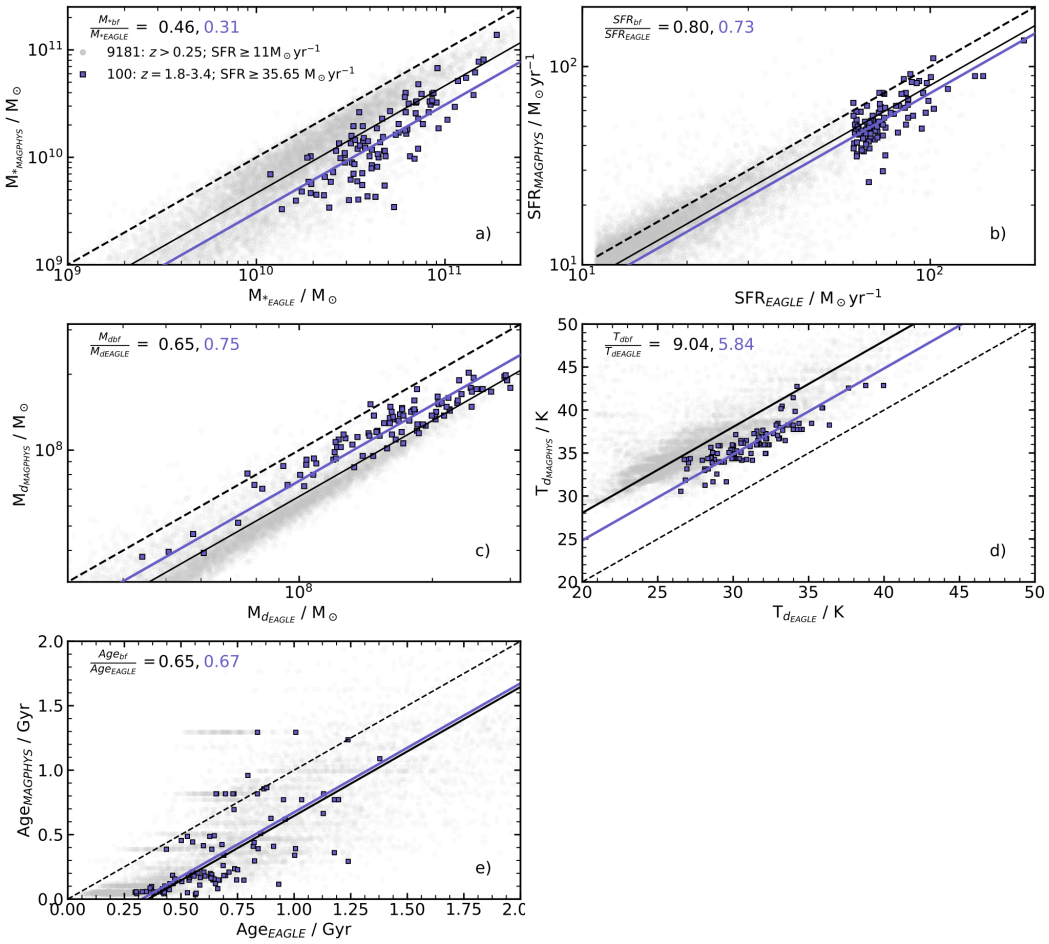

Figure 2.1: Comparison of MAGPHYS predicted parameters to EAGLE values. Two subsets are shown: 1) grey points show results for all EAGLE sample galaxies at $z > 0.25$ with SFR $\geq 11\,M_\odot yr^{-1}$, 2) purple squares show a subset of a 100 EAGLE galaxies that have the highest star-formation rates in the inter-quartile redshift range of the AS2UDS sample ($z = 1.8$–3.4). In each plot the dashed line shows a one-to-one relation, and solid black and purple lines indicate the best fit line for the Subset 1 and Subset 2 of EAGLE sample galaxies respectively. Both lines are fitted at a fixed gradient of $m = 1$ and the fractional offset is given in the top left of each plot. From top left: (a) Stellar mass, (b) Star-formation rate, (c) Dust mass, (d) Dust temperature, (e) Mass-weighted age.

on the stellar mass, star-formation rate, mass-weighted age, dust temperature and dust mass, since these are the quantities we will focus on in Chapters 3. 4 and 5. We note that there are systematic differences in the derived quantities from MAGPHYS compared to the expected values from EAGLE, although in all cases MAGPHYS provide remarkably linear correlations with the intrinsic values (see Fig. 2.1). The largest difference is in the stellar mass, where MAGPHYS predicts a stellar mass that is 0.46 ± 0.10 dex lower than the "true" stellar mass in EAGLE, consistent with previous studies of systematic uncertainty in SMG masses (e.g. Hainline et al., 2011). We also note, that similarly, $\sim$0.3 dex lower stellar masses were found when using MAGPHYS in comparison with CIGALE on strongly lensed ALMA galaxies (Solimano et al., 2021). This difference is likely to be attributed to variations in the adopted star-formation histories, dust model and geometry between MAGPHYS and those in the radiative transfer code SKIRT. Accounting for these differences is beyond the scope of this work, and indeed, more critical for our analysis is the scatter around the line of best fit, since we can use this to estimate the minimum uncertainty on a given parameter in our data (even if the PDF suggests the parameter is more highly constrained).

The stellar and dust masses have a scatter of 30 per cent and 10 per cent around the best fit, respectively. The star-formation rates have a scatter of 15 per cent around the best fit, and the scatter in the ages is 50 per cent. The scatter in dust temperature is 9 per cent, and we note that dust temperatures are estimated using very different methods in the simulations and from the observations. Finally, we also use the quartile range of the scatter as a proxy to assess the significance of any trends we observe in Chapters 3 and 4 (i.e. we adopt a significance limit that any trend in these derived quantities seen in the SMGs must be greater than the quartile range of the scatter in Fig. 2.1). These correspond to ratios of the $R = 75\text{th}/25\text{th}$ quartile values of $R(T_\mathrm{d}) \simeq 1.2$, $R(\mathrm{A}ge_\mathrm{m}) \simeq 4.2$, $R(M_\mathrm{d}) \simeq 2.7$, $R(M_*) \simeq 3.7$ and $R(\mathrm{S}FR) \simeq 2.6$.

2.3 Selection of high redshift star-forming galaxies for MAGPHYS testing

Having tested MAGPHYS on simulated galaxies and established the systematic uncertainties on the derived physical parameters, we now model the SEDs of K-band-selected star-forming 'main-sequence' galaxies from the UKIDSS UDS (Almaini et al. in prep) and 870μm-selected SMGs from AS2UDS (Stach et al., 2019; Dudzevičiūtė et al., 2020) to better understand the strengths and shortcomings of this SED fitting code, before using it to analyse these high redshift star-forming galaxies at $z \sim 2.5$ in Chapter 3 as well as 450μm-selected sources in Chapter 4.

2.3.1 Observations and sample selection

In this section, we describe the multi-wavelength photometric data that we use to derive the SEDs for each galaxy in the AS2UDS sample, which can then be modelled using MAGPHYS to test and calibrate the code. From these SEDs, we aim to derive the photometric redshifts and physical properties for each SMG (such as their star-formation rate, stellar, dust and gas masses) to fully analyse the population of dusty star-forming galaxies in Chapters 3 and 4. To aid the interpretation of our results, we also exploit the $\sim$300,000 K-selected field galaxies in the UKIDSS UDS. We measure the photometry and SEDs for the field galaxies and SMGs in a consistent manner and describe the sources of these data and any new photometric measurements below.

2.3.1.1 ALMA

A detailed description of the ALMA observations, data reduction and construction of the catalogue for the SMGs in our sample can be found in Stach et al. (2019). Briefly, the ALMA/SCUBA-2 UDS Survey (AS2UDS; Stach et al., 2019) is a follow-up survey of a complete sample of 716 SCUBA-2 sources that are detected at >4-σ ($S_{850} \geq 3.6$ mJy) in the SCUBA-2 Cosmology Legacy Survey (S2CLS) map

of the UKIDSS UDS field (Geach et al., 2017). The S2CLS map of the UDS covers an area of $0.96\,\mathrm{deg}^2$ with noise level below 1.3 mJy and a median depth of $\sigma_{850} = 0.88\,\mathrm{mJy\,beam}^{-1}$. All 716 SCUBA-2 sources detected in the map were observed in ALMA Band 7 (344 GHz or 870 μm) between Cycles 1, 3, 4 and 5 (a pilot study of 27 of the brightest sources observed in Cycle 1 is discussed in Simpson et al. 2015c, 2017). Due to configuration changes between cycles, the spatial resolution of the data varies in range 0.15–0.5″ FWHM, although all of the maps are tapered to 0.5″ FWHM for detection purposes (see Stach et al., 2019, for details). The final catalogue contains 708 precisely located (to within $\ll 0.1''$) individual ALMA SMGs spanning $S_{870} = 0.6$–$13.6\,\mathrm{mJy}$ ($>4.3\sigma$) corresponding to a 2 per cent false-positive rate. We remove one bright, strongly lensed source (Ikarashi et al., 2011) from our analysis and the remaining 707 ALMA-identified SMGs are the focus of this study of the physical properties. AS2UDS provides the largest homogeneously-selected sample of ALMA-identified SMGs currently available, $\sim 6\times$ larger than the largest existing ALMA surveys (Hodge et al., 2013; Miettinen et al., 2017).

2.3.1.2 Optical U-band to K-band photometry

At the typical redshift of 850μm-selected SMGs, $z \sim 2.5$ (e.g. Chapman et al., 2005; Simpson et al., 2014; Danielson et al., 2017; Brisbin et al., 2017), the observed optical to mid-infrared corresponds to the rest-frame UV/optical/near-infrared, which is dominated by the (dust-attenuated) stellar continuum emission, emission lines, and any possible AGN emission. The rest-frame UV/optical/near-infrared also includes spectral features that are important for deriving photometric redshift, in particular, the photometric redshifts have sensitivity to the Lyman break, Balmer and/or 4000Å break and, the (rest-frame) 1.6-μm stellar "bump".

To measure the optical/near-infrared photometry for the galaxies in the UDS, we exploit the panchromatic photometric coverage of this field. In particular, we utilise the UKIRT Infrared Deep Sky Survey (UKIDSS: Lawrence et al., 2007) UDS data release 11 (UKIDSS DR11), which is a K-band selected photometric catalogue

(Almaini et al., in prep.) covering an area of $0.8\,\mathrm{deg}^2$ with a 3-σ point-source depth of $K = 25.7$ mag (all photometry in this section is measured in $2''$ diameter apertures and has been aperture corrected, unless otherwise stated). This K-band selected catalogue has 296,007 sources, of which more than 90 per cent are flagged as galaxies with reliable K-band photometry. For any subsequent analysis, we restrict our analysis to 205,910 sources that have no contamination flags. The UKIDSS survey imaged the UDS field with the UKIRT WFCAM camera in K, H and J bands and the DR11 catalogue also includes the matched photometry in J- and H-band to 3-σ depths of $J = 26.0$ and $H = 25.5$.

In addition, Y-band photometry was also obtained from the VISTA/VIDEO survey, which has a 3-σ depth of 25.1 mag and $BVRi'z'$-band photometry was obtained from Subaru/Suprimecam imaging, which has 3-σ depths of 28.2, 27.6, 27.5, 27.5, and 26.4 mag, respectively. Finally, U-band photometry of the UDS field from the CFHT/Megacam survey is also included in the DR11 catalogue. This U-band imaging reaches a 3-σ point-source depth of 27.1 mag.

To derive the photometry of the ALMA SMGs in the optical/near-infrared, first, we align the astrometry between the UKIDSS DR11 catalogue with the ALMA astrometry by matching the positions of the ALMA SMGs to the K-band catalogue, identifying and removing an offset of $\Delta\mathrm{RA} = 0.1''$ and $\Delta\mathrm{Dec} = 0.1''$ in the K-band. We find that 634/707 SMGs lie within the deep regions of the K-band image, after excluding regions masked due to noisy edges, artefacts, and bright stars. The two catalogues are then matched using a radius of $0.6''$ (which has a false-match rate of 3.5 per cent; see An et al. 2018 for details). This results in 526/634 SMGs with K-band detections (83 per cent). We note that 43 of these sources are within a K-band region flagged with possibly contaminated photometry; however, the inclusion of these sources in our analysis does not change any of our conclusions of this study, thus we retain them and flag them in our catalogue.

Our detection fraction is comparable to, but slightly higher than, the fraction identified in smaller samples of SMGs in other fields, which is likely due to the very deep near-infrared coverage available in the UDS. For example, in the ALMA

survey of the ECDFS, ALESS – Simpson et al. (2014) show that 61 / 99 (60 per cent) of the ALMA SMGs have K-band counterparts to a limit of $K = 24.4$. This is significantly lower than the detection rate in our UDS survey, although cutting our UDS catalogue at the same K-band limit as the ECDFS results in a detected fraction of 68 per cent. Similarly, 65 per cent of the ALMA SMGs in the CDFS from Cowie et al. (2018) (which have a median 870-μm flux of $S_{870} = 1.8$ mJy) are brighter than $K = 24.4$. Finally, Brisbin et al. (2017) identify optical counterparts to 97 / 152 (64 per cent) of ALMA-identified SMGs from a Band 6 (1.2 mm) survey of AzTEC sources using the public COSMOS2015 catalogue (Laigle et al., 2016), which is equivalent to $K \lesssim 24.7$, for the deepest parts. Thus, our detection rate of 83 per cent of ALMA SMGs with K-band counterparts is consistent with previous surveys but also demonstrates that even with extremely deep near-infrared imaging, a significant number (17 per cent or 108 galaxies) are faint or undetected in the near-infrared at $K \geq 25.7$.

Since SMGs are dominated by high redshift, dusty highly-starforming galaxies, their observed optical/near-infrared colours are typically red (e.g. Smail et al., 1999, 2004), and so the detection rate as a function of wavelength drops at shorter wavelengths, reaching just 26 per cent in the U-band (Table 2.1). We will return to a discussion of the detected fraction of SMGs as a function of wavelength, their colours, and implications on derived quantities in § 2.4.

2.3.1.3 *Spitzer IRAC & MIPS observations*

Next, we turn to the mid-infrared coverage of the UDS, in particular from *Spitzer* IRAC and MIPS observations. At these wavelengths, the observed 3.6–8.0 μm emission samples the rest-frame near-infrared at the expected redshifts of the SMGs. These wavelengths are less dominated by the youngest stellar populations, and significantly less affected by dust than the rest-frame optical or UV. Observations of the UDS in the mid-infrared were taken with IRAC onboard the *Spitzer* telescope as part of the *Spitzer* Legacy Program (SpUDS; PI: J. Dunlop).

We obtained reduced SpUDS images of the UDS from the *Spitzer* Science Archive.

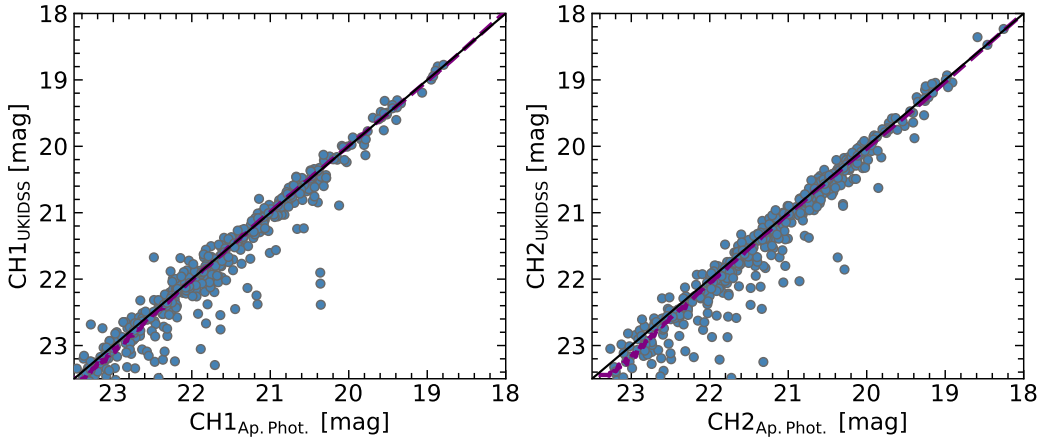

Figure 2.2: The IRAC 3.6μm (left) and 4.5μm (right) magnitudes from aperture photometry using ALMA positions in comparison with the UKIDSS DR11 catalogue (Almaini et al., in prep) for the AS2UDS sample (blue points). The running median for the K-selected sources from the UKIDSS DR11 is shown as a purple dashed line. As expected, there is higher scatter for fainter sources. However, overall, we see good agreement between our measurements and the UKIDSS DR11 catalogue with $\Delta[3.6]\,/\,[3.6]_{\rm DR11} = 0.001^{+0.007}_{-0.005}$ and $\Delta[4.5]\,/\,[4.5]_{\rm DR11} = 0.002^{+0.009}_{-0.003}$ for the UKIDSS DR11 sample.

These IRAC observations at 3.6, 4.5, 5.8 and 8.0 μm reach 3-σ depths of 23.5, 23.3, 22.3 and 22.4 mag, respectively. The astrometry of all four IRAC images was aligned to the ALMA maps by stacking the IRAC thumbnails of the ALMA positions of 707 AS2UDS sources and corrections in RA/Dec of (+0.00″, +0.15″), (+0.08″,+0.12″), (+0.08″,+0.00″) and (+0.60″,−0.08″) were applied to the 3.6, 4.5, 5.8 and 8.0 μm images, respectively. To measure the photometry, and minimise the effect of blending, we extract 2″-diameter aperture photometry for all of the ALMA SMGs, as well as for all 205,910 galaxies in the UKIDSS DR11 catalogue, and calculate aperture corrections to total magnitudes from point sources in the images. The UKIDSS DR11 catalogue contains aperture-corrected magnitudes measured in the 3.6- and 4.5-μm bands and we confirm our photometry at these wavelengths by comparing the respective magnitudes in Fig. 2.2, with relative offsets of just $\Delta[3.6]\,/\,[3.6]_{\rm DR11} = 0.001^{+0.007}_{-0.005}$ and $\Delta[4.5]\,/\,[4.5]_{\rm DR11} = 0.002^{+0.009}_{-0.003}$.

Due to the relatively large PSF of the IRAC images (typically $\sim$2″ FWHM), blending with nearby sources is a potential concern (see Figs. 2.3 & 2.4). We, therefore,

identify all of the ALMA SMGs that have a second, nearby K-band detected, galaxy within 2.5″ and calculate the possible level of contamination assuming that the flux ratio of the ALMA SMG and its neighbour is the same in the IRAC bands as observed in the higher-resolution K-band images. This is conservative as the SMGs are expected to be typically redder than any contaminating field galaxies. For any ALMA SMG, if the contamination from the nearby source is likely to be more than 50 per cent of the total flux, the respective IRAC magnitudes are treated as 3-σ upper limits. This transformation of detected fluxes into upper limits affects 109 sources. For any K-band sources from the UKIDSS UDS DR11 catalog that are within 1" of the ALMA position we include the UV/optical/near-IR photometry as the ALMA counterpart. We flag all of these sources in the online catalogue. In Fig. 2.3, we show the difference in the derived SEDs (see § 3.3 in Chapter 3) for two sources where the IRAC photometry was changed from the original aperture photometry value (when assuming no contamination). We see that the model SEDs (thus the derived redshift and physical properties for a given galaxy) change significantly, highlighting the importance of taking blending into account in IRAC photometry.

From the photometry of the ALMA SMGs in the IRAC bands, we determine that 581 / 645 or 90 per cent of the SMGs covered by IRAC are detected at 3.6 μm, or 73 per cent when we apply the conservative blending criterion from above. The increased fraction of the sample that are detected in the IRAC bands, compared to K-band, most likely reflects the (rest-frame) 1.6-μm stellar "bump" that is redshifted to $\gtrsim 3\,\mu$m for an SMG at $z \gtrsim 1$. We will return to a discussion of the mid-infrared colours in § 2.3.2.

To demonstrate the typically red colour of the SMGs (in particular compared to the foreground field galaxy population), in Fig. 2.4 we show colour images (composed of K, IRAC 3.6-μm and 4.5-μm bands) for 100 representative AS2UDS SMGs ranked in terms of S_{870} and photometric redshift (see § 3.2 in Chapter 3 for the determination of the photometric redshifts). This figure demonstrates that SMGs generally have redder near-/mid-infrared colours than neighbouring field galaxies

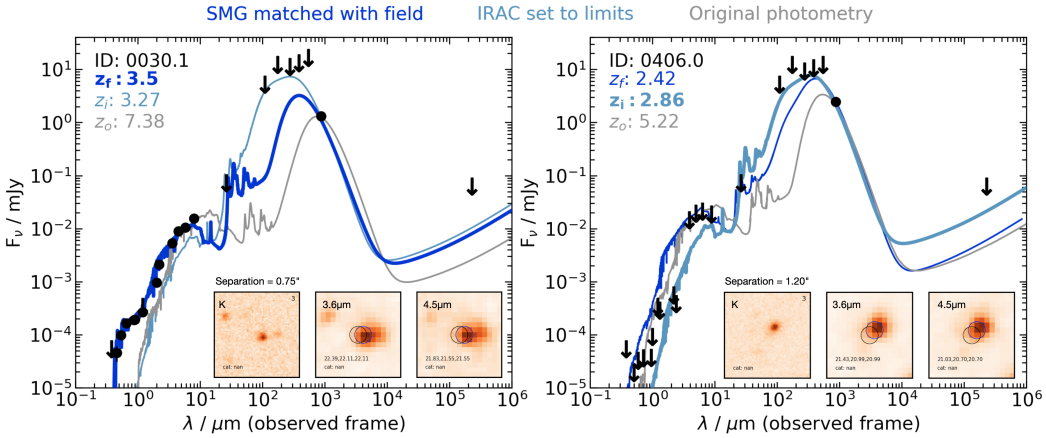

Figure 2.3: Model SEDs (see § 2.4.3) assuming no contamination in IRAC bands (original photometry), setting IRAC to limits and matching with a K-band counterpart. Photometric redshift of each SED is noted at top left of the panel in the respective colour. Inset panels show K-band, 3.6μm and 4.5μm thumbnails. **Left:** Example of an SMG where the separation between the ALMA and K-band counterpart is $<1''$. Therefore, we match it as a counterpart and adopt the UV/optical/near-IR photometry. **Right:** Example of an SMG where the separation between the ALMA and K-band counterpart is $>1''$. We flag this source as contaminated and set all 4 IRAC channels to limits. We see that the way the IRAC photometry is treated has a significant effect on the model SEDs, highlighting the importance of taking blending into account in IRAC photometry.

and also that on average higher-redshift SMGs are fainter and/or redder in the near-infrared bands than low redshift ones for each of the ALMA flux bins. We see no strong trends in observed properties with 870-μm flux density in any redshift bin.

Mid-infrared observations of the UDS were also taken at 24 μm with the Multiband Imaging Photometer (MIPS) on board *Spitzer* as part of SpUDS. The 24-μm emission provides useful constraints on the star formation and AGN content of bright SMGs since at the typical redshift of our sample, the filter samples continuum emission from heated dust grains. This spectral region also includes broad emission features associated with polycyclic aromatic hydrocarbons (PAHs) – the most prominent of which appear at rest-frame 6.2, 7.7, 8.6, 11.3, and 12.7 μm, as well as absorption by amorphous silicates centred at 9.7 and 18 μm (Pope et al., 2008; Menéndez-Delmestre et al., 2009). This MIPS 24-μm imaging is also employed to provide a constraint on the positional prior catalogue that is used to deblend the *Herschel* far-infrared maps (e.g. Roseboom et al., 2012; Magnelli et al., 2013; Swin-

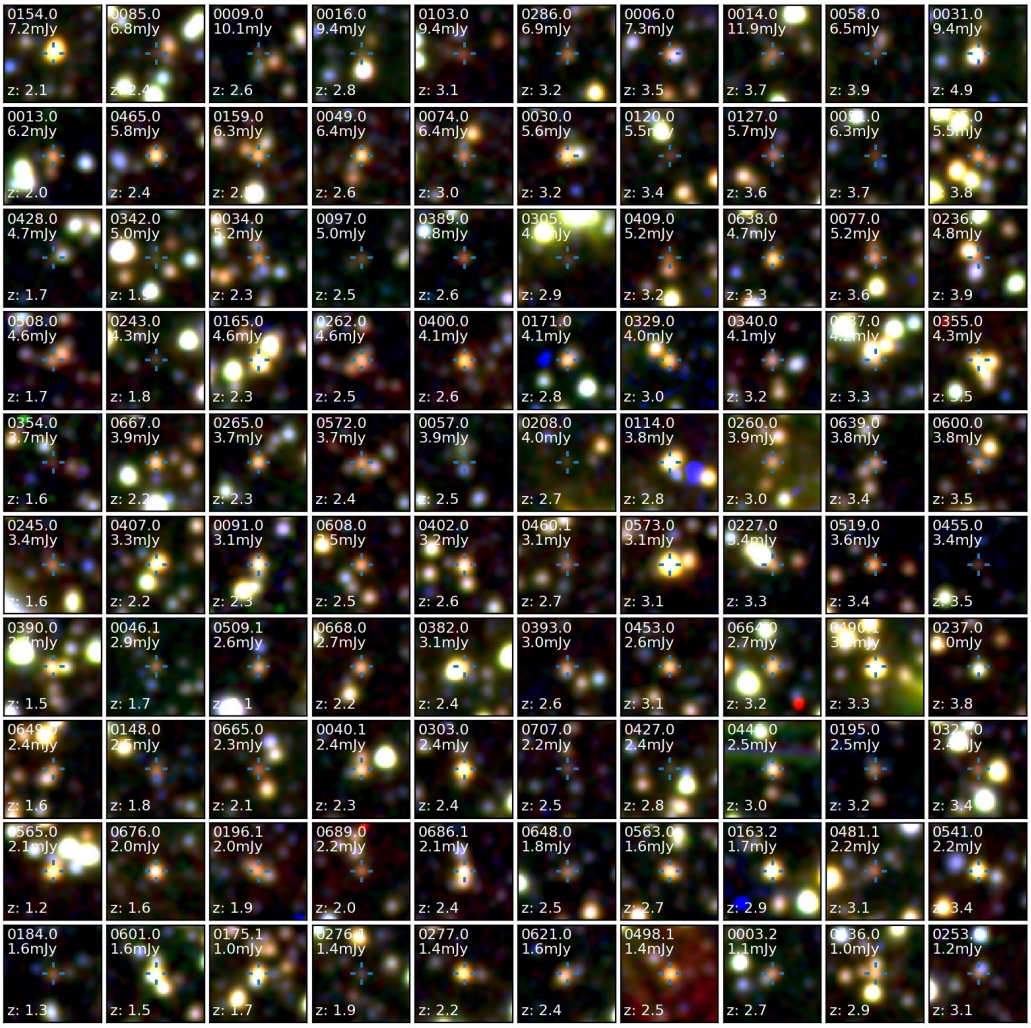

Figure 2.4: Examples of 100 of the AS2UDS ALMA-identified SMGs from our sample. The $25'' \times 25''$ ($\sim$200-kpc square at their typical redshifts) colour images are composed of K, IRAC 3.6μm and IRAC 4.5 μm bands with the ALMA position of the source given by the open cross. The sources are selected to be representative of the near-infrared properties of the full sample: thumbnails are ranked in deciles of flux (each row) and deciles of $z_{\rm phot}$ within each flux range (each column). SMGs are in general redder than the neighbouring field galaxies. There is a weak trend for SMGs to become fainter and/or redder with redshift, but there is no clear trend of observed properties with S_{870} flux density.

Table 2.1: Photometric coverage and detection fractions for AS2UDS SMGs in representative photometric bands.

Band	$N_{covered}$	$N_{\rm detected}$	$\%_{\rm detected}$	Depth (3-σ)
U	634	162	26	27.1 AB
V	590	330	56	27.6 AB
K	634	526	83	25.7 AB
3.6 μm	644	580[1]	90[2]	23.5 AB
24 μm	628	304	48	60 μJy
350 μm	707	417	59	8.0 mJy
1.4 GHz	705	272	39	18 μJy

[1] Including 109 potentially contaminated sources (see §2.3.1.3)
[2] 73% if excluding 109 potentially contaminated sources
Notes: $N_{covered}$ – number of SMGs covered by imaging; $N_{\rm detected}$ – number of SMGs detected above 3-σ; $\%_{\rm detected}$ – per centage of total sample detected.

bank et al., 2014). We obtained the reduced SpUDS / MIPS 24-μm image from the NASA Infrared Astronomy Archive. This imaging covers the entire UDS survey area and reaches a 3-σ (aperture corrected) limit of 60 μJy. From the 24-μm image, we identify $\sim$35,000 sources, and cross-matching the >3-σ detections in the 24-μm catalogue with our ALMA catalogue with a 2″ matching radius, we determine that 48 per cent of the SMGs are detected. This detected fraction is also consistent with that of other fields with similar ALMA and MIPS coverage (e.g. 41 per cent in ALESS from Simpson et al. 2014).

2.3.1.4 *Herschel SPIRE & PACS observations*

To measure reliable far-infrared luminosities for the ALMA SMGs, we exploit observations using the Spectral and Photometric Imaging Receiver (SPIRE: Griffin et al., 2010) and the Photodetector Array Camera and Spectrometer (PACS: Poglitsch et al., 2010) on board the *Herschel* Space Observatory. These observations were taken as part of the *Herschel* Multi-tiered Extragalactic Survey (HerMES; Oliver et al. 2012) and cover the observed wavelength range between 100–500 μm. These wavelengths are expected to span the dust-peak of the SED, which (in local ULIRGs) peak around 100 μm, corresponding to a characteristic dust temperature of $T_{\rm d} \simeq 35$ K (e.g. Symeonidis et al., 2013; Clements et al., 2018). At $z \sim 2.5$, the dust SED is expected to peak around an observed wavelength of 350 μm (e.g. see Casey et al.

2014 for a review).

Due to the coarse resolution of the *Herschel* / SPIRE maps ($\sim 18''$, $25''$ and $36''$ FWHM at 250, 350 and 500 μm, respectively), we need to account for the effect of source blending (Roseboom et al., 2012; Magnelli et al., 2013). We, therefore, follow the same procedure as Swinbank et al. (2014). Briefly, the ALMA SMGs, together with *Spitzer* / MIPS 24-μm and 1.4-GHz radio sources, are used as positional priors in the deblending of the SPIRE maps. A Monte Carlo algorithm is used to deblend the SPIRE maps by fitting the observed flux distribution with beam-sized components at the position of a given source in the prior catalogue. To avoid "over-blending" the method is first applied to the 250-μm data, and only sources that are either (i) ALMA SMGs, or (ii) detected at >2-σ at 250-μm are propagated to the prior list for the 350-μm deblending. Similarly, only the ALMA SMGs and/or those detected at >2-σ at 350 μm are used to deblend the 500-μm map. The uncertainties on the flux densities (and limits) are found by attempting to recover fake sources injected into the maps (see Swinbank et al. 2014 for details), and the typical 3-σ detection limits are 7.0, 8.0 and 10.6 mJy at 250, 350 and 500 μm respectively. The same method is applied to the PACS 100- and 160-μm imaging, with the final 3-σ depths of 5.5 mJy at 100 μm and 12.1 mJy at 160 μm.

Given the selection of our sources at 870 μm, the fraction of ALMA SMGs that are detected in the PACS and/or SPIRE bands is a strong function of 870-μm flux density, but we note that 69 per cent (486/707) of the ALMA SMGs are detected in at least one of the PACS or SPIRE bands. This is important in § 3.4 of Chapter 3 when deriving useful constraints on the far-infrared luminosities and dust temperatures.

In terms of the field galaxies, just 3.6 per cent of the K-band sample have a MIPS 24-μm counterpart, and of these only 2,396 (out of a total of 205,910 galaxies in DR11) are detected at 250 μm, with 1,497 and 500 detected at 350 μm and 500 μm, respectively. Thus the majority of the field population are not detected in the far-infrared (in contrast to the ALMA SMGs, where the majority of the galaxies are detected).

2.3.1.5 VLA 1.4 GHz Radio observations

Finally, we turn to radio wavelengths. Prior to ALMA, high-resolution ($\sim 1''$) radio maps had often been employed to identify likely counterparts of single-dish sub-millimetre sources (e.g. Ivison et al., 1998). Although the radio emission does not benefit from the negative k-correction experienced in the sub-millimetre waveband (see § 3.1), the lower-redshift ($z \lesssim 2.5$) ALMA SMGs tend to be detectable as μJy radio sources due to the strong correlation between the non-thermal radio and far-infrared emission in galaxies (e.g. Yun et al., 2001; Ivison et al., 2002, 2007; Vlahakis et al., 2007; Biggs et al., 2011; Hodge et al., 2013). The standard explanation of this relationship is that both the far-infrared emission and the majority of the radio emission traces the same population of high-mass stars ($\gtrsim 5\,\mathrm{M}_{\odot}$). These stars both heat the dust (which then emits far-infrared emission) and produce the relativistic electrons responsible for synchrotron radiation when they explode as supernovae (e.g. Helou et al., 1985; Condon, 1992). However, the lack of a negative k-correction in the radio waveband means that at higher redshifts ($z \gtrsim 2.5$), where a large fraction of the SMGs lie, their radio flux densities are often too faint to be detectable, for example, Hodge et al. (2013) show that up to 45 per cent of ALMA SMGs in their ALESS survey are not detected at 1.4 GHz.

The UDS was imaged at 1.4 GHz with the Very Large Array (VLA) using ~ 160 hours of integration. The resulting map has an rms of $\sigma_{1.4GHz} \simeq 6\,\mu\mathrm{Jy\,beam}^{-1}$ (Arumugam et al. in prep.; for a brief summary see Simpson et al., 2013). In total 6,861 radio sources are detected at SNR> 4, and 706/707 of the ALMA SMGs are covered by the map. Matching the ALMA and radio catalogues using a $1.6''$ search radius ($\sim$1 per cent false-positive matches) yields 273 matches at a 3-σ level, corresponding to a radio detection fraction of 39 per cent (see also An et al. 2018), which is similar to the detected radio fraction in other comparable SMG surveys ($\sim$30–50 per cent; e.g. Hodge et al. 2013; Biggs et al. 2011; Brisbin et al. 2017, although see Lindner et al. 2011). We discuss the influence of radio emission on the SED modelling we perform in § 2.4.3, as well as the redshift distribution of the radio-detected versus non-detected fractions in Chapter 3 (§ 3.2).

2.3.2 Photometric properties of SMGs in comparison to the field population

To illustrate the broad photometric properties of our SMG sample and the constraints available on their SEDs, we list the number of SMGs detected (above 3-σ) in a range of representative optical and infrared photometric bands in Table 2.1. It is clear that fewer detections are observed in the bluer optical wavebands, while $\sim$70–80 per cent of the sample (which are covered by the imaging) are detected in K or the IRAC bands; this drops to 56 per cent in the V-band. In the far-infrared, 69 per cent of the ALMA SMGs are detected in at least one of the PACS or SPIRE bands. Thus we have good photometric coverage for the bulk of the sample longward of the near-infrared, but with more limited detection rates in the bluer optical bands.

Before we discuss the testing of MAGPHYS by fitting of multi-wavelength SEDs, we first compare the optical and near/mid-infrared colours of the SMGs and field galaxies in our sample. As this study makes use of a K-band selected catalogue for testing and comparison purposes, we investigate the distribution of K-band magnitudes compared to the ALMA S_{870} fluxes Fig. 2.5. No strong correlation of 870-μm flux density and K-band magnitude is observed, but we highlight that we see a two order of magnitude range in K-band brightness at a fixed 870-μm flux density.

Colour selection of galaxies can provide a simple method to identify high-redshift galaxies. For example, Daddi et al. (2004) suggested a criteria based on $(B-z)$ and $(z-K)$ (BzK) with $BzK = (z-K)-(B-z)$ to select star-forming galaxies at $z \simeq 1.4$–2.5. Although the SMGs are likely to be more strongly dust-obscured than typical star-forming galaxies at these redshifts, this diagnostic still provides a useful starting point to interpret the rest-frame UV/optical colours, and we show the SMGs in the $(z-K)-(B-z)$ colour space in Fig. 2.6a. We see that compared to a field galaxy sample, as expected, the SMGs are significantly redder, likely due to their higher dust obscuration and higher redshifts. Nevertheless, for our

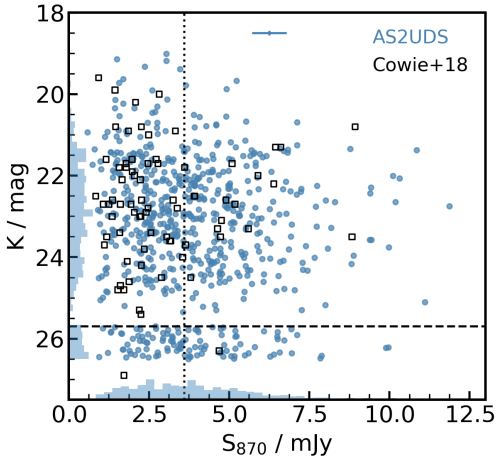

Figure 2.5: K-band magnitude versus S_{870} flux density of the AS2UDS SMGs. The horizontal dashed line shows the K-band 3-σ limit of $K = 25.7$ and the vertical dotted line indicates the flux limit of the parent SCUBA-2 survey at $S_{870} = 3.6$ mJy. There are 526 K-band detections of SMGs and we plot the 108 limits scattered below the K-band limit. The histograms show the K-band magnitude distribution as the ordinate and S_{870} flux density distribution as the abscissa. For comparison, we also show the Cowie et al. (2018) sample from CDFS, which covers a similar parameter range. No strong correlation of 870-μm flux density and K-band magnitude is observed, but we highlight that we see a two order of magnitude range in K-band brightness at a fixed 870-μm flux density.

sample of 290 AS2UDS SMGs with detections in all three B, z and K-bands, 87 per cent (253/290) of sources lie above $BzK = -0.2$, which is the suggested limit that separates star-forming galaxies from passive galaxies, indicating that the majority of these BzK-detected (hence bluer than average) SMGs have the colours expected for a star-forming population. However, we caution that 14 per cent of our sample of these BzK-detected highly dust-obscured star-forming galaxies are misclassified as "passive". Moreover, we note that the SMG sub-set shown on this BzK plot is strongly biased due to the large fraction that are not shown because they are undetected in the optical bands, especially the B-band. To highlight this, we overlay the track for our composite SED (see § 3.3 in Chapter 3), which should more accurately represent the "typical" SMG, as a function of increasing redshift. This indicates that at $z \simeq 1.5$–2.5 the *average* SMG has BzK colours which lie on the border of the star-forming criterion, suggesting that a significant fraction of $z \lesssim 2.5$ SMGs would not be selected as star-forming systems based on their BzK colours, even if we had extremely deep B-band observations.

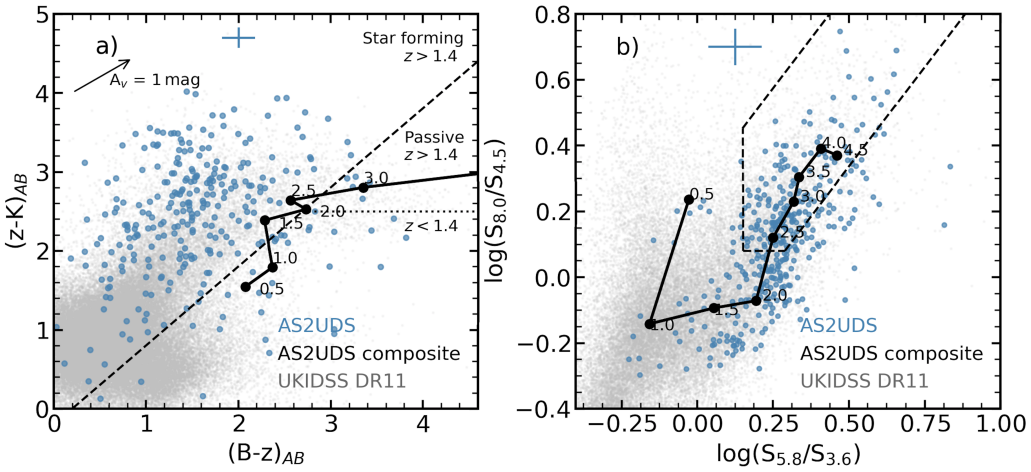

Figure 2.6: Photometric properties of the AS2UDS sample. **(a)** $(z-K)$ versus $(B-z)$ colour-colour diagram for 290 SMGs with detections in all three bands and the BzK classification regions. We stress that these are typically the brighter and bluer examples and so are not representative of the full population. The placement of the sources on the diagram suggests that the majority (253/290) of these SMGs are high-redshift star-forming galaxies, most of which are significantly redder than the field population. The reddening vector for one magnitude of extinction in the V-band is plotted in the top left. The solid line shows the track predicted by the composite SMG SED track at increasing redshift (labelled). Dashed line separates star-forming galaxies at $z > 1.4$ and dotted line further isolates passive galaxies at $z > 1.4$. We see that the average colours of SMGs lies close to the classification boundary and so it is likely that fainter and redder SMGs would be misclassified using the BzK colours. **(b)** IRAC colour-colour diagram for 388 SMGs detected in all four IRAC bands. The dashed line indicates the IRAC colour criteria for AGN selection (up to a redshift of $z \sim 2.5$) from Donley et al. (2012). The solid line shows the composite SED as a function of redshift (labelled). We see that a large fraction of SMGs have colours suggestive of AGN, but the majority of these lie at too high redshifts ($z \gtrsim 2.5$) for the reliable application of this classification criterion – with their power-law like IRAC colours resulting from the redshifting of the 1.6-μm bump longward of the 5.8-μm passband. The field galaxies are also plotted (in grey) and it is clear that SMGs have significantly redder colours, with the bulk of the field sample falling off the bottom left corner of the plot. The typical error is shown in the top of each panel.

Given that the detection rate of ALMA SMGs is much higher in the mid-infrared IRAC bands, in Fig. 2.6b we show the $S_{5.8}/S_{3.6}$ versus $S_{8.0}/S_{4.5}$ colour-colour plot for 388 SMGs that are detected in all four IRAC bands. This colour-colour space has been used to identify high-redshift star-forming galaxies, as well as isolate candidate AGN at $z \lesssim 2.5$ from their power-law spectra (e.g. Donley et al., 2012). In this figure, the IRAC-detected ALMA SMGs are again, on average, significantly redder than the field population (see also Stach et al., 2019). We overlay the track formed from the composite SED of our sample (see § 3.3 in Chapter 3), which demonstrates that these IRAC-detected SMGs are likely to lie at $z \simeq 2$–3. Hence, although it might appear from Fig. 2.6b that many of the SMGs have mid-infrared colours suggestive of an AGN (power-law like out to 8 μm), this is simply because many of these lie at $z > 2.5$ where sources cannot be reliably classified using this colour selection. Indeed, Stach et al. (2019) estimates a likely AGN fraction in AS2UDS based on X-ray detections of just 8 ± 2 per cent. As seen from the composite SED track, the sources in the AGN colour region are on average at higher redshifts ($z > 2.5$), where the 1.6-μm stellar "bump" falls beyond the 5.8-μm band, and the Donley et al. (2012) AGN criteria breaks down.

In summary, the basic photometric properties of SMGs show them to be redder than average field galaxies across most of the UV/optical to mid-infrared regime, likely due to a combination of their higher redshifts and higher dust obscuration. High-redshift SMGs are also fainter than the low-redshift SMGs in the optical and near-infrared wavebands (Fig. 2.4), but with a large dispersion in properties at any redshift.

2.4 Testing MAGPHYS on high-redshift star-forming galaxies

In this section we fit the SEDs of dust-obscured star-forming galaxies as well as more typical star-forming 'main-sequence' galaxies at high redshift, which we described and compared in terms of photometry in the previous section, to test whether the

physical properties derived from the MAGPHYS SED models are consistent with the photometric trends observed in § 2.3.2.

2.4.1 Dealing with photometry limits

A significant fraction of the SMGs in the AS2UDS sample are faint or undetected in one or more of the 22 wavebands that we employ in our analysis – most frequently this is at the bluest optical wavelengths (see Table 2.1) due to their high redshift and dusty nature. Thus, we first assess how the flux limits affect the model fitting.

As a first step, in any given waveband, we treat a source as detected if it has at least a 3-σ detection. For non-detections, we conservatively adopt a flux of zero and a limit corresponding to 3-σ in the UV-to-mid-infrared bands (i.e. up to 8 μm). This is motivated by a stacking analysis of ALMA SMGs in ALESS where the individually optically faint or undetected SMGs yielded no or only weak detections in the stacks (e.g. Simpson et al., 2014). In the far-infrared, most of the "non-detections" occur in the *Herschel* maps, which are confusion-noise dominated. Stacking analysis of SMGs at 250–500 μm has demonstrated that the flux densities of ALMA SMGs at these wavelengths are often just marginally below the confusion noise (e.g. Simpson et al., 2014). To this end, for non-detected sources in the infrared (beyond 10 μm), we adopt a flux density of $1.5 \pm 1.0\sigma$. Other choices of limits were tested (e.g. $0 \pm 1\sigma$ for all wavebands, $0 \pm 1\sigma$ for optical/near-infrared and $1.5 \pm 1.0\sigma$ for infrared) with no significant changes found for any of the derived physical parameters.

We run MAGPHYS on all 707 ALMA SMGs in our sample, and in Fig. 2.7 we show the observed photometry and best-fit MAGPHYS model for four representative examples. All SED fits are available online through MNRAS* (Dudzevičiūtė et al., 2020). These examples are selected to span the range in the number of photometric detections included in the SEDs: from sources that are detected in all of the available 22 photometric bands (37 per cent of sources have coverage in 22–16 bands), 16 bands (28 per cent have coverage in 16–11 bands), 11 bands (20 per cent have

*https://doi.org/10.1093/mnras/staa769

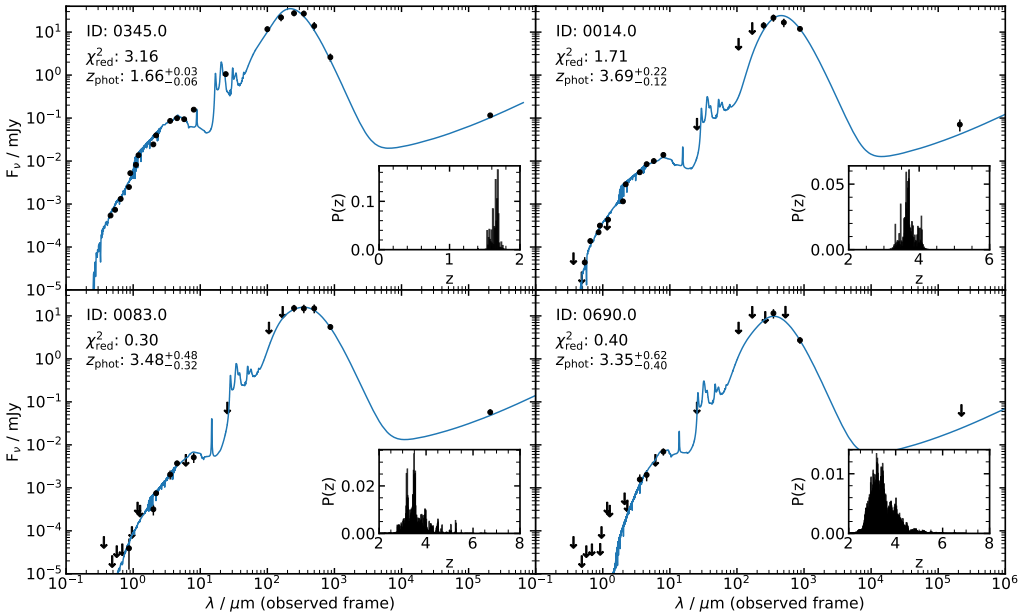

Figure 2.7: The observed-frame optical to radio spectral energy distributions of four example AS2UDS SMGs selected to have a decreasing number of photometric detections: 22/22, in top left; 16, in top right; 11, in bottom left; and 5 in bottom right. Limits in the optical/near-infrared wavebands (U-band to IRAC 8μm) were treated as $0 \pm 3\sigma$, while those beyond 10 μm (MIPS 24μm to Radio 1.4GHz) are set to $1.5\sigma \pm 1\sigma$. These limits are indicated as arrows. The solid line shows the predicted SED at the peak redshift of the best-fit PDF. The inset plots show the redshift probability distributions. As expected, as the number of photometric detections decreases, the redshift distribution becomes wider and the predicted photometric redshifts becomes more uncertain. For reference, of our 707 SMGs 50 per cent have ≥ 11 photometric detections, while 82 per cent have ≥ 5 detections.

coverage in 11–5 bands) and down to 5 bands (15 per cent have coverage in 5 or less bands). The median number of detections for the full SMG sample is 12. For comparison and testing purposes, we also run MAGPHYS on ∼300,000 K-band-selected sources from UKIDSS UDS including photometry up to 8μm and treating limits consistently with the SMG sample - flux of zero and a limit corresponding to 3-σ.

2.4.2 Redshift recovery with MAGPHYS

Before we can address any derived physical properties and test their consistency with the observed photometric trends (Fig. 2.5 and Fig. 2.6), we first confirm the reliability of MAGPHYS to measure photometric redshifts, and critically their uncertainties (see also Battisti et al., 2019) by comparing the photometric and

spectroscopic redshifts for both the SMGs and the field galaxies in the UDS.

Examples of output photometric redshift PDFs are shown in Fig. 2.7 for each of the four example SMGs. The figure demonstrates that when the SED is well-constrained (e.g. the galaxy is detected in a large fraction of the photometric bands), the range of possible photometric redshifts is narrow, e.g. with a median 16–84$^{\rm th}$ percentile range of $\Delta z = 0.20$ for SMGs with detections in all 22 bands. However, as the number of detection decreases, this range broadens. For our full sample of SMGs, the median number of bands that are detected is 12, which yields a median 16–84$^{\rm th}$ percentile redshift range on any given SMG of $\Delta z = 0.50$. For reference, the median uncertainty for the 18 per cent of SMGs that are detected in ≤ 6 bands is $\Delta z = 0.86$. Note also that in some cases the reduced χ^2 decreases as the number of detections decreases. This does not necessarily indicate a better fit, but rather often reflects the large uncertainties in non-detected wavebands.

There are a few approaches of selecting the representative photometric redshift for a given galaxy from the output PDF. The photometric redshift could be chosen at the redshift of the best-fit model (best redshift), at the peak of the photometric redshift PDF (peak redshift) or the median value of the PDF (median redshift). In Fig. 2.8, we show that, overall, the three estimates are in good agreement, and do not have any significant offsets when compared to the available spectroscopic redshifts (described in § 2.4.2.1). This agreement is also shown for individual sources in panels (a) and (b) in Fig. 2.8, for a single-peaked and double-peaked redshift distribution, respectively. However, due to the finite sampling in the SED fitting for some of the sources, the peak and best redshift estimates are at very different values (when the distribution is double-peaked; see panel c) or even outside the 16-84th percentile range (panel d) where a single redshift value has an anomalous peak in the PDF. This shows that to encompass the range of uncertainty in photometric redshift for these sources, using the median redshift is the best approach. Therefore, for the best estimate of the photometric redshift as well as for the derived parameters (e.g. stellar mass, SFR etc) we take the median from the respective PDF, with uncertainties reflecting the 16–84th percentile values of the distribution.

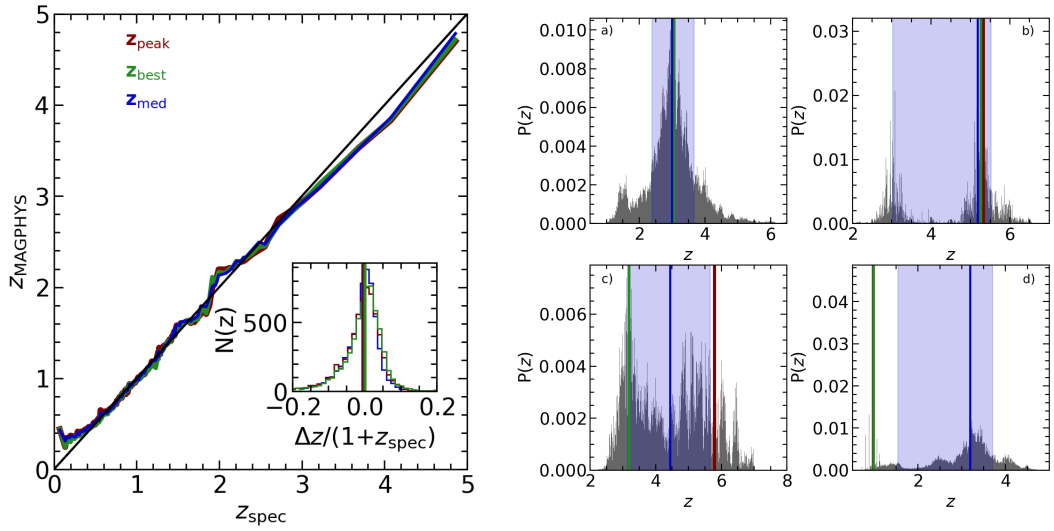

Figure 2.8: **Left:** The binned-median trends of photometric redshift estimates at the peak ($z_{\rm peak}$) and median ($z_{\rm med}$) of the redshift PDFs, and the redshift of the best-fitting model ($z_{\rm best}$) in comparison to the spectroscopic redshift for the 6,719 UKIDSS UDS sources (see § 2.4.2.1). Overall, there is good agreement between the three estimates of the photometric redshift, and, on average, they all trace the spectroscopic redshift equally well. **Right:** The photometric redshift PDFs for four example sources, with the peak, median and best redshift lines indicated in their respective colour. The 16-84th percentile is shown as the blue region. The three redshift estimates agree well for single-peaked (panel a), and some double-peaked PDFs (panel b). However, for some double-peaked PDFs, the peak and best values reside at different peaks (panel c). Also, due to finite sampling, the peak and/or best redshift estimates can be outside the 16-84th percentile of the PDF (panel d). Therefore, for the best estimate of the photometric redshift (as well as for the derived parameters, e.g. stellar mass, SFR etc) we take the median from the respective PDF, with uncertainties reflecting the 16–84th percentile values of the distribution for all galaxies analysed in this thesis.

We note that if we instead adopted the peak/best value from the PDF, none of the conclusions in this thesis are significantly affected, however picking a single (median) value for all sources means the analysis is done in a consistent manner for all galaxies in our samples. In a small number of cases, the SEDs are overly constrained due to the finite sampling, and the PDFs are highly peaked, meaning the returned uncertainties are unrealistically low. In these cases, we take a conservative approach and adopt the median uncertainty from the full sample for that derived parameter. We flag the sources where this has occurred in the published on-line catalogue.

In § 2.4.1, we described our approach on setting the limits in the UV/optical/near-

IR and far-infrared wavebands. As a first check, we test whether our approach in dealing with the photometry limits has any effect on the derived photometric redshifts. The detection fraction is lowest in the bluest wavebands (U, B) for our sample SMGs, thus we check whether the limits in the U and B bands (setting the flux to zero with a 3σ uncertainty) weighs the UV part of the SED to significantly lower values in the χ^2 fitting and thus, affects the derived photometric redshift. We find no significant changes in the derived photometric redshift, with any differences being encompassed in the redshift error range. We note that the redshift prior in MAGPHYS has a broad peak at $z \sim 1.5$ (see Fig. 3.1a), thus we have also tested the influence of the prior on the photometric redshifts by running MAGPHYS on all of the SMGs with a flat prior distribution (in range of $z = 0$–7). The resulting change in the redshift distribution is negligible, with $\Delta z = 0.100 \pm 0.007$. Hence, we conclude that the prior does not have a significant effect on our estimate of the photometric redshift distribution.

Finally, before testing the accuracy of the photometric redshifts, we ensure that the energy balance technique is appropriate and the far-infrared photometry is not affecting the redshift prediction significantly. We run MAGPHYS on SMGs with K-band detections including only photometry up to 8 μm and compare the predicted photometric redshifts to the values derived using the full UV-to-radio photometry. We find that the scatter of photometric redshifts is within the error range with a median of $(z_{\rm full} - z_{\leq 8\mu m})/(z_{\rm full}^{84th} - z_{\rm full}^{16th}) = 0.11$ and 68$^{\rm th}$ percentile range of -1.0–0.95. Thus, coupling far-infrared information into the estimation of photometric redshifts is not introducing any significant biases.

2.4.2.1 Testing against spectroscopic redshifts

Archival spectroscopic redshifts are available for 6,719 K-band detected galaxies (that have no photometric contamination flags) in the UKIDSS DR11 catalogue (Smail et al. 2008; Hartley et al. in prep.; Almaini et al. in prep.). This includes 44 of the SMGs from our AS2UDS sample (including new spectroscopic redshifts from KMOS observations; Birkin et al. in prep.). We note that it is possible, and

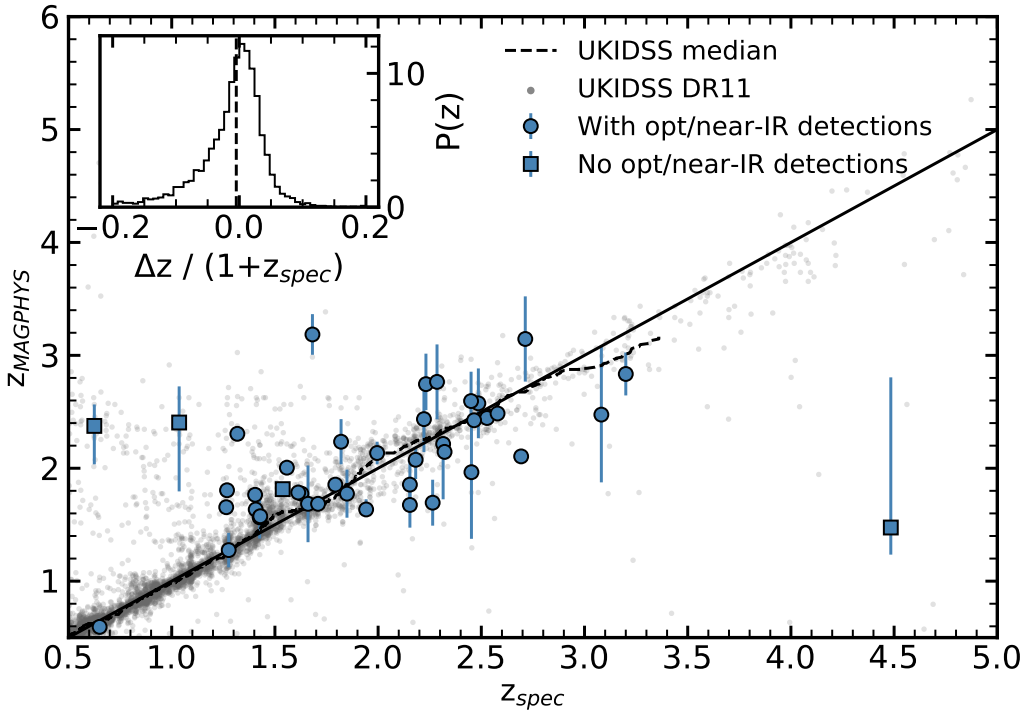

Figure 2.9: Comparison of MAGPHYS photometric redshifts versus spectroscopic redshifts. The 44 AS2UDS SMGs with spectroscopic redshifts are plotted, as well as field sample of 6,719 K-detected UDS galaxies with spectroscopic redshifts. The solid line indicates a one-to-one relation and the dashed line shows the running median for the field galaxies, which tracks the spectroscopic redshifts closely up to $z \sim 3.5$. For the SMGs, we identify the four that lack detections in the optical bands. The inset panel shows the fractional offset of photometric redshifts from spectroscopic values for the field sample. The median offset is $(z_{spec} - z_{phot})/(1 + z_{spec}) = -0.005 \pm 0.003$ with a dispersion of 0.13.

indeed probable, that given the wide variety of sources from which these redshifts were taken and the faintness of many of the target galaxies, that some of these spectroscopic redshifts are incorrect. As a result, we concentrate on the quality of the agreement achieved for the bulk of the sample, giving less emphasis to outliers. We also note that, given the heterogeneous sample selection, the UKIDSS UDS sample contains a mix of populations, which is likely to include an increasing fraction of AGN-hosts at higher redshifts, the SEDs for which are not reproduced by the current version of MAGPHYS.

We isolate a sub-sample of all field galaxies with no photometric contamination flags above $z = 2$ and include 500 galaxies with spectroscopic redshifts below $z = 2$

to form a field sample biased towards higher-redshift/fainter sources that is more representative of the distribution of high-redshift SMGs. MAGPHYS run on this sub-sample yields a median offset between the spectroscopic- and photometric-redshifts of $\Delta z/\,(1+z_{spec}) = 0.004 \pm 0.001$, although with larger systematic offsets at redshift above $z \simeq 2.5$ ($\Delta z/\,(1+z_{spec}) = 0.040 \pm 0.003$). At these redshifts, the photometric redshift has sensitivity to the intergalactic medium (IGM) opacity as the Lyman break (rest-frame $\lambda = 912$–1215Å) pass through the observed B-band for sources that are bright enough to be detectable. Adjusting the IGM absorption coefficient in the SED model can reduce this systematic Δz offset (e.g. Wardlow et al., 2011). The IGM effective absorption optical depth of each model is drawn from a Gaussian distribution centred at the mean value given in Madau (1995), with a standard deviation of 0.5. We, therefore, rerun MAGPHYS for the spectroscopic sample with IGM absorption coefficients between 0.2–1.0 of each drawn model value. From this test, we find that tuning the IGM coefficient to 0.5 of the initially drawn value minimises the systematic offset between the spectroscopic and photometric redshifts above $z \sim 2$, whilst maintaining the closest match at lower redshift, thus we adopt it in any subsequent analysis. In Fig. 2.9, we show the comparison of the spectroscopic and photometric redshifts for the field galaxies and SMGs. We see that for the SMGs the three most extreme outliers are optically undetected, leading to uncertain estimation of their redshifts. The fourth outlier is a secondary ALMA source within a single SCUBA-2 map, where the optical photometry may have been mismatched. Over the full redshift range, the offsets between the spectroscopic and photometric redshifts for all 6,719 field galaxies is $\Delta z/\,(1+z_{spec}) = -0.005 \pm 0.003$, and $\Delta z/\,(1+z_{spec}) = -0.02 \pm 0.03$, with a 1σ scatter of $\Delta z/\,(1+z_{spec}) = 0.13$, if we just consider the 44 SMGs. The photometric redshift accuracy we obtain is comparable to that found for SMGs in the COSMOS field by Battisti et al. (2019).

2.4.3 Comparing observed and MAGPHYS-derived quantities

In this section, we compare the derived quantities returned from MAGPHYS with the observables that they are empirically expected to correlate with (e.g. the dust

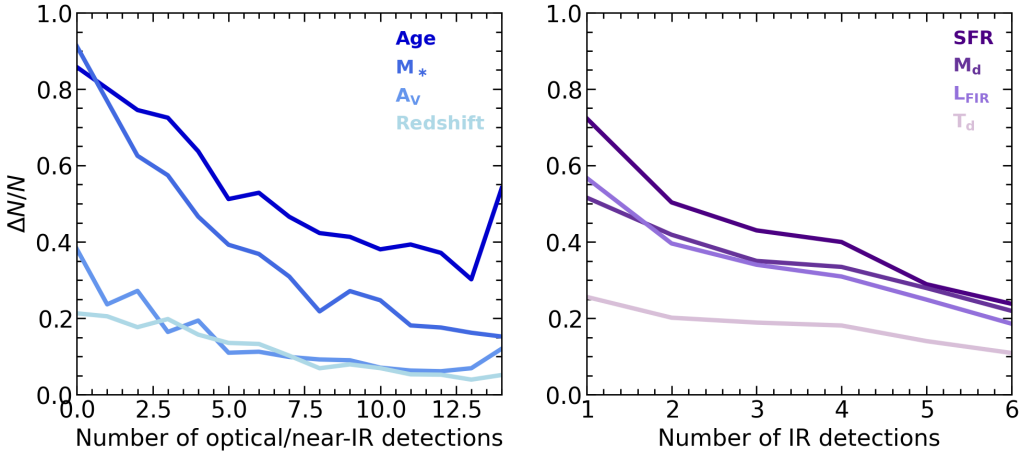

Figure 2.10: Fractional error on mass weighted age, stellar mass, dust attenuation, and redshift as a function of number of detections in the optical/near-infrared (left), and star-formation rate, dust mass, far-infrared luminosity and dust mass as a function of number of detections in the far-infrared (right). As expected, the fractional error on any given parameter decreases as the SED becomes more constrained with a higher detection fraction.

mass is expected to correlate broadly with 870-μm flux density).

We first check what effect the error on the photometric redshift has on our inferred physical properties by running MAGPHYS on the AS2UDS sub-sample of 44 SMGs with spectroscopic redshifts at their fixed spectroscopic redshifts. We investigate whether the change in the derived value of the property at the spectroscopic redshift and the photometric redshift is encompassed by the quoted errors (at the photometric redshift and including the covariance due to the uncertainty in this value) by calculating the fractional difference, $X_{\rm spec}/X_{\rm phot}$, where X is any given parameter. The change for all the predicted parameters was, on average, less than $\lesssim$15 per cent, which is less than the typical uncertainty. Therefore, we confirm that the uncertainty effect on any given parameter is captured in its error range and is not affecting final parameter distribution.

To check how the uncertainties in the derived parameters correlate with the number of photometric constraints, in Fig. 2.10, we show the fractional error in the derived quantities as a function of optical/near-IR (up to 8μm; maximum of 14 bands) or far-infrared detections (160–870μm; maximum of 6 bands). As expected, sources

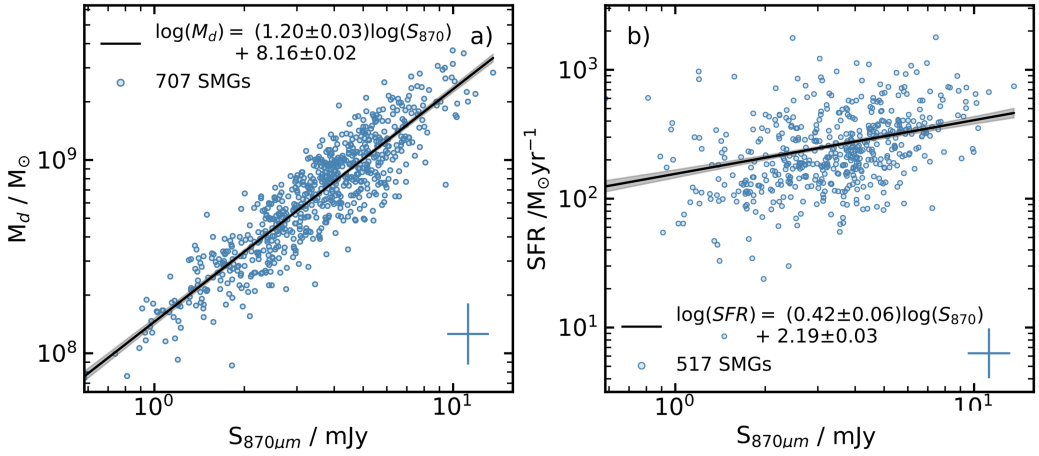

Figure 2.11: Dust mass and SFR versus 870μm flux density for SMGs. The typical errors are shown in the bottom right of each panel. **(a)**: Dust mass versus ALMA 870μm flux for all 707 SMGs. The best-fit line has a slope of 1.20±0.03 and the shaded region indicates the $\pm1\sigma$ error range. The strong positive correlation between the observed 870-μm flux and dust mass indicates that the 870-μm emission has the most sensitivity to cold dust mass. **(b)**: Star-formation rate versus ALMA 870-μm flux for 517 AS2UDS sources at $z = 1.8$–3.4. We plot the best-fit line with a gradient of 0.42±0.06 and $\pm1\sigma$ errors shown as the shaded region. A positive correlation is observed, as expected for dusty SMGs, where the emission from young/hot starts is re-emitted at far-infrared wavelengths.

with more detections in either optical/near-IR or far-IR bands have lower fractional uncertainty in the parameters that are derived from those bands. In the optical regime, photometric redshift and dust attenuation have the lowest fractional error, while mass-weighted age has a highest uncertainty. In the far-infrared, SFR, M_d and $L_{\rm FIR}$ have comparable fractional uncertainty, while dust mass has the lowest uncertainty. However, we note that the dust temperatures are consistent with the median dust temperature of the whole sample, when taking the uncertainties innto account ($(T_d - T_m)/\delta T \sim 1$). Therefore, dust temperature cannot be reliably constrained for our sample using MAGPHYS model.

2.4.3.1 Far-infrared properties

In this section, we focus on those quantities that are most sensitive to the far-infrared part of the SED and see how these correlate with the far-infrared photometry. The main source of sub-millimetre radiation is the thermal continuum from dust grains – the rest-frame UV/optical radiation from young/hot stars is

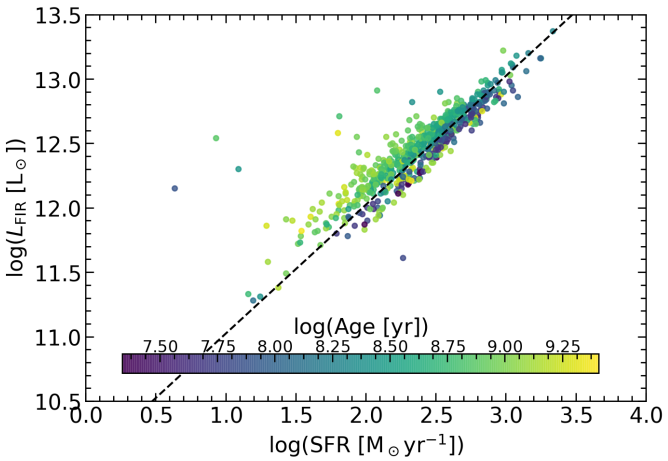

Figure 2.12: Far-infrared luminosity versus star-formation rate coloured by mass-weighted age for the AS2UDS sources. Overall, the correlation between these two parameters closely follow the Kennicutt (1998) relation (black dashed line) with a median offset of SFR/ $\mathrm{SFR_{K98}(L_{FIR})} = 0.87 \pm 0.01$ (where $\mathrm{SFR_{K98}(L_{FIR})}$ is the predicted Kennicutt relation). We see that, at a given star-formation rate, older age results in higher far-infrared luminosity. We note that the upward scatter at low star-formation rates is likely produced by dust-obscured AGN, where the high far-infrared luminosities are a result of AGN heating.

absorbed by dust and re-emitted at far-infrared wavelengths. Hence observed 870-μm flux density should trace both the dust mass and star-formation rate (e.g. Blain et al., 2002; Scoville et al., 2014). In Fig. 2.11a we, therefore, plot the 870-μm flux density versus estimated dust mass. There is a strong correlation between 870-μm flux density and dust mass (M_d), which follows $\log_{10}(M_\mathrm{d}[M_\odot]) = (1.20 \pm 0.03) \times \log_{10}(S_{870}[\mathrm{mJy}]) + 8.16 \pm 0.02$. This tight correlation suggests that, as expected, the 870-μm flux density tracks the cold dust mass (Scoville et al., 2014; Liang et al., 2018). In Fig. 2.11b we also show the trend of 870-μm flux density with star-formation rate for the $z = 1.8$–3.4 subset (which represents the 16–84$^\mathrm{th}$ percentile) to reduce the degeneracies with redshift. There is a clear trend and, fitting to the SMGs, the correlation between 870 μm flux density and star-formation rate has the form $\log_{10}(\mathrm{SFR}[\mathrm{M_\odot yr^{-1}}]) = (0.41 \pm 0.05) \log_{10}(S_{870}[\mathrm{mJy}]) + 2.19 \pm 0.03$. The trend observed with star-formation rate is weaker and has more dispersion than that of dust mass, thus constraints from shorter rest-frame far-infrared wavelengths are needed to reliably measure the star-formation rate.

The predicted star-formation rates and far-infrared luminosities from MAGPHYS

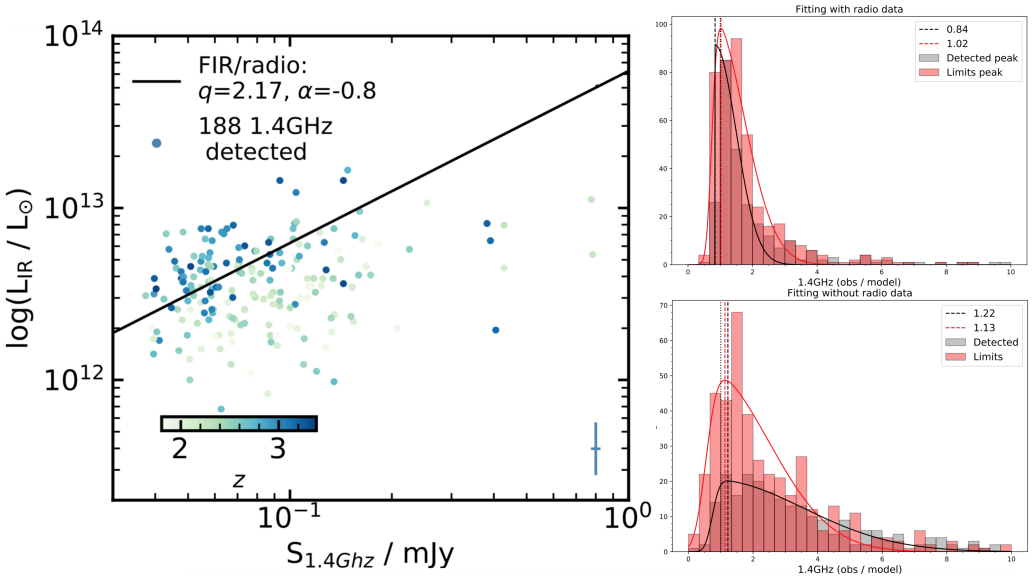

Figure 2.13: **Left:** Far-infrared luminosity versus 1.4-GHz flux for the SMGs at $z = 1.8$–3.4. The solid line shows the FIR–radio correlation with $q_{IR} = 2.17$ at the median redshift of the AS2UDS sample. The radio-detected population are roughly consistent with the trends expected from the FIR–radio correlation with the scatter being mainly driven by redshift variation. The typical uncertainty is shown in the bottom right. **Right:** Comparison the observed 1.4 GHz flux density to the prediction of the flux density from the best-fitting MAGPHYS model when including the radio 1.4 GHz photometric observation (top) and excluding it from the fitting (bottom). The distributions are highly skewed, and on average, there is up to 15 per cent difference between the model and observed values when excluding the radio photometry. However, we note that it is an upper limit. If deeper radio observations were available, this offset would come closer to ∼1.

closely follow the Kennicutt (1998) relation with an offset of SFR/ $\mathrm{SFR_{K98}(L_{FIR})}$ $= 0.87 \pm 0.01$ (where $\mathrm{SFR_{K98}(L_{FIR})}$ is the predicted Kennicutt relation), as shown in Fig. 2.12. In addition, the total far-infrared luminosity should correlate with the *observed* radio luminosity (although this is used in the SED fitting) due to the far-infrared–radio correlation (van der Kruit, 1971, 1973). As mentioned in § 2.3, the radio luminosity is expected to be dominated by synchrotron radiation from relativistic electrons that have been accelerated in supernovae remnants (Harwit & Pacini, 1975). The far-infrared and radio luminosities are correlated since the supernovae remnants arise from the same population of massive stars that heat and ionise the HII regions, which in turn heats the obscuring dust. In Fig. 2.13 we, therefore, plot the MAGPHYS far-infrared luminosity (integrated between 8–1000 μm) as a function of the observed 1.4-GHz flux density, again restricting the

sample to a redshift range of $z = 1.8$–3.4 (to reduce the effects of the geometrical dimming). We overlay the far-infrared/radio correlation from Ivison et al. (2010) for the median redshift of our sample SMGs ($z = 2.61$) with $q_{\rm IR} = 2.17$ (Magnelli et al., 2010) and $\alpha = -0.8$ (Ivison et al., 2010), appropriate for high redshift, strongly star-forming galaxies (Magnelli et al., 2010), where $q_{\rm IR}$ is the logarithmic ratio of bolometric infrared and monochromatic radio flux and α is the radio spectral index. This shows a rough correlation between the predicted far-infrared luminosities and the observed radio luminosities, which is consistent in form and normalisation with that derived for the AS2UDS sample. The scatter is mainly due to variations in redshift. A more detailed analysis of the far-infrared - radio correlation in AS2UDS is given in Algera et al. (2020).

We also check the FIR-radio correlation in terms of the derived SEDs in Fig. 2.13. We show the comparison between the observed radio 1.4 GHz photometry and the model prediction when fitting the full SED (including radio). The skewed Gaussian fits show that there is good agreement between the model and observed values with a mean of $\sim$1. When fitting the SEDs with no radio information (excluding the radio 1.4 GHz photometric point), we get a fair estimation on what the far-infrared to radio correlation in MAGPHYS is predicting, and how well it is estimating the long wavelength regime of the SMG SEDs. For all the galaxies in our sample (detected and undetected in the radio) the mean offset is ~ 1.15. Thus, there is up to 15 per cent difference between the model and observed values, however we note that this is an upper limit. If deeper radio observations were available, this offset would come closer to $\sim$1. Therefore, the modelling adopted by MAGPHYS for the far-infrared/radio SED is consistent with the observed photometry.

2.4.3.2 Optical/near-IR properties

To test how the derived stellar mass, optical extinction and redshift correlate with basic observables, in this section we turn to the optical and near-infrared wavelengths. The observed optical/near-infrared emission at $z \sim 2$ corresponds to rest-frame far-UV to R band, which traces the stellar-dominated SED around the

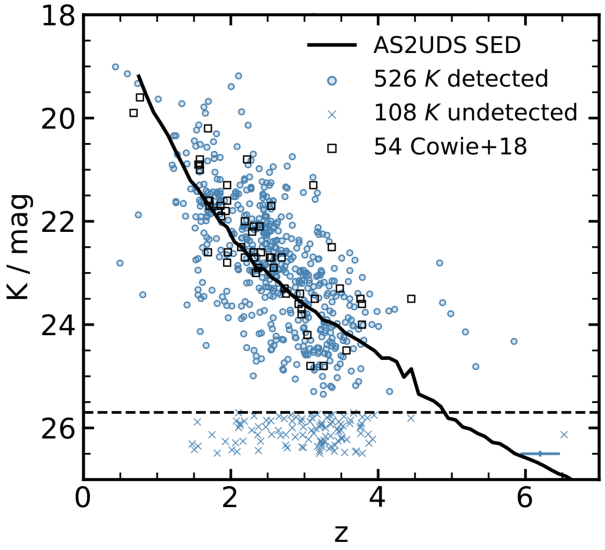

Figure 2.14: K-band magnitude versus photometric redshift for 526 K-band detected SMGs. The 108 SMGs with no K-band detection are plotted below the K-band aperture-corrected magnitude limit of $K = 25.7$. We see a negative correlation due to the positive k-correction in the K-band. The fact that K-band undetected SMGs have redshifts down to $z \sim 1.5$–2.5 highlights that some of the sources may be very obscured. The expected variation with redshift for the composite SED from our SMG sample is shown as a solid line. The typical error is shown in the bottom right of each panel.

Balmer ($\lambda = 3646$Å) and 4000Å breaks – the former is more prominent in star-forming galaxies, while the latter is more prominent in older, quiescent galaxies, giving an indication of the galaxy's recent star-formation history.

In Fig. 2.14, we plot the K-band magnitude. versus redshift. The value of the observed K-band magnitude increases with increasing redshift, as a result of positive k-correction (Smail et al., 2004). As a guide, we overlay the average K-band magnitude expected as a function of redshift based on the composite SMG SED from our sample (see § 3.3 in Chapter 3). We also overlay the ALMA-detected SMGs in the CDFS from Cowie et al. (2018) which show a similar trend. We note that there are 108 SMGs in our sample that are undetected in the K-band ($K > 25.7$). The MAGPHYS-derived redshifts for this sub-sample lie in the range $z = 1.5$–6.5 with a median of $z = 3.0 \pm 0.1$. We will discuss this population further in § 3.2 of Chapter 3.

Next, we assess the V-band dust attenuation, A_V. The optical extinction returned from MAGPHYS reflects the stellar luminosity-weighted average across the source.

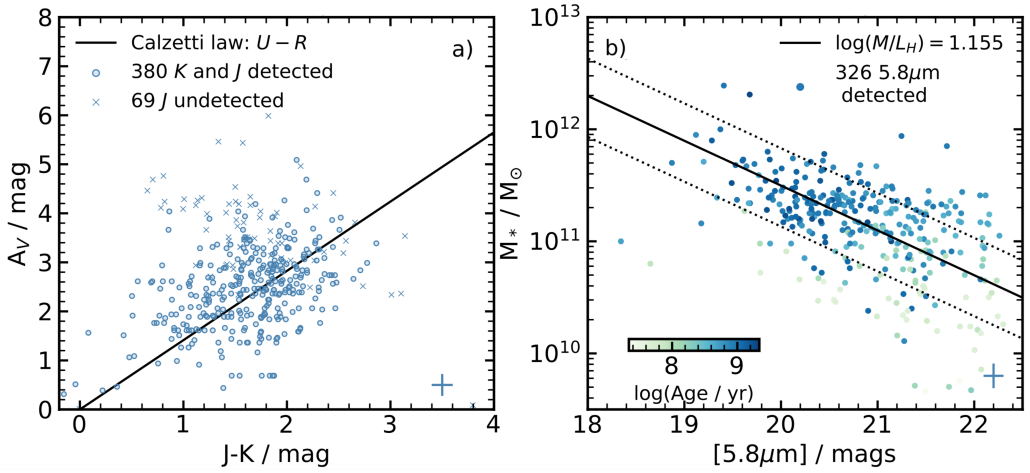

Figure 2.15: Observed photometry versus predicted optical physical parameters for the AS2UDS SMGs at $z = 1.8$–3.4. In all panels, circles indicate sources that are detected. The typical errors are shown in the bottom right of each panel. **(a)**: V-band dust attenuation versus $(J - K)$ colour. The solid line shows the predicted reddening from the Calzetti et al. (2000) reddening law. As expected, the rest-frame $(U - R)$ colour (observed $(J - K)$ at the median redshift of AS2UDS) follows the predicted reddening law well, indicating that SMGs with redder colours are likely to be more dust-obscured. **(b)**: Stellar mass versus IRAC 5.8-μm magnitude, coloured by estimated age. The solid line shows the track of the mass inferred from the median H-band mass-to-light ratio at the median redshift. The dashed lines indicate H-band mass-to-light ratios of $\log(M/L_{\rm H}[M_\odot/L_\odot]) = 2.5$ and $\log(M/L_{\rm H}[M_\odot/L_\odot]) = 0.5$. Rest-frame H-band (corresponding to $\sim 5.8\,\mu$m at the median redshift of the AS2UDS SMGs) correlates well with the predicted stellar mass. The scatter is mainly due to covariance of the mass with the mass-weighted age, as shown by the age trend at a given 5.8-μm magnitude.

At $z \sim 2$, the extinction is expected to correlate with the rest-frame optical colours. In Fig. 2.15a we, therefore, plot the A_V versus $(J - K)$ colour (which corresponds approximately to rest-frame $(U - R)$ colour at these redshifts and so is indicative of the optical SED slope). We also overlay a track representing the expected rest-frame $(U - R)$ colours (corresponding to observed $(J - K)$ at the median redshift of AS2UDS) based on the Calzetti reddening law (Calzetti et al., 2000). This reproduces the trend we see and suggests that our estimates of A_V for the SMGs from MAGPHYS are reliable. Reassuringly, the majority of the 181 SMGs with no detection in either J- or K-band have a higher A_V, indicating that it is likely that their higher dust obscuration is responsible for their non-detection.

Finally, we turn to the stellar mass. It is expected that the dominant stellar population by mass in these galaxies arises from the lower mass stars, which can

be better traced from the rest-frame H-band luminosity. At $z \sim 2$, this corresponds to the mid-infrared, around $\sim 6\mu$m and so, in Fig. 2.15b, we plot the MAGPHYS-derived stellar mass as a function of the observed-frame IRAC 5.8-μm magnitude. As expected, brighter 5.8-μm magnitudes correspond to higher stellar masses and for SMGs in the range $z \sim 1.8$–3.4 we derive a correlation with $\log M_* = (-0.25 \pm 0.03)\, S_{5.8} + (16.4 \pm 0.6)$. We also overlay the prediction of stellar mass for a median H-band mass-to-light ratio (1.155) for our sample SMGs and find that it follows the observed properties well. The correlation in Fig. 2.15b shows a scatter of 0.05 dex at fixed 5.8 μm magnitude. This scatter is due to variations in the star-formation history and dust extinction, but is also correlated with the predicted mass-weighted age of the stellar population in the sense that for a given observed 5.8-μm magnitude, the younger the inferred age of the galaxy the lower the stellar mass. We note that independent tests of the reliability of the MAGPHYS predictions for the reddening and stellar masses using the simulated EAGLE galaxies also provide mutual support for the reliability of these parameters, given the strong covariance expected between these two quantities in any SED fit (see Fig. 2.1).

2.4.3.3 Predicting the far-infrared properties of the field galaxies in UDS

In this section, we test the dust attenuation laws (and the degeneracies between age and reddening), by determining whether far-infrared luminosity can be predicted by fitting just the optical/near-infrared part of the SED (in wavebands up to 8μm) using the K-band selected galaxies from the UKIDSS UDS survey and AS2UDS SMGs, which were analysed in a similar manner.

In Fig. 2.16, we plot predicted far-infrared luminosity versus redshift for the K-band selected field galaxy sample. We also plot those SMGs that are K-band detected and where we have similarly derived the predicted far-infrared luminosities based on MAGPHYS modelling of *just* their optical/near-infrared photometry up to 8.0 μm. Remarkably, on average MAGPHYS is able to identify the SMGs as dusty and highly star-forming, and thus far-infrared luminous, using only the in-

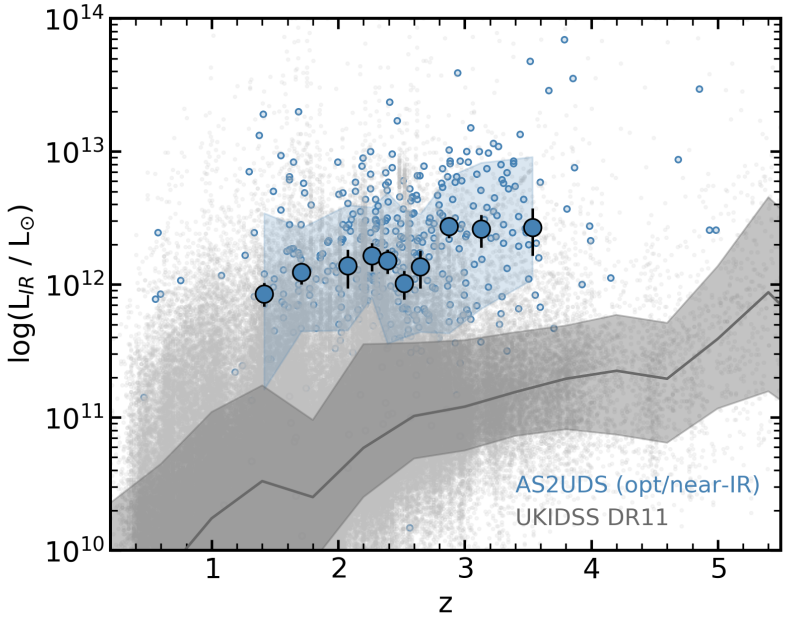

Figure 2.16: Predicted far-infrared luminosity as a function of redshift for a K-band selected field galaxy sample with the most reliable photometry based on a MAGPHYS analysis of the photometry shortward of the IRAC 8.0-μm band. The solid line shows the running median and the shaded region indicates the inter-quartile range. We also plot the far-infrared luminosity derived for the 511 K-band detected SMGs, similarly limiting the model fit to photometry shortward of 8.0 μm. We indicate with filled circles the binned medians of samples of 50 SMGs ranked in redshift and the blue region shows the 16-84$^{\rm th}$ percentile range. Even when MAGPHYS only has information on the optical/near-infrared SED, it still predicts AS2UDS SMGs to be significantly more far-infrared luminous than a typical field galaxy.

formation shortward of $\sim$2 μm in the rest-frame. Indeed, for the K-band detected $S_{870} > 3.6$ mJy ALMA SMGs, the mean ratio of far-infrared luminosity from the $\leq$8-μm fit to that from the full-SED including far-infrared/sub-millimetre photometry is $L_{\rm IR}^{\leq 8\mu{\rm m}}/L_{\rm IR}^{\rm full} = 1.1 \pm 0.1$.

However, it is clear from Fig. 2.16 that MAGPHYS also predicts a population of $\sim$2,000 galaxies at $z \sim 1.5$–4, which are claimed to be far-infrared luminous, but which are not detected in the SCUBA-2 850-μm survey. We suspect that many of these faux-SMGs may be either sources with AGN contributions to their optical/near-infrared SEDs or hotter dust sources, missed by our 850-μm selection. Hence, while this test does confirm that the dust modelling and energy balance in MAGPHYS provides robust constrains on the far-infrared emission, it can only be

used reliably if far-infrared photometric constraints are available, otherwise, the false-positive rate is high.

This comparison of derived parameters from MAGPHYS modelling of the complete SEDs of SMGs, compared to the results when restricted to *only* fitting photometry shortward of 8 μm, indicates a poor recovery of those parameters that are most sensitive to details of the dust SED, such as dust temperature or dust mass. However, it also suggests little change for this K-detected sub-set of the SMG population in the derived median: photometric redshifts, $(z^{\rm full} - z^{\leq 8\mu{\rm m}})/(1+z^{\rm full}) = 0.008 \pm 0.004$ (with 1σ dispersion of 0.13); dust reddening, $(A_V^{\rm full} - A_V^{\leq 8\mu{\rm m}})/A_v^{\rm full} = 0.01 \pm 0.02$ (with 1σ dispersion of 0.30); and stellar mass, $(M_*^{\rm full} - M_*^{\leq 8\mu{\rm m}})/M_*^{\rm full} = -0.02 \pm 0.01$ (with 1σ dispersion of 0.68); and a modest bias towards younger ages when including the $>10\,\mu$m photometry: $({\rm Age}_m^{\rm full} - {\rm Age}_m^{\leq 8\mu{\rm m}})/{\rm Age}_m^{\rm full} = -0.25 \pm 0.05$ (with 1σ dispersion of 1.85).

2.5 Conclusions

In this chapter, we have tested and calibrated an SED fitting code MAGPHYS (da Cunha et al., 2015) using $\sim$9000 galaxies from the EAGLE simulation, $\sim$300,000 star-forming 'main-sequence' galaxies in the UDS field (Almaini et al., in prep) and 707 dusty star-forming galaxies at high redshift from the AS2UDS survey (Stach et al., 2019). We assessed the properties of galaxies from the multi-wavelength photometric data and fit spectral energy distribution models to the available UV-to-radio photometry. We also tested the derived photometric redshifts and physical properties against the photometric observations. Our main findings are:

- Analysis on the $\sim$9000 galaxies from the EAGLE simulation revealed systematic offsets in the derived physical properties, such as star-formation rate, mass-weighted age, dust temperature, dust and stellar mass. Though differences are expected due to the differences in the models, further detailed analysis would be needed to understand the intricacies of the systematics. For any results in Chapter 3, we adopt a significance limit that the trends seen in SMGs must be

greater than the quartile range of this scatter.

- Comparison of the predicted photometric redshift with the available spectroscopic redshifts showed good agreement with an offset of $\Delta z/(1+z_{spec}) = -0.005 \pm 0.003$ for the UKIDSS UDS sample or $\Delta z/(1+z_{spec}) = -0.02 \pm 0.03$, with a 1σ scatter of $\Delta z/(1+z_{spec})$ =0.13, if only considering the AS2UDS SMGs. We also confirm that the error due to uncertainty in the photometric redshift on any given physical parameter is captured in the quoted error and is not affecting the final parameter distribution. Furthermore, MAGPHYS derived physical properties agree well with the observables which they are empirically expected to correlate with, both in the optical and far-infrared.

- The comparison of the derived parameters from MAGPHYS modelling of the complete SEDs of SMGs, compared to the results when restricted to *only* fitting photometry shortward of $8\,\mu$m, indicate that MAGPHYS provides robust constrains on the total far-infrared emission. However, it can only be used reliably if far-infrared photometric constraints are available, otherwise, the false-positive rate is high.

- For the 870μm-selected SMGs with a median 870-μm flux density of $S_{870} = 3.6$ mJy, $\sim$80 per cent of the galaxies are detected in the extremely deep K-band data available for the UKIDSS UDS field (3-σ limit of $K = 25.7$). This demonstrates that $\sim$20 per cent of SMGs are undetectable in very deep optical/near-infrared observations and hence, that there exists a significant population of strongly star-forming, but strongly dust-obscured galaxies missed by surveys in those wavebands. The 870-μm selected sample of SMGs most closely resembles a sample selected on dust mass, with a ratio of dust mass in $M_\odot$ to 870-μm flux of $\log_{10}(M_{\rm d}[M_\odot]) = (1.20 \pm 0.03) \times \log_{10}(S_{870}[{\rm m}Jy]) + 8.16 \pm 0.02$. There is a weaker correlation between 870-μm and far-infrared luminosity (or star-formation rate, with ${\rm SFR} \propto S_{870}^{0.42\pm0.06}$). In the next chapter we discuss the science results, focussing on the analysis of the physical properties of the ALMA SMGs from the AS2UDS survey, as derived by MAGPHYS.

Chapter 3

Physical properties and evolution of strongly star-forming galaxies at $z \sim 2.5$

Preamble

In this chaper we analyse the physical properties of a large, homogeneously selected sample of ALMA-located sub-millimetre galaxies (SMGs). We interpret their UV-to-radio SEDs that we have derived using MAGPHYS in Chapter 2, and determine a median redshift of $z = 2.61 \pm 0.08$, with just ~ 6 per cent at $z > 4$. Our survey provides a sample of massive dusty galaxies at $z \gtrsim 1$, with median dust and stellar masses of $M_{\rm d} = (6.8 \pm 0.3) \times 10^8\,{\rm M}_\odot$ (thus, gas masses of $\sim 10^{11}\,{\rm M}_\odot$) and $M_* = (1.26 \pm 0.05) \times 10^{11}\,{\rm M}_\odot$. The space density and masses of SMGs suggest that almost all galaxies with $M_* \gtrsim 3 \times 10^{11}\,{\rm M}_\odot$ have passed through an SMG-like phase. The redshift distribution is well fit by a model combining evolution of the gas fraction in halos with the growth of halo mass past a critical threshold of $M_{\rm h} \sim 6 \times 10^{12}\,{\rm M}_\odot$, thus SMGs may represent the highly efficient collapse of gas-rich massive halos. We show that SMGs are broadly consistent with simple homologous systems in the far-infrared, consistent with a centrally illuminated starburst. Our study provides strong support for an evolutionary link between the active, gas-rich SMG population at $z > 1$ and the formation of massive, bulge-dominated galaxies

across the history of the Universe. This work has been published as a first author paper (Dudzevičiūtė et al., 2020).

3.1 Introduction

Analysis of the relative brightness of the extragalactic background in the UV/optical and far-infrared/sub-millimetre suggest that around half of all of the star formation that has occurred over the history of the Universe was obscured by dust (e.g. Puget et al., 1996). In the local Universe, the most dust-obscured galaxies are also some of the most actively star-forming systems: ultra-luminous infrared galaxies (ULIRGs; Sanders & Mirabel, 1996) with star-formation rates of $\gtrsim 100\,\mathrm{M}_{\odot}\,\mathrm{yr}^{-1}$. These radiate $\gtrsim 95$ per cent of their bolometric luminosity in the mid-/far-infrared as a result of strong dust obscuration of their star-forming regions. These galaxies have relatively faint luminosities in UV/optical wavebands, but far-infrared luminosities of $L_{IR} \geq 10^{12}\,\mathrm{L}_{\odot}$ and hence they are most easily identified locally through surveys in the far-infrared waveband (e.g. *IRAS* 60μm). It has been suggested that the high star-formation rates of ULIRGs arise from the concentration of massive molecular gas reservoirs (and thus, high ISM densities and strong dust absorption) in galaxies that are undergoing tidal interactions as a result of mergers (Sanders et al., 1988).

The far-infrared ($\gtrsim$100μm) spectral energy distribution (SED) of the dust-reprocessed emission from ULIRGs can be roughly approximated by a modified blackbody. The rapid decline in the brightness of the source at wavelengths beyond the SED peak on the Rayleigh-Jeans tail creates a strong negative k-correction for observations of this population at high redshifts (Franceschini et al., 1991; Blain & Longair, 1993). Hence, a dusty galaxy with a fixed far-infrared luminosity and temperature will have an almost constant apparent flux density in the sub-millimetre waveband (which traces rest-frame emission beyond the redshifted peak of the SED) from $z \sim 1$ to $z \sim 7$ (see Casey et al. 2014). As a result, surveys in the sub-millimetre waveband in principle allow us to construct luminosity-limited samples of obscured,

star-forming galaxies over a very wide range of cosmic time, spanning the expected peak activity in galaxy formation at $z \gtrsim 1$–3 (e.g. Chapman et al., 2005; Casey et al., 2012; Weiß et al., 2013; Simpson et al., 2014; Brisbin et al., 2017; Strandet et al., 2016).

Sub-millimetre galaxies (SMGs) with 850-μm flux densities of $S_{850} \gtrsim 1$–10 mJy were first uncovered over 20 years ago using the atmospheric window around 850-μm with the SCUBA instrument on the James Clerk Maxwell Telescope (JCMT) (Smail et al., 1997; Barger et al., 1998; Hughes et al., 1998; Eales et al., 1999). SMGs have some observational properties that appear similar to those of local ULIRGs, such as high far-infrared luminosities and star-formation rates; however, their space densities are a factor of $\sim 1{,}000\times$ higher than the comparably luminous local population (e.g. Smail et al., 1997; Chapman et al., 2005; Simpson et al., 2014). Thus, in contrast to the local Universe, these luminous systems are a non-negligible component of the star-forming population at high redshift. Very wide-field surveys with the SPIRE instrument on *Herschel* have traced this dusty luminous population, using very large samples, to lower redshifts and lower far-infrared luminosities (e.g. Bourne et al., 2016). However, the modest angular resolution of *Herschel*/SPIRE and resulting bright confusion limit, at longer far-infrared wavelengths limits its ability to select all but the very brightest (unlensed) sources at the era of peak activity in the obscured population at $z \gtrsim 1$–2 (Symeonidis et al., 2011). Such low-resolution far-infrared-selected samples are also more challenging to analyse owing to the ambiguities in source identification that results from ground-based follow-up to locate counterparts, which is necessarily undertaken at longer wavelengths than the original far-infrared selection.

With very high star-formation rates, SMGs can rapidly increase their (apparently already significant) stellar masses on a timescale of just ~ 100 Myr (e.g. Bothwell et al., 2013). High star-formation rates and high stellar masses of this population, along with the high metallicities suggested by the significant dust content, have been used to argue that they may be an important phase in the formation of the stellar content of the most massive galaxies in the Universe, being the progenitors of

local luminous spheroids and elliptical galaxies (Lilly et al., 1999; Chapman et al., 2005; Simpson et al., 2014). There have also been suggestions of an evolutionary link with quasi-stellar objects (QSOs) (e.g. Swinbank et al., 2006; Wall et al., 2008; Simpson et al., 2012; Hickox et al., 2012) due to the similarities in their redshift distributions. More recently these systems have been potentially linked to the formation of compact quiescent galaxies seen at $z \sim 1$–2 (e.g. Whitaker et al., 2012; Simpson et al., 2014; Toft et al., 2014) as a result of their short gas depletion timescales. This connection has been strengthened by recent observations in the rest-frame far-infrared that suggest very compact extents of the star-forming regions (Toft et al., 2014; Ikarashi et al., 2015; Simpson et al., 2015a; Gullberg et al., 2019). Thus several lines of evidence suggest that SMGs are an important element for constraining the models of massive galaxy formation and evolution.

In the first few years of operations, ALMA has been used to undertake a number of typically deep continuum surveys of small contiguous fields (Walter et al., 2016; Hatsukade et al., 2016; Dunlop et al., 2017; Umehata et al., 2018; Hatsukade et al., 2018; Franco et al., 2018; Muñoz Arancibia et al., 2018), with areas of 10s of arcmin^2 (including lensing clusters and proto-cluster regions). These small field studies typically contain sources at flux limits of $S_{870} \simeq 0.1$–$1\,\mathrm{mJy}$ (corresponding to star-formation rates of ~ 10–$100\,\mathrm{M_\odot\,yr^{-1}}$ or far-infrared luminosities of $\sim (0.5$–$5)\times10^{11}\,\mathrm{L_\odot}$) and so provide a valuable link between the bright SMGs seen in the panoramic single-dish surveys and the populations of typically less-actively star-forming galaxies studied in UV/optical-selected surveys. However, owing to their small areas they do not contain more than a few examples of the brighter SMGs. To efficiently study the brighter sources requires targeted follow-up of sources from panoramic single-dish surveys. Hence, ALMA has also been employed to study the dust continuum emission from samples of $\lesssim 100$ SMGs selected from single-dish surveys at 870 or $1100\,\mu$m (e.g. Hodge et al., 2013; Brisbin et al., 2017; Cowie et al., 2018). The primary goal of these studies has been to first precisely locate the galaxy or galaxies responsible for the sub-millimetre emission in the (low-resolution) single-dish source and to then understand their properties (e.g. Simpson et al., 2014;

Brisbin et al., 2017).

The first ALMA follow-up of a single-dish sub/millimetre survey was the ALESS survey (Karim et al., 2013; Hodge et al., 2013) of a sample of 122 sources with $S_{870} \geq 3.5\,\mathrm{mJy}$ selected from the $0.25\,\mathrm{deg}^2$ LABOCA 870-μm map of the Extended *Chandra* Deep Field South (ECDFS) by Weiß et al. (2009). The multi-wavelength properties of 99 SMGs from the robust main sample were analysed using the MAGPHYS SED modelling code by da Cunha et al. (2015) (see also the MAGPHYS analysis of a similar-sized sample of 1.1-mm selected SMGs in the COSMOS field by Miettinen et al. 2017). This approach of using a single consistent method to model the UV/optical and far-infrared emission provides several significant benefits for these dusty and typically very faint galaxies, over previous approaches of independently modelling the UV/optical and far-infrared emission (e.g. Clements et al., 2008; Cowie et al., 2018). In particular, the use in MAGPHYS of an approximate energy balance formulation between the energy absorbed by dust from the UV/optical and that re-emitted in the far-infrared provides more reliable constraints on the photometric redshifts for the SMGs (e.g. da Cunha et al., 2015; Miettinen et al., 2017). This is particularly critical in order to derive complete and unbiased redshift distributions for flux-limited samples of SMGs, as $\sim$20 per cent of SMGs are typically too faint to be detected at wavelengths shortward of the near-infrared (e.g. Simpson et al., 2014; Franco et al., 2018) and hence are frequently missing from such analyses. The energy balance coupling is also expected to improve the derivation of physical properties of these optically faint systems, such as stellar masses and dust attenuation, which are otherwise typically poorly constrained (Hainline et al., 2011; Dunlop, 2011).

While the studies by da Cunha et al. (2015) and Miettinen et al. (2017) have provided improved constraints on the physical parameters of samples of $\sim$100 SMGs, the modest size of these samples does not allow for robust analysis of the evolutionary trends in these parameters within the population (da Cunha et al., 2015), or to study sub-sets of SMGs, such as the highest-redshift examples (Coppin et al., 2009; Swinbank et al., 2012) or those that show signatures of both star-

formation and AGN activity (Wang et al., 2013). To fully characterize the population of SMGs and interpret their role in the overall galaxy evolution requires a large, homogeneously selected sample with precisely located sub-millimetre emission from sub/millimetre interferometers. We have therefore recently completed an ALMA study of a complete sample of 716 single-dish sources selected from the SCUBA-2 Cosmology Legacy Survey (S2CLS) 850-μm map of the UKIDSS UDS field (S2CLS is presented in Geach et al., 2017). This targetted ALMA study – called AS2UDS (Stach et al., 2019) – used sensitive 870-μm continuum observations obtained in Cycles 1, 3, 4 and 5 to precisely locate (to within $\ll 0.1''$) 707 SMGs across the $\sim 0.9\,\mathrm{deg}^2$ S2CLS–UDS field. AS2UDS provides the largest homogeneously-selected sample of ALMA-identified SMGs currently available, $\sim 6\times$ larger than the largest existing ALMA surveys (Hodge et al., 2013; Miettinen et al., 2017).

In this chapter, we use the UV-to-radio SEDs of the 707 ALMA-identified SMGs constructed using MAGPHYS+photo-z in Chapter 2. We interpret the SEDs and investigate the stellar and dust properties of the SMGs. This sample allows us to both improve the statistics to search for trends within the population (e.g. Stach et al., 2018, 2019) and to understand the influence of selection biases on our results and the conclusions of previous studies. With a statistically well-constrained and complete understanding of their redshift distribution and physical properties, we are able to address what place the SMG phase takes in the evolution of massive galaxies. Throughout this chapter, we compare our results to samples of both local ULIRGs and near-infrared selected high-redshift field galaxies, which we analyse in a consistent manner to our SMG sample to avoid any systematic uncertainties affecting our conclusions.

The chapter is structured as follows. We present the redshift distribution in § 3.2. In § 3.3 we examine their multi-wavelength properties through spectral energy distributions. In § 3.4, we assess the physical properties and evolutionary trends of the AS2UDS SMG population. We discuss the implications of our results in § 3.5 and present our conclusions in § 3.6. Unless stated otherwise, we use ΛCDM cosmology with with $H_0 = 70\,\mathrm{km\,s^{-1}\,Mpc^{-1}}$, $\Omega_\Lambda = 0.7$, $\Omega_m = 0.3$. The AB photometric

magnitude system is used throughout.

3.2 Redshift distribution of SMGs

The redshift distribution of SMGs can provide stringent constraints on galaxy formation models, and indeed, in some instances has forced changes in the way rapidly star-forming galaxies are modelled (e.g. Baugh et al., 2005). The early measurements of the redshift distribution of SMGs were hampered by incompleteness and errors in the identification of counterparts for single-dish sources (Chapman et al., 2005; Pope et al., 2006; Wardlow et al., 2011), although the results favoured a median redshift of $z \simeq 2.3$. More recent studies have overcome some of the weaknesses of the early work, both by unambiguously identifying the SMGs using sub-/millimetre interferometry with ALMA, and also by using a variety of methods to account for incompleteness in the estimation of redshift for the $\sim$10–20 per cent of SMGs that are too faint in the optical/near-infrared to locate multi-wavelength counterparts (Simpson et al., 2014; da Cunha et al., 2015; Danielson et al., 2017; Miettinen et al., 2017; Cowie et al., 2018).

These studies suggest a slightly higher median redshift, $z \simeq 2.6$ (e.g. Simpson et al., 2014), for the SMG population at mJy-flux density limits. However, exploiting these samples to go beyond just a crude redshift distribution to investigate evolution in the properties of SMGs with redshift, have been hampered by the modest sample sizes available ($\lesssim$100 SMGs), which weakens our ability to statistically identify trends in the data (e.g. with 870 μm flux density, star-formation rate or mass).

Our sample of 707 ALMA-identified SMGs, combined with the MAGPHYS analysis of their multi-wavelength properties from deep ancillary data (see Chapter 2), provides both, *complete* redshift information and the large sample size necessary to simultaneously sub-divide the sample on the basis of, e.g. mass and star-formation rate to search for evolutionary trends (e.g. McAlpine et al., 2019). In Chapter 2, we have confirmed the reliability of MAGPHYS in deriving photometric redshifts, thus we begin by deriving the photometric redshift distribution for the whole SMG

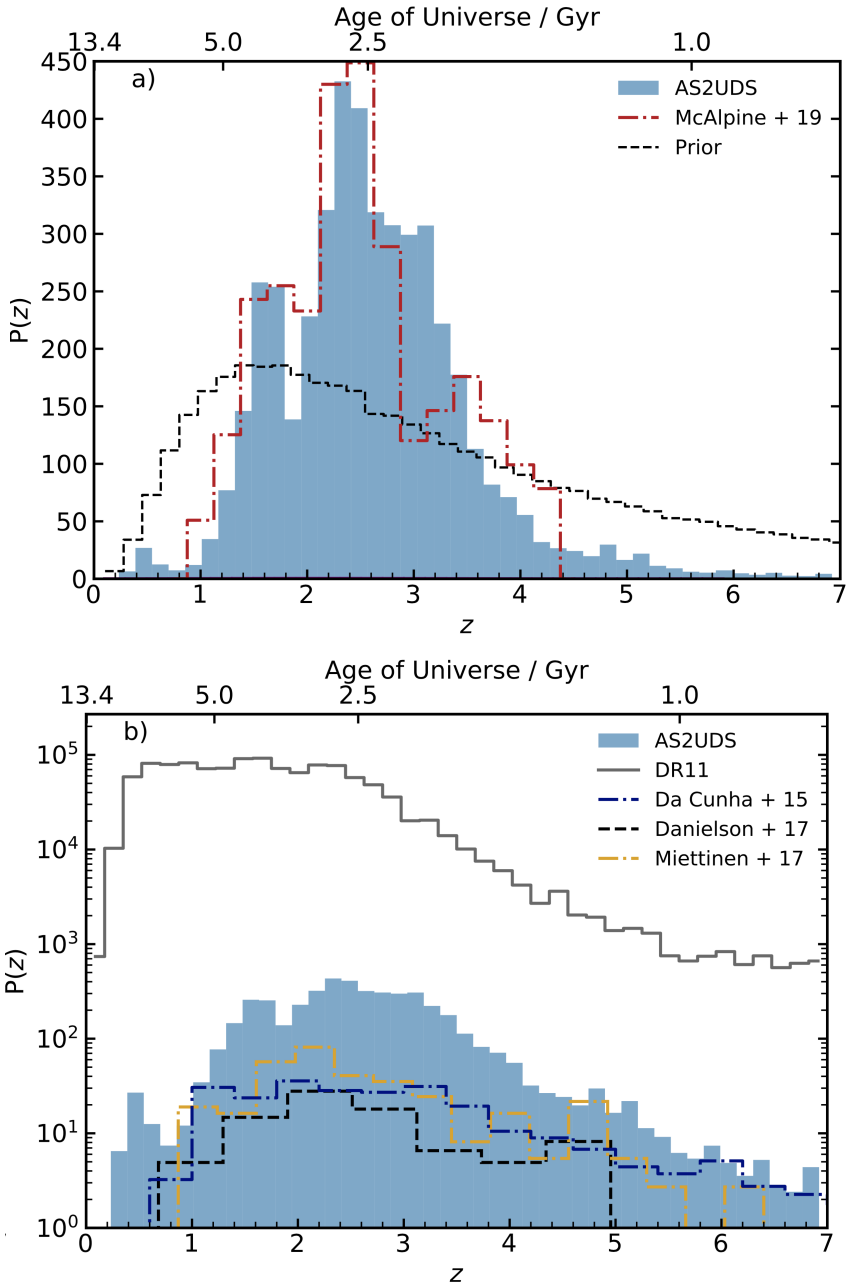

Figure 3.1: **(a)** The redshift distribution from summed likelihood distributions for our complete sample of 707 AS2UDS SMGs with a median of $z = 2.61 \pm 0.08$ (68th per centile range of $z = 1.8$–3.4 and 6 per cent at $z > 4$). The dashed line indicates the prior distribution. For comparison, we also overlay theoretical predictions for SMG type galaxies from McAlpine et al. (2019), who find a median redshift of $z = 2.4 \pm 0.1$. **(b)** Comparison of the AS2UDS redshift distribution to the equivalent distribution for the 99 ALESS SMGs from da Cunha et al. (2015), 52 spectroscopically identified ALESS SMGs from Danielson et al. (2017) and 124 spectroscopically identified SMGs from Brisbin et al. (2017). We also include a comparison to the field galaxies from our MAGPHYS-derived distribution for 205,910 K-band selected UKIDSS UDS sources with a median redshift of $z = 1.75 \pm 0.03$. The distributions are normalised by their survey area.

population and show this in Fig. 3.1a. To capture the uncertainties in the redshifts (and the range of quality reflected in their PDFs) we stack the individual likelihood redshift distributions of all of the SMGs. For the complete sample of 707 870 μm selected SMGs, we determine a median redshift of $z = 2.61 \pm 0.08$. The quoted error combines the systematic uncertainty derived from comparison of the MAGPHYS redshifts to those for the 6,719 K-band galaxies with spectroscopic redshifts in the UDS and the bootstrap error on the redshift distribution. The photometric redshift distribution is strongly peaked, with a 16–84th percentile range of $z = 1.8$–3.4 and just $\sim$6 per cent of SMGs at $z > 4$, while we find only five examples of SMGs at $z < 1$ even though this redshift range encompasses 57 per cent of the age of the Universe – underlining the identification of SMGs as a high-redshift population. Moreover, it is possible that some of these $z < 1$ systems are incorrectly identifications resulting from galaxy-galaxy lensing (e.g. Simpson et al., 2017; Danielson et al., 2017). In Fig. 3.1a, we also overlay the predicted redshift distribution for SMGs with $S_{850} \geq 1$ mJy from the EAGLE simulation (McAlpine et al., 2019). The median redshift for the EAGLE SMGs is $z = 2.4 \pm 0.1$, with a sharp decrease above $z \sim 2.5$, driven in part by an increasing dust temperature in sources at higher redshifts. Therefore, this model distribution is a reasonable match to our observations.

In Fig. 3.1b we, next, compare our sample to the earlier study of 99 SMGs from ALESS (da Cunha et al., 2015). This sample has a single-dish 870-μm flux density limit of $S_{870} \geq 3.5$ mJy, similar to our survey and the photometric redshifts were also derived using MAGPHYS. da Cunha et al. (2015) estimate a median redshift of $z = 2.7 \pm 0.1$ for their sample, comparable to what we find, although the ALESS SMGs appear to have a shallower decline in number density beyond $z \gtrsim 3.5$–4, compared to AS2UDS. In Fig. 3.1b we also compare to the 1.1-mm selected sample of 124 SMGs in COSMOS from Miettinen et al. (2017), who have also used MAGPHYS to derive their properties. Miettinen et al. (2017) estimated a median redshift for their sample, which has a median equivalent 870 μm flux density of 4.2 ± 0.2 mJy (adopting $S_{870} \,/\, S_{1100} \sim 2.7$, Ikarashi et al. 2015), and a median red-

shift of $z = 2.30 \pm 0.13$, marginally lower than our measurement. The significance of this difference is only $\sim$2-σ, before considering cosmic variance or differences in the initial waveband selection, and so we conclude that the distributions are consistent.

We next compare our distribution to those from spectroscopic SMG samples. Danielson et al. (2017) provides spectroscopic redshifts for 52 ALMA-identified SMGs from ALESS with $S_{870} > 2$ mJy. This sample has a median redshift of $z = 2.4 \pm 0.1$ (see Fig. 3.1b), which is also similar to the median of the redshift distribution from the spectroscopic survey of radio-identified SMGs in Chapman et al. (2005). Both of these results are slightly lower than the median we derive, most likely due to a combination of selection effects: both the optical/near-infrared brightness of the counterparts (which aids spectroscopic identifications) and in the case of Chapman et al. (2005), radio biases. To assess the former bias, we note that the majority of spectroscopic SMGs in Danielson et al. (2017) have $K \lesssim 23.5$. Cutting our sample at $K \leq 23.5$ yields a median redshift of $z = 2.44 \pm 0.08$, in much better agreement to their result. Similarly, to demonstrate the potential influence of the radio identifications, if we limit our sample in AS2UDS to the 273 radio-detected SMGs then we obtain a median redshift of $z = 2.5 \pm 0.1$, which is within the uncertainty of the result from Chapman et al. (2005).

In addition, as we have also run MAGPHYS on all 205,910 K-band selected galaxies in the field with no contamination flags in Chapter 2, we are able compare the properties of the ALMA SMGs directly to the less active field population in a consistent manner. The redshift distribution of the field sample is also shown in Fig. 3.1b, where we derive a median redshift of $z = 1.75 \pm 0.08$.

One major benefit of the use of MAGPHYS in our analysis is the inclusion of the far-infrared and radio photometry in the SED modelling and the photometric redshift determination. Hence, we are able to investigate the redshift distribution of optical/near-infrared-faint and -bright SMGs using redshifts derived in a consistent manner. The photometric redshift distribution for the SMGs which are undetected in the K-band (17 ± 1 per cent), with $K > 25.7$ has a median redshift of $z = 3.0 \pm 0.1$,

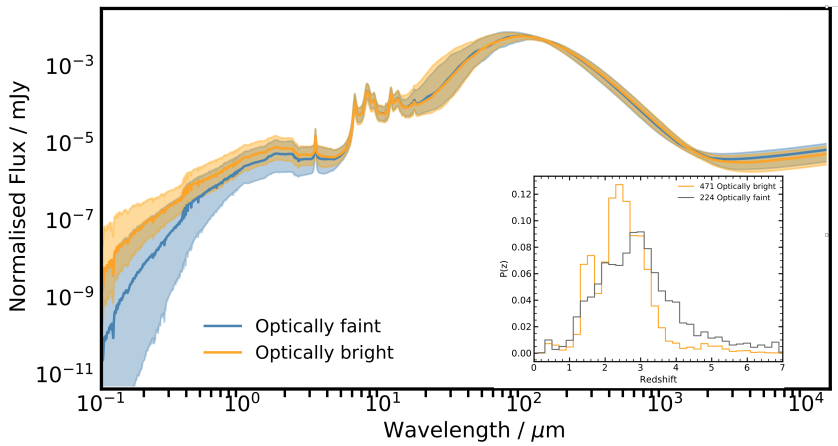

Figure 3.2: Comparison of the composite SEDs of optically bright versus optically faint (detections in less than 4 photometric bands up to IRAC 8μm) SMGs normalised to the median far-infrared luminosity of each subset. Both subsets have comparable dust SEDs indicating no systematic differences in the far-infrared luminosity or dust mass. Optically faint SMGs have systematically lower optical/near-IR emission, which we find to be due to higher dust attenuation (rather than lower stellar mass). Inset panel shows the redshift distributions for both subsets, indicating that optically faint SMGs lie at higher redshift. Thus, combination of dust attenuation and higher redshift is the driver of optical faintness in these systems. More analysis on the optically undetected SMGs can be found in Smail et al. (2021).

but exhibits a broad distribution with a 16–84$^{\rm th}$ percentile range of $z = 2.0$–3.8 (see Fig. 2.11). Thus, MAGPHYS predicts that the K-blank SMGs are typically at higher redshifts than the $K \leq 25.7$ sub-set (which have $z = 2.55 \pm 0.08$), although there is considerable overlap between the two redshift distributions and we particularly highlight that around ~ 25 per cent of the near-infrared-blank SMGs lie at relatively low redshifts, $z \leq 2.5$. MAGPHYS indicates that the main reason for the difference in the K-band brightness of these two sub-samples is dust reddening: the K-detected SMGs have optical reddening of $A_V = 2.61 \pm 0.05$, but the K-blank SMGs exhibit much higher reddenings, $A_V = 5.33 \pm 0.18$ (and $A_V = 6.0 \pm 0.2$ for those K-blank SMGs at $z < 2.5$), see Fig. 3.2. Thus while higher redshifts is an explanation for the K-band faintness of many of these SMGs, that is not the case for all. As both sub-samples have similar dust mass values and far-infrared luminosities, the difference in the dust attenuation cannot be attributed to higher dust content in the K-band undetected SMGs. Instead those K-band undetected SMGs at $z \lesssim 3$ must differ physically in the geometry of their dust and stars – either they have

different viewing angles (disk-like systems viewed edge-on would result in higher dust attenuation) or these are more compact sources with higher dust column. In fact, from the sub-sample of AS2UDS SMGs with 870-μm sizes from Gullberg et al. (2019), K-band faint sources have smaller sizes of $R_e = 1.60 \pm 0.10$ kpc, compared to those detected in the K-band, $R_e = 1.98 \pm 0.10$ kpc (Gullberg et al., 2019). This suggests that the relative distribution of stars and dust may be the main factor in their near-infrared faintness. For a detailed analysis of the optically-faint AS2UDS SMGs, we refer to Smail et al. (2021).

3.3 SMG spectral energy distributions

In this section, we analyse the SEDs of the 707 ALMA SMGs in our sample in order to quantify the variation in SEDs within the SMG population, and to compare the overall properties of the SMGs to other populations, including local galaxies.

In Fig. 3.3a we plot the rest-frame SEDs of all the SMGs in our sample. We normalise the SEDs by their far-infrared (8–1000μm) luminosity to roughly the median of our sample, $L_{IR} = 2 \times 10^{12}\,\mathrm{L}_{\odot}$. Each of the SEDs is colour-coded by the source's estimated V-band dust attenuation (A_V), which indicates that the galaxies with the reddest UV/optical SEDs are also the most highly obscured. We derive a composite SED for our whole population by measuring the median value at each wavelength, and overlay this on to the individual spectra in Fig. 3.3a. We also indicate the variation in the dispersion between the SEDs of SMGs as a function of wavelength. This highlights the wide variation in the rest-frame UV/optical luminosities for a far-infrared selected sample. In the wavelength range 0.1–5 μm (rest-frame UV/optical–near-infrared), the dispersion is $\sim$1–2 dex, with the full range of the population spanning five orders of magnitude. It should be stressed that this variety is for a population which has far-infrared luminosities in excess of $L_{\mathrm{FIR}} \sim 10^{12}\,\mathrm{L}_{\odot}$ and typical stellar masses in the range $M_* \sim 10^{10-11}\,\mathrm{M}_{\odot}$. This highlights the difficulty in constructing complete samples of star-forming galaxies in the optical/near-/mid-infrared and how even near-infrared surveys are unable

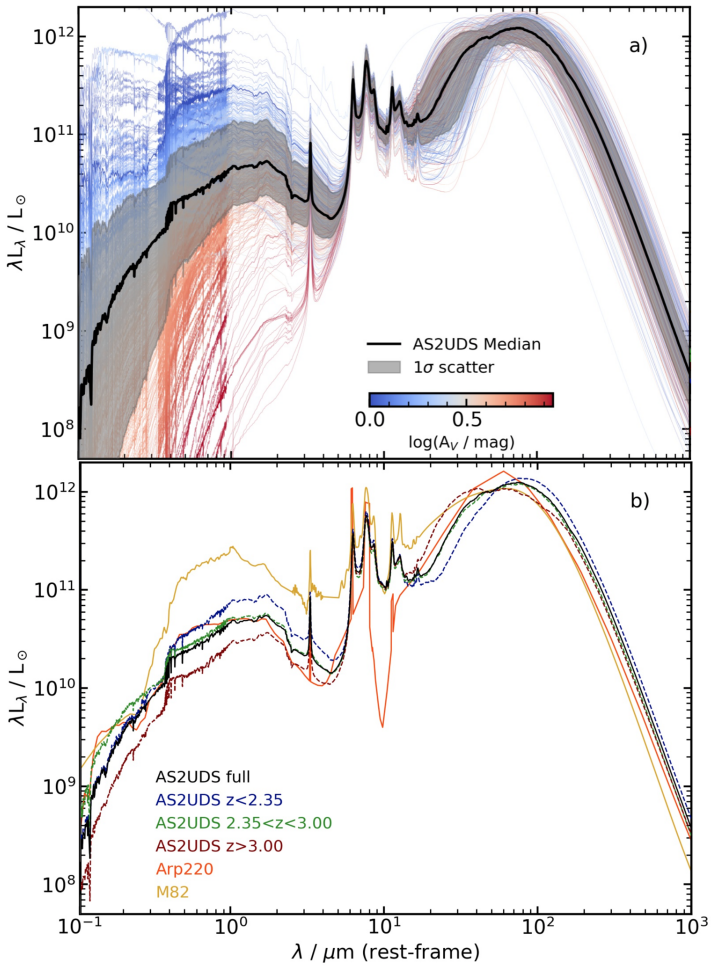

Figure 3.3: **(a)** The best-fit rest-frame SEDs of all 707 AS2UDS SMGs normalised to $L_{IR} = 2 \times 10^{12}\,L_{\odot}$. The individual SEDs are coloured by their V-band dust attenuation. The dispersion in the flux between the SEDs in the far-infrared and sub-millimetre is $\sim$2–3×, but this increases below $\sim 5\mu$m to several orders of magnitude at rest-frame wavelengths of $\lesssim 1\,\mu$m. The thick solid line shows the median composite SED from this sample and the shaded region indicates the 16–84th percentile region. We see that AS2UDS SMGs have a wide variety of colours and luminosities even in the rest-frame optical, thus it is very hard to construct a sample of star-forming galaxies which is complete for even the most obscured examples based on selection in the observed optical or even near-infrared wavelengths. **(b)** A comparison of AS2UDS composite to local galaxies. We plot the composite of the full sample and the SEDs for sub-samples split on redshift (dashed lines) into roughly equal-sized sub-sets: $z < 2.35$, $z = 2.35$–3.00 and $z > 3.00$. We see that high-redshift SMG's composite SED is more dust-obscured and peaks at shorter wavelength (i.e. hotter dust temperatures) than the lower-redshift composites. For comparison, we also plot the SEDs of the local galaxies M82 and Arp 220. The full AS2UDS composite appears to be much more dust-obscured than M82, while it resembles Arp 220 quite closely at optical and near/mid-infrared wavelengths. However, in the far-infrared Arp 220's SED peaks at shorter wavelengths (e.g. hotter characteristic dust temperature) than the majority of the SMGs at $z < 3$. Thus Arp 220 is a poor far-infrared template for typical SMGs, but can provide an appropriate match to the typically hotter sources seen at higher redshift ($z > 3$).

to identify fully mass-complete samples of strongly star-forming galaxies.

To search for evolution in the SEDs of SMGs, we split our sample into three redshift ranges containing roughly equal numbers of sources: $z < 2.35$, $z = 2.35$–3.00 and $z > 3.00$, with median redshifts of $z = 1.86 \pm 0.05$, $z = 2.58 \pm 0.02$ and $z = 3.35 \pm 0.04$ respectively. We determine the median SED of each sample and overlay these in Fig. 3.3b. At $\lesssim 5\mu$m we see a factor of ~ 3–$4\times$ variation in brightness of the composite SEDs between the different redshift ranges – with the lower redshift samples being consistently brighter in the rest-frame optical/near-infrared than those at higher redshifts (we see the same trend when we limit our sample to the luminosity-selected SMGs, see § 3.4.1). Looking at the derived median far-infrared luminosities, stellar masses and dust reddening for the three sub-sets (see § 3.4), this variation appears to be due primarily to higher far-infrared luminosities and dust temperatures at higher redshifts, along with slightly higher reddening and slightly lower stellar masses. There are few observational constraints on the shape of the SED at rest-frame $\sim 10\mu$m and perhaps, as a result, the three sub-sets show similar mid-infrared luminosities. At longer wavelengths, there is one notable difference between the SEDs, with the higher-redshift sub-sets peaking at progressively shorter wavelengths, indicating hotter characteristic dust temperatures (a similar trend was indicated da Cunha et al. (2015), although sample size did not allow for confirmation), which are further discussed in § 3.4.2.

For comparison to our SMG composites, we also show the SEDs of local starburst galaxies M82 and Arp 220 (scaled to the same far-infrared luminosity) in Fig. 3.3b. The full-sample AS2UDS SED (and all three sub-sets) differs significantly from M82, which is much brighter in the optical/infrared relative to the far-infrared than a typical SMG. The full SED of the SMGs is better matched to Arp 220 in the rest-frame optical/near-infrared. In the mid-infrared, Arp 220 has a strong silicate absorption feature at 9.8μm which falls in a poorly sampled part of our SED, where the predicted SED is dependent upon the details of the model in MAGPHYS (as this wavelength is only sampled at $z < 1$ by our MIPS coverage where we have few SMGs). However, the limited mid-infrared spectroscopy available for SMGs

indicates that most do not show silicate absorption as strong as seen in Arp 220 (Farrah et al., 2008; Menéndez-Delmestre et al., 2009). While in the far-infrared, the SED of Arp 220 peaks at a shorter wavelength ($\lambda_{\rm peak} \sim 60\mu$m) than the full SMG SED, which peaks at $\lambda \sim 70$–80μm, implying a hotter characteristic dust temperature in Arp 220. The far-infrared SED of Arp 220 is better matched to the higher redshift bins with $z > 2.5$ and the ratio $L_{\rm opt}/L_{\rm FIR}$ of Arp 220 is similar to $z \sim 2.5$ SMGs. Hence, Arp 220 template may be an appropriate template for SMG dust SED-fitting in the high-redshift regime ($z > 2.5$), but is not well matched to the typical SMGs below $z \sim 2.5$.

3.4 Physical properties of SMGs

The composite SEDs of our SMGs shown in Fig. 3.3b indicate potential differences between the properties of low- and high-redshift SMGs, suggesting evolutionary changes within the population (or the influence of sample selection). In the following, we investigate the physical properties of SMGs and the variation within the population, to search for evolutionary trends.

To quantify the typical properties of the SMGs, we begin by constructing the stacked likelihood distributions of far-infrared luminosity ($L_{\rm IR}$), dust mass ($M_{\rm d}$), age, V-band dust attenuation (A_V), star-formation rate, stellar mass (M_*), and rest-frame H-band mass-to-light ratio (M/L_H), and show these in Fig. 3.4. We also include a histogram of the characteristic dust temperature from the modified blackbody fits ($T_{\rm d}^{MBB}$), which is further explained in §3.4.2. By stacking the likelihood distributions we include the uncertainties (and covariance) between the derived values, such as the uncertainties in the photometric redshifts. Where applicable, in Fig. 3.4 we also overlay the MAGPHYS prior in order to illustrate their potential influence on our derived distributions. We note that the reliability of some of these derived quantities have been demonstrated by their correlation with the observables as discussed in § 2.4 of Chapter 2.

Before we discuss these derived quantities, we identify a comparison sample of

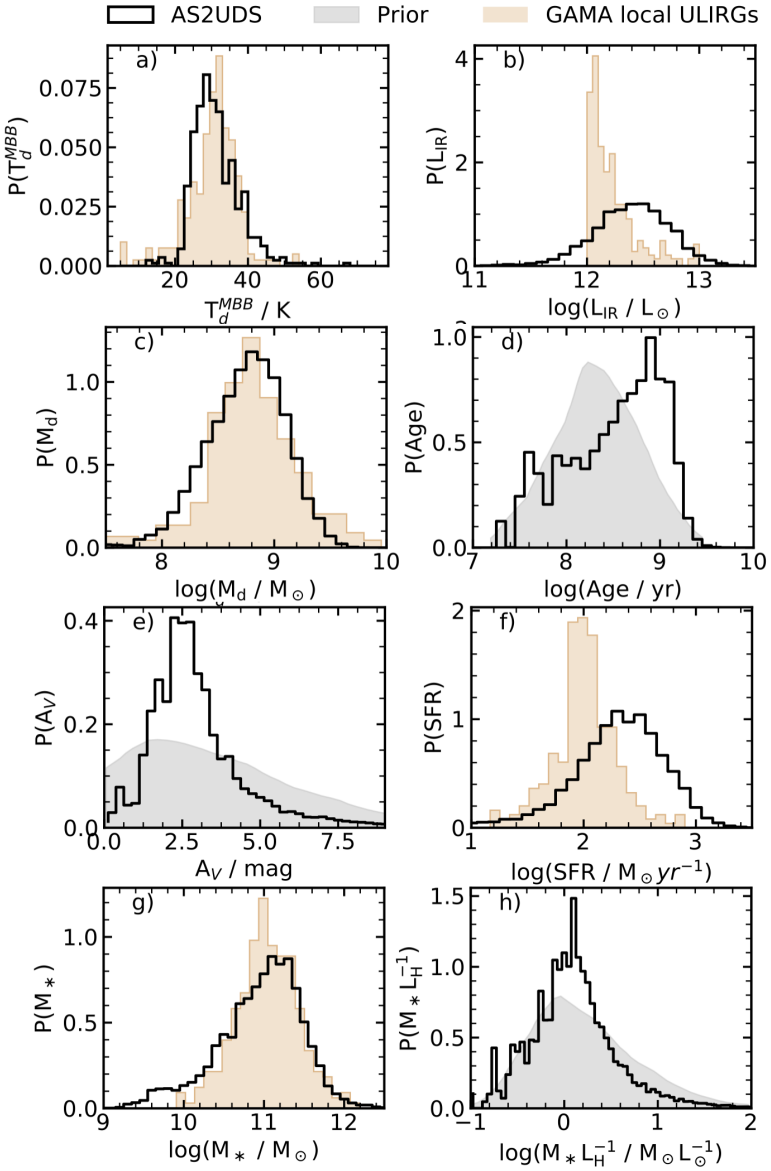

Figure 3.4: Distributions of the physical properties of the AS2UDS SMG population predicted by MAGPHYS or derived directly from the SEDs. To demonstrate that the posterior likelihood distributions are not affected by the model priors, we overlay them where applicable. For comparison the available properties from a sample of local ULIRGs from the GAMA survey (Driver et al., 2018), selected to have $L_{IR} > 10^{12}\,L_\odot$ and $z < 1$, is also shown. In each panel, we plot the median stacked likelihood distribution from combining the PDFs of the individual SMGs. From top left the distributions show: (a) Optically thin modified blackbody temperature (T_d) for those galaxies that are detected in at least one SPIRE band; (b) Far-infrared luminosity (L_{IR}); (c) Stellar mass (M_*); (d) Mass-weighted age, (e) V-band dust attenuation (A_V); (f) Star-formation rate, g) Dust mass (M_d), (h) restframe H-band mass-to-light ratio (M/L_H). We see broad similarities between the properties of the SMGs and the local ULIRGs, with the exception that the SMGs (which have much higher volume densities than the comparably luminous galaxies at $z < 1$) are typically more luminous in the far-infrared and have correspondingly higher star-formation rates.

local ULIRGs with which we can compare these distributions and average properties. For this purpose, we select ULIRGs from analysis of the GAMA survey undertaken by Driver et al. (2018). They used MAGPHYS to model the multi-wavelength photometry of this sample from rest-frame UV–radio wavelengths, including both, *GALEX* far-UV and *Herschel*/SPIRE far-infrared photometry, which broadly matches the rest-frame wavelength coverage of the AS2UDS SMGs. This similarity in the multi-wavelength coverage and the use of the same SED modelling code will minimise systematic uncertainties in any comparison of the properties of these local ULIRGs with high-redshift SMGs. The GAMA local ULIRG sample we use comprises 353 galaxies which have spectroscopic redshifts of $z < 1$ (with a median of $z = 0.59$), are brighter than $r \leq 19.8$ (roughly equivalent to $H \sim 24$ at $z \sim 2.5$), have at least one PACS or SPIRE detection and have far-infrared luminosities $L_{IR} > 10^{12}\,\mathrm{L}_{\odot}$. For comparison, we plot the distributions of the available parameters for the local ULIRGs in Fig. 3.4. Throughout this section, we similarly compare to previously published results on two high-redshift ULIRG samples from the MAGPHYS analyses of the 870 μm ALMA sample in ALESS (da Cunha et al., 2015) and a comparably sized 1.1-mm selected SMG sample in COSMOS studied with ALMA by Miettinen et al. (2017).

3.4.1 Far-infrared luminosity

To investigate the dust properties of SMGs, we first determine their far-infrared luminosities, which is derived by integrating the rest-frame SED between 8–1000 μm. For our sample, the median far-infrared luminosity is $L_{\mathrm{IR}} = (2.88 \pm 0.09) \times 10^{12}\,\mathrm{L}_{\odot}$, with a 16–84$^{\mathrm{th}}$ per centile range of $L_{IR} = (1.5\text{–}5.4) \times 10^{12}\,\mathrm{L}_{\odot}$. The vast majority of our sample are classed as ULIRGs with $L_{\mathrm{IR}} = 1\text{–}10 \times 10^{12}\,\mathrm{L}_{\odot}$, with 53 (7 per cent) being LIRGs with $L_{\mathrm{IR}} < 1 \times 10^{11}\,\mathrm{L}_{\odot}$ typically at $z \sim 1.8$, and 14 (2 per cent) are HyLIRGs with $L_{\mathrm{IR}} > 1 \times 10^{13}\,\mathrm{L}_{\odot}$ lying at $z \sim 3.5$. Comparison to local ULIRGs in Fig. 3.4b shows that local ULIRGs have considerably lower far-infrared luminosities with a median of $L_{\mathrm{IR}} = (1.41 \pm 0.03) \times 10^{12}\,\mathrm{L}_{\odot}$ and a 16–84$^{\mathrm{th}}$ percentile range of $L_{\mathrm{IR}} = (1.1\text{–}2.4) \times 10^{12}\,\mathrm{L}_{\odot}$.

3.4.1. Far-infrared luminosity

Restricting the sample at the original SCUBA-2 single-dish flux density limit of $S_{850} > 3.6\,\mathrm{mJy}$, yields 364 SMGs with a median of $L_{\mathrm{IR}} = (3.80 \pm 0.14) \times 10^{12}\,\mathrm{L}_{\odot}$. In the following analysis, we also make use of a sub-set of our sample which are detected in at least one of the *Herschel* SPIRE bands, as these sources have more reliable measurements of their dust temperatures and hence their far-infrared luminosities. There are 475 SMGs in this SPIRE-detected subset with a median $L_{\mathrm{IR}} = (3.39 \pm 0.14) \times 10^{12}\,\mathrm{L}_{\odot}$ and a 68^{th} percentile range of $L_{\mathrm{IR}} = (1.7\text{–}5.9) \times 10^{12}\,\mathrm{L}_{\odot}$ and lying at a median redshift of $z = 2.48 \pm 0.08$ (68^{th} percentile range of $z = 1.8$–3.2).

The median far-infrared luminosity of our SMGs is comparable with that derived for the sample in ALESS $L_{\mathrm{IR}} = (3.7 \pm 0.1) \times 10^{12}\,\mathrm{L}_{\odot}$ for a similar 870μm flux density limit (da Cunha et al., 2015), and also comparable to the median far-infrared luminosity of the 1.1-mm selected SMG sample from Miettinen et al. (2017)* who derive a median of $L_{\mathrm{IR}} = (4.0 \pm 0.3) \times 10^{12}\,\mathrm{L}_{\odot}$ for a sample with an equivalent 870 μm flux density range of 1.5–20 mJy (adopting $S_{870}/S_{1100} \sim 1.8$, equivalent to a $\nu^{-2.5}$ spectral index, based on the average flux ratio of AS2UDS SMGs with published 1.1-mm photometry from ALMA in Ikarashi et al. 2017).

To illustrate the evolution in our sample, we plot the variation of far-infrared luminosity with redshift for the AS2UDS SMGs in Fig. 3.5. We include in this plot only those SMGs which have at least one SPIRE detection. The SMGs show a trend in redshift for the brightest luminosities which is roughly reproduced by evolution of the form $L_{IR} \propto (1+z)^{\gamma}$, with $\gamma \sim 4$, consistent with the behaviour previously claimed for luminous dusty galaxies at $z < 2$ (e.g. Béthermin et al., 2011). We also need to consider the influence of our sample selection on this trend and so we also show in Fig. 3.5 the far-infrared luminosity of a source with a dust SED modelled by a modified blackbody with a temperature of $T_{\mathrm{d}} = 32\,\mathrm{K}$ (the median for this sample) and an 870 μm flux density $S_{870} = 1\,\mathrm{mJy}$, which is the typical depth of our ALMA maps. We see that due to the negative k-correction the resulting far-infrared luminosity limit is almost constant out to $z \sim 6$. In addition, we overlay a

*Note that the errors on Miettinen's values are the 16–84^{th} percentile ranges, rather than the uncertainty in the median value.

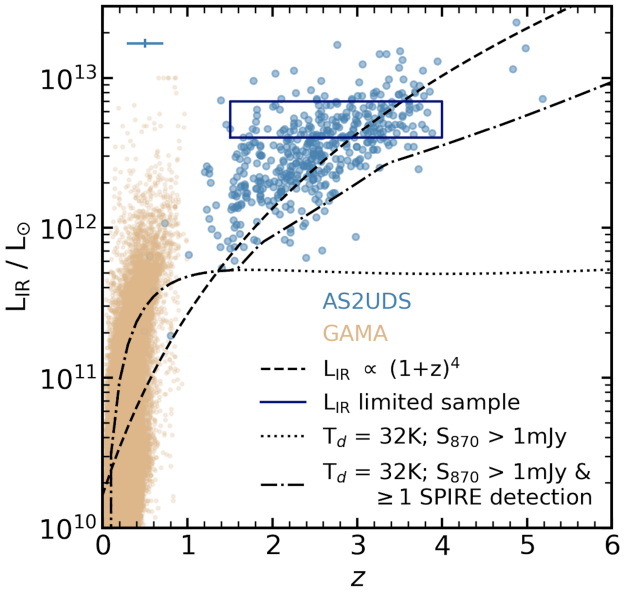

Figure 3.5: The far-infrared luminosity of the AS2UDS SMGs as a function of redshift for those sources which have at least one SPIRE detection. The dashed line shows the luminosity evolution according to $L_{IR} \propto (1+z)^4$. The dotted line denotes the selection function of a $S_{870} \gtrsim 1$ mJy SMG for a modified blackbody dust SED with the median dust temperature of the sample, $T_{\rm d} = 32$K. While the dot-dashed line shows the selection including the requirement that the dust SED includes at least one detection above the flux limits of the available SPIRE observations at 250, 350 or 500 μm. We see that the latter model provides a reasonable description of the variation of the lower boundary in L_{IR} with redshift which we observe. The rectangle shows the limits of the unbiased, luminosity-limited sub-set we use to test evolutionary trends. We also show the low redshift ($z < 1$) sample of far-infrared detected galaxies from the GAMA survey (Driver et al., 2018) and note that we compare to the $\geq 10^{12} L_\odot$ sub-set of these.

selection function for the same $T_{\rm d} = 32$ K model with the additional constraint that the SED must be detected in at least one SPIRE band at 250, 350 or 500 μm, which is the requirement placed on the sub-set of the AS2UDS sample we are plotting. We see that this selection results in an increasing far-infrared luminosity limit at higher redshifts, which reproduces the behaviour we see in our sample. Hence, the apparent deficit in Fig. 3.5 of lower luminosity sources (with $L_{IR} \lesssim 2$–$3 \times 10^{12}\,L_\odot$) at $z \gtrsim 2.5$–3, can be accounted for by the sample selection. While the SPIRE-detected subset of our SMG sample is biased towards more luminous sources at higher redshifts, we retain this selection because these have more robust estimates of their far-infrared properties. However, to control for the resulting bias in far-infrared luminosity with redshift, and so assess evolutionary trends, we will also

exploit our large sample to construct an *unbiased* sample of SMGs at $z = 1.5$–4, selected to lie in a narrow range of far-infrared luminosity ($L_{IR} = 4$–$7 \times 10^{12}\,\mathrm{L}_{\odot}$), where our sample is complete with respect to the SPIRE detection limits (this selection is shown by the rectangle plotted in Fig. 3.5).

3.4.2 Characteristic dust temperature

Although MAGPHYS can estimate a characteristic dust temperature, it is derived from a complex calculation involving five free parameters which describe the temperature and luminosity contributions from the warm (birth cloud) and cold (diffuse inter-stellar medium) components. The far-infrared SEDs of our sources are covered by at most six photometric bands, and our analysis in § 2.4.3 of Chapter 2 shows that MAGPHYS predicted dust temperatures for the AS2UDS sources are not constrained (consistent with a single value). Thus, we choose to adopt a simpler, more conservative approach and fit modified blackbody functions to the available *Herschel* PACS and SPIRE, and ALMA 870-μm photometry. This approach also has an added advantage that the dust SEDs of the comparison samples can be fitted in a very similar way, allowing for more reliable comparison, free from systematic uncertainties resulting from the fitting procedures. We use a modified blackbody function of the form:

$$S_{\nu_{\rm obs}} \propto (1 - e^{-\tau_{\rm rest}}) \times B(\nu_{\rm rest}, T), \tag{3.1}$$

where $B(\nu_{\rm rest}, T)$ is the Planck function, $\tau_{\rm rest}$ is the frequency-dependent optical depth of the dust of the form $\tau_{\rm rest} = \left(\frac{\nu_{rest}}{\nu_0}\right)^{\beta}$, ν_0 is the frequency at which optical depth is equal to one and β is the dust emissivity index. We adopt $\beta = 1.8$ as used in previous SMG studies and consistent with the finding for local star-forming galaxies (Planck Collaboration et al., 2011; Clemens et al., 2013; Smith et al., 2013). Making the assumption that the region from which the dust emission originates is optically thin, thus $\nu_0 \gg \nu_{rest}$, Eq. 3.1 simplifies to:

$$S_{\nu_{\rm obs}} \propto \nu_{\rm rest}^{\beta} \times B(\nu_{\rm rest}, T), \tag{3.2}$$

The dust temperature derived using the optically-thin approximation does not represent the true temperature of the dust emission regions, as Riechers et al. (2013); Simpson et al. (2017) and others have shown that the emission from SMGs is, on average, optically thick at $\lambda_0 \lesssim 75\,\mu$m (we explore this further in § 3.4.6). Thus, this estimate is only a simplified model which we will refer to as the characteristic dust temperature. The best-fit temperature is acquired by fitting this modified blackbody function using a Markov Chain Monte Carlo sampler (see Simpson et al. 2017).

The resulting characteristic temperature distribution for our SPIRE-detected SMGs is shown in Fig. 3.4a. Comparing the dust temperatures for the SMGs from the modified blackbody fits with the predicted characteristic dust temperature from MAGPHYS, we find a typical fractional difference of $(T_{\rm d}^{\rm MBB} - T_{\rm d}^{\rm MAGPHYS})/T_{\rm d}^{\rm MBB} = -0.28\pm0.01$. The median characteristic dust temperature for our ALMA SMGs with at least one SPIRE detection is $T_{\rm d}^{\rm MBB} = 30.4 \pm 0.3\,{\rm K}$ with a $68^{\rm th}$ percentile range of $T_{\rm d}^{\rm MBB} = 25.7$–$37.3\,{\rm K}$, this is shown in Fig. 3.4a. For comparison, the same method to derive characteristic dust temperature was applied to the local ULIRGs sample. The median temperature of the local ULIRGs sample is slightly higher but within error range to SMGs, with a median characteristic dust temperature of $T_{\rm d}^{\rm MBB} = 31.1 \pm 0.4\,{\rm K}$. However, we stress that the typical far-infrared luminosity of the GAMA ULIRGs is a factor of 2–3 $\times$ lower than the SMGs and, as we discuss below, when we compare $L_{\rm IR}$-matched samples then the local ULIRGs are on average hotter than the SMGs.

Due to the similarities in their physical properties (e.g. stellar mass and dust mass, see Fig. 3.4), SMGs have been proposed to be analogues of the local ULIRGs. Indeed, as seen in Fig. 3.3b the SED for at least one archetypal ULIRG, Arp 220, shares some similarities with the higher-redshift SMGs. Local ULIRGs exhibit a dust temperature–luminosity relation, so we now investigate the correlation between far-infrared luminosity and characteristic dust temperature for the AS2UDS SMGs in Fig. 3.6a. We find a positive correlation between far-infrared luminosity and dust temperature for the AS2UDS SMGs similar to previous SMG studies (e.g

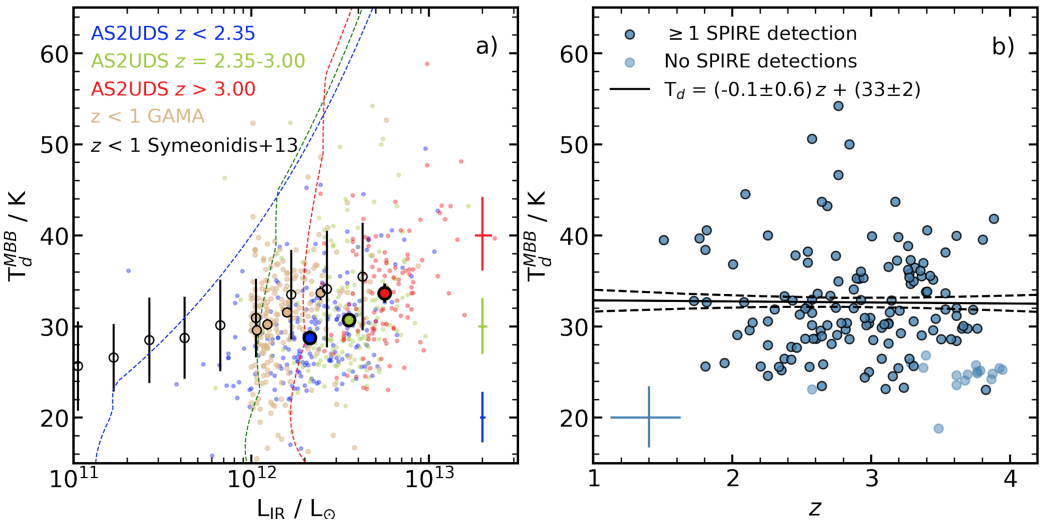

Figure 3.6: **(a)** The temperature–luminosity relation of those AS2UDS SMGs with at least one SPIRE detection, split into three redshift bins: $z < 2.35$, $z = 2.35$–3.00 and $z > 3.00$. We highlight the median values of each of the redshift sub-samples with their associated uncertainties. The selection function of AS2UDS sources with at least one SPIRE detection and $S_{870} \geq 1$ mJy at redshifts of $z = 1$, 2.35 and 3.00 are plotted. We see an apparent evolution of the far-infrared luminosities and dust temperatures of the SMGs which is roughly parallel to the trend seen within each redshift slice and does not appear to be influenced by the selection limits. For comparison, we plot the median values from local $z = 0$–1 SPIRE-selected LIRGs and ULIRGs from (Symeonidis et al., 2013) and the distribution with the median values derived for the ULIRGs from the GAMA survey. These show that the 870-μm selected SMGs are between $\sim$4–7 K cooler than comparably far-infrared luminous galaxies at $z < 1$. **(b)** The variation in dust temperature with redshift for our complete luminosity-limited SMG sample, which lies within the rectangle plotted in panel (a) ($L_{IR} = (4$–$7) \times 10^{12}\,L_\odot$ and $z = 1.5$–4.0). No evolution is seen in the dust temperature at fixed luminosity across this redshift range.

Magnelli et al., 2012; Symeonidis et al., 2013; Swinbank et al., 2014). Moreover, we see a correlation between luminosity and temperature within each of the three redshift sub-sets and a similar trend between the medians of the three sub-sets. We also show in Fig. 3.6a the selection functions for three redshifts which illustrate the selection of our 870μm observations as a function of redshift, far-infrared luminosity and dust temperature. Comparing these selection boundaries to our SPIRE-detected samples indicates that they should not be strongly influencing the correlations we observe. Indeed, when we look at the variation of $T_{\rm d}$ with L_{IR} for our unbiased luminosity-limited sub-sample, we find a similarly strong L_{IR}–$T_{\rm d}$ trend, $\Delta T_{\rm d} \sim 12\,\Delta \log_{10}(L_{IR})$.

Fig. 3.6a also shows the L_{IR}–$T_{\rm d}$ distribution for $z = 0$–1 SPIRE-selected LIRGs and ULIRGs from Symeonidis et al. (2013) and the $z < 1$ ULIRGs from the GAMA survey. These show an offset in dust temperature at a fixed luminosity relative to the SMGs: $\Delta T_{\rm d} = 3 \pm 1\,{\rm K}$ for samples with $L_{IR} \sim 2$–$4 \times 10^{12}\,{\rm L}_{\odot}$. This comparison ought not to be influenced by the selection limits on our SMG sample, although we have not modelled those for the local samples. We note, that the temperature difference between the samples is comparable with the uncertainty derived from EAGLE comparison, however, this is a systematic offset at all luminosity bins. So we tentatively conclude that at a fixed luminosity the AS2UDS SMGs appear to show cooler median dust temperatures than the local samples, possibly due to more compact dust distribution in local ULIRGs (Iono et al., 2009; Wilson et al., 2014).

The median values at each redshift slice in Fig. 3.6a may suggest a trend of characteristic dust temperature with redshift. Thus, we select the unbiased luminosity-limited sample sources and plot the variation of their dust temperature with redshift in Fig. 3.6b. No evolution in the dust temperature at a fixed luminosity is seen in this redshift range.

3.4.3 Star-formation rate

Far-infrared luminosity traces dust-obscured star formation, thus it is possible to infer star-formation rates using the conversion from $L_{\rm IR}$ given in Kennicutt (1998). Models in MAGPHYS, however, allow dust heating by old stellar populations and thus the model also estimates the star-formation rate in the optical regime after accounting for dust attenuation. Even though a wide range of model star-formation histories were included, we find a good correlation between the far-infrared and MAGPHYS derived star-formation rates for the SPIRE-detected sub-set, with a dispersion of ~ 25 per cent estimated from the 16–84th percentile range. We determine a median star-formation rate of ${\rm SFR} = 290 \pm 14\,{\rm M}_{\odot}\,{\rm yr}^{-1}$ with a 68th percentile range of ${\rm SFR} = 124$–$578\,{\rm M}_{\odot}\,{\rm yr}^{-1}$ (based on the SPIRE-detected sub-sample) which is consistent with da Cunha et al. (2015) who found ${\rm SFR} = 280 \pm 70\,{\rm M}_{\odot}\,{\rm yr}^{-1}$ for the ALESS sample. In comparison to the local ULIRG sample from GAMA, the typ-

ically higher far-infrared luminosities of our SMGs suggest higher star-formation rates, which is indeed the case, with the former having a median star-formation rate of $108\pm4\,\mathrm{M}_\odot\,\mathrm{yr}^{-1}$ (see Fig. 3.4f).

We investigate the evolution of star-formation rate in the SMGs with redshift in Fig. 3.7a. We also include the local ULIRGs sample, and as noted earlier, we observe that local ULIRGs typically have lower star-formation rates than seen in the SMGs in our sample. The best-fit line with a gradient of $d(\log_{10}(SFR))/dz = 0.22 \pm 0.02$ indicates a significant 11-σ trend. However, as seen in §3.4.1, our selection affects the trends seen with redshift. When we limit our sample to the unbiased luminosity-selected sample, we observe no significant star-formation rate evolution with $d(\log_{10}(SFR))/dz = 0.05\pm0.03$, as seen in Fig. 3.7a. We compare the star-formation rates of SMGs at different redshifts with the UKIDSS DR11 field sample. For this comparison we select field galaxies which have stellar masses above the 16^{th} percentile value of the AS2UDS sample ($M_* > 3.5\times10^{10}\,\mathrm{M}_\odot$). The shaded regions shows the 16–84^{th} percentile ranges of the SMGs and the field sample in their respective colours. As seen in Fig. 3.7a, the typical SMGs in our sample have significantly higher star-formation rate than a mass-selected sample at all redshifts probed.

3.4.4 Stellar Emission Properties

Next, we look at the physical properties inferred from the stellar emission which typically dominates the rest-frame UV/optical/near-infrared region of the SED of galaxies. We investigate the derived stellar masses as it is one of the most fundamental properties of SMGs. Robust stellar masses can provide tests of the evolutionary links between the SMGs and field galaxies, such as determining the fraction of massive galaxies which may have evolved through an SMG-like phase.

The median stellar mass of the full AS2UDS sample is $M_* = (12.6\pm0.5)\times10^{10}\,\mathrm{M}_\odot$ and we see no strong variation in this with redshift, as shown in Fig. 3.7b. Our median mass is in good agreement with the 1.1-mm selected sample from Miettinen et al. (2017) who find median a stellar mass of $M_* = 12^{+19}_{-9}\times10^{10}\,\mathrm{M}_\odot$ and also see

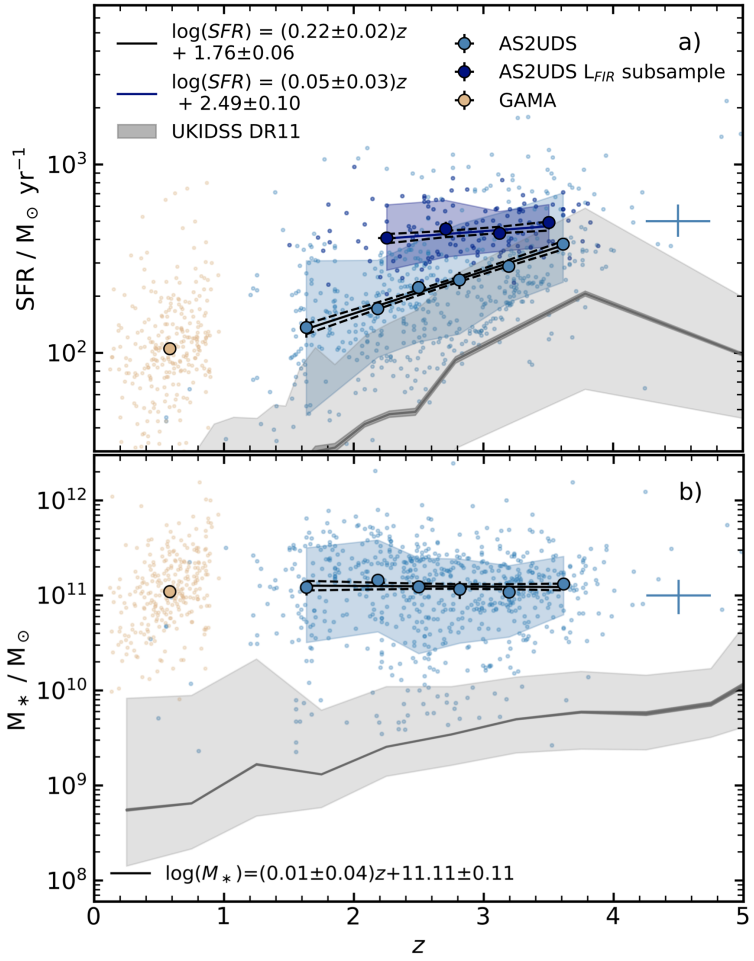

Figure 3.7: The evolution of SFR and stellar mass with redshift. In each panel, the large circles show the median in bins with equal number of sources. The sample of $z < 1$ ULIRGs from the GAMA survey and their median are similarly shown. The solid line shows the best-fit to the the binned medians and the dashed lines show the associated uncertainty. The median error on any individual source is shown on the right side of each panel. The 16–84th percentile range of the given property are shown as blue shaded regions. We overlay the median trend derived from the UKIDSS DR11 field population with the error on the median in the grey shaded region and their associated 16–84th percentile range indicated as the light shaded region. **(a)** Star-formation rate versus redshift for the SPIRE-detected SMG sample and the unbiased luminosity-selected sub-sample. As with the variation of L_{IR} with redshift shown earlier, there is a highly significant increase in median SFR with redshift within our sample, however, when the sample is limited to the unbiased luminosity-selected sub-sample this trend disappears. In comparison to a K-selected sample we again see that typical SMGs are significantly above the median trend seen in "normal" star-forming field galaxies at all redshifts. **(b)** Stellar mass versus redshift for the AS2UDS SMGs. We see no strong variation in the estimated stellar mass of the SMGs with redshift, with this extending down to the $z < 1$ ULIRGs. In comparison to K-band selected sample, SMGs have significantly higher stellar masses at all redshifts.

no evolution with redshift in their sample. However, our derived mass is higher than the $M_* = (8.9 \pm 0.1) \times 10^{10}\,\mathrm{M}_\odot$ found by da Cunha et al. (2015). Limiting both samples to the same 870-μm flux limit doesn't eliminate this disagreement, but we note that due to the broad distribution of $P(M_*)$ there is a wide range of acceptable stellar masses for our sample, the 16–84th percentile range for AS2UDS being 5.9×10^{10} to $22 \times 10^{10}\,\mathrm{M}_\odot$ (see Fig.3.4). This difference may, therefore, be due to either sampling statistics or cosmic variance.

When comparing with local ULIRGs (see Fig. 3.4g), we see no significant differences in the distributions of stellar mass, even though the Universe is roughly three times older at the epoch of the GAMA population than it was at the era when the SMGs peak. However, the r =19.2 mag limit of GAMA is $\sim$1.5 mag brighter than our equivalent H-band limit (at $z \sim 2.5$), thus GAMA may be biased to higher stellar masses.

Next, we investigate the attenuation of stellar emission at UV to near-infrared wavelengths, which, in MAGPHYS, is estimated using a two-component model of Charlot & Fall (2000). The two components model the effective attenuation in the V-band from dust in both stellar birth clouds and in the diffuse ISM. The median V-band dust attenuation derived for the AS2UDS sample is $A_V = 2.89 \pm 0.04$ mags with a 68th percentile range of $A_V = 1.89$–4.24 mags. The posterior likelihood distribution is significantly more peaked than the prior (see Fig. 3.4e). Moreover, the prediction, shown in Fig. 2.16 of Chapter 2, that the vast majority of SMGs are indeed far-infrared luminous based solely on the MAGPHYS modelling of the U–8.0 μm SEDs provides strong support that the derived A_V have diagnostic power as this parameter is the main driver of that prediction. As expected, we find that optically brighter SMGs (those with more than three detections in the optical/near-infrared bands) have $A_V = 2.5 \pm 0.2$ mags, while the optically fainter examples (fewer than four detections) have $A_V = 3.6 \pm 0.2$ mags. We note that this estimate of reddening is an angle averaged dust attenuation, which is measured by the classical definition – comparing the intrinsic and obscured V-band magnitudes. Even though they are lower limits on the true total extinction (as they give lower weight to more extinct

emission), they are still significant and underline the difficulty of constructing robust mass-limited samples of high redshift galaxies in the face of the significant dust obscuration found in some of the most active and massive examples.

We compare our sample to the 99 ALESS SMGs from da Cunha et al. (2015) which yields a median $A_V = 1.9 \pm 0.2$ mags (restricting this analysis to the sub-set of 52 of these SMGs with spectroscopic redshifts from Danielson et al. 2017 doesn't change this estimate). This is significantly lower than the median reddening derived for the AS2UDS galaxies, although both distributions span a similar range in A_V. This difference does not seem to relate to differences in the 870 μm flux density limits, redshift distributions or stellar masses of the two samples. Instead, it appears to reflect a population of highly obscured, $A_V \gtrsim 3.5$, SMGs at $z \lesssim 3.0$, which are seen in AS2UDS, but are absent in ALESS.

Finally, to measure the overall age of a given source, MAGPHYS outputs a mass-weighted age, which depends strongly on the form of the star-formation history. We find a median age for our SMGs of $\mathrm{Age_m} = (4.6 \pm 0.2) \times 10^8$ yr. We note that the posterior likelihood distribution differs significantly from the prior in Fig. 3.4d, suggesting the model is varying this parameter when fitting the SED. We return to compare the mass-weighted ages of the SMGs to other estimates of age from the derived physical properties in §3.5.1.1.

3.4.5 Comparison with the "main-sequence" of star-forming galaxies

We wish to relate the SMG population to the more numerous and less active and massive galaxies seen in the field population. One tool to do this is to assess the distribution of this population on the stellar mass versus star-formation rate plane, in particular, the relative position of the SMGs compared to the broad relation between star-formation rate and stellar mass exhibited by star-forming galaxies (the so-called "main sequence", Daddi et al. (2007)) – as assessed through their relative specific star-formation rates ($\mathrm{sSFR} = \mathrm{SFR}/M_*$). Specific star-formation rates significantly above the median trend of the field population have been argued

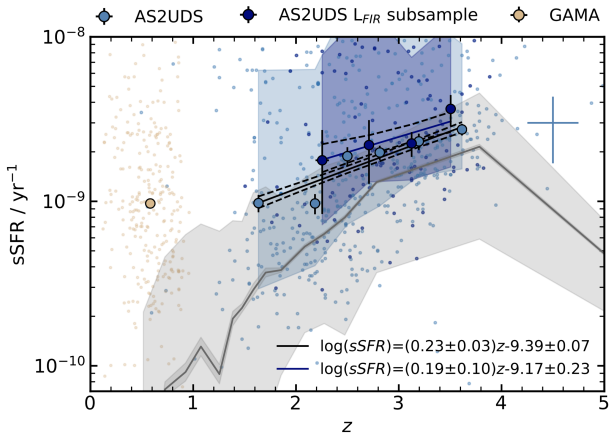

Figure 3.8: The evolution of specific star-formation rate with redshift. The large circles show the median in bins with equal number of sources. The sample of $z < 1$ ULIRGs from the GAMA survey and their median are similarly shown. The solid line shows the best-fit to the the binned medians and the dashed lines show the associated uncertainty. The median error on any individual source is shown on the right. The 16–84th percentile range of the given property are shown as blue shaded regions. Though this shows a 7.5σ trend of $d(\log_{10}(\mathrm{s}SFR))/dz = 0.23\pm0.03$, the trend weakens as we limit the sample to the unbiased luminosity-selected sub-set. SMGs lie above the median of a K-band selected sample out to $z \sim 3$–4. We overlay the median trend derived from the UKIDSS DR11 field population with the error on the median in the grey shaded region and their associated 16–84th percentile range indicated as the light shaded region.

to be a signature of starburst activity, potentially resulting from galaxy-galaxy mergers and interactions which enhance the star-formation rates of galaxies and so increase their sSFR (Magnelli et al., 2012). Alternatively, it may be possible for galaxies to achieve high star-formation rates without such triggers, merely through significant gas accretion – enabling high star-formation rate systems to inhabit the high-mass end of the sequence of normal star-forming galaxies (Davé et al., 2010). Alternatively, samples of highly star-forming galaxies could represent a heterogeneous mix of these two classes of systems, encompassing both physical processes (e.g. Hayward et al., 2011; Narayanan et al., 2015; McAlpine et al., 2019).

In Fig. 3.8 we look at the variation with redshift in the sSFR estimates for the SMGs compared to the less-active field population (derived in the same manner with robustness tested in § 2.4). We observe a modest positive correlation between specific star-formation rate and redshift for the SMGs. As shown in Fig. 3.7a, we find no evolution of stellar mass with redshift for our SMG sample, thus this trend is set by the variation in the star-formation rate. However, as we showed before,

the latter is due to selection effects on far-infrared luminosity. Indeed, when we limit our sample to the unbiased luminosity-selected sample, we find no significant trend in sSFR with redshift, with the SMG population on average spanning an order of magnitude in sSFR at all redshifts.

We compare the SMGs to the distribution from our MAGPHYS analysis of the K-band selected sample of galaxies in the UDS field, which we take to represent the "main sequence" (consistent with Tasca et al. 2015). For a consistent comparison, we select field galaxies that have stellar masses above the 16^{th} percentile of the AS2UDS sample ($M_* \gtrsim 3.5\times10^{10}\,\mathrm{M}_\odot$). Fig. 3.8 demonstrates that the field population has lower median sSFR values at all redshifts, but the difference between two populations decreases with redshift and SMGs lie close to the evolved "main sequence" at $z \gtrsim 3.5$, at which point the number density of SMGs in our sample is declining rapidly (see also da Cunha et al. 2015). This suggests that the bulk of the SMG population we detect, brighter than $S_{870} \sim 1\,\mathrm{mJy}$, have specific star-formation rates which put them above the "main-sequence" at their respective redshifts. Indeed, using the sources in our 16–84^{th} percentile range of $z = 1.8$–3.4, we find that 82 ± 4 per cent lie above the "main-sequence" defined by the K-band selected sample, with 34±3 per cent lying more than a factor of four above it (the arbitrary definition of a "starburst").

3.4.6 Dust and gas masses

We now investigate the properties of dust and gas in SMGs. Dust mass estimates, together with properties calculated from stellar emission, allow us to assess how efficient SMGs are at forming stars from gas, which in turn can provide a constraint on the lifespan of the sub-millimetre luminous phase in these systems.

We derive a median dust mass for the full AS2UDS sample of $M_\mathrm{d} = (6.8\pm0.3)\times10^8$ $\mathrm{M}_\odot$ with a 68^{th} percentile range of $M_\mathrm{d} = (3.0$–$12.6)\times10^8\,\mathrm{M}_\odot$, which broadly agrees with the median estimated for the ALESS sample: $M_\mathrm{d} = (5.6\pm0.1)\times10^8$ $\mathrm{M}_\odot$ (da Cunha et al., 2015). Similarly, Miettinen et al. (2017) estimate a median dust mass of $M_\mathrm{d} = 10^{+6}_{-5}\times10^8\,\mathrm{M}_\odot$ for their 1.1-mm selected SMG sample, which again is

similar to our measurement. It is expected that dust mass will be closely correlated with sub-/millimetre flux density, hence this agreement may simply reflect the roughly similar effective flux density limits of the single-dish surveys followed-up in these three ALMA studies.

Indeed, in Fig. 3.9a we see a relatively tight lower boundary to the distribution (for the $S_{870} \geq 3.6\,\mathrm{mJy}$ sample this corresponds to $M_\mathrm{d} \geq 5 \times 10^8\,\mathrm{M}_\odot$), confirming that the 870 μm flux density selection provides an approximately uniform dust mass selection across a wide redshift range. The ratio of dust mass to 870 μm flux density gives a simple conversion between the observable and the intrinsic property of $\log_{10}(M_\mathrm{d}[M_\odot]) = (1.20 \pm 0.03) \times \log_{10}(S_{870}[\mathrm{m}Jy]) + 8.16 \pm 0.02$, with a 1-$\sigma$ dispersion of $\sim$30 per cent, within the error derived from EAGLE comparison. We also see only a moderate increase in dust mass with redshift in our sample, corresponding to $\sim$30 per cent across the redshift range $z = 1.8$–3.4. This is qualitatively consistent with the variation in median redshift with S_{870} flux density found by Stach et al. (2019) – who demonstrated that SMGs from AS2UDS which are brighter at 870 μm on-average lie at higher redshifts. However, this trend weakens when we only consider the unbiased luminosity-selected sub-sample (see Fig. 3.9a).

We note that if the gas-to-dust ratio of this strongly star-forming population does not vary significantly over this redshift range, then our 870 μm selection will correspond to a similarly uniform selection in terms of molecular gas mass. The conversion factor from dust mass to molecular gas mass has been derived for a small sample of high-redshift SMGs with CO(1–0) observations, yielding a gas-to-dust ratio, δ_{gdr}, of $\sim$100 (Swinbank et al., 2014) similar to that estimated for Arp 220, which we adopt for our study. We note that the gas-to-dust ratio is expected to vary as a function of metallicity and hence potentially stellar mass and redshift. However, the lack of reliable gas-phase metallicities for SMGs means we choose to adopt a fixed ratio in our analysis.

We see an order of magnitude range in both M_d and L_{IR} across our sample in Fig. 3.9b with a weak correlation between these two parameters, although there is a clear variation across the distribution in terms of dust temperature. We also overlay

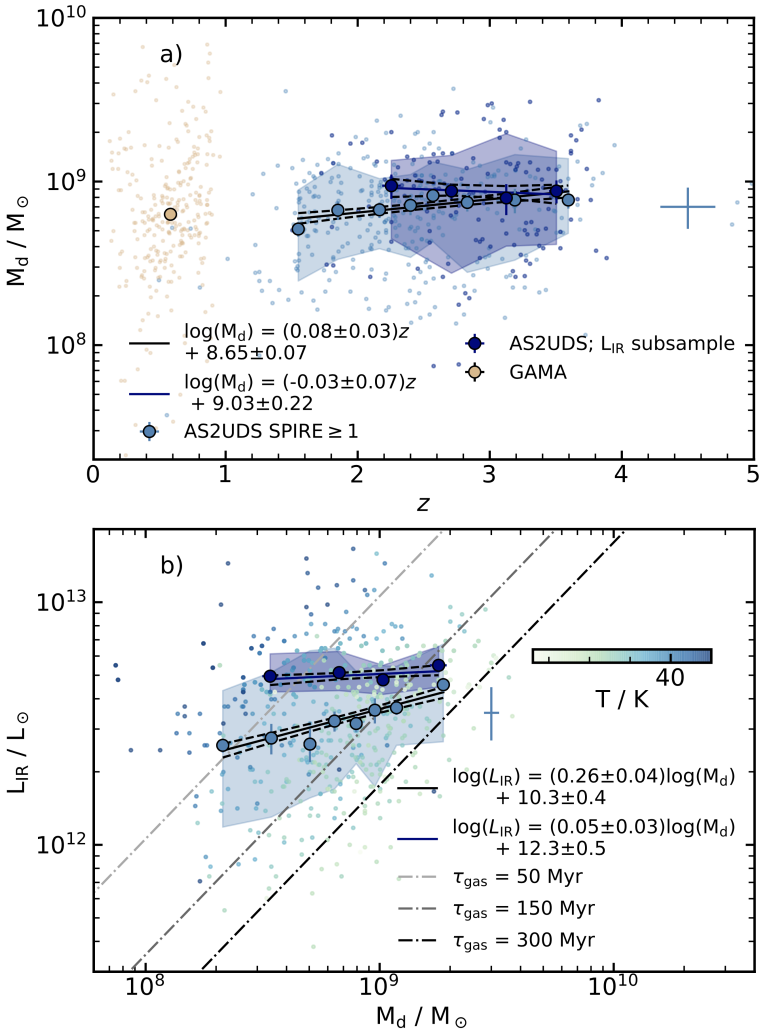

Figure 3.9: The dust properties for those AS2UDS SMGs detected in at least one SPIRE band and the unbiased luminosity-selected sub-sample of SMGs. In each panel the large circles show the binned median in bins with equal numbers of sources, the solid line shows the best-fit line to the binned data and the dashed lines show the associated uncertainty. The 16–84th percentile range of the given property are shown as blue shaded regions. The sample of $z < 1$ ULIRGs from the GAMA survey and their median are similarly shown. The median error on any individual AS2UDS source is shown in each panel. **(a)** Dust mass as a function of redshift. We see that the 870-μm selection of our joint S2CLS/ALMA survey yields a uniform selection in dust mass with redshift over the full redshift range probed by our study, with no evolution seen in the median dust mass with redshift. **(b)** Dust mass versus far-infrared luminosity. Our sample spans an order-of-magnitude range in both L_{IR} and $M_{\rm d}$ with a weak positive correlation with a slope of 0.26±0.04. We note that the dispersion is driven in part by variations in dust temperature, whereby SMGs that have lower temperatures are observed to have higher dust masses for a given far-infrared luminosity. We also indicate lines of constant gas depletion.

onto the figure lines corresponding to constant gas depletion (or star-formation efficiency), which we estimate assuming half of the gas is available to form stars (the other half being expelled) (Pettini et al., 2002):

$$\tau_{\mathrm{d}ep} \sim \frac{0.5 \times M_{gas}}{\mathrm{S}FR} \tag{3.3}$$

We see that the population spans a range of a factor of six in gas depletion timescales, from 50 to 300 Myr with a median of 146±5 Myr. Hence, the estimated length of the SMG phase, assuming the sources are typically seen half-way through this period, is ∼300 Myr. We also observe that the SMGs with the hottest characteristic dust temperatures show the shortest gas depletion timescales (or equivalently the highest star-formation efficiencies).

As a corollary to the L_{IR}–M_{d} plane, in Fig. 3.10a we plot the ratio of L_{IR} (as a simple observable linked to star-formation rate) and M_{d} (as a proxy for gas mass) in our sample as a function of redshift. This ratio reflects the expected gas depletion timescale and we see that it declines by a factor of ∼2 between $z = 1.5$ and $z = 4.0$ from ∼200 Myrs to ∼50 Myrs (da Cunha et al. 2015 analysis of the ALESS sample shows very similar behaviour). However, as seen in Fig. 3.10a, when we restrict our analysis to the unbiased, luminosity-limited sub-set this trend weakens suggesting that it is driven primarily by the incompleteness in L_{IR}, and thus star-formation rate, with redshift – rather than a fundamental variation in the gas depletion timescale with redshift.

We can also compare the estimates of the dust and stellar masses for the SMGs. For our full SMG sample we derive a median dust to stellar mass ratio of $M_{\mathrm{d}}/M_* = (5.4 \pm 0.2) \times 10^{-3}$ with a 16–84th range of 0.0028–0.0131 and little change with redshift, while for the GAMA ULIRGs we estimate $M_{\mathrm{d}}/M_* = (11 \pm 2) \times 10^{-3}$. At the upper end of our observed range these values are above the expected yields for dust from SNe and AGB stars (Calura et al., 2017) unless the IMF is biased to high-mass stars (Baugh et al., 2005; Zhang et al., 2018) or that much of the dust grain growth in these systems occurs in the ISM (Draine, 2009; Burgarella et al., 2020), which

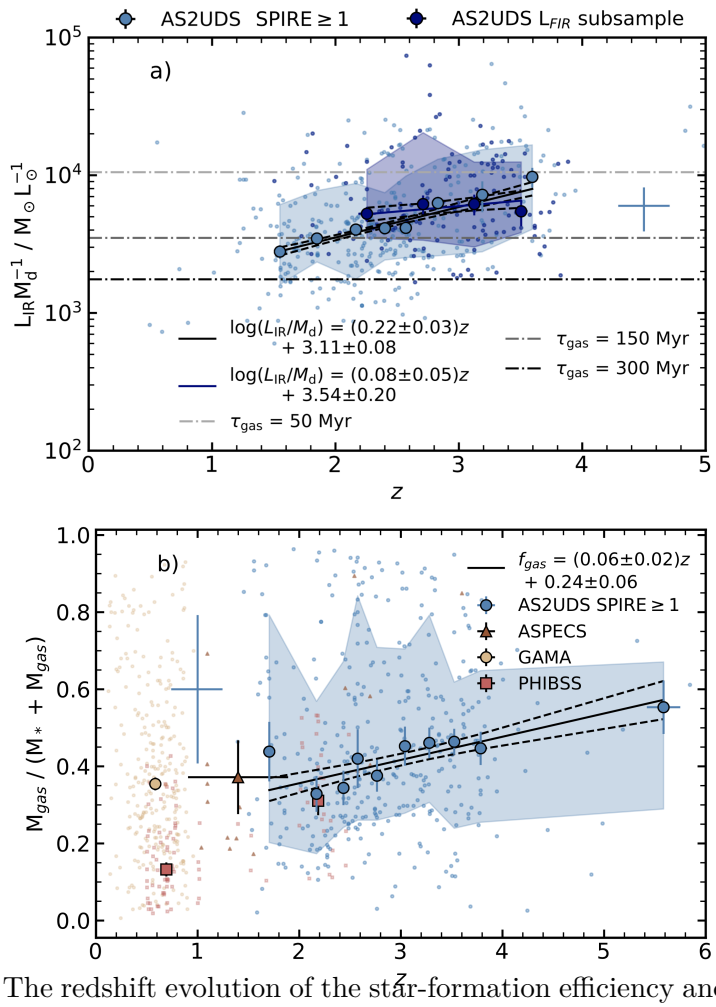

Figure 3.10: The redshift evolution of the star-formation efficiency and gas fraction for those AS2UDS SMGs detected in at least one SPIRE band and the unbiased luminosity-selected sub-sample of SMGs. In each panel the large circles show the binned median in bins with equal numbers of sources, the solid line shows the best-fit line to the binned data and the dashed lines show the associated uncertainty. The 16–84th percentile range of the given property are shown as blue shaded regions. The sample of $z < 1$ ULIRGs from the GAMA survey and their median are similarly shown. The median error on any individual AS2UDS source is shown in each panel. **(a)** The ratio of far-infrared luminosity to dust mass, a proxy for star-formation efficiency (or the inverse of gas depletion timescale), versus redshift. We indicate lines of constant gas depletion. We see a strong increase in star-formation efficiency with increasing redshift within our SPIRE-detected sample with a gradient of 0.22 ± 0.03. However, this trend weakens significantly if we restrict our analysis to the unbiased, luminosity-limited sub-set suggesting that it is driven primarily by the variation in L_{IR} or star-formation rate with redshift. **(b)** Gas fraction as a function of redshift. We derive a median gas mass fraction of $f_{gas} = 0.41 \pm 0.02$ with a 68th percentile range of $f_{gas} = 0.24$–0.72 and we see modest evolution of this quantity with redshift, with a gradient of 0.06±0.02. For comparison we overlay results from the ASPECS blind CO-survey from Aravena et al. (2019) and the CO-detected typical star-forming galaxies at $z \sim 1$–3 from Tacconi et al. (2018).

might be a result of the high ISM densities found in the SMGs (Swinbank et al., 2011; Simpson et al., 2017; Zhukovska et al., 2018).

We also derive the gas fraction, the ratio of the molecular gas mass to the total baryonic mass of the galaxy:

$$f_{gas} = \frac{M_{gas}}{M_{gas} + M_*} \tag{3.4}$$

and show its variation with redshift in Fig. 3.10b. We derive a median gas mass fraction of $f_{gas} = 0.41 \pm 0.02$ with a 68^{th} percentile range of $f_{gas} = 0.24$–0.72, comparable to the median gas fraction of $f_{gas} = 0.38 \pm 0.03$ for the local ULIRGs from the GAMA survey estimated in an identical manner. We see modest evolution of f_{gas} with redshift, with a gradient of $df_{gas}/dz = 0.06 \pm 0.02$. For comparison we overlay the ASPECS blind CO-selected sample from Aravena et al. (2019) and the CO-detected "main sequence" galaxies from the PHIBSS compilation of star-forming galaxies by Tacconi et al. (2018). Gas fraction of SMGs and "main sequence" galaxies at z$\gtrsim$2 appears to be similar.

Finally, we estimate the dust obscuration to the source of far-infrared emission averaged along the line-of-sight. In order to estimate this dust obscuration, we first estimate the column density of hydrogen atoms for the 154 sources that have 870μm sizes (Gullberg et al. 2019, further discussed in § 3.5.5) assuming $\delta_{gdr} = 100$ to convert dust mass to gas mass, and find a median of $N_{\rm H} = (1.66 \pm 0.14) \times 10^{24}\,{\rm cm}^{-2}$. Dust attenuation is related to hydrogen column density by, $N_{\rm H} = 2.21 \times 10^{21}\,A_V$, and thus we find a median line-of-sight dust attenuation of $A_V = 750 \pm 60$ mags. The result is within the error range of Simpson et al. (2017) (who found a median $A_V = 540^{+80}_{-40}$ mags) when samples are selected in the same manner, having detections in all three SPIRE bands, resulting in a median $A_V = 700 \pm 90$ mags.

As the hydrogen column and dust attenuation results are suggesting dusty, highly obscured systems, we estimate the wavelength at which the optical depth, τ, becomes optically thin, λ_0. We, first, derive the brightness temperature of the SMGs with 870-μm sizes using:

$$B_{\nu_{rest}}(T_B) = 0.5 S_{\nu_{rest}}(1+z)^3/\Omega_{\nu_{obs}}, \tag{3.5}$$

where $B_{\nu_{rest}}$ is the full Planck function and the solid angle subtended by the source is $\Omega_{\nu_{obs}} = \pi R_\nu^2/D_{\rm A}^2$, where R_ν is the emission region size and $D_{\rm A}$ is the angular diameter distance. The factor of 0.5 is included as we are considering the emission within the half-light radius. Using Eq. 3.5 we estimate a median brightness temperature of $T_B = 21 \pm 1\,$K, with a 16–84th per centile range of 16–28 K. The brightness temperature can be related to the true dust temperature and optical depth by:

$$\frac{1}{e^{h\nu/kT_{\rm B}}-1} = \frac{1-e^{-\tau_\nu}}{e^{h\nu/kT_{\rm D}}-1}. \tag{3.6}$$

As in § 3.4.2, we used fixed dust emissivity index of $\beta = 1.8$ in the calculation of optical depth. We make the assumption that the emission region at 250, 350 and 500 μm is the same size as that measured at 870 μm. We note that, for a given source, the observed size of the emission varies with optical depth as it increases with frequency. Thus, our assumption overestimates the flux density within the 870μm half-light radius for 250, 350 and 500μm emission. Therefore, our estimated dust temperature and optical depth are the lower limits of the true values.

We use a sub-sample of 64 sources that have 870 μm sizes and detections in all three SPIRE bands to solve for both, dust temperature and optical depth, using Monte Carlo Markov Chain method. We estimate a median true dust temperature of $\rm T_D = 40 \pm 2\,$K and a median optical depth of unity, $\lambda_0 = 106 \pm 6\,\mu$m and we note that both of these quantities are the lower limit estimates. The wavelength estimate is comparable to the results from Simpson et al. (2017) who found $\lambda_0 \gtrsim 75\,\mu$m for a small sub-sample of 14 UDS SMGs.

3.5 Discussion

Having analysed the physical properties of SMGs and their evolution, in this section we focus on combining these results to investigate three main aspects in detail:

formation and evolution of SMGs, their relationship to the wider population of massive galaxies and insights into the distribution of the star-forming regions within this population.

3.5.1 Evolution and lifetimes

It is expected to be challenging to reliably constrain the age of the stellar populations in SMGs due to their high obscuration and the influence of the intense recent star formation on the SED, as well as the degeneracies between age and other parameters such as redshift. Nevertheless, the analysis of the model SEDs of simulated strongly star-forming galaxies from EAGLE (described in §2.2.1) suggests that there is some diagnostic information in the derived ages from MAGPHYS, as there is a positive linear correlation between these and the mass-weighted stellar ages in the model (see Fig. 2.1 in Chapter 2). In Fig. 2.1 we see that the median scatter around the best fit line is $\|(\mathrm{A}ge_{\mathrm{MAGPHYS}} - \mathrm{Age}_{\mathrm{best-fit}})\|/\mathrm{Age}_{\mathrm{MAGPHYS}} = 0.52$ for the sample. In comparison, the median fractional error on ages in the AS2UDS sample is 0.54. These errors are comparable, thus the systematic error is encompassed in the error returned from MAGPHYS. As such mass-weighted ages may be used to infer the typical formation epoch of the SMGs and to assess the evolution of properties of this population.

3.5.1.1 Mass-weighted ages

We first compare the mass-weighted ages to estimates of ages of SMGs derived from other physical properties. We derive a median mass-weighted age of our sample of $\mathrm{Age_m} = (0.46 \pm 0.02)\,\mathrm{Gyr}$. We note that the posterior likelihood distribution in Fig. 3.4d differs significantly from the prior, suggesting the model is varying this parameter when fitting the SED.

We have two other methods to estimate "ages" for the SMGs. Firstly, we can take the derived stellar mass and the current star-formation rate and ask how long it would take to form the observed mass? This age parameter, M_*/SFR, has a

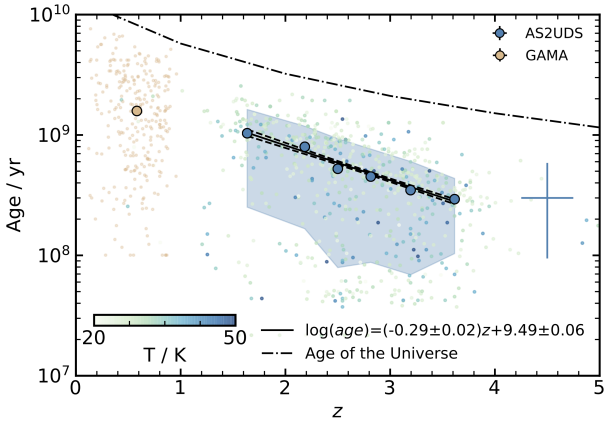

Figure 3.11: The evolution of mass-weighted age with redshift. Large circles show the median in bins with equal number of sources. The sample of $z < 1$ ULIRGs from the GAMA survey and their median are similarly shown. The solid line shows the best-fit to the the binned medians and the dashed lines show the associated uncertainty. The median error on any individual source is shown on the right. The 16–84$^{\rm th}$ percentile range of the given property are shown as blue shaded regions. The median derived age for the SMGs is $(4.6\pm0.2)\times10^8$ yr and the best-fit line has a gradient of $d(\log_{10}(Age_{\rm m}))/dz = -0.29\pm0.02$. The AS2UDS points are coloured by dust temperature, showing that the strength of this trend could be partly due to the model assigning younger ages to galaxies with higher dust temperatures (and far-infrared luminosities), which are typically found at higher redshifts. The dashed line shows the maximum formation redshift allowed by MAGPHYS, which corresponds to a cosmological lookback time of 13.4 Gyrs at $z \sim 0$.

median ratio of $M_*/{\rm SFR} = 0.51\pm0.03$ Gyr, and correlates very closely with ${\rm Age_m}$ for ages $\lesssim 0.7$ Gyrs (corresponding to the bulk of the population at $z \gtrsim 2$–3). ~ 25 per cent of SMGs, mostly at $z \lesssim 2$ have $M_*/{\rm SFR}$ higher than ${\rm Age_m}$ indicating either a declining star-formation rate or significant previous stellar mass in these galaxies.

The second estimate we can obtain comes from the expected lifetime of the current star-formation event, given by the ratio of the estimated gas mass to the star-formation rate: $M_{\rm gas}/{\rm SFR}$. This characteristic lifetime is also twice the gas depletion timescale as we assume to be observing the SMGs half way through the burst. This was estimated in § 3.4.6 as 146 ± 5 Myrs, yielding a lifetime of 292 ± 10 Myrs. This shows a weak correlation with ${\rm Age_m}$ with significant dispersion and around ~ 20 per cent of the SMGs (covering the whole redshift range) have gas depletion times which are longer than their mass-weighted ages, suggesting that the current star-formation event may represent the first major star-formation episode. How-

ever, for the bulk of the population, it appears that there is a pre-existing (older) stellar population in these systems.

In Fig. 3.11 we plot mass-weighted age as a function of redshift. We show the limit provided the age of the Universe at a given redshift. The best-fit trend to the $\mathrm{Age_m}$–z plot suggests a statistically significant evolutionary trend of age with redshift with a gradient of $d\mathrm{A}ge_\mathrm{m}/dz = -0.29\pm0.02$, so that higher-redshift SMGs are systematically younger. However, we caution that this may be a consequence of the code fitting younger ages to hotter dust components which are more prevalent at higher redshifts. For comparison, we overlay the local ULIRGs sample from the GAMA survey. We see that the median age from the local ULIRG sample agrees with the trend we observe at higher redshift, with these galaxies having overall older mass-weighted ages (as expected).

To assess the influence of the current star-formation activity on the evolution of the SMGs we determine when the current star-formation is likely to cease. Again, using our estimate a median gas depletion timescale of $\tau_{\mathrm{d}ep} = 146\pm5$ Myr with a 68^{th} percentile range of $\tau_{\mathrm{d}ep} = 53$-321 Myr for the SMGs at $z = 1.8$–3.4, this indicates that the star-formation activity in this population is expected to cease by $z \sim 2.5$, soon after their peak at $z = 2.6$. The stellar populations in these systems would then evolve to become red and quiescent by $z \sim 2$, in the absence of subsequent gas accretion and star formation. Similarly, assuming that, on average, we see the SMGs half way through their most active phase, we can adopt this depletion timescale as the likely age of the SMG-phase at the point we observe the SMG. Comparing this estimate to the median mass-weighted age of the $z = 1.8$–3.4 SMG sub-sample, 490 ± 20 Myr (68^{th} percentile range of 97–960 Myr), suggests that the bulk of the population had some pre-existing stellar population before the onset of the current star-formation event. We can also consider the mass produced in the last ~ 150 Myr (when the SMG-phase started) assuming a constant star-formation rate. We find a median fraction of $M_{150\mathrm{M}yr}/M_* \sim 0.3$. This means that, for an average SMG, ~ 30 per cent of the current stellar mass was formed in the last 150 Myr, and by the end of the SMG-phase these systems would have roughly

doubled their pre-existing stellar masses.

3.5.1.2 Lifetimes of SMGs

As seen in Fig. 3.1, the redshift distribution of our *complete* sample of 707 ALMA-identified AS2UDS SMGs has a median redshift of $z = 2.61 \pm 0.08$, with a 68^{th} percentile range of $z = 1.8$–3.4. The rapid decline in the number density of SMGs we see at both $z \lesssim 2$ and $z \gtrsim 3.5$ is striking. We stress that by virtue of employing full-SED modelling with MAGPHYS, the redshift distribution in Fig. 3.1 comprises the summed PDFs of all of the SMGs in our sample, not just the biased sub-set which are detectable in the optical/near-infrared (e.g. Simpson et al., 2014) and without having to employ a heterogeneous mix of redshift estimators (e.g. Brisbin et al., 2017; Cowie et al., 2018). We find a highly-peaked redshift distribution, which drops rapidly at higher redshifts, with ~ 30 per cent of the SMGs lying at $z > 3$, and just ~ 6 per cent at $z > 4$. Equally, we find only five examples of SMGs at $z < 1$, some of which may be unidentified weakly amplified galaxy-galaxy lenses (e.g. Simpson et al., 2017).

For the subsequent analysis, we use only the 364 ALMA SMGs with $S_{870} \geq 3.6\,\mathrm{mJy}$. This matches the flux density limit of the parent S2CLS survey (Geach et al., 2017), which covers an area of $0.96\,\mathrm{deg}^2$ and so allows us to estimate the appropriate volume densities from the sample. We also correct our estimates for the incompleteness in SCUBA-2 850μm sample in the UDS field (Geach et al., 2017). In Fig. 3.12a we recast our redshift distribution to illustrate the variation in volume density (ϕ) of bright SMGs with cosmic time. Fig. 3.12a shows that the volume density of AS2UDS SMGs peaks around $\sim 2.4\,\mathrm{Gyr}$ after the Big Bang with a 16–84^{th} per centile range of 1.8–4.5 Gyr. The distribution is log–normal, with a mean of $\mu = 0.97 \pm 0.03\,\mathrm{Gyr}$, standard deviation of $\sigma = 0.32 \pm 0.04\,\mathrm{Gyr}$ and a normalisation of $c = (1.7 \pm 0.2) \times 10^{-4}\,\mathrm{Mpc}^{-3}\mathrm{Gyr}^{-1}$. We also combine the redshifts with the mass-weighted ages of each SMG (see § 3.5.1.1) to predict the distribution of formation ages of the SMGs. This distribution also follows a log–normal shape with a median cosmic time at formation of $\sim 1.8\,\mathrm{Gyr}$ after the Big Bang,

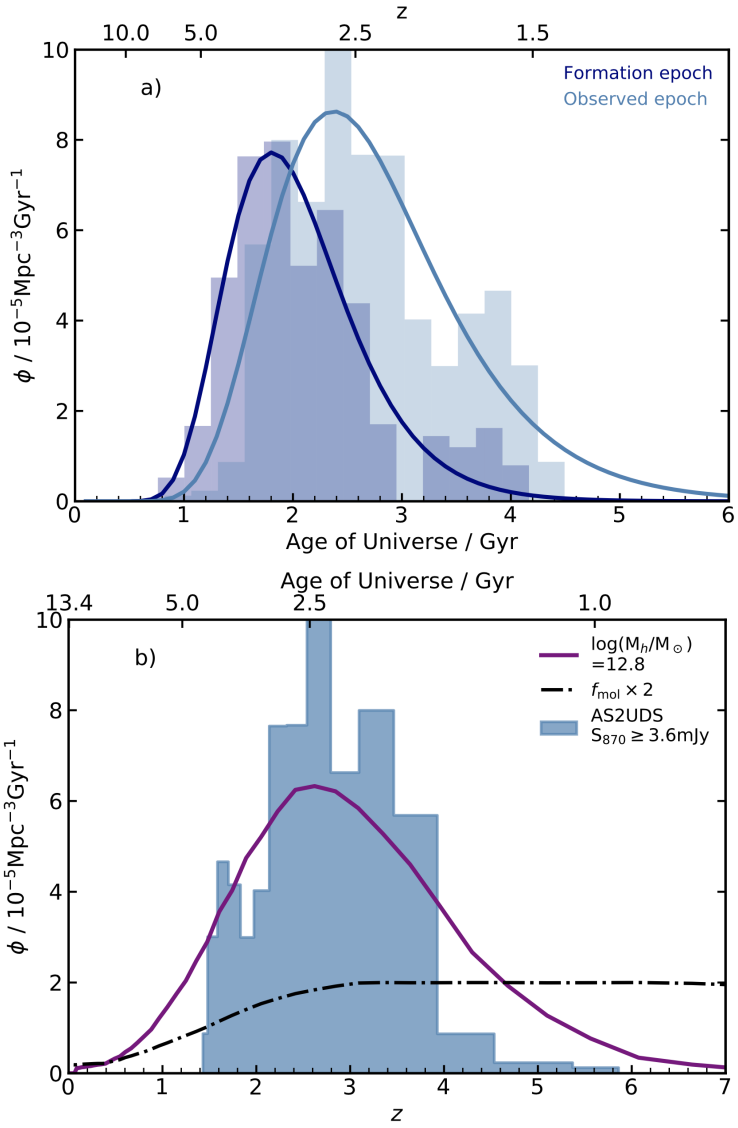

Figure 3.12: **(a)** The distribution of cosmic ages for the observed epochs of the AS2UDS SMGs and the inferred formation epochs for these galaxies (calculated from their estimated ages) corrected for incompleteness following (Geach et al., 2017). The solid lines show log-normal fits to the respective distributions. We see that the observed age distribution peaks at $\sim$2.4 Gyr, while the inferred formation-age distribution peaks at $\sim$1.8 Gyr ($z \sim 3.5$), with both well described by log-normal distributions. **(b)** The stacked likelihood redshift probability distribution of the sample of 364 AS2UDS SMGs that have $S_{870} \geq 3.6$ mJy corrected for incompleteness following (Geach et al., 2017). We overlay a simple analytic model assuming that SMGs reside in haloes whose mass crosses a characteristic threshold of $\sim 6 \times 10^{12}\,\mathrm{M}_\odot$ and accounting for the evolution of molecular gas fraction with redshift (f_{mol}, scaled by a factor of 2×, is shown as dashed line) in the halos. The model follows our distribution well as shown by the solid line.

and log–normal parameterisation of $\mu = 0.68 \pm 0.03\,\mathrm{Gyr}$, $\sigma = 0.30 \pm 0.03\,\mathrm{Gyr}$ and $c = (1.08 \pm 0.08) \times 10^{-4}\,\mathrm{Mpc}^{-3}\mathrm{Gyr}^{-1}$. Fig.3.12a shows that the SMGs begin to form in large numbers at a cosmic time of $\sim 1.8\,\mathrm{Gyr}$, corresponding to $z \sim 3.5$. This confirms that the rapid rise in number density we see in the redshift distribution at $z \lesssim 3.5$ is being driven by the onset of this population.

3.5.1.3 Formation of SMGs

Previous measurements of the spatial clustering of SMGs imply dark matter halo masses for SMGs of $M_{\mathrm{h}} \sim 10^{13}\,\mathrm{M}_{\odot}$ (Hickox et al., 2012; Wilkinson et al., 2017). More crucially, Hickox et al. (2012) suggested that the SMG redshift distribution is related to the growth rate of cosmological structures. The basis of this model is the concept of a *critical threshold mass* for halos, which has been developed to interpret the clustering evolution of QSOs (e.g. Overzier et al., 2003; Farrah et al., 2006). To investigate this further, we use the Millennium Simulation (Springel et al., 2005) to determine the growth rate of dark matter halos as a function of redshift. Using the dark matter merger trees from this $500\,h^{-1}\,\mathrm{Mpc}^3$ simulation, we measure the volume density of dark matter halos at each redshift that pass through mass thresholds of $M_{\mathrm{h}} = 10^{11}$–$10^{15}\,\mathrm{M}_{\odot}$ in steps of 0.05 dex. To account for the evolution of the molecular mass fraction within halos, we convolve these volume densities with the molecular gas fraction evolution (e.g. Lagos et al., 2011) and derive the redshift at which these distributions peak. By matching the distributions predicted by this simple model to our observed redshift, we estimate a "critical-mass" for haloes of bright SMGs with $S_{870} \gtrsim 3.6\,\mathrm{mJy}$ of $\log(M_{\mathrm{h}}) \sim 12.8\,\mathrm{M}_{\odot}$. In Fig. 3.12b we plot the volume density of bright SMGs in our sample, limiting the SMGs to those brighter than $S_{870\mu m} = 3.6\,\mathrm{mJy}$ (which represents the flux density limit of the parent survey) and overlay the redshift distribution of these dark matter halos for a critical mass of $\log(M_{\mathrm{h}}) \sim 12.8\,\mathrm{M}_{\odot}$.

In this model the rapid decrease in the number density of SMGs at $z \lesssim 1.5$–2 is explained by the decline in the molecular gas fraction in the halos (Geach et al., 2011; Lagos et al., 2011; Tacconi et al., 2018), as well as the decrease in the number of

dark matter haloes that transit above the mass threshold as the Universe expands. Fig. 3.12b shows that the shape of the redshift distribution of SMGs appears to be reasonably well described by this combination the cosmological growth of structure and the evolution of the molecular gas fraction in galaxies.

The halo mass of $\sim 6\times10^{12}\mathrm{M}_{\odot}$, estimated from the SMG redshift distribution, is comparable to the clustering results for SMGs (Hickox et al., 2012; Chen et al., 2016; Wilkinson et al., 2017; Stach et al., 2021), which suggest that they occupy halos of $\sim 10^{13} M_{\odot}$ at $z > 2.5$. This halo mass is also similar to that estimated from clustering studies for L^{*} QSOs at $z \sim 1$–2 (Ross et al., 2009), supporting the evolutionary association between SMG and QSOs suggested by Hickox et al. (2012) and others. Cosmological models of halo growth indicate that a dark matter halo mass of $M_{\mathrm{h}} \sim 6 \times 10^{12}\, M_{\odot}$ at $z \sim 2.6$, corresponds to a median descendent halo mass at $z \sim 0$ of $\gtrsim 10^{13}\, M_{\odot}$, which is consistent with the 2–4 L^{*} ellipticals at the present day (Zehavi et al., 2011). Moreover, the characteristic halo mass we estimate agrees well with the theoretical prediction of the maximum halo mass where gas can cool and collapse within a dynamical time White & Rees (1978) and is thus also the halo mass associated with the highest star-formation efficiency (Gerhard et al., 2001; Behroozi et al., 2013).

This may suggest that SMGs represent efficient collapse occurring in the most massive, gas-rich halos which can host such activity. This simple model provides a natural explanation for them representing the highest star-formation rate sources over the history of the Universe, as well as for the details of their redshift distribution (Fig. 3.12). Moreover, it offers a description of why their massive galaxy descendants at $z \sim 0$ have the highest stellar baryonic to halo mass ratios of any collapsed systems (Gerhard et al., 2001).

3.5.2 Evolution of the far-infrared luminosity and gas mass functions

Having determined the redshifts, far-infrared luminosities and dust masses for our SMG sample, we can exploit the fact that our survey is derived from a uniformly-

selected sample of 850-μm SCUBA-2 sources across a degree-scale field (Geach et al., 2017) to determine the luminosity and gas mass functions of SMGs and their evolution. We, therefore, use the sub-set of 364 ALMA SMGs brighter than the flux density limit of the SCUBA-2 catalogue, $S_{870} \geq 3.6\,\mathrm{mJy}$, and correct for incompleteness ($\sim$20% at $S_{870} = 3.6\,\mathrm{mJy}$, Geach et al. 2017) to obtain an 870-μm selected sample across the full UDS field. We note that ~ 74 per cent of these SMGs are detected in at least one SPIRE band and hence have robust far-infrared luminosities.

3.5.2.1 Far-infrared luminosity function

We calculate the far-infrared luminosity function for the 870-μm selected AS2UDS sample within the accessible volume using $\phi(L_{IR})\Delta L_{IR} = \Sigma(1/V_i)$, where $\phi(L)\Delta L$ is the number density of sources with luminosities between L and $L+\Delta L$ and V_i is the co-moving volume within which the i-th source would be detected in a given luminosity bin. We split the sample of the 364 AS2UDS SMGs brighter than $S_{870} = 3.6\,\mathrm{mJy}$ into three redshift bins with similar number of galaxies in each: $z < 2.35$, $z = 2.35$–3.00 and $z > 3.00$. The resulting luminosity functions are shown in Fig. 3.13a. Errors are estimated using a bootstrap method by re-sampling the photometric redshift and luminosity probability distribution functions. We fit the luminosity functions using Schechter functions of the form, $\phi = (\phi^*/L^*)(L/L^*)^{\alpha} e^{-L/L^*}$, where ϕ^* is the normalisation density, L^* is characteristic luminosity and α is the power-law slope at low luminosities (Schechter, 1976). Clemens et al. (2013) derive $\alpha = -1.3$ for their *Planck* detections of a local volume-limited galaxy sample, Dunne et al. (2011) derive $\alpha = -1.2^{+0.4}_{-0.6}$ for a SPIRE-selected sample out to $z \sim 0.5$, while other studies have yielded values ranging $\alpha = -1.0$ to -1.7 (Vlahakis et al., 2005; Dunne et al., 2011). As our sample covers only a relatively narrow range in far-infrared luminosity at each redshift we are unable to constrain α directly and so instead we choose to fix it to $\alpha = -1.5$. The Schechter fits to each redshift slice are shown in Fig. 3.13a.

To demonstrate the evolution of the ULIRG population across our survey volume,

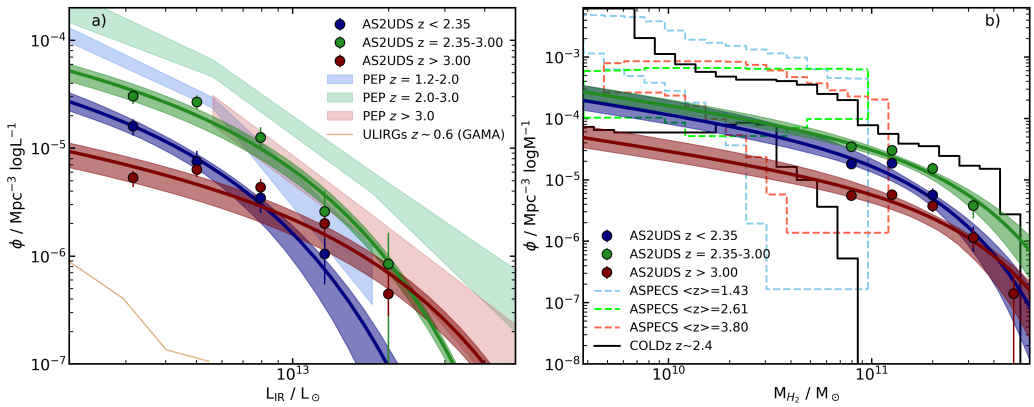

Figure 3.13: The evolution of the far-infrared luminosity function and molecular gas mass function from the flux-limited sample of $S_{870} \geq 3.6$ mJy AS2UDS SMGs corrected for incompleteness. These are both plotted for three independent redshift bins with similar number of galaxies: $z < 2.35$, $z = 2.35$–3.0, $z > 3.0$. Each of the bins is fitted with a Schechter function which is shown as the solid line in the respective colour. 1-σ errors were obtained by resampling the luminosity or gas mass and redshift PDFs and the 1-σ fitting error is shown as the shaded area. **(a)** We compare the AS2UDS far-infrared luminosity function to the PEP survey 100- and 160−μm selected samples from Gruppioni et al. (2013). We also compare to local sample of ULIRGs ($z \sim 0.6$) from the GAMA survey. This demonstrates the roughly two orders of magnitude increase in space density of ULIRGs between $z \sim 0$ and $z \sim 2$–3, with the space density peaking at $z = 2.35$–3.00 and then declining at higher redshifts. **(b)** We compare the AS2UDS gas mass function to results from the ASPECS blind mid-J CO survey (Decarli et al., 2019) for three corresponding redshift ranges, where the ASPECS gas masses have been converted to the equivalent scale as our MAGPHYS estimates. We see good agreement between the gas mass functions from the two surveys across the three redshift slices at higher mass end. We also compare to results from the COLDz blind low-J CO survey (Riechers et al., 2019). We see good agreement between the $z \sim 2.4$ CO (1–0) sources and $z = 2.35$–3.00 SMGs luminosity functions.

we also plot in Fig. 3.13a an estimate of the local far-infrared luminosity function from the sample derived from the GAMA survey from Driver et al. (2018) at $z \sim 0.6$. Examining the evolution in the luminosity function within our survey in Fig. 3.13a, we see that the space density increases from the $z < 2.35$ to peak in the $z = 2.35$–3.00 bin (median redshift $z \sim 2.6$) and then declines at $z > 3.00$. Compared to local ULIRGs, we conclude that the AS2UDS SMGs have a space density that is a factor of $\sim 100\times$ higher, similar to the findings for the smaller ALESS sample from Swinbank et al. (2014). In comparison to other estimates of the high-redshift far-infrared luminosity function, we find that our measurements for this rest-frame 200–300 μm-selected samples lie below those from the PEP survey from Gruppioni

et al. (2013), which is based on 100- and 160-μm selected samples. This is due to the fact that our 870-μm selection is sensitive to cooler sources, with $T_d \lesssim 50$–$60\,\mathrm{K}$, out to $z \sim 4$, thus we are incomplete for the hottest sources (such as in Gruppioni et al. 2013, see also Symeonidis et al. 2011; Gruppioni & Pozzi 2019).

3.5.2.2 Gas mass function

In an equivalent manner as in § 3.5.2.1, we have estimated the gas mass function for the SMG population and its variation with redshift in three broad redshift ranges, illustrated in Fig. 3.13b.

Here, we compare estimates of the gas mass function derived from the ASPECS blind mid-J CO survey from Decarli et al. (2019) to the space densities for our gas mass functions in Fig. 3.13b. We note that for this comparison we have converted the ASPECS gas masses, which are based on a conversion from CO luminosity to molecular gas mass adopting $\alpha_{CO} = 3.6$, to agree with the gas masses derived from MAGPHYS dust masses with a gas-to-dust ratio of 100. Decarli et al. (2016) show that this translates to a reduction in their estimated gas masses of a factor of $5.3 \pm 0.8\times$ and so we apply this conversion to compare to our MAGPHYS-derived estimates.

Our estimates of the gas mass function and those from ASPECS agree at the high gas mass end for all three redshifts (we show the corresponding 1-σ confidence level measurements at $z = 1.4$, $z = 2.6$ and $z = 3.8$ from ASPECS), with the wide-field AS2UDS estimates adding information at the high gas mass end of the distribution which is missing from ASPECS owing to its modest survey volume. We see that the extrapolated low-mass space densities from AS2UDS, based on our Schechter function fits with a low-mass slope of $\alpha = -1.5$, are broadly in agreement with the ASPECS samples down to masses of $\sim 10^{10}\,\mathrm{M}_\odot$, but fall below at lower masses, however, we note that these differences could be accounted for by the uncertainty in our adopted α value. We also compare our results to the gas mass function derived from the COLDz blind low-J CO survey of Riechers et al. (2019) in Fig. 3.13b (converting from CO luminosity to molecular gas mass in an equivalent manner

to ASPECS). The $z \sim 2.4$ CO (1–0) sources and $z = 2.35$–3.00 SMGs agree very well across the whole gas mass range. Thus, broadly, the evolution of the gas mass function from the combined AS2UDS + CO-selected samples appears to be best characterised by an increasing space density of galaxies at a fixed gas mass from $z \sim 3.5$ down to $z \sim 1.5$, with a hint that we may be seeing the space density of massive gas-rich systems beginning to decline at $z < 2.5$.

3.5.3 Stellar mass function

We next investigate what fraction of massive galaxies may have experienced a high star-formation rate phase, which would correspond to an SMG, and hence whether SMGs are a phase that all massive galaxies go through. For this comparison, we estimate the number density of massive galaxies using our MAGPHYS analysis of the K-band sample in the UDS field. This approach has the advantage that the stellar masses, redshifts and survey volumes are estimated in an identical manner to those employed for the SMGs. We select those field galaxies that have redshifts lying in the 16–84th percentile range of the AS2UDS redshift distribution ($z = 1.8$–3.4). To ensure we have robust stellar mass estimates, we limit the field sample to galaxies with the best photometry and SED fits with a reduced $\chi^2 < 4$. We determine the influence of these cuts on the resulting sample size and increase the normalisation of the field sample by a factor of 1.35 to correct for this. The UDS field catalogue is selected in the K-band, with a 3σ limit of $K = 25.7$ mag, which roughly corresponds to $M_* \sim 5{\times}10^9\,\mathrm{M}_\odot$ at $z \sim 3$ for typical star-formation histories. Therefore, for the field, we construct the stellar mass function above this stellar mass threshold to avoid incompleteness. We sum the number of galaxies in each stellar mass bin and divide by the volume defined by the span of their redshifts.

We calculate the SMG stellar mass function in an equivalent manner and then calculate the duty cycle of the SMGs by comparing the visibility time to the age spanning a given redshift slice (ΔT_z): duty-cycle correction as $\Delta T_z / T_{vis}$. We define the visibility time from the gas-depletion timescale and, for the redshift range of $z = 1.8$–3.4, we find a median corresponding duty correction factor of 5.1×, which

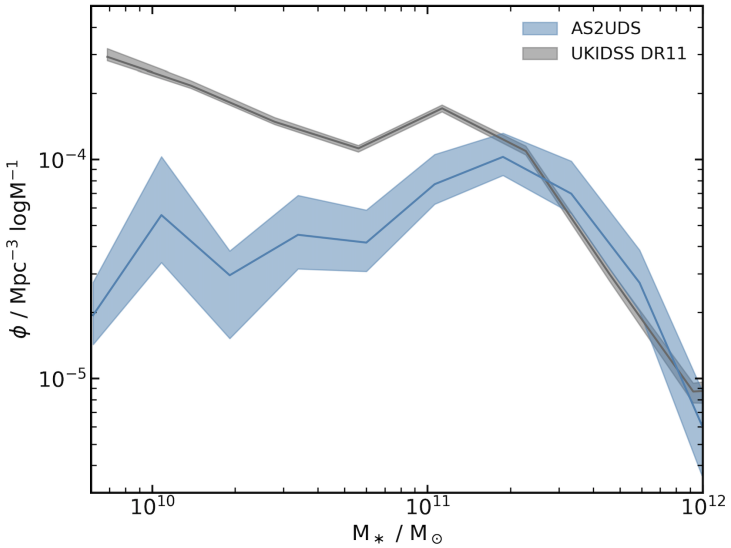

Figure 3.14: The stellar mass function for $S_{870} \geq 3.6$ mJy SMGs at $z = 1.8$–3.4. The blue line shows the expected number density of galaxies which had passed through an SMG-like phase, estimated from the distribution of the AS2UDS SMGs and corrected for duty cycle by a factor of $5.1\times$, with the respective 1-σ error shown as the blue shaded region. The grey line shows the stellar mass function of K-band selected galaxies in the UDS field with the 1-σ error as the grey shaded region. We see that the SMGs make an increasing contribution to the total mass density distribution at higher stellar masses. The corrected volume density of AS2UDS SMGs corresponds to ~ 30 per cent of the total number density of galaxies above $M_* = 3 \times 10^{10}\,\mathrm{M}\odot$, but this fraction increases rapidly so that ~ 100 per cent of galaxies at $M_* \gtrsim 3 \times 10^{11}\,\mathrm{M}_\odot$ are expected to have passed through an SMG-phase.

we apply to the SMG mass function. The uncertainties for both field and SMG stellar mass functions were obtained by re-sampling the stellar mass and redshift probability distributions and taking the 16–84th percentile range as the 1-σ error.

Overlaying the corrected SMG mass function on the field in Fig. 3.14, we see that at lower stellar masses, galaxies which have passed through an SMG-phase would account for only a modest fraction of the total space density, e.g. ~ 30 per cent of galaxies above $M_* = 3 \times 10^{10}\,\mathrm{M}_\odot$. This fraction increases to ~ 100 per cent at $M_* \gtrsim 3 \times 10^{11}\,\mathrm{M}_\odot$, indicating that all of the galaxies above this mass are likely to have experienced an SMG-phase in the course of their evolution. The results from the EAGLE simulation presented in McAlpine et al. (2019) indicates that effectively all galaxies at $z \sim 0$ in the simulation with stellar masses above $M_* = 2 \times 10^{11}\,\mathrm{M}_\odot$ experienced a ULIRG-like phase where their star-formation rate exceeded $\sim 100\,\mathrm{M}_\odot\,\mathrm{yr}^{-1}$. This result is consistent with our finding as there is little

evolution of the stellar mass function of these galaxies in this mass range since $z \lesssim 1.5$ (Kawinwanichakij et al., 2020).

3.5.4 Co-moving star-formation rate density

To investigate the contribution of SMGs to the total star-formation rate density (SFRD) as a function of redshift we make use of the predicted star-formation rates of AS2UDS sources. We calculate the star-formation rate density for two sub-sets of our sample SMGs: those SMGs with $S_{870} \geq 3.6\,\mathrm{mJy}$ (which is the limit of the parent survey) and those with $S_{870} \geq 1\,\mathrm{mJy}$ SMGs. For the $S_{870} \geq 3.6\,\mathrm{mJy}$ sub-sample we correct for the incompleteness using the number counts from Geach et al. 2017. We also correct the estimated star-formation rate of an SMG within its redshift PDF to account for the variation as a function of redshift in the inferred star-formation rate. We correct the number of $S_{870} \geq 1\,\mathrm{mJy}$ sources from our survey to match the expected number counts to this flux limit. We derive these using the ALMA 1.13-mm counts in the GOODS-S field from Hatsukade et al. (2018) and a factor of 1.8 to convert the 1.13-mm flux densities to 870μm.

The resulting star-formation rate density of the AS2UDS SMGs is shown in the Fig. 3.15. For comparison we overlay the combined optical and infrared star-formation rate density from Madau & Dickinson (2014), this represents the total star-formation rate density in the Universe at $z \lesssim 3$, above which it is constrained only by surveys in the UV (unobscured sources). This comparison demonstrates that the activity of SMGs peaks at $z \sim 3$, higher than the peak of the Madau & Dickinson (2014) SFRD at $z \sim 2$. This suggests that more massive and obscured galaxies are more active at earlier times. Fig. 3.15 also shows that contribution to the total star-formation rate density increases steeply from $z \sim 1$ with the peak contribution being ~ 15 per cent at $z \sim 3$ for the $S_{870} \geq 3.6\,\mathrm{mJy}$ sub-sample or ~ 60 per cent for sources brighter than $S_{870} = 1\,\mathrm{mJy}$. This indicates that roughly half of the star-formation rate density at $z \sim 3$ arises in ULIRG-luminosity sources and this population appears to decline only slowly across the 1 Gyr from $z \sim 3$ to $z \sim 6$.

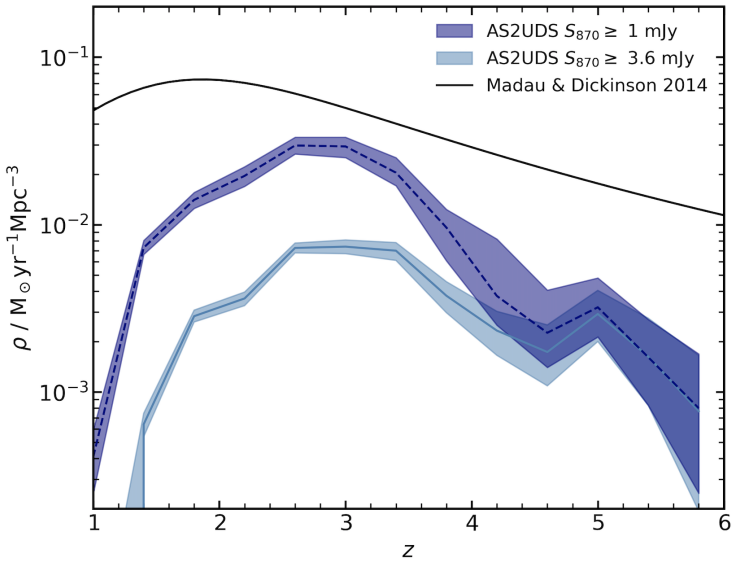

Figure 3.15: The co-moving cosmic star-formation density as a function of redshift. We show the contribution of AS2UDS sources for SMGs brighter than $S_{870} = 3.6\,\mathrm{mJy}$ and also brighter than $S_{870} = 1\,\mathrm{mJy}$, where we correct the numbers of fainter sources using the 850-μm number counts (Geach et al., 2017) and 1.13-mm number counts (Hatsukade et al., 2018), adopting S_{870}/S_{1130} =1.8. The shaded regions represent the 1-σ error which has been calculated by re-sampling the redshift probability distribution while taking into account the star-formation–redshift correlation. This shows that the contribution from SMGs peak at higher redshift ($z \sim 3$) than the total star-formation rate density (Madau & Dickinson, 2014) at which epoch SMGs with $S_{870} \geq 3.6\,\mathrm{mJy}$ contribute ~ 15 per cent to the total SFRD, and ~ 60 per cent if we integrate down to the $S_{870} \geq 1\,\mathrm{mJy}$.

3.5.5 The scale of far-infrared emission in SMGs

Finally, we wish to investigate what we can learn about the conditions and structure of the star-forming regions of SMGs from our sample. For this, we will employ sizes for a sub-set of our SMGs which have been derived from the analysis of high-resolution dust continuum observations of 154 SMGs in A2SUDS by Gullberg et al. 2019. This work exploits the fact that the Cycle 3 observations for AS2UDS were obtained with ALMA in an extended configuration which yielded a synthesised beam with a FWHM of 0.18″ ($\sim 1\,\mathrm{kpc}$). Gullberg et al. 2019 undertook extensive testing and analysis of the constraints on the sizes, profiles and shapes of SMGs provided by these high-resolution 870-μm maps. On the basis of these tests they restricted their analysis to only the highest angular resolution data available and in addition, applied a further cut that the sources had to be detected in a 0.5″-tapered

map with a signal-to-noise of SNR > 8. This ensured that the resulting profile and shape measurements were unbiased and of sufficient quality. The resulting sizes have median errors of just 20 per cent for a sample of 154 SMGs, broadly representative of the full population of AS2UDS SMGs. Gullberg et al. 2019 measure a number of profile, shape and size parameters for the SMGs from fits to the *uv* amplitudes in Fourier space and also image-plane fits to the reconstructed maps. They show that dust emission from typical SMGs are well-fit by exponential profiles described by a Sersic model with $n \sim 1$ (see also Hodge et al., 2016; Simpson et al., 2017; Hodge et al., 2019). In the analysis here, we make use of the circularised effective radii derived from fits to the *uv* amplitudes for the sources adopting $n = 1$ Sersic profiles. We then convert these angular sizes into physical units using the photometric redshifts determined for the individual sources. The median physical size, expressed as R_e, of the sample is 0.83 ± 0.01 kpc.

3.5.5.1 Star-formation conditions in SMGs

The high median star formation of the AS2UDS sources (see Fig. 3.4) may be a result of SMGs behaving as Eddington-limited starbursts (Andrews & Thompson, 2011), where the radiation pressure from massive stars is sufficient to quench further activity. To test this, we plot the 870-μm physical sizes versus the star-formation rate for the SMGs in Fig. 3.16a. For comparison, we overlay two other studies which employed similar signal-to-noise ALMA observations, but at lower resolution ($0.3''$–$0.7''$ FWHM), of samples of SMGs in the UDS field: an 870-μm sizes from the AS2UDS-pilot study of bright SMGs by Simpson et al. (2015a), which have a median effective radius of $R_e = 0.79 \pm 0.05$ kpc, and a sub-set of AS2UDS SMGs detected using the AzTEC camera on the ASTE telescope and followed-up with ALMA at 1.1-mm by Ikarashi et al. (2017), which yield a median effective radius of $R_e = 1.1 \pm 0.1$ kpc. Even though these two samples use lower resolution observations, they recover similar distributions in terms of the physical sizes of the SMGs.

We observe no strong trend in size with star-formation rate and so we now test whether the star-formation activity in SMGs is affected by their approaching the

Eddington luminosity limit for their observed sizes and star-formation rates. We follow Andrews & Thompson (2011) who demonstrated that the balance of radiation pressure from star formation with self gravity results in a maximum star-formation rate surface density (in units of $\mathrm{M_\odot\,yr^{-1}\,kpc^{-2}}$) of:

$$\mu_{SFR}^{max} = 11 f_{gas}^{-0.5} \delta_{GDR}, \tag{3.7}$$

where f_{gas} is the gas fraction in the star-forming region and δ_{GDR} is the gas-to-dust ratio which (as mentioned in § 3.4.6, we adopt 100). The equation assumes optically-thick dust emission and no heating from an AGN. Our estimated galaxy-integrated gas fractions from Fig. 3.10b are $f_{gas} \sim 0.4$ and we see no significant variation in this with redshift. However, the available near-infrared imaging suggests that the stellar mass component, which is used to estimate f_{gas}, is likely to be more extended than the size of the dust continuum emission, potentially by a factor of $\sim 4\times$ (Simpson et al. 2017; Ikarashi et al. 2015; Lang et al. 2019; Gullberg et al. 2019. Due to uncertainty in the calculated gas fraction, we take a conservative approach and adopt a gas fraction of unity, which provides the lower limit of the star-formation rate surface density (for comparison, the Eddington limit assuming f_{gas}= 0.4 is shown in Fig. 3.16a).

The resulting maximum star-formation rate surface density predicted by the model is $1{,}100\,\mathrm{M_\odot yr^{-1}\,kpc^{-2}}$ and we show this line in Fig. 3.16a. Comparing the AS2UDS SMGs to this line, we see that very few have sizes which are compact enough for them to approach the Eddington limit for their observed star-formation rates. On average the AS2UDS have sizes around ten times larger than an Eddington-limited system with their same star-formation rate, indicating that averaged on kpc-scales the radiation pressure from the on-going star formation in these systems is not sufficient to quench their activity. However, if the star-forming region for a given galaxy is "clumpy" on small scales (Swinbank et al., 2011; Danielson et al., 2011; Menéndez-Delmestre et al., 2013), then individual regions on sub-kpc scales may be Eddington limited.

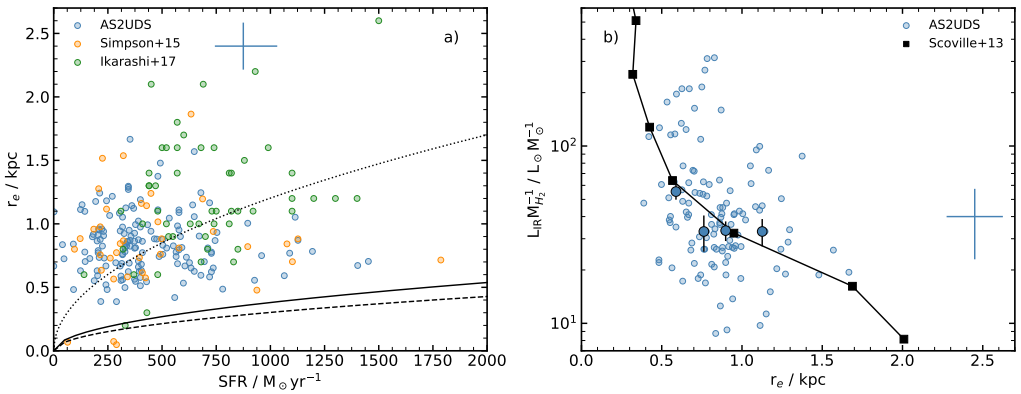

Figure 3.16: **(a)** The variation of 870-μm dust continuum size from (Gullberg et al., 2019) with star-formation rate for the AS2UDS SMGs. We also plot the sizes derived from lower-resolution ALMA continuum observations of samples of SMGs in the UDS field at 870μm from Simpson et al. (2015c) and 1.1-mm by Ikarashi et al. (2017) (the SFR for these are derived from our MAGPHYS analysis of these galaxies). We see a weak trend of increasing size at higher star-formation rates, with significant scatter. We compare this trend to the boundary expected from the estimated Eddington limit following Andrews & Thompson (2011) for f_{gas}= 1, which is shown as the solid line. The dotted line indicates the 0.1× this Eddington limit, which roughly goes through the median of our sample. The dashed line indicates the Eddington limit for f_{gas} = 0.4. We see that very few of the SMGs have sizes which are compact enough for them to approach the Eddington limit at their star-formation rate. On average, AS2UDS sources have sizes around ten times larger, and thus areas approaching two orders of magnitude larger than an Eddington-limited system with their star-formation rate, suggesting that this fundamental feedback process will not quench their activity. **(b)** 870-μm dust continuum size as a function of far-infrared luminosity-to-gas mass ratio for SMGs with at least one SPIRE detection. Large circles are the median values binned by radius of ∼30 sources and the median error for individual sources is indicated at the top of the panel. We overlay the model of an optically-thick dust cloud from the Scoville (2013). The AS2UDS SMGs have a similar trend to this model, however with scatter below the model at low luminosity-to-mass ratios and above the prediction for high ratios. The overall agreement between model and AS2UDS sizes at a given radius indicates that SMGs are possibly homogenous, and thus homologous, systems in the far-infrared, behaving as expected for a single dust cloud.

3.5.5.2 Structure of the far-infrared regions of SMGs

We now turn to examine the possible structure of the far-infrared luminous component of the SMGs. As suggested in §3.5.5.1, the conditions of star formation are dependent on whether the far-infrared sources have a single homogenous dust cloud structure or are "clumpy" systems. We investigate this by comparing our results to an optically-thick model from Scoville (2013).

As outlined in Scoville (2013), internally heated far-infrared sources are described by two properties: the luminosity of the central heating source and total dust mass in the surrounding envelope. Thus, this structure can be characterised by a single parameter: their luminosity-to-mass ratio. The far-infrared SEDs can be calculated for this using a temperature profile, which is estimated from a combination of optically-thin dust emission at the inner region (where $T_{\rm d} \propto r^{-0.42}$), optically-thick (where $T_{\rm d} \propto r^{-0.5}$ as the photons heating the grains and those that are emitted by the grains have similar wavelength distributions) at intermediate radii and optically-thin again at larger radii (Scoville, 2013). The inner radius is taken at 1 pc (where $T_{\rm d}$=1000 K, close to the dust sublimation limit) and the outer radius is taken at 2 kpc, which is roughly appropriate for SMGs (Gullberg et al., 2019). In the plot, the effective radius of the model is defined as radius of the shell producing the largest fraction of the overall luminosity for each of the $L/M_{\rm ISM}$ values, where $M_{\rm ISM} = M_{\rm HI}+M_{\rm H_2}$. A full description can be found in Scoville (2013). In Fig. 3.16b we show results for an optically-thick, radiative transfer modelling of the dust emission for a r^{-1} dust density distribution (they found similar results were found with other reasonable power laws) from Scoville (2013). They set the luminosity as $10^{12}\,{\rm L}_{\odot}$ and vary the total dust mass in the range of 10^{7}–$10^{9}\,{\rm M}_{\odot}$ (both appropriate for our sample) and calculate the effective radius as the radius of the shell producing the majority of the overall luminosity. In our analysis we assume a dust-to-gas ratio of 100 to estimate the gas mass of SMGs, which is comparable to the $\rm M_{ISM}$ definition of the model used in Scoville (2013) who adopt a ratio of ∼100.

As mentioned above, the model in Fig. 3.16b assumes SMGs are described by

a single homogeneous optically-thick dust cloud. In order to compare how the effective radius of SMGs varies with the luminosity-to-mass ratio, we overlay the results derived for the 122 AS2UDS sources which have 870μm size information and at least one SPIRE detection. We split the sources by radius into four bins to assess the broad trends. We see an overall trend of decreasing dust continuum size with increasing luminosity-to-mass ratio. The observations broadly agree with the ratio of size to L/M_{ISM} in the Scoville (2013) model, suggesting that the dust emission from our SMG sample is, on average, consistent with a homogeneous and homologous population of centrally-illuminated dust clouds. The scatter we observe could partly be due to the variation of profiles in the clouds.

We note the structure of the dust clouds in SMGs did not necessarily have to follow this trend: some studies have claimed "clumpy" structure of the star-forming regions in SMGs (Swinbank et al., 2011; Danielson et al., 2011; Menéndez-Delmestre et al., 2013). If the structure of dust clouds in the SMGs was indeed "clumpy", the radial extent of the emission would be higher for a given luminosity-to-mass ratio. Thus, from their far-infrared emission, SMGs appear to, on average, behave as a sample of sources with very similar structures where the emission is consistent with a central source (starburst) illuminating a surrounding dust/gas reservoir with relatively similar sizes, densities and profiles.

3.6 Conclusions

In this chapter, we investigated the physical properties of 707 ALMA-identified sub-millimetre galaxies from the AS2UDS survey (Stach et al., 2019), with flux densities in the range $S_{870} = 0.6$–13.6 mJy (with a median of 3.7 mJy). We derived physical properties, such as their photometric redshifts, stellar and dust masses and far-infrared luminosities, of each SMG from MAGPHYS SED fits (which were modelled in Chapter 2). Our homogeneously selected survey with uniform photometric coverage allowed us to construct sub-samples (including an unbiased luminosity-selected sub-sample) to investigate the evolutionary behaviour of this population. Our main

findings are:

- The redshift distribution of our full sample of SMGs has a median of $z = 2.61 \pm 0.08$ with a 68^{th} percentile range of $z = 1.8$–3.4, which is consistent with results for smaller samples of SMGs in other fields using photometric or spectroscopic redshifts. Those SMGs which are undetected in the K-band appear to preferentially lie at higher redshifts, with $z = 3.0 \pm 0.1$, while SMGs which are detected at 1.4 GHz lie at redshift comparable to the median of the whole SMG population, $z = 2.5 \pm 0.1$. The volume density of SMGs has a distribution which is log-normal, peaking ~ 2.4 Gyr after the Big Bang with the 16–84^{th} percentile range of 1.8–4.5 Gyr. The inferred formation age distribution peaks at $\sim$1.8 Gyr ($z \sim 3.5$).

- The SMG redshift distribution can be reproduced by a simple model describing the growth of halos through a characteristic halo mass of $\sim 6 \times 10^{12}\,\mathrm{M}_{\odot}$, combined with an increasing molecular gas fraction at higher redshifts. This model suggests that SMGs may represent efficient collapse occurring in the most massive halos that can host such activity. For a dark matter halo mass of $6 \times 10^{12}\,\mathrm{M}_{\odot}$ at $z \sim 2.6$, the median descendent halo mass at $z \sim 0$ is $\gtrsim 10^{13}\,\mathrm{M}_{\odot}$, which is consistent with these galaxies evolving into 2–4 L^{*} ellipticals at the present day.

- The median dust mass of our sample is $M_d = (6.8 \pm 0.3) \times 10^{8}\,\mathrm{M}_{\odot}$. Adopting a gas-to-dust ratio of $\delta_{GDR} = 100$, this implies a median molecular mass of $M_{\mathrm{H2}} \sim 7 \times 10^{10}\,\mathrm{M}_{\odot}$. The median far-infrared luminosity of the SMGs in our sample is $L_{IR} = (2.88 \pm 0.09) \times 10^{12}\,\mathrm{L}_{\odot}$ and, with a median star-formation rate of SFR $= 236 \pm 8\,\mathrm{M}_{\odot}\,\mathrm{yr}^{-1}$ (68^{th} percentile range of SFR $= 113$–$481\,\mathrm{M}_{\odot}\,\mathrm{yr}^{-1}$), suggests a gas depletion times of approximately 150 Myr (or an SMG-phase lifetime of $\sim$300 Myr assuming that, on average, we are witnessing the SMG halfway through its peak star-formation rate phase). The characteristic gas depletion timescale declines by a factor of ~ 2–$3\times$ across $z = 1$–4 the trend being driven by an increase in far-infrared luminosity with redshift in our sample as a result of selection effects.

- The average mass produced since the start of the SMG-phase (the last $\sim$150 Myr) assuming a constant star-formation rate compared to the total stellar mass has a median of $M_{150\mathrm{M}yr}/M_{*} \sim 0.3$. Therefore, for an average SMG, $\sim$30 per cent of

the current stellar mass was formed in the last 150 Myr, and by the end of the SMG-phase these systems are likely to roughly double their pre-existing stellar masses.

- For SMGs with well-constrained far-infrared SEDs, we show that the median characteristic dust temperature for our sample is $T_{\rm d}^{MBB} = 30.4 \pm 0.3$ K with a 68^{th} percentile range of $T_{\rm d}^{MBB} = 25.7$–37.3 K, with a trend of increasing temperature with luminosity. With a L_{IR}-complete sample across $z = 1.5$–4 we are able to exclude the covariance with redshift. We see no evidence for a variation of dust temperature with redshift at fixed luminosity in this sub-sample, suggesting that previous claims of such behaviour are a result of luminosity evolution in the samples employed. However, we note that there is an apparent offset in dust temperature between our high-redshift sample and ULIRGs at $z < 1$, with the high-redshift SMGs being 3 ± 1,K cooler at fixed L_{IR}, but this comparison is complicated by the selection function of the local samples. We suggest the origin of this offset, if real, is likely to be due to the more compact dust distributions in the ULIRG population at $z < 1$.

- We find that the gas mass fraction of the SMGs evolves weakly from ~ 30 per cent at $z \sim 1.5$ to ~ 55 per cent at $z \sim 5$. These gas fractions are similar to those suggested for other high-redshift star-forming populations from mass and gas-selected samples. We note that the gas mass fraction of SMGs is similar to that estimated in an identical manner for *Herschel*-detected ULIRGs with comparable star-formation rate at $z < 1$ from the GAMA survey: ~ 35 per cent. Thus, the primary differences we infer for ULIRGs at $z < 1$ is a much lower space density and more compact ISM distribution than those at $z \gg 1$.

- We find that the median stellar mass of the SMGs is $M_* = (12.6 \pm 0.5) \times 10^{10}\,{\rm M}_\odot$ with a 16–68^{th} percentile range of $M_* = (3.5$–$26.9) \times 10^{10}\,{\rm M}_\odot$. The typical mass does not evolve strongly with redshift, varying by < 10 per cent over the redshift range $z = 1$–4, although star-formation rates for our sample increase by a factor ~ 3 over this same range (driven by the luminosity-redshift trend from the selection). In terms of the specific star-formation rate (SFR/M_*), we see that, at $z \sim 1$, typical

SMGs lie a factor of ~ 6 above the "main sequence" (defined by the field population modelled using MAGPHYS for consistency). By $z \sim 4$ SMGs lie a factor of two above the "main-sequence", due to the strong evolution of sSFR of the "main-sequence".

- By comparing to the stellar mass function of massive field galaxies, and accounting for the duty cycle of SMGs due to gas-depletion, we show that above a stellar mass of $M_* > 3 \times 10^{10}\,\mathrm{M}_\odot$, ~ 30 per cent of all galaxies at $z \sim 1.8$–3.4 (the quartile range of our sample) have gone through a sub-millimetre-luminous phase, rising to ~ 100 per cent at $M_* \gtrsim 3 \times 10^{11}\,\mathrm{M}_\odot$. This is in good agreement with the predictions of simulations.

- We also show that the volume density of massive, gas-rich galaxies from our survey is $\sim 3{\times}10^{-4}\,\mathrm{Mpc}^{-3}$ for galaxies with H_2 masses of $\sim 10^{11}\,\mathrm{M}_\odot$ at $z \sim 2.6$ and that extrapolating to lower masses this broadly agrees with results from recent blind surveys for CO-emitters with ALMA and JVLA. Thus, panoramic sub-millimetre surveys provide an efficient route to identify and study the most massive gas-rich galaxies at high redshifts.

- The contribution of 870-μm selected SMGs to the total star-formation rate density in the Universe increases steeply with redshift from $z \sim 1$, with the peak contribution being ~ 15 per cent at $z \sim 3$ for the $S_{870} \geq 3.6\,\mathrm{mJy}$ sub-sample and ~ 60 per cent for SMGs brighter than $S_{870} = 1\,\mathrm{mJy}$. Thus, roughly half of the star-formation rate density at $z \sim 3$ arises in ULIRG-luminosity sources and the star formation contribution from this population appears to decline only slowly across the 1 Gyr from $z \sim 3$ to $z \sim 6$.

- Finally, we investigate the scale of the rest-frame far-infrared emission in SMGs. We determine that the star-formation rate in the SMGs is significantly sub-Eddington, with a typical Eddington ratio of ~ 0.1. We find that the far-infrared spectral energy distributions of SMGs are consistent with a modified blackbody model which has an optical depth (τ) of unity at $\lambda_0 \geq 100\,\mu\mathrm{m}$, and the 870-$\mu$m sizes of SMGs are broadly consistent with them acting as a homologous population of centrally illuminated dust clouds.

Our analysis underlines the fundamental connection between the population of gas-rich, strongly star-forming galaxies at high redshifts and the formation phase of the most massive galaxy populations over cosmic time. We suggest that the characteristics of these short-lived, but very active systems represent events where massive halos (with characteristic total masses of $\sim 6 \times 10^{12}\,\mathrm{M}_{\odot}$) with high gas fractions transform their large gas reservoirs into stars on a few dynamical times. Analysis of the dust continuum morphologies of AS2UDS and ALMA observations of other SMG samples suggests that the continuum emission arises from bar-like structures with diameters of ~ 2–$3\,\mathrm{kpc}$ in more extended gas disks, which suggests that their strong evolution is likely driven by dynamical perturbations of marginally stable gas disks (Hodge et al. 2019; Gullberg et al. 2019).

Chapter 4

Tracing the evolution of dust-obscured activity across the cosmic noon

Preamble

In the previous chapter we have analysed the most strongly star-forming galaxies at $z \geq 2$ that are selected at 850μm. However, to get a more complete view of the infrared-luminous activity across cosmic noon at $z \approx 1$–3, emission closer to the peak of the dust spectral energy distribution (SED) has to be considered. In this chapter, we analyse the physical properties of 121 sub-millimetre galaxies (SMGs) from the STUDIES 450-μm survey and compare the results to the 850-μm-selected SMG sample from AS2UDS, to understand the fundamental physical differences between the two populations at the observed depths. We find that the fainter 450-μm sample has ~ 14 times higher space density than the brighter 850-μm sample at $z \lesssim 2$, and a comparable space density at $z = 2$–3, before rapidly declining, suggesting LIRGs are the main obscured population at $z \sim 1$–2, while ULIRGs dominate at higher redshifts. We construct rest-frame ~ 180-μm-selected and dust-mass-matched samples at $z = 1$–2 and $z = 3$–4 from the 450-μm and 850-μm samples, respectively, to probe the evolution of a uniform sample of galaxies spanning the cosmic noon era. Using far-infrared luminosity, dust masses and an

optically-thick dust model, we suggest that higher-redshift sources have higher dust densities due to inferred dust continuum sizes that are roughly half of those for the lower-redshift population at a given dust mass, leading to higher dust attenuation. We track the evolution in the cosmic dust mass density and we suggest that the dust content of galaxies is governed by a combination of both the variation of gas content and dust destruction timescale. This work has been published as a first author paper (Dudzevičiūtė et al., 2021).

4.1 Introduction

In the mid-1990s, the first surveys at sub-millimetre wavelengths (450 μm and 850 μm) using the Sub-millimeter Common User Bolometric Array (SCUBA) on James Clerk Maxwell Telescope (JCMT) began to resolve the far-infrared/sub-millimetre background into its constituent galaxies and identified the first statistical samples of high-redshift, sub-millimetre bright galaxies (SMGs – Smail et al. 1997; Hughes et al. 1998; Barger et al. 1998; Eales et al. 1999). These surveys confirmed the cosmological significance of far-infrared-luminous galaxies, in particular their potentially significant contribution to the star-formation rate density at high redshifts (see Madau & Dickinson, 2014). Due to atmospheric transmission, large-scale surveys of the high-redshift SMG populations are primarily undertaken in wavebands between 850 μm and 1.2 mm (e.g. Coppin et al., 2006; Scott et al., 2008; Weiß et al., 2009; Hatsukade et al., 2011; Mocanu et al., 2013; Umehata et al., 2014; Geach et al., 2017; Miettinen et al., 2017; Cowie et al., 2018; Stach et al., 2019; Simpson et al., 2020). However, these wavebands typically select galaxies based on their luminosity at rest-frame wavelengths around 300 μm and are thus sensitive to the cool dust mass of the galaxies (see Chapter. 3; and Dudzevičiūtė et al. 2020, hereafter D20; Ikarashi et al. in prep). Subsequent studies of this population have suggested that these galaxies are strongly dust obscured systems with high far-infrared luminosities and lying at high redshifts, with a number density peaking at $z \sim 2$–3 (Chapman et al. 2005; Ivison et al. 2011; Bothwell et al. 2013; da Cunha et al. 2015; Danielson et al. 2017; Koprowski et al. 2016; Brisbin et al. 2017;

D20). Although these studies have provided insight into the physical properties of the SMGs, observations at such long wavelengths do not sample the peak of the far-infrared emission and, as noted in Chapter 3, are more sensitive to sources with larger masses of cool dust, as well as those at higher redshifts (Blain & Longair, 1993).

At high redshift ($z > 2$), selection at shorter submillimetre or far-infrared wavelengths (e.g. $\leq 500\,\mu$m) samples the spectral energy distribution (SED) of the dust continuum emission closer to the peak of the far-infrared emission, rather than the Rayleigh-Jeans tail which is traced by the $850\,\mu$m and 1.2 mm surveys. Therefore, surveys at shorter wavelengths are more sensitive to far-infrared luminosity, than the cold dust mass. This can potentially lead to surveys detecting physically different sources when selected at different wavebands and redshifts.

The pre-eminent surveys at far-infrared wavelengths, specifically 250, 350 and $500\,\mu$m, have used the SPIRE instrument on *Herschel* and mapped hundreds of square degrees of sky (e.g. Eales et al., 2010; Oliver et al., 2012; Wang et al., 2014; Valiante et al., 2016). While covering huge areas, these surveys are limited in sensitivity for direct detection of sources due to the large beam size and resulting bright confusion limit*, which makes it challenging to detect all but the brightest (unlensed) sources at $z \gtrsim 1$ (Symeonidis et al. 2011, although see Shu et al. 2016; Jin et al. 2018; Liu et al. 2018). Moreover, the large beam size makes it difficult to reliably locate counterparts needed to understand their properties. However, higher-resolution imaging at similar wavelengths can be obtained from single-dish telescopes on the ground through the atmospheric windows at $350\,\mu$m (Khan et al., 2007; Coppin et al., 2008) and $450\,\mu$m (Blain et al., 1999; Chen et al., 2013). Unfortunately the atmospheric transmission at $450\,\mu$m is around half of that at $850\,\mu$m, and obtaining deep, large-area surveys with ground-based observations is therefore challenging. Although Atacama Large Millimeter Array (ALMA) could in principle produce deep, high-resolution imaging at $450\,\mu$m, large surveys would be observationally expensive due to the very limited field of view of $\sim 0.02\,\mathrm{arcmin}^2$ at this

*Defined as the sensitivity limit arising from unresolved sources which cannot be improved by increasing the integration time.

wavelength. In contrast, the SCUBA-2 camera (Holland et al., 2013) on the JCMT, with a field of view of 45 arcmin^2 and a beam size of 7.9 arcsec at 450 μm (yielding an approximately 20 times lower confusion limit than SPIRE at 500 μm), provides the sensitivity and angular resolution necessary to identify 450-μm sources and their counterparts over fields of 100s arcmin^2.

Surveys of sources selected at 450 μm, closer to the peak of the far-infrared emission in systems at the epoch of peak star formation ($z \sim 2$–3), have suggested that the 450-μm-selected population at mJy flux limits lies at lower redshift than those selected at 850 μm, with a distribution that peaks at $z \sim 1.5$–2.0 (Casey et al., 2013; Geach et al., 2013; Roseboom et al., 2013; Zavala et al., 2014, 2017; Bourne et al., 2017; Lim et al., 2020). 450-μm-selected sources are also suggested to have higher characteristic dust temperatures than 850-μm-selected SMGs by $\Delta T_{\rm d} \simeq 10$ K (Casey et al., 2013; Roseboom et al., 2013), although this may be partly due to selection effects. However, the identification of differences in the physical properties of SMGs selected in the different submillimetre wavebands from such studies have been limited by their modest sample sizes and also their biases towards brighter sources due to the sensitivity limits at 450 μm. Comparison to the 850-μm population is further complicated by uncertain or incomplete identifications in the longer wavelength samples (e.g. Hodge et al., 2013), as well as the use of different photometric redshift and SED modelling methods on different samples.

This study aims to better understand the physical properties of SMGs and in particular the relationship between samples selected at 450- and 850-μm, by exploiting a very deep 450-μm imaging survey: the SCUBA-2 Ultra Deep Imaging EAO Survey (STUDIES; Wang et al., 2017; Lim et al., 2020) in the Cosmic Evolution Survey (COSMOS; Scoville et al., 2007) field. STUDIES is a multi-year JCMT survey within the CANDELS region ($\sim$300 arcmin^2), which obtained the deepest single-dish map at 450 μm currently available, with a 1-σ depth of 0.65 mJy. The source catalogue and physical properties of the 450-μm sample are presented in Lim et al. (2020), while the structural parameters and morphological properties have been analysed by Chang et al. (2018).

In this chapter, we compare the properties of galaxies selected from deep 450-μm-observations to those selected from typical 850-μm surveys. SCUBA-2 simultaneously maps at 450 μm and 850 μm, however, the STUDIES 850-μm map is confusion limited at an 850-μm flux density limit of ~ 2 mJy and it cannot be used to reliably identify faint 850-μm sources. Therefore, for our 850-μm comparison sample we utilise the largest available ALMA-identified 850-μm-selected SMG sample, from the ALMA/SCUBA-2 Ultra Deep Survey (AS2UDS, Stach et al. 2019) that we analysed in Chapter 3.

We revisit the modelling of the UV-to-radio SEDs of the 450-μm galaxies using MAGPHYS+photo-z (da Cunha et al., 2008, 2015; Battisti et al., 2019), which was tested and calibrated in Chapter 2 and fitted to the AS2UDS 850-μm sample in Chapter 3, thus ensuring that the comparison of the physical properties between the two samples is free from systematic differences due to the modelling. With these two large, consistently analysed samples we empirically compare the physical properties of 450-μm-detected galaxies with the 850-μm population. At the observed depths, the two surveys sample down to the ULIRG/LIRG boundary ($10^{11-12}\,L_{\odot}$) at $z = 1$–3 and although there is some overlap between these flux-limited samples, as discussed in Lim et al. (2020), the combination and comparison of 450-μm and 850-μm surveys provide a more complete view of luminous far-infrared activity in the Universe over a wider redshift range than possible with either individual sample. In particular, we exploit these large samples to construct subsets that are matched in rest-frame wavelength to allow us to quantify the physical differences between an identically selected sample of dusty galaxies across ~ 2.5 Gyr of lookback time at $z \sim 1.5$ and $z \sim 3.5$.

The chapter is structured as follows. In § 4.2 we give details on the multi-wavelength data which we use to construct the SEDs for our sources. In § 4.3 we present our results, including a comparison of the STUDIES 450-μm selected galaxies to the 850-μm selected galaxies from the AS2UDS survey. We discuss the implications of our results in § 4.4 and present our conclusions in § 4.5. As in the previous chapters, we adopt a ΛCDM cosmology with with $H_0 = 70\,\mathrm{km\,s^{-1}\,Mpc^{-1}}$,

$\Omega_\Lambda = 0.7$, $\Omega_\mathrm{m} = 0.3$. When quoting magnitudes, we use the AB photometric system.

4.2 Observations & SED Fitting

4.2.1 Photometric coverage

STUDIES is a SCUBA-2 450-μm imaging survey within the CANDELS region in the COSMOS field. A detailed description of the SCUBA-2 observations and data reduction can be found in Wang et al. (2017) and Lim et al. (2020). Briefly, the 450 μm data from STUDIES, combined with archival data taken by Geach et al. (2013) and Casey et al. (2013), yields the deepest single-dish map currently available at 450 μm, reaching a 1-σ noise level of 0.65 mJy. This survey detects 256 sources with a signal-to-noise ratio (SNR) of SNR ≥ 4, of which 126 have SNR ≥ 5, in an area of 300 arcmin^2. The confusion-limited 850-μm map reaches an instrumental noise level of 0.10 mJy in the deepest regions and has an estimated confusion noise of 0.7 mJy (Lim et al., 2020). The 850-μm flux densities of the 450-μm-selected STUDIES sources were obtained from the 850-μm map at the 450-μm positions. The source is classed as detected at 850 μm if the flux density has SNR ≥ 5, otherwise it is treated as a limit.

In this section, we provide a brief description of the counterpart identification and multi-wavelength photometric data available for the sample from UV to radio wavelengths, which is used to model the SEDs of the sources. For a full description of the photometric data and counterpart identification for the STUDIES 450-μm sample, we refer to Lim et al. (2020).

4.2.1.1 Counterpart identification

The identification of optical counterparts for the STUDIES 450-μm sources is described in Lim et al. (2020). Briefly, the 450-μm sources were matched with the VLA-COSMOS 3-GHz catalogue (Smolčić et al., 2017) using a 4 arcsec search radius (set by the JCMT 450-μm beam) yielding ~ 1 per cent false positive rate

(based on the probability of false matches using the number densities of both catalogues). For the 450-μm sources above SNR ≥ 5 this yielded 89/126 counterparts (and 134/256 for SNR ≥ 4). These radio counterparts were cross matched with *Spitzer* IRAC catalogue (Sanders et al., 2007) using a 1 arcsec search radius and a ~ 3 per cent false positive rate. For the 450-μm sources that did not have 3-GHz radio counterparts, these were cross matched with the *Spitzer* MIPS 24-μm catalogue (Sanders et al., 2007) with a search radius of 4 arcsec resulting in 27/37 matches for 450-μm sources with SNR ≥ 5 (and 76/122 for SNR ≥ 4). These MIPS counterparts were in turn used to find IRAC counterparts within 2 arcsec with a ~ 2 per cent false positive rate. The detection rates in different ancillary bands is presented in Lim et al. (2020). The remaining ten SNR ≥ 5 450-μm sources with no radio or MIPS counterparts (and the 46 with SNR ≥ 4) were matched using a 1 arcsec matching radius to the catalogue of colour/radio-selected candidate submillimetre counterparts from An et al. (2019). This catalogue was constructed using a radio+machine-learning method applied to a training set comprising ALMA-identified 870-μm SMGs in the COSMOS and UDS fields with the goal of identifying multi-wavelength counterparts of S2COSMOS 850-μm single-dish detected sub-millimetre sources. This produced five identifications for the SNR ≥ 5 sources (and 15 at SNR ≥ 4).

For the SNR ≥ 5 450-μm sample this process yields reliable counterparts for 121/126 (96 per cent) of the sources, which declines to 207/256 (81 per cent) for those with SNR ≥ 4. As we wish to have a highly-complete and hence unbiased sample, in this chapter we analyse the SNR ≥ 5 450-μm sources, equivalent to $S_{450} \geq 3.25$ mJy, which have almost complete identifications. For this sample of 126 sources: 89 are located through radio counterparts, 27 are identified through MIPS counterparts and from the remaining ten sources, five have counterparts derived from the machine-learning method. In total 109 of the counterparts have IRAC detections. Although some studies have shown that mis-identifications are possible due to the large beam sizes ($\sim$15–20 arcsec FWHM) of single-dish telescopes at long wavelengths (e.g. Hodge et al., 2013), this is much less of an issue for the 450-μm

beam (7.9 arcsec FWHM) and is further reduced by the SNR ≥ 5 cut as the centroid position is more precise ($\lesssim 1$ arcsec).

For our sample, we find that, on average, the sources are detected in 19 bands (16–84th percentile range of $N_{\rm det} = 13$–22). The detection rate is 70/105 in B-band, 87/87 in z-band, 115/116 in H-band, 107/109 at 4.5 μm, 91/121 at 250 μm and 43/121 at 850 μm.

4.2.1.2 Far-infrared to radio observations

To constrain the SED of each galaxy at radio wavelengths we utilise 1.4-GHz and 3-GHz data from the Very Large Array (VLA)-COSMOS Large Project (Schinnerer et al., 2010; Smolčić et al., 2017). The 3-GHz survey has a noise of 2.3 μJy beam^{-1} and an angular resolution of 0.7 arcsec. The 1.4 GHz data is compiled in the COSMOS2015 catalogue (Laigle et al., 2016) and covers the entire COSMOS field with $\sigma = 12\,\mu$Jy beam^{-1} with an angular resolution of 2.5 arcsec.

At $z \simeq 2$, a source with a far-infrared SED with a characteristic temperature of $T_{\rm d} \sim 30$ K is expected to peak at an observed wavelength of $\sim 300\,\mu$m. Hence, to better constrain the shape of the far-infrared SEDs for the galaxies in our sample, and so improve the constraints on the far-infrared luminosities, we include observations with SPIRE and PACS on the *Herschel Space Observatory*. We specifically make use of the 100 and 160 μm PACS (Lutz et al., 2011), and 250 and 350 μm SPIRE observations taken as part of the *Herschel* Multi-tiered Extragalactic Survey (HerMES; Oliver et al. 2012). For the PACS 100- and 160-μm flux densities we adopt values from Lutz et al. (2011) (as listed in the the COSMOS2015 catalogue), who presented the observations of the 2 deg^2 COSMOS field which reach a 3-σ depth of 10.2 mJy at 160 μm.

Due to the coarse resolution of the SPIRE maps, ~ 18 arcsec and ~ 25 arcsec FWHM at 250 and 350 μm, we use the method described in Swinbank et al. (2014) to deblend these maps and obtain reliable flux densities for our catalogue. The deblending of the SPIRE maps used positional priors for sources based on the 3-

GHz and 24-μm (see below) catalogues, as well as machine-learning identified SMG counterparts from An et al. (2019) (see § 4.2.1.1). The observed flux density distribution is fitted with beam-sized components at the position of a given source in the prior catalogue using a Monte Carlo algorithm. The method is first applied to the 250-μm data, then to avoid "over-blending" only sources that are detected at > 2-σ at 250 μm are propagated to the prior list for the 350-μm deblending. The uncertainties on the flux densities (and limits) are found by attempting to recover model sources injected into the maps (see Swinbank et al. 2014 for details), and yield typical 3-σ detection limits of 7.0 and 8.0 mJy at 250 and 350 μm, respectively*.

4.2.1.3 Optical to near-/mid-infrared observations

To model the stellar SEDs of the counterparts to our 450-μm sources, we require the photometry in the optical/infrared bands. For the $u^*Bgrizy$ bands we adopt the photometry from COSMOS2015 (Laigle et al., 2016) catalogue. The u^*-band data is from the Canada-France-Hawaii Telescope (CFHT/MegaCam; Boulade et al., 2003) and covers the entire COSMOS field with a 5-σ depth of $u^* \simeq 26.5$ (Ilbert et al., 2009). The B-band imaging was taken with Subaru Suprime-Cam as part of COSMOS-20 survey (Taniguchi et al., 2007) and has a 5-σ depth of $B = 27.2$ in a 2 arcsec diameter aperture. Images in the $grizy$-bands are taken from the second data release (DR2) of the Hyper-SuprimeCam (HSC) Subaru Strategic Program (SSP; Aihara et al., 2019). The nominal 5-σ depths are $g = 27.3$, $r = 26.9$, $i = 26.7$, $z = 26.3$ and $y = 25.3$ in 2 arcsec diameter apertures.

In addition we employ $YJHK_{\rm s}$ imaging from the fourth data release (DR4) of the UltraVISTA survey (McCracken et al., 2012). In an equivalent manner to Simpson et al. (2020), we measure 2 arcsec diameter aperture photometry at the positions of each SMG in each band. The uncertainty on the derived flux densities is estimated in a 1×1 arcmin^2 region centred on the position of each SMG. Finally, we convert the derived flux densities to a total flux density by applying an aperture correction

*Comparison of our measurements to the deblended *Herschel* sources from Jin et al. (2018) showed agreement within the quoted errors with abs(S-$S_{\rm Jin+2018}$)/$S_{\rm err}$ of 1.25 and 1.15 at 250 μm and 350 μm, respectively.

of a factor of 1.80, 1.74, 1.52 and 1.46 for the $YJHK_{\rm s}$ bands, respectively. This is done by comparing the DR4 photometry to the UltraVISTA DR2 photometry from COSMOS2015, for those SMGs with a counterpart in the catalogue.

For the near-infrared photometry, we employ the *Spitzer* IRAC data from Sanders et al. (2007). IRAC 3.6-, 4.5-, 5.8- and 8.0-μm imaging was obtained as part of the S-COSMOS survey, which covers the entire COSMOS field and has an angular resolution of 1.7 arcsec at 3.6 μm. The 24-μm catalogue was generated by Lim et al. (2020), who used the S-COSMOS 24 μm image (Sanders et al., 2007). The catalogue has a 3.5-σ limit of 57 μJy.

We correct the u^*-band to IRAC 8.0-μm photometry of each source for Galactic extinction based on its sky position, the extinction maps of Schlafly & Finkbeiner (2011), and the extinction curve of Fitzpatrick (1999), assuming a reddening law with $R_V = 3.1$. For each filter, the correction is determined by convolving the filter response with the scaled extinction curve.

4.2.2 SED fitting model

To derive the physical properties of the STUDIES SMGs employ MAGPHYS+photo-z (da Cunha et al., 2015; Battisti et al., 2019) to model the SEDs from optical to radio wavelengths, using the available photometry in 24 bands. This is the same modelling code as in Chapter 2 and Chapter 3 and thus, provides a consistent methodology to that applied to the large ALMA-identified 850-μm SMG sample from the AS2UDS survey. Hence, the derived physical properties of the two samples can be investigated for any differences arising from the different wavelength selection. For the description, testing and calibration of the SED fitting code, see Chapter 2.

We note that the far-infrared SEDs of our SMGs are covered by at most six photometric bands (see Fig. 4.1), with weaker constraints near the peak of the SEDs, hence to provide a robust estimate of dust temperature, we adopt a conservative approach and fit a single modified blackbody to the available *Herschel* 100-, 160-, 250- and 350-μm photometry and the SCUBA-2 flux densities at 450 μm and

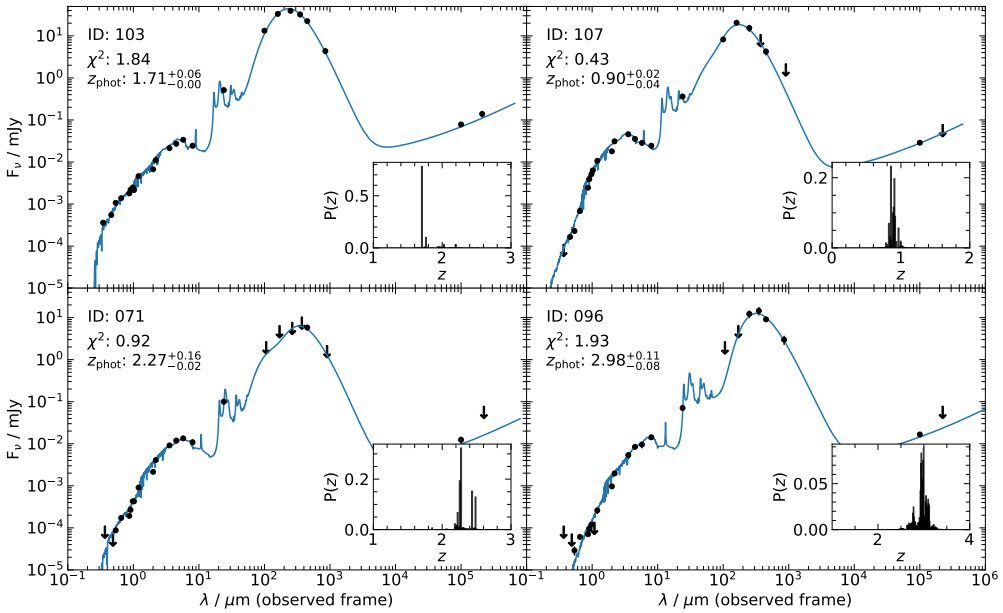

Figure 4.1: Example observed-frame optical-to-radio SEDs for four STUDIES sources selected across a wide redshift range. The solid lines show the SEDs at the peak redshift of the corresponding best-fitting model from MAGPHYS+photo-z. The arrows indicate 3σ upper limits in the photometric observations. We see that the SEDs are well constrained at these redshifts, since the 450-μm sample is, on average, detected in 19 bands, with a 16–84th percentile range of 13–22 bands.

850 μm, consistent with the methodology in Chapter 3. Thus, this approach allows for a simple comparison with similar fits to other 450-μm, 850-μm and ALMA samples. We estimate the characteristic dust temperature using a modified black body, in the same manner as in Chapter 3, using Eq. 3.1. We adopt the same value of $\beta = 1.8$, as used in Chapter 3, as well as previous SMG studies and consistent with that estimated for local star-forming galaxies (Planck Collaboration et al., 2011; Clemens et al., 2013; Smith et al., 2013). For the purpose of calculating canonical values, we adopt an optically thin prescription to describe the region from which the dust emission originates, thus Eq. 3.1 simplifies to Eq. 3.2. However, we stress that it is likely that the dust emission from the sources in our sample is not optically thin in the far-infrared, and $T_{\rm d}^{\rm MBB}$ and $M_{\rm d}$ (through strong dependence on $T_{\rm d}^{\rm MBB}$) are affected by the dust opacity assumptions. If we instead adopted a modified black body with an opacity term (Eq. 3.1), systematic offsets arise, with lower ν_0 leading to higher $T_{\rm d}^{\rm MBB}$ and thus $M_{\rm d}$ (see Casey et al., 2014).

We note that there is a systematic offset of $L_{\rm IR}^{\rm MBB}/L_{\rm IR} = 0.85$ between the far-

infrared luminosity calculated from a modified black body fit and MAGPHYS+photo-z fit, which includes the emission on the Wein side of the SED. Thus, we apply this factor to any subsequent modified black body luminosities (see § 4.3.3.1) to homogenise the two fitting methods. The systematic offset between the dust masses retrieved using these two different methods is $\lesssim$10 per cent, which is within the uncertainty of the MAGPHYS+photo-z dust mass values.

We run MAGPHYS+photo-z on the available photometry of our 121 SNR $\geq$ 5 450-μm sources to obtain the best-fitting model SEDs. To correct for calibration differences between our multiwavelength photometry and the stellar template libraries used in MAGPHYS+photo-z, we follow Feldmann et al. (2006) and iteratively determine the systematic offsets between the observed photometry and the predicted photometry from the best-fitting model SEDs. We estimate the median difference at each band for our whole sample and use these values to adjust the zero-points of the filters from the u^* band to IRAC 8.0 μm. The applied fractional offsets to the flux densities are: u^* ($-$0.165); B ($-$0.023); g (+0.019); r ($-$0.009); i (+0.062); z (+0.103); y ($-$0.041); Y ($-$0.024); J ($-$0.030); H (+0.036); $K_{\rm s}$ (+0.061); 3.6 μm ($-$0.037); 4.5 μm ($-$0.108); 5.8 μm ($-$0.135); 8.0 μm ($-$0.233). Given the absence of an AGN component in the MAGPHYS+photo-z modelling and the relative paucity of constraints at far-infrared and sub-millimetre wavelengths, we do not apply any offsets at wavelengths beyond 8 μm. We then re-run MAGPHYS+photo-z with the adjusted photometry to obtain the best-fitting SEDs, redshift and physical properties for the 450-μm sources. In case of limits in any given band, we adopt values of 0$\pm$3σ in the optical-to-8 μm and 1.5$\sigma\pm$1σ in the 8 μm-to-radio bands, consistent with the methodology applied for the 870μm SMGs in Chapter 3. Four examples of the 450μm-selected SMG SEDs are shown in Fig. 4.1. We observe that, on average, 450μm-selected SMGs are optically brighter than those selected at 850μm (see Fig. 2.7 in Chapter 2), and thus their optical/near-IR SEDs are better constrained, leading to lower uncertainties in the derived photometric redshift (discussed in § 4.3.2). All STUDIES SEDs can be found at MNRAS online.*

*https://doi.org/10.1093/mnras/staa3285

From our 450-μm sample, 32 sources have spectroscopic redshifts and we find a fractional offset of $\Delta z/(1+z_{\rm spec}) = -0.03 \pm 0.04$, with a 1-$\sigma$ range of -0.27–0.11, similar to the results obtained when testing the SED fitting code in Chapter 2. We also test for systematic differences between the MAGPHYS+photo-z redshifts determined in this work with those used by Lim et al. (2020). The latter comprises a mix of spectroscopic redshifts, photometric redshifts from Laigle et al. (2016) and cruder redshift estimates from fitting an SMG template SED. We determine a fractional redshift offset for the 450-μm SNR ≥ 5 sample of $(z_{\rm MAGPHYS} - z_{\rm Lim})/(1+z_{\rm MAGPHYS}) = -0.007 \pm 0.013$. We conclude that on average the redshifts derived here are consistent with previous estimates for this sample.

We note that, for consistency, we use the MAGPHYS+photo-z derived photometric redshifts for all sources in the analysis in this chapter. To test the effect of photometric redshift estimates on the predicted physical properties (which are presented in § 4.3.3) we run MAGPHYS+photo-z on the 32 450-μm sources at their fixed spectroscopic redshifts. We calculate the fractional difference $(X_{\rm spec} - X_{\rm phot})/X_{\rm phot}$, where X is a given physical parameter, between the physical parameter values derived at the spectroscopic and photometric redshifts. We find that the typical systematic offset for any given physical property (SFR, $L_{\rm FIR}$, M_*, $M_{\rm d}$, $A_{\rm V}$) is $\sim$10 per cent, which is within the typical uncertainties. Therefore, the redshift uncertainty effect on any given parameter is captured within its error range.

4.3 Analysis & Results

In this section, we investigate the broad photometric properties and the derived physical properties of the 450-μm sample based on our MAGPHYS+photo-z analysis of their SEDs. We compare the results of the 450-μm-selected sample to the 850-μm-selected sample, AS2UDS, which has been analysed in a consistent manner in Chapter 3 after fitting MAGPHYS+photo-z to the available photometry in 22 bands in Chapter 2. Throughout this chapter, we will refer to this as the 850-μm sample (we note that this ALMA selection formally corresponds to 870μm, which is the

wavelength used in the analysis).

4.3.1 Photometric properties of 450-μm sources

Before we discuss the physical properties of the STUDIES 450-μm SMGs in detail, we first investigate the observed and rest-frame optical and infrared colour properties of the sample. In this chapter, we compare the 450-μm-selected population to the AS2UDS 850-μm-selected sample, hence we start by comparing the features of the near- and far-infrared photometry of the two samples to assess their broad properties and where they fall in two commonly used photometric classifications. By assessing the best-fitting MAGPHYS+photo-z SEDs, we find that 14 per cent of 450-μm-selected SMGs are expected to be brighter than the UDS SCUBA-2 850-μm flux density limit of $S_{850} = 3.6$ mJy at 850 μm. Similarly, if we look at the 850-μm sources from AS2UDS, we find that 98 per cent are expected to be brighter than 3.25 mJy at 450 μm (the STUDIES limit). This suggests that the deep, but relatively narrow-field, STUDIES 450-μm survey is probing to lower dust masses than the shallower, wide-field AS2UDS 850-μm survey.

In Fig. 4.2, we show the distribution of $K_{\rm s}$-band magnitude versus 450-μm flux density for our 450-μm sources and the full 850-μm sample. For 850-μm sources, we show the predicted 450-μm flux density based on the model SED of each source. The two populations have comparable 450-μm flux densities, with the 850-μm sample having a slightly higher predicted median. The 450-μm sample has considerably brighter K_s-band magnitudes, with the median ($K_{\rm s} = 21.5\pm0.2$ mag) being comparable to the 16th percentile value ($K_{\rm s} = 21.52\pm0.06$ mag) of the 850-μm sample. We also note that 17 per cent of the 850-μm SMGs are undetected in the $K_{\rm s}$-band (see § 2.3 in Chapter 2), while the upper limit of $K_{\rm s}$-band non-detections in the 450-μm sample is $< 5/126$ (< 4 per cent), corresponding to only those sources lacking counterparts. The results indicate that the 450-μm population is potentially at lower redshift, has higher stellar masses and/or lower dust attenuation.

The rest-frame optical/near-infrared colours of galaxies have long been employed to classify high-redshift galaxy populations (e.g., Smail et al., 1993). These methods

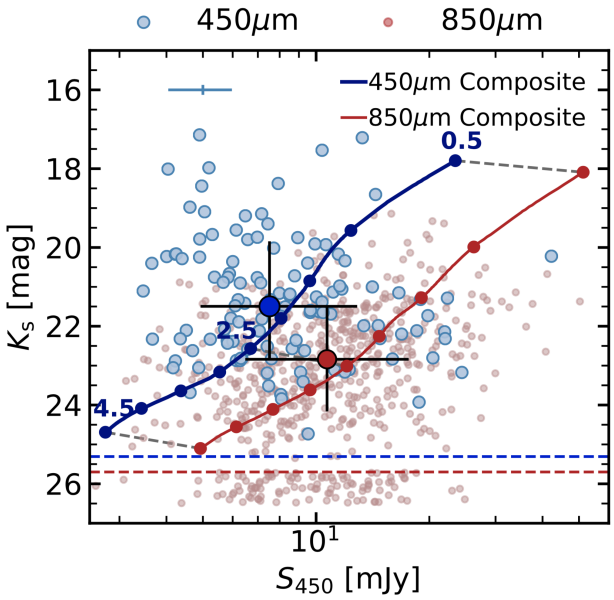

Figure 4.2: The distribution of K_s-band magnitude versus 450-μm flux density for our SNR ≥ 5.0 450-μm sample. For comparison, we also overlay the wide-field 850-μm SMG sample from Chapter 3, for which the 450-μm flux density is estimated from the MAGPHYS+photo-z best-fitting SEDs. We indicate the median for each sample as a large circle in the respective colour, with the 16–84th percentile range shown as the black error bar. 450-μm-selected sources cover a similar range in 450-μm flux density to the 850-μm population, but, on average, have brighter K_s-band magnitudes, likely reflecting their lower redshifts, higher stellar masses and/or lower dust attenuation. We overlay the tracks of the composite SEDs in $\Delta z = 0.5$ increments. The grey dashed lines show the difference in SEDs at the same redshift and indicates that both samples have similar K_s-band magnitudes at a given redshift, suggesting that redshift is the main driver of the differences in K_s-band brightness between the two samples. The limiting K_s-band magnitude for each sample is indicated as the dashed line in the respective colour. The median error on any individual source is shown in the top left in light blue.

primarily rely on contrasting the colour measured from a combination of photometric bands that span the Balmer/4000Å break in the galaxy rest-frame to the colour in a pair of bands at longer wavelengths, to attempt to differentiate between quiescent and star-forming SEDs. One frequently used combination of passbands is rest-frame UVJ, where redder rest-frame $(U-V)$ colours at similar rest-frame $(V-J)$ colours indicate more quiescent populations. We show the UVJ classification scheme from Whitaker et al. (2012) in Fig. 4.3a. We plot the rest-frame UVJ colours of the 450-μm and 850-μm populations using values from the MAGPHYS+photo-z best-fitting SED of each source and, to ensure that there are meaningful constraints on the shape of the SEDs, we require that the sources are

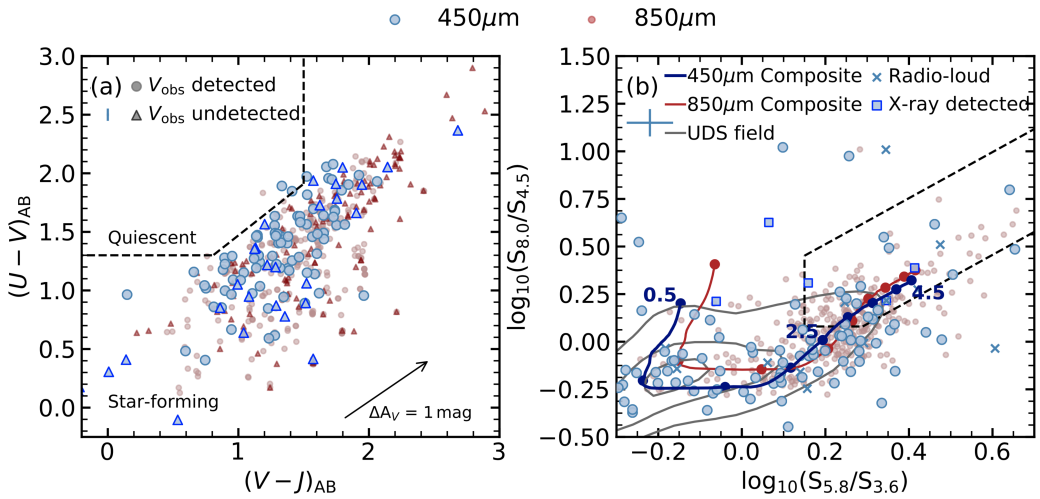

Figure 4.3: Photometric trends for the 450μm sample compared to 850μm-selected sources. **(a)** Rest-frame $(U-V)$ versus $(V-J)$ colour-colour diagram for 450-μm- and 850-μm-selected sources detected in the observed-frame J and 4.5-μm bands. We indicate those detected (circles) and undetected (triangles) in the observed V-band. We overlay the selection criteria for star-forming galaxies from Whitaker et al. (2012). We observe that the bulk of the STUDIES and AS2UDS sources have colours consistent with them being star forming, but potentially $\sim$5 per cent have colours or limits which could place them in the "Quiescent" classification even though they are likely to be strongly star forming. The rest-frame values were obtained from the MAGPHYS+photo-z best-fit SEDs. The error due to redshift uncertainty on each source is shown at the top left. The reddening vector for one magnitude of extinction in the V-band is shown in the bottom right of the panel. **(b)** IRAC colour-colour diagram for the 450-μm sources. We indicate radio-loud sources and those with an X-ray-detected counterpart as identified by Lim et al. (2020). The dashed lines indicate the IRAC selection criteria for AGN at $z \leq 2.5$ from Donley et al. (2012). For comparison, we overlay the AS2UDS sources with $z \leq 3$ and the tracks of the composite SED of 850-μm AS2UDS SMGs and 450-μm STUDIES SMGs at $z = 0.5$–4.5 redshifts in $\Delta z = 0.5$ increments. We also overlay a contour of the density of K-band selected UDS field galaxies, which shows that both SMG samples have redder IRAC colours than the field population. 850-μm sources have colours which cluster in a region that matches their redshifted template at $z \sim 1.5$–4 and are typically redder than the 450-μm selected population which have colours consistent with their template in a broad range at $z \sim 1$–3.

detected in the observed J and 4.5 μm bands (roughly corresponding to rest-frame V and J at the typical redshifts). We observe that the bulk of the 450-μm and 850-μm populations have UVJ colours consistent with them being star-forming sources and that both populations show a spread which is aligned with the reddening vector. As shown in Fig. 4.3a, around 5 per cent of the 450-μm sources have limits (and two sources have colours, although these lie near the classification boundaries) which could place them in the "quiescent" classification even though they are likely to be strongly star forming. We note that red ($U - V$) and blue ($V - J$) rest-frame colours can be mimicked by dusty star-forming galaxies at high redshift (Chen et al., 2016).

At $z \gtrsim 1$–2 the rest-frame H-band, which samples the stellar "bump" at 1.6 μm due to the H^- opacity minimum, is redshifted into the IRAC bands at $\gtrsim 3.6\,\mu$m. Thus, IRAC colours, indicating a peak at these wavelengths, can crudely indicate the redshift of a source (Sawicki, 2002) and can be used to distinguish between star-forming galaxies and AGN, which have power-law emission in the mid-infrared. Across the 450-μm sample there are 100/109 SMGs with detections in all four IRAC bands, which are shown in Fig. 4.3b. We consider the Donley et al. (2012) selection criteria, which is used to identify AGN at $z \lesssim 2.5$. There are 19/109 (17 per cent) sources with colours suggesting power-law spectra (7 at $z < 2.5$) and thus are consistent with the presence of an AGN, with four radio-loud sources (from Lim et al. 2020, who applied a redshift-dependent threshold in radio excess) and three detected in the X-rays (see Lim et al. 2020). We overlay the track of the composite SED of the 450-μm sample (further discussed in §4.3.3) as a function of redshift, which demonstrates that IRAC-colours indicative of AGN are degenerate with those expected for dusty star-forming galaxies at $z \gtrsim 2$–3 (see also § 2.3.2 in Chapter 2), where many members of this population lie. This is simply a result of the fact that above $z \sim 3$ the 1.6-μm stellar bump moves into the reddest IRAC band at 8.0 μm and thus the IRAC colours of dusty star-forming SMGs mimic an AGN-like power-law behaviour (e.g. Wang et al., 2010), and hence this colour selection cannot reliably classify these high-redshift sources.

For comparison to the 450-μm population, we also show in Fig. 4.3b the IRAC colours of 850-μm sources with $z \leq 3$, as well as the track of the 850-μm AS2UDS composite SED as a function of redshift. We note that the composite SED of the 450-μm sample has bluer IRAC colours at $z \lesssim 2$ compared to the 850-μm composite (see also § 4.3.3.2). However, at $z \gtrsim 2.5$ the colours of both populations are comparable. The 450-μm population clusters around its composite SED track at colours corresponding to $z \sim 1$–3, while the 850-μm population shows a distribution with colours matching the corresponding composite SED at $z \sim 1.5$–4. We stress that both 450-μm and 850-μm-selected populations have much redder IRAC colours, on average, than the K-selected field population (UKIDSS UDS; Almaini et al. in prep.), likely as a result of their higher dust attenuation and typically higher redshifts.

4.3.2 Redshift distribution

The redshift distribution is a fundamental quantity providing constraints on formation models for the given population and is also essential for reliable derivation of their intrinsic properties and evolutionary trends. To derive a photometric redshift distribution reflecting the uncertainties in any individual SED fit (and hence the quality of the fitting), we stack the individual redshift likelihood distributions from our MAGPHYS+photo-z analysis for all of the 450-μm SMGs and show this in Fig. 4.4a. For the full sample of 121 (SNR ≥ 5) 450-μm SMGs, we measure a median redshift of $z = 1.85 \pm 0.14$. The quoted uncertainty is the combination of the systematic uncertainty from the comparison of MAGPHYS+photo-z redshifts to spectroscopic redshifts of 6,719 K-band galaxies in the UDS (see § 2.4 in Chapter 2) and the bootstrap error on the stacked redshift distribution. The SNR ≥ 5 450-μm SMG population, which is brighter than $S_{450} \geq 3.25$ mJy, shows a peaked but broad redshift distribution with a 16–84th percentile redshift range of $z = 1.0$–2.7 and only 9 per cent of sources lying at $z \geq 3$ (Fig. 4.4a).

Our median redshift is comparable to that derived for a sample of 64 450-μm-selected galaxies, with $S_{450} \gtrsim 3.6$ mJy, from the S2CLS Extended Groth Strip field

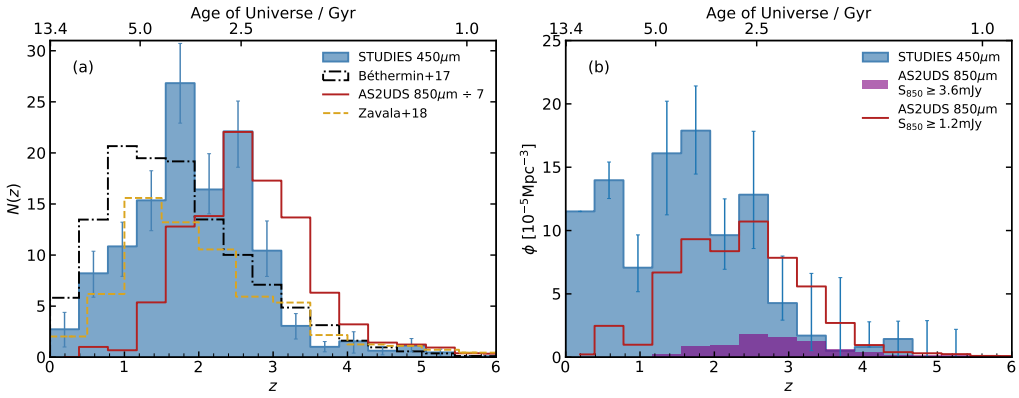

Figure 4.4: **(a)** Stacked likelihood redshift distribution for the 121 sources selected at 450 μm with a median redshift of $z = 1.85 \pm 0.14$ and 9 per cent of the sample at lying at $z \geq 3$. For comparison, we overlay the stacked likelihood distribution of 65 450-μm detected sources from Zavala et al. (2018) (with a similar median redshift), and the $\sim$700 850-μm selected SMGs from the AS2UDS survey (scaled down in normalisation by a factor of seven) with a median redshift of $z = 2.61 \pm 0.08$. We also show the prediction from the galaxy evolution model by Béthermin et al. (2017) with $S_{450} > 3.25$ mJy, normalised to the number of sources in our 450-μm sample, which peaks at lower redshift than our sample. The 450-μm sources peaks at lower redshifts than 850-μm sources, which can be explained by the luminosity function and luminosity-redshift relation for these selections. The errors shown on the 450-μm histogram are estimated from the bootstrap resampling of the redshift likelihood distributions. **(b)** Variation in the space density of our 450-μm-selected population with redshift, showing that the space density of 450-μm-selected sources decreases with increasing redshift. For comparison, we overlay the redshift distribution for a bright $S_{850} \geq 3.6$ mJy (limit of the parent S2CLS survey) subset of the 850-μm sample after correcting for the modest incompleteness above this flux density limit. We also overlay a subset of 850-μm SMGs with $S_{850} \gtrsim 1.2$ mJy (850-μm population with more comparable far-infrared luminosities to our 450-μm sample), where the number density has been corrected for incompleteness in the 850-μm sample below $S_{850} \sim 4$ mJy. For this subset, we see that the 450-μm-selected sources have a similar space density to an 850-μm population with a comparable far-infrared luminosity at $z \sim 2$–3.

by Zavala et al. (2018), who found a median redshift of $z = 1.66 \pm 0.18$, which is within $1.5\,\sigma$ of our result (before considering excess variance). Similarly, the 450-μm SCUBA-2 survey of 78 SMGs above a flux density $S_{450} \simeq 15\,\mathrm{mJy}$ ($3.6\,\sigma$ significance) in the COSMOS field by Casey et al. (2013) yielded a median redshift of $z = 1.95 \pm 0.19$, also agreeing with our result.

One of the aims of this chapter is to study the relationship between the 450-μm and 850-μm selected populations, thus we investigate how the selection wavelength affects the redshift distribution at our observed depths. The 850-μm sample from AS2UDS has a median redshift of $z = 2.61 \pm 0.08$, with a 16–84th percentile range of $z = 1.8$–3.4 (see Fig. 4.4a). We note that the subset with $S_{850} \geq 3.6\,\mathrm{mJy}$ (the completeness limit of the SCUBA-2 parent survey) has a very similar shape with a slightly higher median redshift of $z = 2.78 \pm 0.09$. The median redshifts of the 850-μm and 450-μm samples are different at $\sim 5.5\,\sigma$ significance. We also compare the distributions using a two sample Kolmogorov-Smirnov (K-S) test and find a probability of $P = 2 \times 10^{-13}$, indicating that the two distributions are significantly different. This result is contrary to the findings of Casey et al. (2013), who suggest that the 450-μm and 850-μm populations occupy a similar redshift range at these flux density limits. The disagreement is due to their 850-μm sample having a considerably lower median redshift of $z = 2.16 \pm 0.11$, most likely a result of incompleteness in their identifications compared to the ALMA-located AS2UDS survey.

In Fig. 4.4a, we also compare to a simple model of galaxy evolution based on the observed evolution of the stellar mass function, the main-sequence of star-forming galaxies, and the SEDs by Béthermin et al. (2017), who address the selection effects on the redshift distribution (we discuss this further in § 4.3.3.1). Their predicted distribution is roughly similar to that of the 450-μm population, but with a lower median redshift of $z = 1.58 \pm 0.01$ for $S_{450} > 3.25\,\mathrm{mJy}$ sources. This 2-σ difference suggests that the luminosity function evolution might have to be stronger than that adopted in their model, in order to produce more sources at higher redshift and thus match the observed 450-μm redshift distribution.

To compare the 450 and 850 μm selections in more detail, we take advantage of our well-defined and effectively almost complete redshift distribution to investigate the space density of the 450-μm-selected population. We highlight that STUDIES 450-μm survey area of $\sim 300\,\mathrm{arcmin}^2$ is ~ 10 times smaller than the AS2UDS 850-μm survey area of $\sim 3200\,\mathrm{arcmin}^2$. Since the depth of the 450-μm map varies due to the map coverage, each source has a different effective survey area. Thus, we estimate the survey area for each of the sources by calculating the area in the SCUBA-2 map within which each SMG would be detectable at $\mathrm{SNR} \gtrsim 5$, given their 450-μm flux density, using the 450-μm RMS map from Lim et al. (2020). The space density is then calculated in redshift bins using the median redshift estimates of each of the SMGs. We estimate the uncertainties by resampling the redshift probability distribution of each source 500 times. The corresponding space density as a function of redshift is shown in Fig. 4.4b. There is a decrease in space density for the 450-μm-selected population with increasing redshift, which is particularly marked above $z \gtrsim 2.5$.

For comparison, we calculate the space density evolution for the 850-μm sample with $S_{850} \geq 3.6\,\mathrm{mJy}$. This is the flux density limit of the AS2UDS's parent survey: the UDS field of S2CLS (Geach et al., 2017) that covers an area of $0.96\,\mathrm{deg}^2$ (see Stach et al., 2019). This flux limit corresponds to $L_{\mathrm{FIR}} \gtrsim 2 \times 10^{12}\,\mathrm{L}_{\odot}$ (meaning these sources are all ULIRGs) for typical dust temperatures, compared to $L_{\mathrm{FIR}} \gtrsim 0.5\text{–}1 \times 10^{12}\,\mathrm{L}_{\odot}$ for our 450-μm sample, corresponding to the bright-end of the LIRG population. We correct for incompleteness down to $S_{850} = 3.6\,\mathrm{mJy}$ in the parent SCUBA-2 850-μm sample (used as the basis for the AS2UDS study) in the UDS field following Geach et al. (2017). As seen in Fig. 4.4b, the space density for the $S_{850} \geq 3.6\,\mathrm{mJy}$ subset of the AS2UDS SMGs is significantly lower than the 450-μm population, however, this is primarily due to the different flux density and luminosity limits of the two studies. To better compare the two populations, we calculate the median S_{450}/S_{850} ratio using the composite 450-μm SED (further discussed in § 4.3.3) and find that an average 450-μm source at $z \sim 2.5$ is expected to have an 850-μm flux density of $S_{850} \sim 1.2\,\mathrm{mJy}$. Thus, we select all of the 850-μm

SMGs in AS2UDS above this flux density limit and correct for the survey completeness assuming the count slope from the ALMA 1.13-mm number counts in the GOODS-S field from Hatsukade et al. (2018). The corresponding space density for the complete $S_{850} \geq 1.2\,\mathrm{mJy}$ AS2UDS sample is shown in Fig. 4.4b. The 450-μm population has on average ~ 14 times (at 12-σ significance) higher space density up to a redshift of $z \sim 2$, but a similar space density at $z \sim 2$–3 as the $S_{850} \geq 1.2\,\mathrm{mJy}$ 850-μm population. We test whether the two distributions are significantly different by using a χ^2 test to compare the space density values in each bin including the errors. The resulting $\chi^2_{\mathrm{red}} = 10$ indicates that the two distributions are significantly different. This suggests that 450-μm-detectable LIRGs are the main obscured population at $z \sim 1$–2, while ULIRGs (which make up the samples selected at 850-μm at the flux limits probed here) dominate at higher redshifts (see § 4.3.3.1). We further discuss the physical properties of both population at $z \sim 2$–3, where the space density is comparable, in § 4.3.3.2.

4.3.3 Physical properties of 450-μm sources

In this section, we analyse the derived physical properties from MAGPHYS+photo-z of the 121 SMGs selected at 450 μm and their variations with redshift, and compare and contrast these with the equivalent properties of the 850-μm population.

4.3.3.1 Far-infrared properties

As the majority of the emission from these dusty systems is coming from the far-infrared, we begin by investigating the dust properties of the SMGs by deriving their far-infrared luminosities. The median far-infrared luminosity of the 450-μm sample is $L_{\mathrm{IR}} = (1.5 \pm 0.2) \times 10^{12}\,\mathrm{L}_{\odot}$, with a 16–84th percentile range of $L_{\mathrm{IR}} = (0.7\text{–}4.7) \times 10^{12}\,\mathrm{L}_{\odot}$. In comparison, the AS2UDS 850-μm sample has a median far-infrared luminosity of $(2.88 \pm 0.09) \times 10^{12}\,\mathrm{L}_{\odot}$. The 850-$\mu$m SMGs have significantly higher far-infrared luminosities than the 450-μm SMGs primarily due to their brigher effective flux limit.

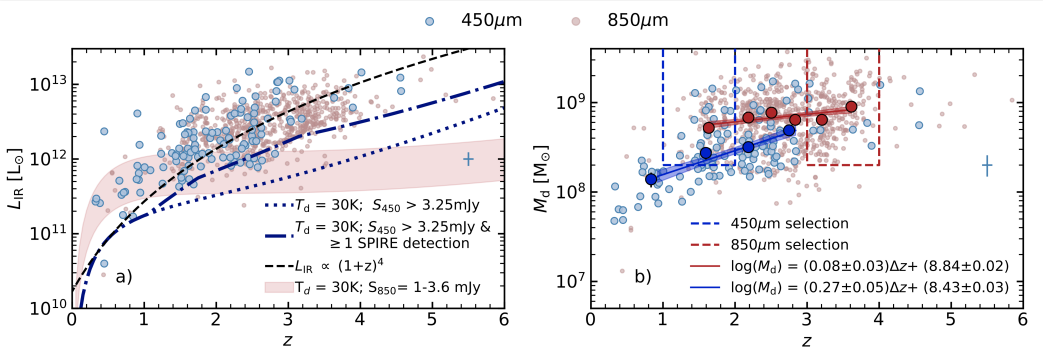

Figure 4.5: The evolution of the dust properties of the 450-μm population with redshift. **a)** Far-infrared luminosity ($L_{\rm IR}$) evolution. The black dashed line shows the luminosity evolution according to $L_{\rm IR} \propto (1+z)^4$. The blue dotted line denotes the selection function of an $S_{450} \gtrsim 3.25$ mJy SMG from a modified black body dust SED with $T_{\rm d} = 30$K (median characteristic dust temperature of the sample). The blue dot-dashed line shows the selection for $S_{450} \gtrsim 3.25$ mJy, including the requirement that the dust SED includes at least one detection above the flux limits of the available SPIRE observations at 250 or 350 μm. The shaded region shows the expected limit for the 850-μm sample from a modified black body dust SED with $S_{850} = 1$–3.6 mJy and $T_{\rm d} = 30$K. We see that the populations and their variations with redshift can be roughly described by these selection bounds. **b)** Dust mass evolution. The large circles show the binned median in bins with equal numbers of sources, the solid line shows the best-fit line around the median redshift (where $\Delta z = z - z_{\rm med}$, $z_{\rm med} = 1.85$ and $z_{\rm med} = 2.61$ for the 450-μm and 850-μm samples, respectively) to the binned data and the shaded regions show the associated uncertainty. The 850-μm sample and median values are similarly shown in red. No evolution with redshift is seen in the AS2UDS sample due to negative k-correction since the source selection is in the Rayleigh-Jeans tail of the SED at the relevant redshifts, which is dominated by the cold dust. There is evolution in the 450-μm sample with redshift, with sources at $z \lesssim 1.5$ having lower dust mass due to the k-correction at 450 μm. To select a uniform population for assessing evolution we construct a rest-frame matched subset with $M_d \geq 2 \times 10^8$ M$_\odot$ over $z = 1$–2 for 450 μm over $z = 3$–4 for the 850-μm sample. This comparison is discussed in § 4.4.

In Fig. 4.5a, we plot the luminosity evolution with redshift for both 450- and 850-μm samples. To consider the influence of sample selection at 450-μm, we also overlay the predicted far-infrared luminosity of a source with a dust SED modelled by a modified black body with a temperature of $T_{\rm d} = 30$ K (the median for this sample) and a 450-μm flux density of $S_{450} = 3.25$ mJy, which is the 5-σ limit of our 450-μm sample. We overlay a selection function for the same $T_{\rm d} = 30$ K model with the additional constraint that the SED must be detected in at least one SPIRE band at 250 or 350 μm. We see that this selection results in an increasing far-infrared luminosity limit at $z \gtrsim 1$ for the 450-μm sample. The trends of far-

infrared luminosity with redshift in our survey can be explained by the flux limit of the sample selection. We also indicate the expected completeness limit for the 850-μm sample in Fig. 4.5a. The limit of the parent SCUBA-2 850-μm survey is 3.6 mJy; however deeper ALMA follow-up observations detect sources down to $S_{870} \sim 1$ mJy, hence the true sample limit is somewhere in-between these values. Due to the negative k-correction (see § 3.1 in Chapter 3), we see little variation in the far-infrared luminosity limit with redshift for the 850-μm selection (see Casey et al., 2014, for presentation of k-correction effects in different bands).

The selection trends in Fig. 4.5a, together with the evolution of the far-infrared luminosity function, explains the lower redshift distribution of the 450-μm sources in comparison to 850-μm selected sources (e.g. Béthermin et al., 2015). As shown in Fig. 4.5a, due to the k-correction, the luminosity limit for a given 450-μm flux density increases quickly with redshift, meaning that the far-infrared luminosity limit is ~ 3 times higher at $z \sim 3$ than at $z \sim 1$. Combined with the steep decrease in the number of sources at the high luminosity end of the luminosity function at low redshifts, this means that the sources at 450-μm are detected at lower redshifts than the 850-μm population. Due to stronger negative k-correction at 850-μm, the luminosity limit for 850-μm sources with $\mathrm{S}_{850} \geq 3.6$ mJy is nearly constant across $z = 1$–6. Similarly, the luminosity limit for 850-μm sources with $\mathrm{S}_{850} \geq 3.6$ mJy, though nearly constant across $z = 1$–6, is higher than the 450-μm limit at $z \leq 1.5$, explaining the lack of sources detected at lower redshift at 850 μm. The different density evolution seen in Fig. 4.4b, together with the far-infrared luminosity trends in Fig. 4.5a, reflect that luminous infrared galaxies (LIRGs; $L_{\mathrm{IR}} \simeq 10^{11-12}\,\mathrm{L}_{\odot}$) are the main obscured population at $z \sim 1$–2, while ultra-luminous infrared galaxies (ULIRGs; $L_{\mathrm{IR}} \simeq 10^{12-13}\,\mathrm{L}_{\odot}$) are more dominant at higher redshifts (Magnelli et al., 2013; Casey et al., 2014).

As both surveys are sampled past the peak of the far-infrared SED in the Rayleigh-Jeans tail at the redshifts of interest, we examine the dust masses of the 450-μm SMGs in comparison to the 850-μm sample to compare the selection effects on the dust mass distributions. The median dust mass for the 450-μm sample is

$M_{\rm d} = (3.6 \pm 0.2) \times 10^8\,{\rm M}_\odot$ with a 16–84th percentile range of $M_{\rm d} = (2.1\text{–}8.2) \times 10^8\,{\rm M}_\odot$. For comparison, the 850-μm sample from Chapter 3 has a significantly higher median dust mass (due to its brighter effective flux limit) of $M_{\rm d} = (6.8 \pm 0.3) \times 10^8\,{\rm M}_\odot$. The dust mass evolution with redshift is shown in Fig. 4.5b. A positive trend of dust mass with redshift is observed for the 450-μm sample, but there is no significant trend for the 850-μm sources. In agreement with the photometric properties of the samples (see § 4.3.1 and Fig 4.2 and 4.3), our dust mass results in Fig. 4.5b, suggest that 450-μm selection is sensitive to lower dust mass sources at lower redshifts. From the dust mass and far-infrared luminosity results in Fig. 4.5, it is clear that selection at 850-μm results in a selection that primarily traces cold dust mass; however this is less true for the 450-μm sample where selection is closer to the peak of the dust SED and thus is more affected by the far-infrared luminosity at $z \gtrsim 2$ (see Ikarashi et al., in prep.).

We now investigate the characteristic dust temperatures derived, for simplicity, from optically-thin modified black body fits, which correspond to the peak of the far-infrared emission. For the 450-μm sample, this method provides a median characteristic temperature of $T_{\rm d}^{\rm MBB} = 33 \pm 1\,{\rm K}$ with a positive evolution of the characteristic dust temperature with redshift seen in Fig. 4.6a. However, we stress that this trend is driven by the increase of luminosity with redshift as a result of selection effects (see Fig. 4.5a), which indeed is found in Lim et al. (2020). We note that Zavala et al. (2018) found a mean dust temperature of $T_{\rm d}^{\rm MBB} = 47 \pm 15\,{\rm K}$. The discrepancy is mostly due to the fitting method as Zavala et al. (2018) adopted $\beta = 1.6$ and assumed the emission becomes optically thin at $\lambda \geq 100\,\mu{\rm m}$, which results in $\sim$20 per cent higher characteristic dust temperature values. Finally, for comparison to the 450-μm SMGs, we overlay a subset of 475 (out of 707) of the 850-μm SMGs that have at least one SPIRE detection (to ensure more reliable temperature measurements). This 850-μm subset has a similar trend, with a comparable gradient and a median characteristic dust temperature of $T_{\rm d}^{\rm MBB} = 30.4 \pm 0.3\,{\rm K}$. At a fixed redshift, the 450-μm population appears to be $\Delta T_{\rm d}^{\rm MBB} = 6.0 \pm 1.5\,{\rm K}$ hotter than the 850-μm sample (Fig. 4.6a), or their dust emission becomes optically thick

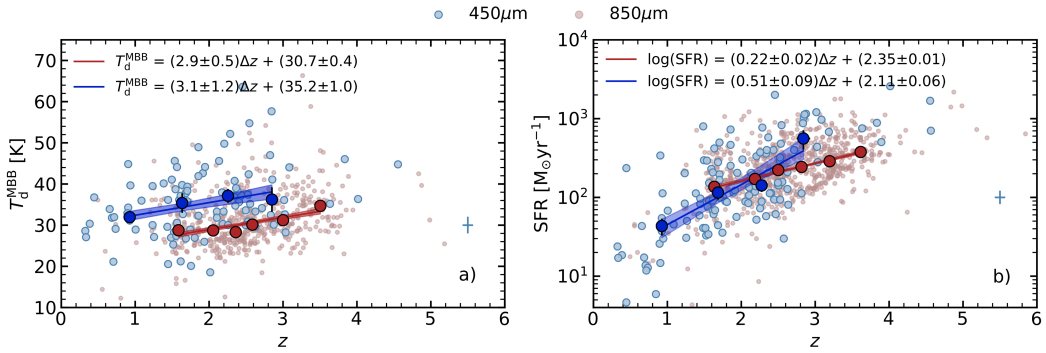

Figure 4.6: The evolution of the dust properties of the 450-μm (in blue) population with redshift. The large circles show the binned median in bins with equal numbers of sources, the solid line shows the best-fit line around the median redshift (where $\Delta z = z - z_{\rm med}$, $z_{\rm med} = 1.85$ and $z_{\rm med} = 2.61$ for the 450-μm and 850-μm samples, respectively) to the binned data and the shaded regions show the associated uncertainty. The 850-μm sample and median values are similarly shown in red. **a)** Dust temperature from the modified black body fits for sources with at least one detection in the SPIRE bands. A positive trend with redshift is seen in both 450-μm and 850-μm samples. The 450-μm sample has a systematically higher characteristic dust temperature than the 850-μm sample. **b)** Star-formation rate evolution. A $\sim$5-σ trend is observed for the 450-μm sample, similar to the trend seen in the 850-μm sample. However, this is mainly due to the selection limit in far-infrared luminosity with redshift (see Fig 4.5a).

at shorter restframe wavelengths.

Finally, we investigate the star-formation rate, as it is best constrained in the far-infrared regime since the optical wavelengths in SMGs are heavily obscured. The current star-formation rate returned by MAGPHYS+photo-z is defined as the average star-formation history over the last 100 Myr. For the 450-μm sample we derive a median star-formation rate of SFR $= 127 \pm 20\,{\rm M}_\odot\,{\rm yr}^{-1}$ with a 16–84th percentile range of SFR $= 40$–$500\,{\rm M}_\odot\,{\rm yr}^{-1}$. Zavala et al. (2018) suggest a similar star-formation rate (derived from $L_{\rm IR}$) of SFR $= 150 \pm 20\,{\rm M}_\odot\,{\rm yr}^{-1}$, in agreement with our study. Comparison of the 450-μm sources to the 850-μm sample shows that the latter has a median star-formation rate that is significantly higher, SFR $= 290 \pm 14\,{\rm M}_\odot\,{\rm yr}^{-1}$, as a result of the brighter effective flux density limit. However, the two distributions overlap as the 850-μm sample has a 16–84th percentile range of SFR $= 120$–$580\,{\rm M}_\odot\,{\rm yr}^{-1}$. For the 450-$\mu$m SMGs we observe a significant ($5\,\sigma$) variation of SFR with redshift (see Fig. 4.6b), which is driven by the variation in the far-infrared luminosity limit of the sample with redshift. The same

trend is observed in the 850-μm sample, and in Fig. 4.6b we show that the SFRs of the two populations overlap at $z \simeq 1.5$–2.5. This indicates that the apparently lower median star-formation rate of the 450-μm sample is primarily due to the selection being weighted towards less active sources at lower redshifts.

The best linear fits to the binned values in Figs. 4.5 and 4.6 indicate possible differences in the dust properties of the two populations, thus we use a K-S statistic to determine whether these results are significant. We select all sources at $z = 1.5$–2.7, to maximise the overlap between the two samples and exclude any evolutionary trends with redshift. The results indicate that the two samples have significantly different far-infrared luminosity ($P = 0.002$), dust mass ($P = 3 \times 10^{-13}$), dust temperature ($P = 2 \times 10^{-9}$), and star-formation rate ($P = 0.008$) distributions.

4.3.3.2 Optical/near-infrared properties

The rest-frame UV/optical/near-infrared features in the SED are dominated by the stellar emission, thus physical properties such as stellar mass and dust attenuation can be inferred. To search for differences in the SED shapes, which also reflect differences in the selection, we stack the rest-frame SEDs of each galaxy that are shown in Fig. 4.7a. The SEDs are normalised by their far-infrared luminosity to the median of the sample, $L_{\rm IR} = 1.6 \times 10^{12}\,{\rm L}_{\odot}$, and a composite SED of the whole population is derived by measuring a median value at each wavelength. Fig. 4.7a highlights the difficulty of constructing complete samples of strongly star-forming galaxies based on UV/optical observations, as the variation in the SEDs span more than an order of magnitude at restframe wavelengths of $\lambda \lesssim 2\,\mu$m (see also D20). The resulting composite 450-μm SED, together with the equivalent median composite SED of the 850-μm sources, normalised to $L_{\rm IR} = 2.88 \times 10^{12}\,{\rm L}_{\odot}$ (the median of the sample, see § 3.4.1 in Chapter 3), are shown in Fig. 4.7b. The error on the median SED is estimated by bootstrap resampling the individual SEDs to form multiple median SEDs and taking the 16th and 84th percentile values at each wavelength. The shape of the optical SEDs suggest that 450-μm sources are brighter at $\lambda \lesssim 2\,\mu$m than the 850-μm population and indeed, we see in Fig. 4.2 that the 450-μm sample

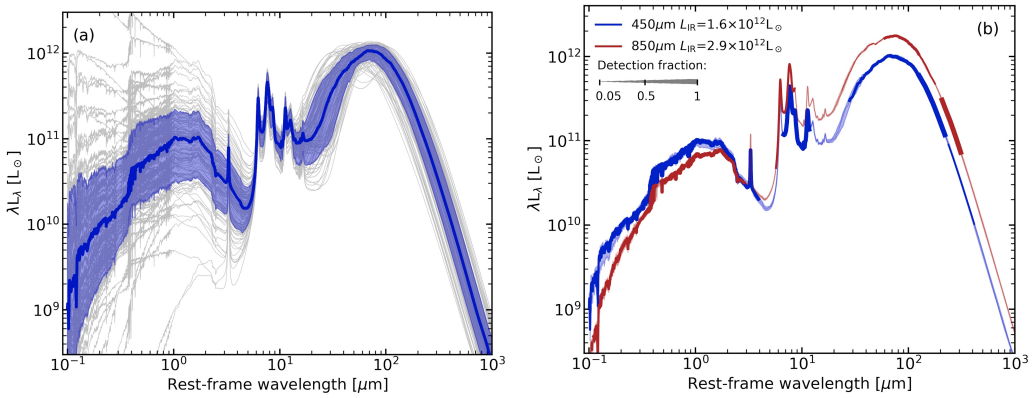

Figure 4.7: **(a)** Best-fitting SEDs of all 121 STUDIES SMGs normalised to the median far-infrared luminosity of the sample, $L_{\rm IR} = 1.6 \times 10^{12}\,{\rm L}_\odot$. We also overlay the median composite SED and indicate the 16–84th percentile region as the shaded area. We observe that the 450-μm SMGs display a wide variety of optical luminosities and colours spanning an order of magnitude at rest-frame K-band and around twice that at shorter wavelengths highlighting the difficulty to produce complete samples of highly star-forming galaxies using UV/optical observations alone. **(b)** Median composite SED derived from the best-fit rest-frame SEDs of all 121 STUDIES sources, normalised to the median far-infrared luminosity of the sample. For comparison, we overlay the composite SED of the 850-μm selected SMGs from the AS2UDS survey, normalised to their median far-infrared luminosity, $L_{\rm IR} = 2.88 \times 10^{12}\,{\rm L}_\odot$. We highlight the reliability of the sections of the SED of each sample with lines of varying thickness corresponding to the detection fraction ($N_{\rm det}/N_{\rm sample}$) in each band. Selection at $z \sim 1.5$ results in sources that are brighter in the rest-frame optical/near-infrared, likely due to higher stellar masses and/or lower dust attenuation. Bootstrap errors are shown as the shaded regions.

has a brighter median observed K-band magnitude by 1.3 ± 0.2 mag. This suggests the latter population either has higher stellar masses, lower dust attenuation, and/or younger ages.* In the far-infrared, the SEDs, where well constrained, have a similar overall shape, peaking (in λL_λ) at similar wavelengths, $\lambda_{\rm rest} \sim 80\,\mu$m. As the composite SEDs suggest differences in the physical properties inferred from the optical emission, we next examine whether this is mainly driven by the differences in the stellar masses and/or the dust attenuation of the two populations.

First, we compare the stellar mass of the two samples. The 450-μm SMGs have a median stellar mass of $M_* = (1.07 \pm 0.12) \times 10^{11}\,{\rm M}_\odot$ with a 16–84th percentile range of $(0.4\text{–}2.3) \times 10^{11}\,{\rm M}_\odot$. In comparison, Zavala et al. (2018) find a mean

*We note, however, that the median sSFR for 850-μm sources (D20) is ~ 0.2 dex higher than that for 450-μm sources (Lim et al., 2020) studied here, suggesting that age is not the main driver of the differences seen in the SEDs.

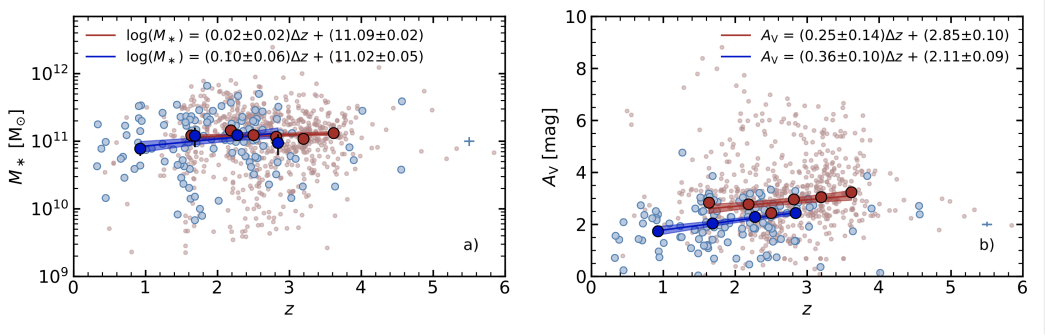

Figure 4.8: The evolution of the optical properties of the 450-μm (in blue) population with redshift. Large circles show the binned median in bins with equal numbers of sources, the solid line shows the best-fit line around the median redshift (where $\Delta z = z - z_{\rm med}$, $z_{\rm med} = 1.85$ and $z_{\rm med} = 2.61$ for the 450-μm and 850-μm samples, respectively) to the binned data and the shaded regions show the associated uncertainty. The 850-μm sample and median values are similarly shown in red. **a)** Stellar mass evolution. Both samples have comparable stellar masses over all redshift ranges and no significant evolution with redshift is seen in either. **b)** V-band dust attenuation evolution. Only weak evolution is seen in both 450-μm and 850-μm samples, with the 850-μm sample having a systematically higher dust attenuation at all redshifts.

stellar mass of $M_* = (0.99 \pm 0.06) \times 10^{11}\,{\rm M}_\odot$, which is within $\sim 1\,\sigma$. We see no evolution of stellar mass with redshift, in agreement with the results for the 850-μm population in the AS2UDS study, as shown in Fig. 4.8a. The median stellar mass of the 850-μm sample is $M_* = (1.26 \pm 0.05) \times 10^{11}\,{\rm M}_\odot$, similar to the 450-$\mu$m population (but typically seen at an earlier epoch).

As both samples have comparable stellar masses but the 450-μm sample is ~ 0.9 mag brighter at the rest-frame V-band, next we assess whether the differences in the rest-frame optical/near-infrared SEDs is due to the different attenuation of the stellar emission by dust in the two populations. The median V-band dust attenuation of the 450-μm sample is $A_V = 2.0 \pm 0.1$ mag with a 16–84th percentile range of $A_V = 1.2$–2.9 mag. The spread at the UV/optical wavelengths seen in Fig. 4.7a highlights the variety of the SEDs of the 450-μm sources, ranging from unobscured (${\rm A}_V \sim 0$) Lyman-break galaxies, through more typical ${\rm A}_V \sim 1$ star-forming galaxies similar to those selected using the BzK criteria (Daddi et al., 2004), to higher-${\rm A}_V$ systems such as Extremely Red Objects (Smail et al., 2004) and the near-infrared faint populations (Simpson et al., 2014; Franco et al., 2018; Umehata et al., 2020).

The median dust attenuation is significantly lower than the AS2UDS value of $A_V = 2.89 \pm 0.04$ mag, as also suggested from the comparison of the rest-frame UV slopes in Fig. 4.7b. The variation of A_V with redshift is shown in Fig. 4.8b, with a $\sim$2-σ positive trend. A similar trend is observed in the AS2UDS sample, but offset to higher extinction. Thus, the difference in the optical/far-infrared SEDs is mainly attributed to the lower median value of dust attenuation of the 450-μm sample compared to 850-μm sample. Since A_V is also correlated with far-infrared luminosity, we pick luminosity-matched subsets with $\log_{10}(L_{\rm FIR}/L_{\odot}) = 12.1$–$12.7$ at $z = 1.5$–2.7 from the 450-μm and 850-μm samples. We find a median dust attenuation of $A_V = 2.29 \pm 0.13$ mag and $A_V = 2.63 \pm 0.07$ mag, respectively. Both subsamples do not show any significant trend in dust attenuation with redshift, meaning that the difference in dust attenuation between the two samples is most likely due to the variation in the far-infrared luminosity with redshift.

The 450- and 850-μm samples appear to be different when considering dust properties (see § 4.3.3.1), therefore we again select all sources at $z = 1.5$–2.7 and use a K-S statistic to test whether the trends of optical properties seen in Fig. 4.8 are significant. We find that the stellar mass distributions are not significantly different ($P = 0.3$), while the dust attenuation has a probability of the two samples being drawn from the same parent distribution of $P = 0.0004$, indicating a significant difference.

In Fig. 4.4b, we show that both samples have a comparable space density at $z = 2$–3. We analyse further whether they are similar populations in terms of their physical properties, by selecting all $z = 2$–3 sources that have $S_{450} \leq 15$ mJy (using the interpolated value from the best-fit SEDs for the AS2UDS sources) and $S_{850} \leq 4$ mJy, resulting in 26 and 195 sources selected at 450 μm and 850 μm, respectively. These flux density cuts minimise the overlap between the two populations by selecting sources that would be harder to find at either 450 or 850 μm, respectively. We find three main differences: the 450-μm sample (those which are harder to find at 850 μm) has a higher stellar mass, lower dust attenuation and higher dust temperature compared to the 850-μm sample. Thus, the same trends as seen in Fig. 4.6

and Fig. 4.8, except for stellar mass, remain for the non-overlapping populations. Since other physical properties are comparable, we conclude that the $z = 2$–3 450-μm sample has a lower dust-to-stellar mass ratio, suggesting more evolved systems with lower gas fractions.

We also calculate the median infrared excess, $L_{\rm FIR}/L_{\rm UV}$, for both 450 and 850-μm samples. The UV luminosity is estimated from the rest-frame composite SEDs (see Fig. 4.7a) at 1600Å. We find a median excess of 240^{+100}_{-25} and 1160^{+180}_{-140}, respectively, where the errors are calculated from the 16–84th percentile range of the rest-frame SEDs. These ratios are much higher than those for similar stellar mass UV-selected galaxies (~ 4–90; Heinis et al., 2013; Bouwens et al., 2016; Álvarez-Márquez et al., 2019).

The results and the properties discussed in § 4.3.1, and shown in Figs. 4.2 and 4.3, show that the 850-μm population is fainter in the optical regime, with ~ 17 per cent of sources being undetected in $K_{\rm s}$-band, compared to only < 4 per cent for the 450-μm sources. The $K_{\rm s}$-undetected 850-μm SMGs reside at higher redshift ($z = 3.19 \pm 0.08$) and have higher dust attenuation dust attenuation ($A_V = 5.3 \pm 0.2$ mag) than the full 850-μm sample, as highlighted in Chapter 3. We also note that this $K_{\rm s}$-undetected subset has slightly higher stellar mass, with a median of $M_* = (1.48 \pm 0.07) \times 10^{11}$ M$_\odot$ and are more luminous, with a median far-infrared luminosity of $L_{\rm IR} = (3.4 \pm 0.2) \times 10^{12}$ L$_\odot$. Other physical properties are comparable to those of the full 850-μm sample. This suggests that the $K_{\rm s}$-undetected 850-μm sources have slightly higher star-formation efficiency and lower gas fraction, although within the uncertainty to the $K_{\rm s}$-detected population. This relative paucity of these extremely dust-obscured sources at 450 μm likely reflects the lower sensitivity to the highest redshift and high dust mass sources in the much smaller 450-μm survey volume (which also makes it harder to detect these rarer extremely dust-obscured sources).

Finally, we look at how the optical properties of the 450-μm sample compare to that selected in the optical/near-infrared, which detects less active star-forming galaxies (the so-called star-forming "main-sequence"). For this, we use the K_s-band

selected UKIDSS UDS field galaxies from Chapter 2, which have been analysed in a consistent manner to our 450-μm sample. We select a subsample of field galaxies with $K_{\rm s} \leq 25.3$ that have no contamination flags, and have star-formation rates higher than the 16th percentile value of the 450-μm sample (SFR $\geq 41\,{\rm M}_{\odot}\,{\rm yr}^{-1}$), to exclude less-active systems. We also restrict both samples to $z = 1.5$–2.7 to exclude any evolutionary effects. We note that K_s-band-selected galaxies have over an order of magnitude higher number density compared to the 450-μm sample in this redshift range. We find that the K_s-band sample has a ~ 9 times lower median stellar mass (at 10-σ significance), similar dust attenuation ($A_V \sim 2.0$), slightly lower star-formation rates (2.5-σ difference) and a similar median redshift ($z \sim 2.15$) to the 450-μm sample. These results are in agreement to the findings from the photometric properties of the two populations in Figs. 4.2 and 4.3. Thus, compared to "normal" star-forming galaxies, the 450-μm selection detects more massive galaxies with higher dust masses, although this higher dust mass is not reflected in higher dust extinction for their restframe $\lesssim 2$–$3\,\mu$m detected stellar continuum emission, as measured by A_V.

4.4 Discussion

So far, we have investigated the physical properties of the full SNR ≥ 5 450-μm-selected sample and compared these to those selected at 850 μm. However, as seen in Figs. 4.5, 4.6 and 4.8, selection at different wavelengths (in populations whose space density peaks at different redshifts, Fig. 4.4b) leads to a range of potential selection effects. To assess the evolution with redshift in physical properties of far-infrared-selected samples, we next exploit the 450-μm and 850-μm surveys to construct two samples matched in terms of selection at rest-frame wavelength, $\lambda_{\rm rest} \sim 180\,\mu$m. We achieve this by selecting 450-μm SMGs in the redshift range of $z = 1$–2 and 850-μm SMGs at $z = 3$–4, shown in Fig. 4.9. We note that the median rest-frame wavelength for the samples at $z = 1$–2 and $z = 3$–4 differs by ~ 5 per cent, but we confirm that precisely matching the redshift distributions to achieve perfect agreement in their median wavelengths does not change our results.

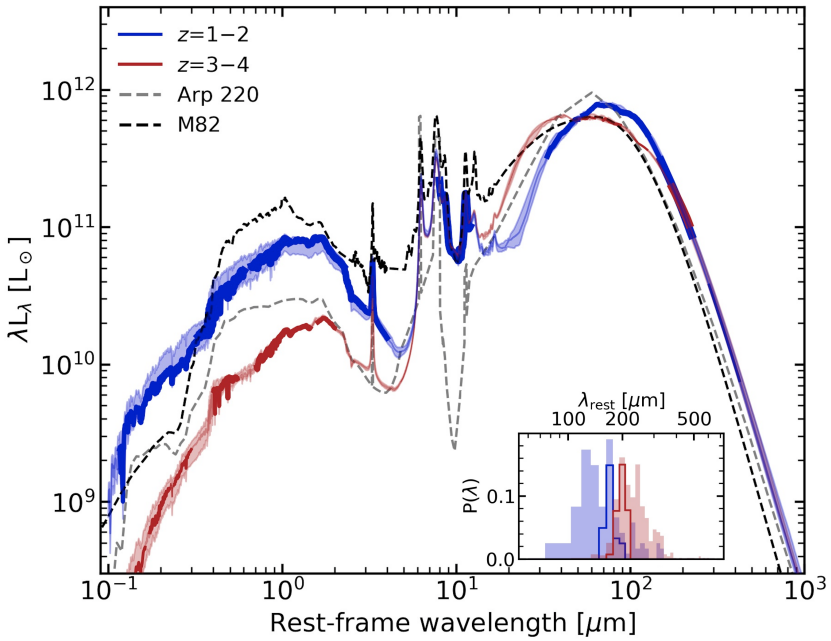

Figure 4.9: Median composite SEDs for the rest-frame-wavelength, $\lambda_{\rm rest} \sim 180\,\mu$m, matched samples of 31 $z \sim 1.5$ sources (selected at observed 450 μm) and 220 $z \sim 3.5$ sources (selected at observed 850 μm), both normalised to the median far-infrared luminosity of the $z \sim 1.5$ subset, $L_{\rm IR} = 1.2 \times 10^{12}\,{\rm L}_{\odot}$. We highlight the reliability of the sections of the SED for each sample with lines of variable thickness. For comparison, we also plot the SEDs of the local galaxies M82 and Arp 220. With similar far-infrared luminosities, the rest-frame near-infrared emission of these two galaxies brackets the $z \sim 1.5$ SED and they are both redder in the rest-frame optical, suggesting higher extinction. On the other hand, the $z \sim 3.5$ SED is much fainter in the rest-frame near-infrared, suggesting a lower typical stellar mass or much higher obscuration. In the far-infrared the $z \sim 1.5$ subset peaks at a longer wavelength (indicating cooler characteristic dust temperatures or higher opacity) and has a similar width to the dust peak of Arp 220 (suggesting a similar far-infrared opacity). In contrast, the $z \sim 3.5$ SED peaks at shorter wavelengths owing to the fact that the subsets are matched in rest-frame wavelength and dust mass, and these higher-redshift sources have typically higher far-infrared luminosities and hence are expected to be hotter by ~ 20 per cent. Bootstrap errors are shown as the shaded regions. The inset panel shows the distributions of rest-frame wavelengths for the 450-μm and 850-μm selected samples as shaded histograms in blue and red, respectively. The solid lines indicate the subsets with $M_{\rm d} \geq 2 \times 10^{8}\,{\rm M}_{\odot}$ at $z = 1$–2 and $z = 3$–4, corresponding to $\lambda_{\rm rest} \sim 180\,\mu$m with a ~ 5 per cent deviation.

As seen in Fig. 4.5b, the 850-μm flux limit corresponds to a higher dust mass, so we match the samples with a further constraint on both the 450-μm and 850-μm subsamples to have dust masses of $M_{\rm d} \geq 2 \times 10^8\,{\rm M}_\odot$ (this selection is shown in Fig. 4.5b). This results in samples comprising 31 sources at $z = 1$–2 from the STUDIES 450-μm survey and 220 sources at $z = 3$–4 from the AS2UDS 850-μm survey, which we will refer to as the "$z \sim 1.5$" and "$z \sim 3.5$" samples, respectively, or "$\lambda_{\rm rest} \sim 180$-$\mu$m matched sample" when we discuss the two samples as a whole (see Fig. 4.9). With both samples selected at the same rest-frame wavelength, $\lambda_{\rm rest} \sim 180\,\mu$m, and occupying the same parameter space in dust mass (roughly equating to sub-millimetre flux limit), we examine whether there are any physical differences between identical far-infrared-selected galaxies as the age of the Universe doubled between $z \sim 3.5$ and $z \sim 1.5$. We then discuss the implications of these results for the evolution of the dust content in galaxies and thus galaxy evolution as a whole.

4.4.1 Comparing rest-frame-selected populations

First, we look at the overall properties of our $z \sim 1.5$ and $z \sim 3.5$ samples by investigating their composite SEDs in Fig. 4.9. The composite SEDs are normalised to the median far-infrared luminosity of the rest-frame $\lambda_{\rm rest} \sim 180$-$\mu$m $z \sim 1.5$ sample, $L_{\rm IR} = 1.2 \times 10^{12}\,{\rm L}_\odot$. The errors on the composite SEDs are estimated by resampling the individual SEDs to form 500 sets of 121 SEDs and constructing composite SEDs for each of those sets. The uncertainty is then estimated by taking the 16th and 84th percentile values at each wavelength. We observe that the far-infrared to optical luminosity ratio, $L_{\rm FIR}/L_{\rm opt}$, of the $z \sim 1.5$ galaxies is much lower than that of the $z \sim 3.5$ population, suggesting that $z \sim 1.5$ population has lower dust attenuation and/or higher stellar masses as discussed for the whole 450-μm sample in § 4.3.3.2.

For comparison, we also show in Fig. 4.9 the SEDs of the local starburst galaxies M82 and Arp 220 (Silva et al., 1998), normalised to the same far-infrared luminosity. Compared to Arp 220, the far-infrared to optical ratio, $L_{\rm FIR}/L_{\rm opt}$, of the $z \sim 3.5$

sources is higher, while that of the $z \sim 1.5$ sources is lower. In the far-infrared, the $z \sim 1.5$ subset peaks at the longest wavelength (possibly indicating lower characteristic dust temperature and/or higher optical depth) and has a similar peak width as Arp 220. In comparison to M82, we observe that in the optical/near-infrared regime M82 is the brightest (at fixed far-infrared luminosity) and has redder UV/optical colours than either of the $z \sim 1.5$ and $z \sim 3.5$ samples. In the far-infrared, the $z \sim 3.5$ population appears to peak at a similar wavelength to M82 and has the broadest far-infrared SED. The broader SED could be the result of a broader distribution of dust temperatures at $z \sim 3.5$ or differences in the dust opacity of the two samples, with the $z \sim 3.5$ sample potentially having lower dust optical depth. However, we note that the constraints near the peak of the dust SED, especially towards shorter wavelengths, for the $z \sim 3.5$ sources are weak and thus uncertained (see Fig 4.9). Hence, the broader far-infrared SED may be simply due to these weakly constrained mid-infrared SEDs, where the detection rate in the PACS filters is low, with only 14 (6 per cent) of the 850-μm sources detected at 100 μm and/or 160 μm. We find that the composite SED of the sources with a detection in at least one PACS band produces SEDs that unsurprisingly peak at shorter wavelengths, while those SEDs constrained only by limits peak at longer wavelengths; thus when these two groups are combined this produces the broad SED. Overall, we conclude that the $z \sim 1.5$ sources have properties lying between those of the local templates of Arp 220 and M82, while the $z \sim 3.5$ sources are more extreme than Arp 220 in terms of their low ratio of rest-frame optical to far-infrared luminosities.

To investigate what drives these differences in the shapes of the SEDs seen in Fig. 4.9, we compare the MAGPHYS+photo-z derived physical properties between the $z \sim 1.5$ and $z \sim 3.5$ samples. We find that at $z \sim 1.5$ the median stellar mass is $M_* = (1.7 \pm 0.4) \times 10^{11}\,\mathrm{M}_\odot$, which is marginally higher than the median stellar mass of the $z \sim 3.5$ sample, $M_* = (1.20 \pm 0.06) \times 10^{11}\,\mathrm{M}_\odot$. Moreover, $z \sim 1.5$ sources have lower dust attenuation, with a median of $A_V = 1.91 \pm 0.16$ mag, compared to a median of $A_V = 3.25 \pm 0.11$ mag for the $z \sim 3.5$ sources. Thus, the brighter optical SED of the $z \sim 1.5$ sample arises from the combination of both slightly

higher stellar mass and lower dust attenuation. In the far-infrared, we see that the median characteristic dust temperature of $T_{\rm d} = 31 \pm 3\,{\rm K}$ for the $z \sim 1.5$ sources is lower, but is consistent within the uncertainties to that of the $z \sim 3.5$ SMGs (with at least one SPIRE detection), $T_{\rm d} = 34 \pm 1\,{\rm K}$. The $z \sim 1.5$ population also has a lower median far-infrared luminosity, $L_{\rm IR} = (1.17 \pm 0.14) \times 10^{12}\,{\rm L}_{\odot}$, and dust mass, $M_{\rm d} = (3.1 \pm 0.5) \times 10^{8}\,{\rm M}_{\odot}$, compared to the $z \sim 3.5$ population, which has median values of $L_{\rm IR} = (3.89 \pm 0.18) \times 10^{12}\,{\rm L}_{\odot}$ and $M_{\rm d} = (7.7 \pm 0.6) \times 10^{8}\,{\rm M}_{\odot}$, respectively.

4.4.1.1 Gas fraction and star-formation efficiency

Our analysis suggests that at $z \sim 1.5$ far-infrared selected galaxies are different to those at $z \sim 3.5$, in both the far-infrared and optical regimes, even when selected at the same rest-frame wavelength and the same dust mass limit. To test how these differences link to the physical properties of the populations, we next compare the available fuel the two populations have for star formation and how efficiently this fuel is used by calculating the gas fraction and the star-formation efficiency for both samples.

We begin by estimating the gas masses from the dust masses and assuming a gas-to-dust mass ratio, $\delta_{\rm gdr}$. We explore two approaches to determine the appropriate value for $\delta_{\rm gdr}$. Firstly, we just use an empirical estimate of $\delta_{\rm gdr} = 100$, since similar values have been derived both for a small sample of high-redshift SMGs with CO(1–0) observations (see Swinbank et al., 2014) and for Arp 220 (Rangwala et al., 2011). A gas-to-dust ratio of 100 is also considered to be the average value for most local, metal-rich galaxies (e.g Draine et al., 2007; Rémy-Ruyer et al., 2014) and SMGs are expected to be metal-rich due to their high stellar mass to star-formation rate ratios (Mannucci et al., 2010). In addition, as gas-to-dust mass ratio is expected to vary with stellar mass and redshift, we can also estimate the expected dust-to-gas ratios for the median stellar mass at the median redshift of each sample. We follow Genzel et al. (2015) using mass-metallicity relations appropriate for each redshift and find a metallicity dependent gas-to-dust ratio with a fitting formula from Leroy et al. (2011), who fit local star-forming galaxies. We find that the gas-

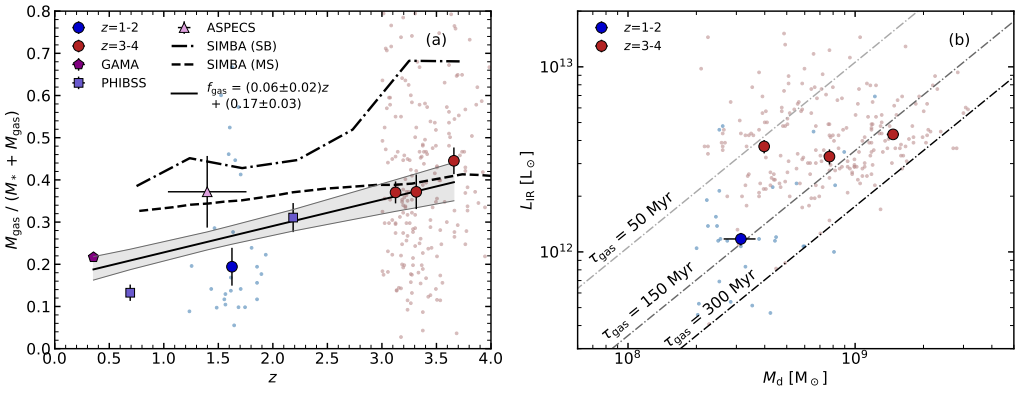

Figure 4.10: The derived far-infrared properties of $z\sim1.5$ and $z\sim3.5$ rest-frame 180-μm matched samples. **(a)** Gas fraction, $f_{\rm gas}=M_{\rm gas}/(M_{\rm gas}+M_*)$, as a function of redshift. We derive a median gas mass fraction of $f_{\rm gas}=0.19\pm0.06$ with a 68th percentile range of $f_{\rm gas}=0.10$–0.58 at $z\sim1.5$ and $f_{\rm gas}=0.40\pm0.02$ with a 68th percentile range of $f_{\rm gas}=0.22$–0.65 at $z\sim3.5$, assuming a gas-to-dust ratio of 100. We also show results from a sample of $z<1$ ULIRGs from the GAMA survey from Driver et al. (2018), the ASPECS blind CO-survey from Aravena et al. (2019) and the CO-detected typical star-forming galaxies at $z\sim1$–3 from Tacconi et al. (2018). For comparison, we also overlay theoretical predictions for main-sequence (MS) and starburst (SB) galaxies from the SIMBA simulations by Davé et al. (2019). The solid line shows the fit to the combined observational data, indicating a modest 3-σ increase in gas fraction with redshift, with the uncertainty shown as the shaded region. **(b)** Far-infrared luminosity as a function of dust mass, the ratio of which is a proxy for star-formation efficiency (or the inverse of gas depletion timescale). The binned median values are shown as large circles, where we split the larger $z\sim3.5$ sample into three independent bins of dust mass, and the errors are derived by a bootstrap method. Lines of constant gas depletion are indicated. On average, the star-formation efficiency at $z\sim1.5$ is comparable to that at $z\sim3.5$, but at a fixed dust (and hence gas) mass the higher redshift sources have ~3 times higher star-formation efficiency.

to-dust mass ratios for both $z\sim1.5$ ($\delta_{\rm gdr}=100^{+260}_{-100}$) and $z\sim3.5$ ($\delta_{\rm gdr}=130^{+300}_{-130}$) samples have significant fitting uncertainties as the mass-metallicity relations are not well constrained, but that both are consistent with the empirical estimate. Therefore we adopt a fixed ratio of $\delta_{\rm gdr}=100$ for both samples. We use this value and the measured dust masses of our $z\sim1.5$ and $z\sim3.5$ samples to estimate their gas masses and gas fractions, $M_{\rm gas}/(M_{\rm gas}+M_*)$, and show these in Fig. 4.10a.

We find a median gas mass of $M_{\rm gas}=(3.1\pm0.5)\times10^{10}\,{\rm M}_\odot$ for the $z\sim1.5$ sample and a median gas fraction of $M_{\rm gas}/(M_*+M_{\rm gas})=0.19\pm0.05$ with a 16–84th percentile range of $f_{\rm gas}=0.10$–0.58. For the $z\sim3.5$ sample we find a median gas mass of $M_{\rm gas}=(7.7\pm0.6)\times10^{10}\,{\rm M}_\odot$. As seen in Fig. 4.10a, the $z\sim3.5$ sample has a

higher median gas fraction of $f_{\rm gas} = 0.40 \pm 0.02$, with a 16–84th percentile range of $f_{\rm gas} = 0.22$–0.65. In Fig 4.10a, we also overlay the results from a similar analysis of a sample of $z < 1$ ULIRGs ($L_{\rm IR} \geq 10^{12}\,{\rm L}_{\odot}$) in the GAMA survey from Driver et al. (2018), as well as the gas fraction derived directly from CO for the ASPECS blind CO-survey from Aravena et al. (2019) and the CO-detected typical star-forming galaxies at $z \sim 1$–3 from Tacconi et al. (2018) (where we use $\alpha_{\rm CO} = 2.5$ to convert to gas mass). Overall, we see a 3-σ trend of increasing gas fraction with increasing redshift. This suggests that one fundamental difference between the $\lambda_{\rm rest} \sim 180$-$\mu$m selected galaxy populations at $z \sim 1.5$, compared to $z \sim 3.5$, is that the former are more evolved, with more gas transformed into stars and thus higher stellar masses and lower gas masses and lower gas fractions. For comparison, we overlay the gas fraction evolution from the cosmological hydrodynamic simulation SIMBA (Davé et al., 2019; Li et al., 2019) for main-sequence (MS) and starburst (SB) galaxies. The galaxy is assumed to be starburst if the positive offset from the main-sequence is ${\rm SFR/SFR_{MS}} \geq 4$, where ${\rm SFR_{MS}}$ is the main-sequence star-formation rate at a given redshift. The SB model predicts higher gas fraction at all redshifts compared to our observed trend for highly star-forming galaxies. The difference may be due to the fact that we assume a constant gas-to-dust ratio of 100, while the simulated values vary between $\sim$100–1000. As the estimates of the gas masses in galaxies depend on the assumed ratio, in § 4.4.2 we compare the simulations and our results in terms of dust mass, which is a more fundamental measurement requiring fewer assumptions.

In Fig. 4.10b, we also plot far-infrared luminosity versus dust mass, where dust mass is a proxy for gas mass and the ratio of these quantities corresponds to the star-formation efficiency (equivalent to the inverse of gas depletion timescale), for the $z \sim 1.5$ and $z \sim 3.5$ samples. Using the gas mass for our $z \sim 1.5$ sample we estimate the gas-depletion timescale, assuming that half of the gas is available to form stars and the other half is expelled (Pettini et al., 2002), $\tau_{\rm dep} = (0.5 \times M_{\rm gas})/{\rm SFR}$, and overlay lines of constant gas depletion timescale in Fig. 4.10b. We find a comparable median gas depletion timescale for both samples, $\tau_{\rm dep} = 150 \pm 40\,{\rm Myr}$

at $z \sim 1.5$ and $\tau_{\rm dep} = 130 \pm 7$ Myr at $z \sim 3.5$. We can estimate the expected lifetime of the current star-formation event as twice the gas depletion timescale, assuming we are observing SMGs halfway through the burst. This approach yields lifetimes of 300 ± 80 Myr and 260 ± 14 Myr for the $z \sim 1.5$ and $z \sim 3.5$ samples, respectively. The results indicate that the star formation is modestly slower at $z \sim 1.5$, while at $z \sim 3.5$ the more gas-rich galaxies are forming stars more rapidly, and so consuming the larger gas reservoirs in a comparable amount of time. We can compare these lifetimes to the time taken to form the observed stellar mass, M_*/SFR. This crude age estimates results in a median of 900 ± 200 Myr for the $z \sim 1.5$ sample and 400 ± 20 Myr for the $z \sim 3.5$ sample. In a simple model where the galaxies are seen on-average halfway through their current star-formation event, the higher formation ages derived from M_*/SFR, compared to their gas depletion timescales, suggest that galaxies in both samples had pre-existing stellar populations before the onset of the current star-formation event, with those in the $z \sim 1.5$ systems being more substantial.

As the median stellar masses of both samples are comparable, we would expect the lower redshift sample to either have similar metallicities (Stott et al., 2013) or higher metallicities if the mass-metallicity has dependence on redshift (Genzel et al., 2015), which in turn should result in comparable or slightly higher dust attenuation. However, we see the opposite trend, with the $z \sim 1.5$ sources having lower dust attenuation than the $z \sim 3.5$ population.

To analyse whether there is any indication of possible differences in the dust continuum structures, specifically the sizes and the dust densities, of the populations at different redshifts, we compare our results to an optically-thick model of the dust emission by Scoville (2013). In Chapter 3, we have shown that the 850-μm SMGs are broadly consistent with this homologous and homogeneous population model of centrally-illuminated dust clouds, with the dust continuum size of SMGs broadly following the expected trend with far-infrared luminosity-to-gas mass ratio. In Fig. 4.10b we see that, on average, both $z \sim 1.5$ and $z \sim 3.5$ populations have comparable $L_{\rm IR}/M_{\rm d}$ ratios, hence, if we assume that the sources in our $z \sim 1.5$ and

$z \sim 3.5$ samples can be modelled as having broadly similar structures for the dust continuum regions, they are expected to have comparable effective dust continuum emission radii of ~ 0.8 kpc. The lower dust density at $z \sim 1.5$, due to lower dust mass but comparable dust continuum sizes, may explain the lower dust attenuation compared to $z \sim 3.5$ population.

We note though that the median dust mass for our $z \sim 3.5$ sample is, on average, two times higher than for the $z \sim 1.5$ population. Thus, to check if dust density is still lower at $z \sim 1.5$ for galaxies at a given dust mass, we restrict our analysis to have comparable dust masses of $M_{\rm d} \simeq (2\text{–}5) \times 10^8\,{\rm M}_\odot$, resulting in 23 sources at $z \sim 1.5$ and 61 sources at $z \sim 3.5$. We find that the $z \sim 1.5$ sources have ~ 3 times lower far-infrared luminosity to gas mass ratios, $L_{\rm IR}/M_{\rm gas}$. This implies that, for a given dust mass, the $z \sim 1.5$ sources potentially have approximately two times larger dust continuum sizes. Thus, $z \sim 1.5$ sources have lower dust densities than the $z \sim 3.5$ population, due to their larger dust continuum sizes for a given dust mass. Both dust-mass-limited and dust-mass-matched samples suggest that the lower dust density at $z \sim 1.5$ is the key parameter leading to lower dust attenuation compared to the $z \sim 3.5$ sample.

4.4.2 Dust properties of far-infrared-selected galaxies

Dust, while a small component of the overall baryonic mass of a galaxy, is a useful tracer of the ISM. Therefore, measuring dust mass, especially at different cosmic epochs, is important for understanding the evolution of the ISM in galaxies. To examine how the dust mass in galaxies has evolved we construct the dust mass function and derive the dust mass density for our $\lambda_{\rm rest} \sim 180$-$\mu$m matched samples at $z \sim 1.5$ and $z \sim 3.5$.

4.4.2.1 Dust mass function

We calculate the dust mass function for the $z \sim 1.5$ sources using an accessible volume method: $\phi(M_{\rm d})\Delta M_{\rm d} = \Sigma(1/V_i)$, where $\phi(M)\Delta M$ is the number density of

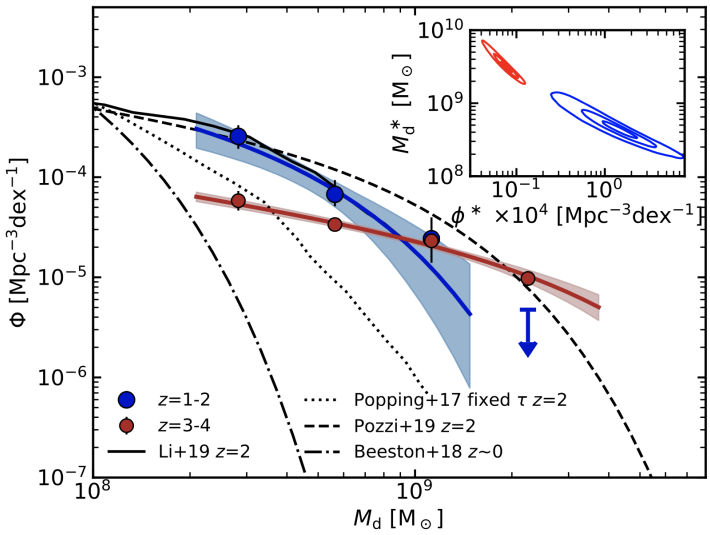

Figure 4.11: Dust-mass function for the $\lambda_{\rm rest} \sim 180$-$\mu$m matched $z \sim 1.5$ and $z \sim 3.5$ samples. The arrow indicates a 2-σ upper limit for the $z \sim 1.5$ sources. For comparison, we overlay the local ($z < 0.1$) dust mass function from the GAMA sample of Beeston et al. (2018) and $z = 2$ results from 160-μm survey by Pozzi et al. (2020). We also show $z = 2$ predictions from a semi-analytical model from Popping et al. (2017) assuming a fixed timescale for dust accretion in the ISM of 100 Myr, and from the cosmological hydrodynamic simulation SIMBA by Li et al. (2019). The difference in the shape of our two dust mass functions indicates that the characteristic dust mass of the high-redshift sources is higher than that of the low-redshift sample. Additionally, the number density is higher at lower redshift for all but the highest dust mass sources. The inset panel shows the correlation between the best-fitting Schechter function parameters, characteristic dust mass and space density, for the two samples in their respective colours. Both characteristic dust mass and space density evolve, thus the two $\lambda_{\rm rest} \sim 180$-$\mu$m-matched samples do not overlap in this parameter space.

sources with dust masses between M and $M+\Delta M$ and V_i is the co-moving volume within which the i-th source would be detected in a given dust mass bin. For each source, the area within which each would have been selected at $\geq 5\sigma$, given its 450-μm flux density, is calculated in the same manner as in § 4.3.2. We show the resulting dust mass function in Fig. 4.11. We indicate a 2-σ limit (corresponding to 2.5 sources) in the highest dust mass bin, which has no detected sources. For the $z \sim 3.5$ sample (derived from the 850-μm AS2UDS sources), we correct for incompleteness at faint flux densities by comparing the number of observed sources to the expected number counts using the slope of the ALMA 1.13-mm counts in the GOODS-S field from Hatsukade et al. (2018). We overlay the resulting dust mass function of the $z \sim 3.5$ sources in Fig. 4.11. The uncertainties on the dust

functions of both samples were calculated by resampling the dust mass and redshift probability distributions to construct multiple dust mass functions. The resulting error bars are taken as the 16th and 84th percentiles of each bin.

To model the mass functions, we fit them using Schechter functions of the form, $\phi = (\phi^*/M_{\rm d}^*)(M_{\rm d}/M_{\rm d}^*)^{\alpha} e^{-M_{\rm d}/M_{\rm d}^*}$, where ϕ^* is the characteristic space density, $M_{\rm d}^*$ is the characteristic dust mass and α is the power-law slope (Schechter, 1976). The power-law slope defines the shape of the function at low dust masses and previous studies have yielded values ranging $\alpha = -1.0$ to -1.7 (Vlahakis et al., 2005; Dunne et al., 2011; Clemens et al., 2013). As our rest-frame $\lambda_{\rm rest} \simeq 180$-$\mu$m matched samples are selected to have dust masses of $M_{\rm d} \geq 2 \times 10^8\,{\rm M}_{\odot}$, we are unable to constrain α directly and so instead we choose to fix it to $\alpha = -1.5$. The Schechter fits to both the $z \sim 1.5$ and $z \sim 3.5$ samples are shown in Fig. 4.11.

The best fit for the $z \sim 1.5$ sample has $M_{\rm d}^* = 3.9^{+3.3}_{-1.5} \times 10^8\,{\rm M}_{\odot}$ and $\phi^* = 1.6^{+2.4}_{-1.0} \times 10^{-4}\,{\rm Mpc}^{-3}\,{\rm dex}^{-1}$, while the best fit for the $z \sim 3.5$ sample has $M_{\rm d}^* = 3.2^{+1.6}_{-0.8} \times 10^9\,{\rm M}_{\odot}$ and $\phi^* = 7.6^{+2.4}_{-2.1} \times 10^{-6}\,{\rm Mpc}^{-3}\,{\rm dex}^{-1}$. In Fig 4.11, we show the covariance of the best-fitting Schechter function parameters for both samples. The χ^2 contours for the two samples do not overlap, indicating evolution in both characteristic dust mass and space density. As these subsets are rest-wavelength matched, this change in the shape of their dust mass function suggests a change of normalisation and characteristic dust mass of galaxies with redshift, similar to the findings of Pozzi et al. (2020). However, since we have only limited constraints on the $z \sim 1.5$ function due to the small sample size, we caution that the uncertainties can be substantial.

For comparison, we overlay the "local" dust mass function of $z < 0.1$ galaxies from the GAMA sample by Beeston et al. (2018). We also show the $z = 2$ results from a 160-μm survey by Pozzi et al. (2020), though we note that at this redshift their selection wavelength is $\sim 50\mu$m and their survey is thus sensitive to relatively hot dust, potentially including AGN-heated sources. We observe that low-redshift sources have higher space density at lower dust masses, but the space density decreases steeply with increasing dust mass. The space density for the low dust

mass galaxies is highest at low redshift, while the space density at the high-mass end is higher for the $z \sim 3.5$ sources. The dust mass functions in Fig. 4.11 suggest that the characteristic dust mass of the $z \sim 3.5$ sources is higher than that of the $z \sim 1.5$ sample, indicating evolution of a factor 8 ± 5 in the characteristic dust mass between $z \sim 1.5$ and $z \sim 3.5$. The normalisations of the best-fit Schechter function suggest that the space density is higher at $z \sim 1.5$; however there is an indication that the space density of the highest dust mass sources is higher at $z \sim 3.5$.

We compare our dust mass functions to predictions from a semi-analytical model by Popping et al. (2017) and hydro-dynamical simulations by Li et al. (2019), both at $z = 2$. We see that Popping et al. (2017) model under predicts the observational data at all dust masses, while Li et al. (2019) provides a rough match to our observations at z=1–2. A description of the models and how they compare to observational results is presented in the subsequent section.

4.4.2.2 Dust mass density

Given the apparently different shapes of the dust mass function in our two $\lambda_{\rm rest} \sim$ 180-μm-matched samples, we opt to assess the evolutionary differences in the dust properties of galaxy populations using integrated dust mass density as the most robust measurement available. To obtain the dust mass density we use our dust mass measurements together with the accessible volume, which we have calculated in § 4.3.2. We derive a dust mass density of $\rho = (2.6 \pm 0.5) \times 10^4\,{\rm M}_\odot\,{\rm Mpc}^{-3}$ at $z \sim 1.5$ and $\rho = (2.41 \pm 0.13) \times 10^4\,{\rm M}_\odot\,{\rm Mpc}^{-3}$ at $z \sim 3.5$, for a sample with $M_{\rm d} \geq 2.0 \times 10^8$ ${\rm M}_\odot$. This indicates that galaxies selected at the same rest-frame wavelength have a similar dust mass density (above a dust mass of $M_{\rm d} \geq 2 \times 10^8\,{\rm M}_\odot$) at $z \sim 1.5$ and $z \sim 3.5$, assuming that the dust properties used to estimate the dust masses are similar at low and high redshift.

To derive the *total* dust mass density, needed to compare to estimates from other studies, we have to extrapolate and integrate the best Schechter fit of each of our samples from our current limit of $M_{\rm d} \geq 2.0 \times 10^8\,{\rm M}_\odot$ down to $M_{\rm d} = 10^4\,{\rm M}_\odot$, we then add this to the dust mass density of those sources with $M_{\rm d} \geq 2 \times 10^8\,{\rm M}_\odot$, which is

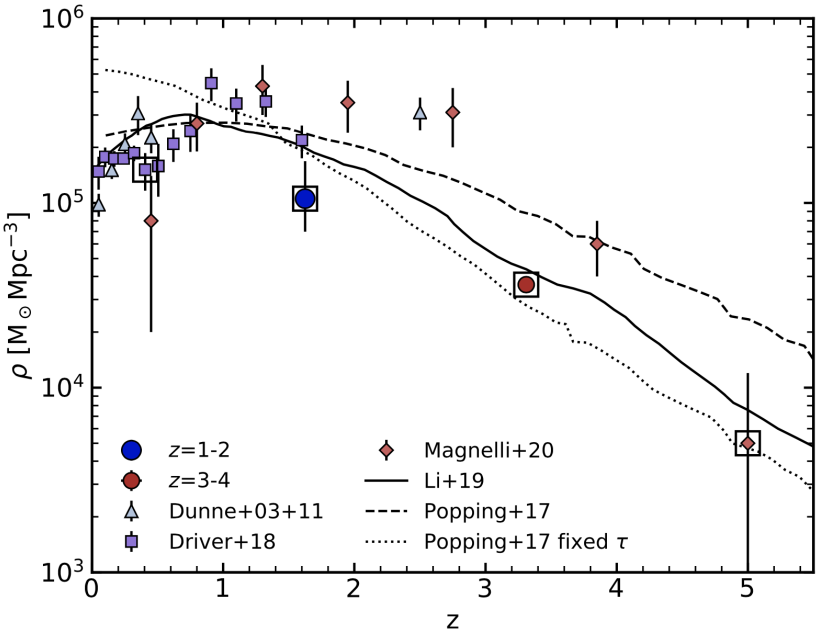

Figure 4.12: Dust mass density as a function of redshift for the rest-frame wavelength $\lambda_{\rm rest} \sim 180$-$\mu$m matched $z \sim 1.5$ and $z \sim 3.5$ samples showing a decline in these matched samples towards higher redshifts. For comparison we overlay results for the total co-moving dust mass densities in galaxies from Dunne et al. (2003, 2011), Driver et al. (2018) and Magnelli et al. (2020). To highlight the results with a comparable selection, we indicate the rest-frame $\lambda_{\rm rest} \sim 180$-$\mu$m selection with black squares. We also show the predictions from a semi-analytical model from Popping et al. (2017), assuming a fixed timescale for dust accretion in the ISM of 100 Myr, which we label "fixed τ", and another model with no dust accretion. Finally, we plot the predicted dust mass densities from the cosmological hydrodynamic simulation of Li et al. (2019) and find that it fits both the low redshift samples and our high redshift observations reasonably well.

calculated above. In this manner, the final total dust mass density we derive for the $z \sim 1.5$ sample is $\rho = (1.1^{+0.6}_{-0.4}) \times 10^5\,{\rm M}_\odot\,{\rm Mpc}^{-3}$, while the $z \sim 3.5$ dust mass density is $\rho = (3.6^{+0.3}_{-0.2}) \times 10^4\,{\rm M}_\odot\,{\rm Mpc}^{-3}$. The uncertainties on the dust mass density are a combination in quadrature of the error on the extrapolated values from the dust mass function and the error on the observed dust density (which is obtained by resampling the dust mass and redshift probability distributions). Thus, the total dust mass density at $z \sim 1.5$ is roughly three times higher compared to $z \sim 3.5$, at a 2-σ level. The larger difference between the extrapolated values is due to the steeper Schechter function for the $z \sim 1.5$ subset, as seen in Fig. 4.11.

Next, in Fig. 4.12, we compare our measurements with observations from other studies to assess the dust mass density evolution and investigate the possible phys-

ical processes responsible for it. Comparing the dust mass density results is complex due to possible selection effects, as well as small number statistics and uncertainties due to excess variance (sometimes referred to as the cosmic variance). To minimise these, we mainly compare to estimates derived in a similar manner from observations in the far-infrared wavebands.

In Fig. 4.12, we compare our high redshift measurements to the dust mass density at $z \simeq 0$–1 from Driver et al. (2018) who use MAGPHYS to obtain dust masses based on SPIRE photometry for $\sim 250{,}000$ galaxies from the GAMA and G10-COSMOS surveys out to $z \sim 1.5$. They corrected for volume-limited effects by fitting a spline to the data above their completeness limits and integrating to obtain total masses. Our $z \sim 1.5$ result is within $1.5\,\sigma$, and thus in agreement with Driver et al. (2018) results at the sampled redshift range of $z \sim 1.5$.

We also include results from a *Herschel* SPIRE study at $z \lesssim 0.5$ by Dunne et al. (2011), who used MAGPHYS to estimates dust masses, finding results which agree with the larger subsequent study by Driver et al. (2018). As well as a high redshift estimate ($z \sim 2.5$) using early SCUBA 850-μm samples by Dunne et al. (2003), who fit a modified blackbody with $\beta = 2$ (leading to ~ 10 per cent systematic difference in dust mass compared to MAGPHYS). We find that their result at $z \sim 2.5$ is $\sim 2\sigma$ higher than our estimate at $z \sim 1.5$.

In addition, we overlay the dust mass density results from Magnelli et al. (2020), who analysed 1.2-mm ALMA-selected sources out to $z \sim 5$ and calculated the dust mass density by stacking the dust continuum for a H-band selected sample, obtaining the total emission for the population. Magnelli et al. (2020) fit a modified blackbody with $\beta = 1.8$ to obtain the dust mass and calculated the dust mass density, which leads to a systematic difference of ~ 20 per cent compared to fitting it with MAGPHYS. For this comparison, we overlay their subset with a stellar mass cut of $M_* \geq 10^9\,\mathrm{M}_\odot$, the estimated completeness level of their sample. At $z \sim 3.5$ we observe that the dust mass density from Magnelli et al. (2020) is marginally higher than our result; however their highest redshift value is consistent with the trend we that see in our subsets.

We note that the Dunne et al. (2003, 2011) and Driver et al. (2018) samples used SCUBA and *Herschel* data, to constrain their far-infrared SEDs, hence there is additional uncertainty in the identification of counterparts and thus redshift and dust mass estimates, due to source confusion. The ALMA 1.2-mm sample of Magnelli et al. (2020) does not suffer from this uncertainty; however, due to the small survey area, the uncertainty in their results arising from excess variance is ~ 45 per cent. We crudely estimate the excess variance in our $z \sim 1.5$ sample, by splitting the survey area into independent halves on $0.04\,\mathrm{deg}^2$ scales and derive a mean variance of ~ 44 per cent, which is comparable to the Magnelli et al. (2020) findings. For our $z \sim 3.5$ sample, which has a larger survey area, this method gives an average excess variance of ~ 12 per cent.

For consistent comparison to our $z \sim 1.5$ and $z \sim 3.5$ samples, we highlight the results corresponding to $\lambda_{\mathrm{rest}} \sim 180$-$\mu$m selection in Fig. 4.12. We observe that the results follow a smooth trend of decreasing dust mass density with redshift. The dust mass density evolution allows us to examine possible models of dust formation and growth in galaxies at different epochs. Dust is primarily produced in low/intermediate mass asymptotic giant branch (AGB) stars (Gehrz, 1989; Sargent et al., 2010) and massive stars at the end of their lives when they explode as supernovae (SNe) (Rho et al., 2008; Dunne et al., 2009). Dust is destroyed by astration, SNe shocks or grain-grain collisions. However, it can reform and grow through accretion in dense and diffuse ISM components. Combining all these processes to predict the lifetime of dust is, therefore, a complicated task, which several groups have attempted to model. Here, we compare our results to the predicted dust mass densities at different epochs from a semi-analytical model by Popping et al. (2017) and hydrodynamical simulation SIMBA by Li et al. (2019). These models differ in several features, most notably Popping et al. (2017) consider Type Ia SNe to have the same efficiency in dust formation as Type II SNe, while Li et al. (2019) do not consider Type Ia SNe to be significant sources of dust production and omit their contribution from their dust formation model.

In Fig. 4.12, we overlay the dust mass density for two of the models by Popping et al.

(2017). The first assumes that the contribution of dust growth on grains to the dust mass of galaxies is negligible; thus, this model turns off the growth of dust through accretion onto grains and increases the efficiency of dust condensation in stellar ejecta to 100 per cent. This model predicts more dust than is seen at either $z \sim 1.5$ or $z \sim 3.5$ in our analysis. Although at low redshift this is only a 1.5-σ difference, at $z \sim 3.5$ it is a significant ~ 18-σ difference, which cannot be accounted for by the excess variance in our sample. The second model, which we label "fixed τ", assumes a fixed timescale for dust accretion in the ISM of $\tau = 100\,\mathrm{Myr}$, independent of gas density and/or gas-phase metallicity. Although this model matches our observations within the uncertainties at $z \sim 1.5$ and $z \sim 3.5$, it does not follow the observational results from other studies at $z \lesssim 1$. At low redshift, it appears that the dominant form of dust production in this model is dust growth by accretion in the ISM since there is no decline at low redshift. The comparison of the model and data suggests that the adopted dust accretion timescale is too short at low redshifts, leading to overestimated dust masses.

We also compare to predicted dust mass densities from a cosmological hydrodynamic simulation, SIMBA, by Li et al. (2019). The predicted dust mass density in their model peaks at $z \sim 1$ and declines to the present day, in agreement with the observations. This is due to the decline, on average, of star formation as a result of the onset of quenching in massive galaxies, which slows down the metal enrichment and limits grain growth. At higher redshifts, the dust mass density declines steeply, in agreement with our observations at $z \sim 1.5$, and slightly overpredicts the dust density at $z \sim 3.5$, after taking excess variance into account. This indicates that the grain growth may be weaker, or the dust destruction is stronger, than assumed in the model, at least at high redshift. In addition, the assumed fixed dust destruction and condensation efficiencies may actually be functions of the local ISM properties. Nevertheless, overall it appears that the assumptions in Li et al. (2019), who combine the dust production by AGB stars and Type II SNe, growth by accretion (with a non-constant accretion timescale) and destruction by thermal sputtering and SNe, may currently provide the best match to observations.

4.5 Conclusions

In this chapter, we have analysed the physical properties of an effectively completely identified sample of 121 SMGs selected at 450 μm from the SCUBA-2 Ultra Deep Imaging EAO Survey (STUDIES; Wang et al., 2017). We used MAGPHYS+photo-z to fit spectral energy distribution models to the available UV-to-radio photometry (a maximum of 24 bands). This allowed us to compare and contrast the population of these 450-μm selected SMGs to the large sample of ALMA-identified 850-μm selected sources from AS2UDS (Stach et al. 2019; D20), which was analysed in a consistent manner in Chapter 3. To investigate how the physical properties of infrared luminous galaxies evolve with redshift, we also select $z = 1$–2 450-μm sources and $z = 3$–4 850-μm sources both with $M_{\rm d} \geq 2 \times 10^8\,{\rm M}_{\odot}$, to construct rest-frame wavelength ($\lambda_{\rm rest} \sim 180\,\mu$m) matched subsets. We summarise our main findings below.

- We derive a median redshift of $z = 1.85 \pm 0.12$ for the 121 SMGs selected at 450 μm with only ~ 9 per cent lying at $z \geq 3$. The distribution can be roughly described by evolution of the far-infrared luminosity function and the 450-μm flux selection limit. The median redshift is significantly lower than the median of the 850-μm selected sample, $z = 2.61 \pm 0.08$. The fainter 450-μm sample has, on average, ~ 14 times higher space density than the brighter 850-μm sample out to $z \sim 2$, and a comparable space density at $z = 2$–3, before declining. For the $z = 2$–3 matched subsets we find that the 450-μm sources have a lower dust-to-stellar mass ratio, suggesting more evolved systems with lower gas fractions.

- We find that the 450-μm sample has a significantly lower dust attenuation of $A_V = 2.1 \pm 0.1$ mag, compared to the $A_V = 2.89 \pm 0.04$ mag of the 850-μm sample. The SEDs of the 450-μm population span a wide range in flux at observed optical wavelengths, from unobscured LBGs, through more typical $A_V \sim 1$ star-forming galaxies, to very obscured and completely optically undetected sources.

- The 450-μm sample has a median dust mass of $M_{\rm d} = (3.6 \pm 0.2) \times 10^8\,{\rm M}_{\odot}$, median far-infrared luminosity of $L_{\rm IR} = (1.5 \pm 0.2) \times 10^{12}\,{\rm L}_{\odot}$ and median star-formation

rate of $\mathrm{SFR} = 130 \pm 20\,\mathrm{M_\odot\,yr^{-1}}$, significantly lower than equivalent measures of the 850-μm sample. These differences are mainly due to the brighter effective flux limit of the 850-μm sample.

- For the rest-frame wavelength-matched, $\lambda_{\rm rest} \sim 180\,\mu$m, subsets, we find that $z \sim 1.5$ subset has a gas fraction of $f_{\rm gas} = 0.19 \pm 0.06$. Combined with previous studies, we see a modest 3-σ trend of increasing gas fraction with increasing redshift in these populations. Overall, the galaxies at $z \sim 1.5$ and $z \sim 3.5$ have comparable star-formation efficiency (although we note that at a fixed dust mass the $z \sim 1.5$ sources have ~ 3 times lower star-formation efficiency). Both the lower gas masses and lower star-formation rates at $z \sim 1.5$, compared to the $z \sim 3.5$ population, lead to comparable remaining lifetimes of the SMG phase of 250–300 Myr.

- By comparing the far-infrared luminosity to gas mass ratios of dust-mass-limited ($M_{\rm d} \geq 2 \times 10^8\,\mathrm{M_\odot}$) samples at $z \sim 1.5$ and $z \sim 3.5$, using an optically-thick model by Scoville (2013), we suggest that the $z \sim 1.5$ population has lower dust density (assuming similar geometry) due to comparable inferred dust emission radii (~ 0.8 kpc) and lower dust mass compared to the $z \sim 3.5$ sources. The same is true for dust-mass-matched ($M_{\rm d} = 2$–$5 \times 10^8\,\mathrm{M_\odot}$) samples, as the $z \sim 1.5$ sources appear to have lower dust densities due to their ~ 2 times larger inferred dust continuum sizes compared to the $z \sim 3.5$ population. Thus, dust density appears to be a key parameter leading to the lower dust attenuation in SMGs seen at $z \sim 1.5$.

- We calculate the total dust mass density for the $\lambda_{\rm rest} \sim 180$-$\mu$m-matched samples at $z \sim 1.5$ and $z \sim 3.5$ by combining the dust mass density estimates extrapolated down to $M_{\rm d} \sim 10^4\,\mathrm{M_\odot}$ from the best-fitting Schechter function for their respective dust mass functions. We find the $z \sim 1.5$ sample to have ~ 3 times higher dust density than our $z \sim 3.5$ estimate. After combining our results with other far-infrared samples, we find that the model from hydrodynamical simulations by Li et al. (2019) combining the dust production by AGB stars and Type II SNe, growth by accretion (with a non-constant accretion timescale) and destruction by thermal sputtering and SNe, is best able to match the observational data. Thus, the dust content in galaxies appears to be governed by a combination of both the variation

of gas content and dust destruction timescale.

Chapter 5

Decomposing rotation curves of star-forming galaxies at cosmic noon

Preamble

In this chapter we present an on-going study on the decomposition of individual high-redshift galaxy rotation curves from a very deep (∼80 h on-source integration) from the KMOS Ultra-deep Rotational Velocity Survey, KURVS. The Hα rotation curves extend to $\sim 3R_{\rm e}$, allowing for comparison with studies of local galaxies. Using spatially-resolved 2D stellar mass maps derived from deep *HST* photometry, we decompose the dynamical mass profile into the baryonic and dark matter components. The preliminary results indicate that KURVS galaxies are dark matter dominated, even at the effective radius, and the dark matter profiles are consistent with theoretical models of adiabatic contraction.

5.1 Introduction

Galaxy rotation curves, describing galaxies' circular velocity as a function of galactocentric radius, provide key measurements of the total (baryonic and dark matter) mass distributions in galaxies. The first speculation of "invisible matter" was

made in the mid-20th century, when rotation measurements revealed large velocities (and flat rotation curves) and raised questions about mass distribution in clusters (Zwicky, 1933) and galaxies (e.g. Babcock, 1939; Oort, 1940). Early radio observations of the rotation curve of M31 using the HI 21 cm emission line showed that the rotation of the galaxy remains approximately flat far beyond the optical radius (≈ 25 kpc; van de Hulst et al., 1957). This is contrary to the expected Keplerian decline, and indicated that there could be large amounts of 'invisible' mass that has a much larger extent than the visible matter (Schmidt, 1957), assuming that the Newtonian physics applies on large scales. The existence of dark matter was later comprehensively acknowledged in early 1970-80s with more statistically robust measurements. The velocities of 67 HII regions in the disk of M31 were measured by Rubin & Ford (1970), showing that the enclosed dynamical mass of the galaxy continues to rise out to at least 24 kpc, far beyond the optical radius. By mid-80s, flat rotation curves (at radii up to 50kpc) were found to be ubiquitous in high luminosity spiral galaxies (Bosma, 1978; Rubin et al., 1978, 1980, 1982, 1985). During this period, the work of observers and theorists converged, culminating in a general assertion that galaxies are immersed in extended dark matter halos (Ostriker & Peebles, 1973; Ostriker et al., 1974; Davis et al., 1985; Frenk et al., 1985). Many subsequent studies of rotation curves of galaxies have confirmed these early results (for a review see Sofue & Rubin, 2001, and references therein). The shapes of the rotation curves remain one of the fundamental pillars of the dark matter paradigm, together with evidence from mass distribution in cluster galaxies (Zwicky, 1933), and strong and weak gravitational lensing (Walsh et al., 1979). Together, these different approaches all suggest that dark matter constitutes a significant fraction ($\approx$24 per cent) of the total energy budget of the Universe (Freedman & Turner, 2003), a significantly larger fraction than that of baryonic matter (≈ 4 per cent).

Currently, the ΛCDM paradigm, where the Universe is dominated by the cold dark matter (CDM) and the cosmological constant (e.g. Blumenthal et al., 1984; Spergel et al., 2003), is the most widely accepted framework for structure forma-

tion and evolution in the Universe. In this framework, gravity drives bottom-up structure formation, where small primordial perturbations (in an otherwise smooth matter distribution) are amplified under gravity, forming initial dark matter haloes (e.g. Davis et al., 1985). Primordial gas cools at the centers of dark matter halos, collapses and star formation starts, eventually forming galaxies (White & Rees, 1978). The latest cosmological simulations, such as Horizon-AGN (e.g. Dubois et al., 2016); Illustris (Genel et al., 2014; Vogelsberger et al., 2014a,b) and the Evolution and Assembly of GaLaxies and their Environments (EAGLE; Schaye et al., 2015), are built on the ΛCDM theory. They successfully recreated some of the observed properties and characteristics of our Universe, including the redshift evolution of the galaxy stellar mass function (e.g Genel et al., 2014; Furlong et al., 2015), the evolution of the mass-size relation of galaxies (e.g Furlong et al., 2017), and the local fundamental plane (Tully & Fisher, 1977; Vogelsberger et al., 2014b; Ferrero et al., 2017). These models also make predictions for the redshift evolution of baryonic and dark matter fractions within galaxies, although these can vary substantially depending on the sub-grid recipes which attempt to capture the baryonic processes (Peirani et al., 2017; Lovell et al., 2018).

The general consensus on the need for dark matter in galaxy formation and evolution, as well as its dominance in the mass budget of galaxies, is mainly based on studies carried out at low-to-intermediate redshifts ($z \lesssim 0.5$–1), however there is less direct observational evidence for this to be the case at high redshift ($z \gtrsim 1$). While studies of galaxy rotation curves at $z \lesssim 1$ have primarily used atomic hydrogen (HI) 21 cm emission lines, such an approach is not currently possible for more distant galaxies as the emission becomes increasingly faint at increasing redshift ($z > 1$, Abdalla et al., 2015). Interferometric millimeter (e.g. ALMA) observations, of carbon monoxide (CO) and ionised carbon [CII] emission, can now be used to trace high redshift galaxy rotation curves out to a few disk scale radii (Ivison et al., 2010; Genzel et al., 2013; Übler et al., 2018; Rizzo et al., 2021). However, the lack of multiplexing capability of ALMA and NOEMA and the faintness of CO in these 'main-sequence' star-forming galaxies makes surveys prohibitively expensive for all

but a very small number of individual systems.

Recently, the technological advances in the near-infrared integral field spectroscopy allowed detailed study of the kinematics of star-forming galaxies (SFGs) at $z = 1$–3 by tracing the ionised emission (e.g. Hα), in particular with the use of KMOS, SINFONI on VLT and OSIRIS on the Keck telescope. However, the typical integration times of ~ 5–20 h adopted in large scale surveys (e.g. SINS; Förster Schreiber et al. 2009, KROSS; Stott et al. 2016; Harrison et al. 2017, KMOS3D; Wisnioski et al. 2015, 2019, KDS; Turner et al. 2017) only allow tracing of the ionised emission out to a few times the galaxy disk-scale radius, equivalent to ~ 1.5 times the half-light radius or $\sim$7 kpc (e.g. Förster Schreiber et al., 2009; Kriek et al., 2015; Wisnioski et al., 2015; Stott et al., 2016; Turner et al., 2017). To match the typical extent of Hα and HI rotation curves measured in the local Universe, and facilitate direct comparison between the two epochs, measurements out to much larger radii, e.g. three times the effective radius, $R_{\rm e}$, are needed at high redshift (Catinella et al., 2006, 2007).

Novel methods, such as stacking Hα emission, have been used to overcome these shortcomings. For example, Lang et al. (2017) suggested that the stacked rotation curve of 101 star-forming galaxies at $z = 0.6$–2.6 exhibits a significant decline at large radii ($\gtrsim$8 kpc), at odds with the flat or rising curve expected for local disk galaxies of similar stellar mass and more consistent with a strongly baryon-dominated system (at least in its central regions) with a correspondingly small dark matter fraction. However it has been demonstrated that subtle differences in how the data are scaled in the stacking can result in large differences in the final derived rotation curves, ranging from flat to declining, which potentially leads to very different conclusions on the significance of dark matter in galaxies at high redshift (Tiley et al., 2019). Recently, individual rotation curves have been analysed for 41 (15 at z=0.6–1.0 and 26 at z=1.2-2.45) massive galaxies by Genzel et al. (2020) (see also Genzel et al., 2017). These studies have found low dark matter fractions in the central regions ($\sim R_{\rm e}$). Together, these results might suggest that dark matter contribution may be much lower in the distant Universe. However,

these studies focus on the very massive end of the 'main-sequence', thus studies of more typical star-forming galaxies, as well as with much deeper Hα observations, are needed to address this issue in detail.

The aim of this chapter is to describe an on-going project to decompose individual $z \sim 1.5$ galaxy rotation curves using very deep (~ 100 h) KMOS integrations from the KMOS Ultra-deep Rotational Velocity Survey (KURVS; PI: M.Swinbank). Using Hα rotation curves that extend out to $\sim 3R_{\rm e}$ ($\sim$12–15 kpc) and resolved 2D stellar mass maps derived from *HST* photometry, we decompose the total mass profile from the Hα dynamics into the baryonic and dark matter components to measure the fraction of dark matter in star-forming galaxies at $z \sim 1.5$ on a case-by-case basis. The chapter is structured as follows. In § 5.2, we introduce the sample and the photometry available for the analysis. § 5.3 explains the SED fitting to derive the 2D stellar mass maps. We describe the method of deriving the mass profiles of each of the mass components (dynamical, stellar, gaseous and dark matter) in § 5.4. We present preliminary results and discussion of the on-going analysis in § 5.5 and note the current conclusions in § 5.6.

5.2 Sample selection and observations

The KURVS VLT Large Programme builds upon the KMOS Galaxy Evolution Survey (KGES, Tiley et al., 2019, 2021), which was a 27 night GTO programme with KMOS studying a statistical sample of star-forming galaxies at $z \sim 1.5$ through redshifted Hα emission in the H-band ($\lambda_{\rm obs} = 1.45$–1.87μm). For a detailed description of the KGES survey, see Tiley et al. (2019, 2021). The KURVS survey targets Hα ($\lambda_{\rm rest} = 0.65628\,\mu$m) nebular emission in 46 star-forming 'main-sequence' galaxies in the CDFS and COSMOS fields. While observations in the COSMOS field are still on-going, the 22 galaxies in the CDFS field are fully complete. 20 our of 22 sources in the CDFS field are selected from the KGES survey while the other two galaxies are selected from the KMOS3D survey (Wisnioski et al., 2019). In this chapter we analyse 18 sources from the KGES survey for which the data reduction

analysis and photometry extraction is complete.

The KMOS observations of the CDFS field were taken between 2018 Oct and 2019 Dec, using 120 observation blocks (OBs) and equating to a total integrating time of ∼100 hours. The average full width half maximum (FWHM) of the seeing for these observations is ∼0.57″. Full details of the observations and data reduction of the KURVS sample will be presented in Puglisi et al. (in prep). Briefly, the data were reduced using the European Southern Observatory (ESO) Recipe Execution Tool (Esorex), which extracts, wavelength calibrates and flat fields the integral field unit (IFU) spectra. The sky subtraction is performed on a frame by frame basis and the remaining sky residuals in the observations are removed with the use of the Zurich Atmospheric Purge tool (ZAP; Soto et al., 2016). The KMOS IFU field of view (2.8″ × 2.8″) corresponds to a physical diameter of ∼24 kpc at $z = 1.5$, which is ∼5–10 times the typical effective radius of star-forming galaxies at these redshifts (e.g. Suess et al., 2019). Hα velocity fields and velocity dispertion maps for the 18 CDFS sources are shown in Fig. 5.1. A brief description of the extraction of velocity rotation curves from the KMOS cubes is given in § 5.4.2.

KURVS sample sources are representative of the star-forming 'main-sequence' at $z \sim 1.5$. To compare with the star-forming galaxy populations studies in Chapters 3 and 4, in Fig. 5.2 we show KURVS galaxies together with the 850μm and 450μm-selected sources in terms of SFR and stellar mass. This comparison to dust-obscured strongly star forming sources (870μm-selected galaxies; from AS2UDS) and more typical dust-obscured star-forming galaxies (450μm-selected galaxies from STUDIES) shows that KURVS galaxies are the lower stellar mass tail of the 450μm-selected star-forming population.

5.2.1 Photometric coverage

To construct stellar mass maps for each galaxy, we exploit the multi-wavelength photometry available for the KURVS sample. The KURVS galaxies lie in the Cosmic Assembly Near-infrared Deep Extragalactic Legacy Survey (CANDELS) region of the CDFS field (Grogin et al., 2011; Koekemoer et al., 2011), thus the

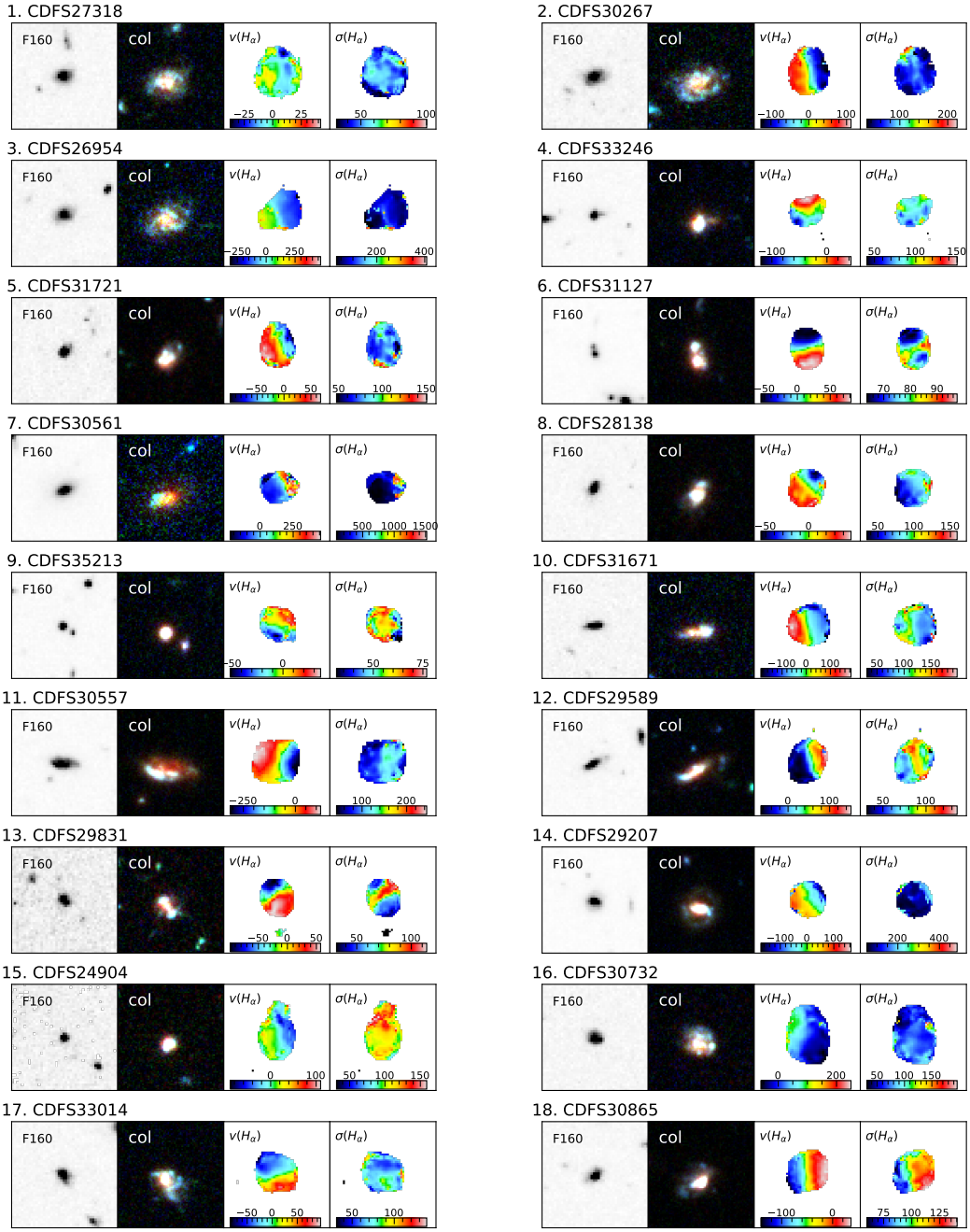

Figure 5.1: Observed properties of KURVS sample galaxies. From left: *HST* F160W thumbnail; *HST* color image constructed from the F160W,F814W and F606W bands; Hα velocity field and its velocity dispersion.

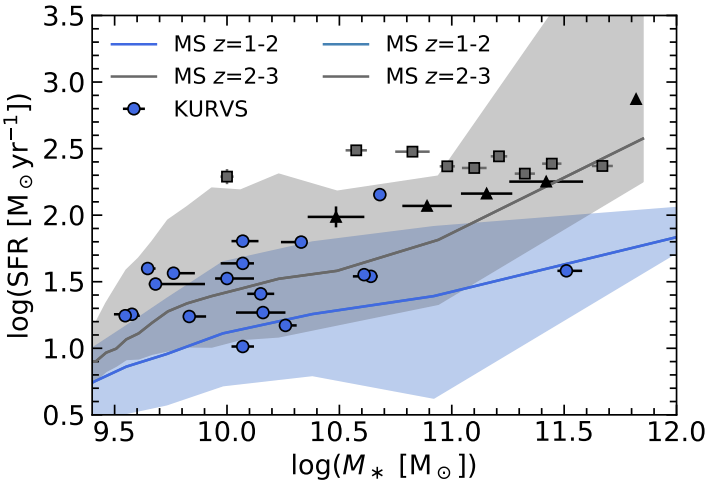

Figure 5.2: The star-formation rate as a function of stellar mass for the $z \sim 1.5$ KURVS sources. 850μm-selected galaxies from AS2UDS studied in Chapter 3 and $z \sim 1.8$ 450μm-selected star-forming galaxies from STUDIES analysed in Chapter 4 are shown for comparison. The "main-sequence" constructed from the UDS K-band field galaxies (Dudzevičiūtė et al., 2020) at relevant redshifts is overlaid for comparison. The KURVS sample is representative of the main sequence at $z \sim 1.5$.

sample has extensive multi-wavelength *HST* coverage. The CANDELS data consist of imaging obtained in the Wide Field Camera 3 and the Advanced Camera for Surveys (ACS). We make use of the images in 10 photometric bands in total: WFC3 F336W, WFPC2 F450W, ACS F606W, ACS F775W, ACS F814W, ACS F850W, WFC3 F105W, WFC3 F125W, WFC3 F140W and WFC3 F160W. These data are publicly available via MAST HLSP*. The images are already aligned and zero-pointed and are at a pixel scale of 0.06″. As the point spread function (PSF) of the reddest band (F160W) is $\sim$0.2″ FWHM, we rebin images in all bands by 3×3 so that the pixel scale roughly matches the PSF of the F160W band.

To obtain the pixel fluxes in each band (which we will later use to construct the 2D stellar mass maps), we co-add all images creating a detection image. We run SExtractor (Bertin & Arnouts, 1996) on the detection images to create a mask. To extract the SExtractor regions we make a cut at 2σ on the combined-filter detection image. We note that even though 2σ is a low isophotal threshold, we are able to exclude any noisy regions and non-detections later in individual bands (see § 5.3.1 for details). For every galaxy, we compared the sum of the pixel photometry

*https://archive.stsci.edu/hlsps/hlf/v2.0/60mas/

to the integrated *HST* photometry in each band and found good agreement, with differences comparable to the aperture correction.

The CDFS field has extensive ancillary photometric data, spanning a wide wavelength range. As a consistency check, in § 5.3.1.1 we also make use of the galaxy integrated mid-infrared photometry from *Spitzer* IRAC (3.6–8 μm), which was imaged as part of the GOODS *Spitzer* Legacy Program (PI: M. Dickinson).

5.3 2D stellar mass maps

The main aim of this on-going study is the direct comparison of the differences between baryonic and the dynamical masses to infer the dark matter fraction in individual star-forming galaxies at $z \sim 1.5$. This section discusses the methods used to extract consistent mass profiles of the different mass components, including the construction of stellar mass maps and the subsequent smoothing to match the seeing to the Hα observations.

5.3.1 Spatially-resolved SED fitting

To derive the pixel-by-pixel stellar mass maps of the KURVS sample galaxies we employ MAGPHYS (da Cunha et al., 2015) to model the optical spectral energy distributions at each pixel, using the available *HST* photometry in 10 bands. This model allows us to constrain the physical parameters of the galaxies, as well as provides a consistent methodology to that applied to the integrated photometry for the KURVS galaxies as part of the KGES sample analysis (Gillman et al., 2020). Thus, the physical properties of the galaxies can be investigated for any differences arising from integrated versus pixel-by-pixel analysis. This version of MAGPHYS is identical to the MAGPHYS+photo-z version (Battisti et al., 2019) described in Chapter 2 in terms of the optical and infrared models used for the fitting. However, the redshift is fixed to the spectroscopic redshift of the source, thus reducing the uncertainties in the derived physical properties. We remind the reader that the code uses stellar population models from Bruzual & Charlot (2003) and a Chabrier

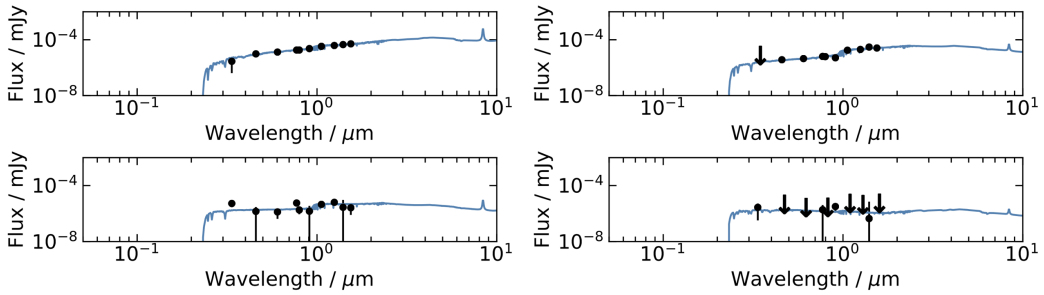

Figure 5.3: Examples of observed-frame best-fitting optical spectral energy distributions to the 10 *HST* photometric bands for four individual pixels in galaxy CDFS30267. The arrows indicate 3σ upper limits in the photometric observations. The photometry is fit well by the models, however at these redshifts *HST* does not sample the rest-frame 1.6-μm stellar bump. Therefore, we conduct further tests in § 5.3.1.1 to confirm the reliability of the derived total stellar mass from the pixel-by-pixel analysis.

(2003) IMF. Full description of this MAGPHYS code and parameter derivation can be found in da Cunha et al. (2015).

We fit the available photometry in each pixel of each galaxy and in case of limits (SNR$\leq$ 3) in any given band, we adopt expectation flux density values of 0 with $\pm3\sigma$ error. Example of best-fitting SEDs to four individual $0.18\times0.18''$ pixels for a KURVS sample galaxy CDFS30267 is shown in Fig. 5.3. We run MAGPHYS on all pixels within the SExtractor region (see § 5.2.1) for each of the KURVS galaxies to obtain a spatially resolved 2D stellar mass map.

5.3.1.1 Robustness of the derived stellar mass

As mentioned in § 5.2.1, the cut for the SExtractor regions to extract pixels capturing the emission from a given galaxy is at 2σ on the combined-filter detection image. Consequently, a significant number of outer pixels have increasingly large numbers of limits in individual photometric bands, which increases the uncertainty in the derived stellar mass and in some cases leads to unphysically large estimates of stellar mass (when compared to surrounding pixels). Therefore, for any pixels with fewer than two detections, we adopt a median mass-to-light ratio of the source to obtain an estimate of the stellar mass at that pixel using observed F160W. We note that the fitting had catastrophic failures in either one or two individual pixels

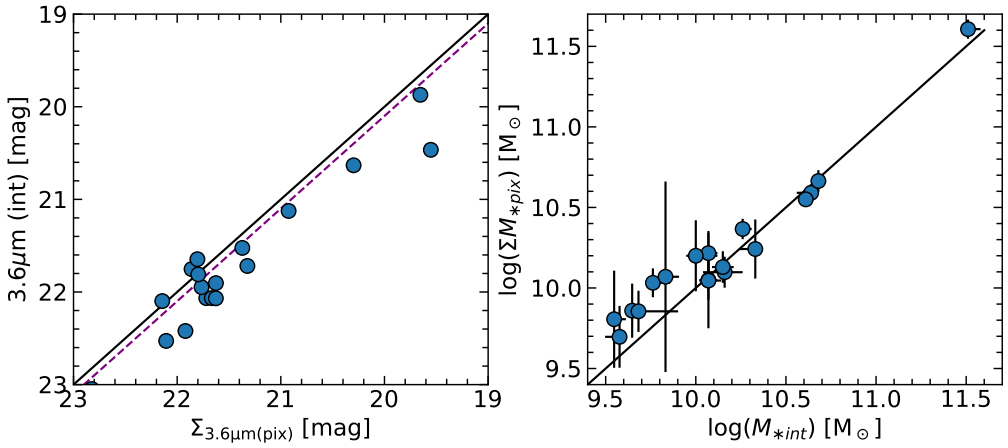

Figure 5.4: **Left:** The integrated IRAC Channel 1 (3.6μm) magnitude versus the predicted 3.6μm magnitude from the sum of best-fitting SEDs of the individual pixels. As shown in Fig. 5.3, the *HST* photometry does not have coverage in the rest-frame near-infrared, where the H-band stellar bump ($\lambda_{\rm rest} \sim 1.6\,\mu$m) lies at the redshift of the KURVS sample ($z \sim 1.5$). The available IRAC data does not have the required resolution to perform pixel-by-pixel analysis, thus we compare the integrated 3.6μm magnitude to the predicted magnitude from pixel-by-pixel analysis to ensure the robustness of the fitting model. We see that the sum of individual pixels returns a magnitude that is, on average, ~ 8 per cent higher than the integrated value (purple dashed line). This offset is within the systematic uncertainties in the photometry and the derived stellar mass. **Right:** The stellar mass from integrated photometry fits (up to and including IRAC Channel 4 8μm) versus the sum of the stellar masses derived from pixel-by-pixel SED fitting. All KURVS sources follow a 1:1 trend within the error, confirming the reliability of the pixel-by-pixel analysis.

for five of the sample galaxies. We have excluded those pixels in comparisons made in this section and replaced them with model values in any further analysis (see § 5.4.1.1). This results in a final 2D stellar mass map of a given galaxy.

The best stellar mass indicator in terms of wavelength is rest-frame H-band, which samples the stellar "bump" at 1.6 μm that arises due to the H^- opacity minimum (John, 1988; Sawicki, 2002). At the redshift of the KURVS sample ($z \sim 1.5$) this feature is redshifted to $\sim 4\mu$m into the IRAC bands. As seen in Fig. 5.3, the pixel-by-pixel photometry does not cover this wavelength range. The SED is constrained out to $\lambda_{\rm obs} \sim 1.6\,\mu$m (rest-frame R-band). Therefore, to check for any systematic differences we compared the flux obtained from the sum of the best-fitting SEDs of all pixels to the galaxy integrated IRAC photometry. KURVS galaxies have IRAC

3.6 μm coverage, and thus have galaxy integrated photometry sampling the stellar "bump". We sum the predicted 3.6 μm flux densities of the best-fitting SED from all individual pixels of a given galaxy and compare with the integrated IRAC 3.6 μm values in Fig. 5.4. Overall, the photometric predictions agree with the integrated values, with a median offset in flux density of $|3.6_{\rm int} - 3.6_{\rm pix}|/3.6_{\rm int} \simeq 0.08$, which is comparable to the expected uncertainty in the aperture correction.

In addition, MAGPHYS SED fitting was performed on the integrated optical and near-infrared photometry, up to IRAC 8 μm by Gillman et al. (2020). In Fig. 5.4, we compare the sum of the pixel-by-pixel stellar mass results with the stellar mass derived from the integrated photometry SED fitting. No significant offsets are found for any KURVS sources, with a 1:1 trend within the uncertainty. Thus, these tests indicate no significant systematic offsets when fitting pixel-by-pixel *HST* photometry to derive stellar masses of KURVS galaxies.

5.4 Decomposition of galaxy rotation curves

The overall rotation curve, as traced by the kinematics of the Hα emitting gas in the galactic disk of a galaxy, is determined by the sum of baryons in the disk and the bulge, and dark matter in the halo. To decompose this rotation curve into its constituent components, most studies use parametric models for the stellar, gaseous and dark matter components (Genzel et al., 2017, 2020; Lang et al., 2017; Rizzo et al., 2021). The available spatially resolved stellar mass maps allows us to improve the constraints on the stellar rotation curve, as minimal assumptions about the shape of the stellar profile are made, which in turn will improve the reliability of the dark matter estimates. This section outlines the methods used to decompose the Hα rotation curves to the baryonic and dark matter components.

5.4.1 Baryonic component

We construct the baryonic contribution to the rotation velocity of a given galaxy using two components: the stellar component which encompases the bulge and the

disk, and an additional gaseous component modelled with a Sérsic profile. The following sections describe the method in detail.

5.4.1.1 Stellar component

To obtain the structural parameters, such as morphological major axis and inclination of each galaxy, we fit a Sérsic profile to the 2D stellar mass maps:

$$I(r) = I_{\rm e} exp\left\{-b_n\left[\left(\frac{r}{r_e}\right)^{\frac{1}{n}} - 1\right]\right\} \tag{5.1}$$

where $I_{\rm e}$ is the intensity at effective radius, $r_{\rm e}$. The value of b_n is such that $\Gamma(2n) = 2\gamma(2n, b_n)$, where Γ is the complete gamma function and $\gamma(2n, b_n)$ is the incomplete gamma function. To optimise these parameters we use a Markov Chain Monte Carlo (MCMC) sampling, with an example shown in Fig. 5.5. We construct a point spread function (PSF) to be applied to the Sérsic models using the F160W image. We extract all point-sources using the CANDELS GOODS-S multiwavelength catalogue (Guo et al., 2013), normalise them to the same peak flux and calculate the stacked median image. The resulting PSF image is then rebinned by 3×3 to match the pixel scale of the 2D stellar mass maps. This PSF is then convolved with the Sérsic models in the MCMC fitting. We resample the posterior distributions of each parameter to constrain the output parameters to the 16-84th percentile range. This forms the final 500 models for each galaxy that encompass the best-fit (median) solution as well as the uncertainties in the model parameters. These 500 models are used for subsequent analysis to define the error range from the Sérsic profile modelling. The median values of the Sérsic profile parameters for each KURVS source are summarised in Table 5.1.

We infer the inclination, i, from the axial ratio b/a derived from fitting the 2D stellar mass maps using:

$$\cos(i) = \sqrt{\frac{(b/a)^2 - q_0^2}{1 - q_0^2}} \tag{5.2}$$

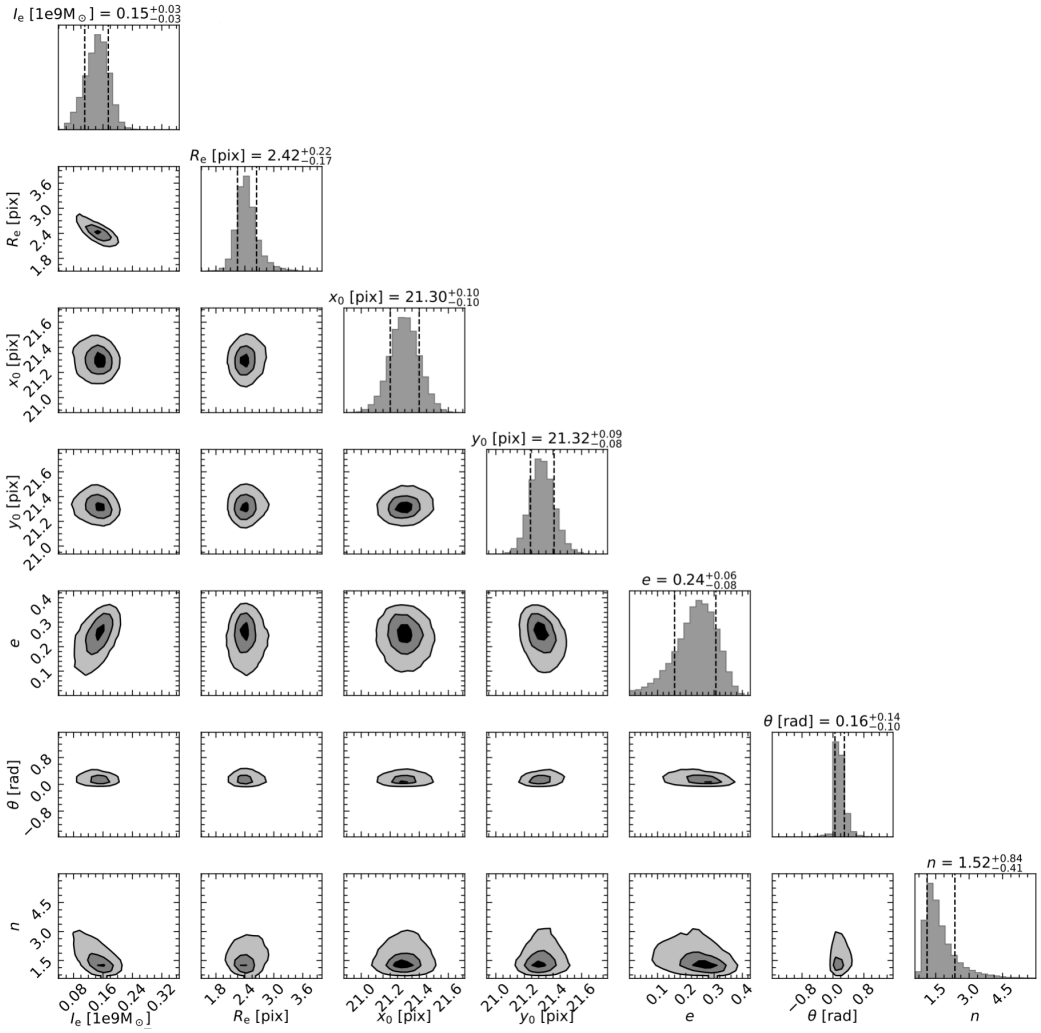

Figure 5.5: Markov Chain Monte Carlo (MCMC) fitting to the 2D stellar mass map of a KURVS galaxy CDFS30267. The fitted parameters are intensity at the effective radius (I_e), intrinsic effective radius (R_e), centre of the galaxy (x_0, y_0), ellipticity (e), positional angle (θ) and Sérsic index (n) (see Eq. 5.1). For each of the galaxies, we select the 16-84th percentile values of each parameter, to fully include the model uncertainties in the analysis.

Table 5.1: Best-fitting Sérsic parameters for KURVS sources: effective radius (R_e), position angle (PA), inclination (i), and Sérsic index (n). Errors on individual sources are the 16–84th percentile values of a given parameter. The median and its error are calculated by combining the probability distributions of all sample galaxies for a given parameter.

ID	R_e [kpc]	PA [deg]	i [deg]	n
CDFS27318	$3.11^{+0.18}_{-0.19}$	2^{+36}_{-36}	22^{+11}_{-8}	$4.2^{+1.2}_{-1.1}$
CDFS30267	$3.70^{+0.20}_{-0.18}$	9^{+8}_{-6}	41^{+8}_{-6}	$1.5^{+0.8}_{-0.4}$
CDFS26954	$3.36^{+0.23}_{-0.19}$	33^{+10}_{-9}	41^{+8}_{-5}	$4.0^{+1.3}_{-1.1}$
CDFS33246	$2.7^{+0.3}_{-0.2}$	33^{+23}_{-24}	35^{+15}_{-9}	$1.5^{+1.9}_{-0.5}$
CDFS31721	$3.7^{+0.3}_{-0.2}$	41^{+7}_{-8}	48^{+7}_{-5}	$2.1^{+1.3}_{-0.8}$
CDFS31127	$3.9^{+0.3}_{-0.3}$	96^{+4}_{-4}	52^{+5}_{-5}	$0.52^{+0.06}_{-0.05}$
CDFS30561	$4.3^{+0.2}_{-0.2}$	16^{+6}_{-18}	62^{+21}_{-8}	$4.1^{+1.3}_{-1.9}$
CDFS28138	$3.04^{+0.19}_{-0.16}$	69^{+8}_{-8}	39^{+7}_{-6}	$1.0^{+0.5}_{-0.2}$
CDFS35213	$1.73^{+0.16}_{-0.16}$	126^{+41}_{-36}	28^{+13}_{-10}	$0.5^{+0.3}_{-0.2}$
CDFS31671	9^{+2}_{-2}	83^{+8}_{-7}	69^{+6}_{-6}	$1.7^{+1}_{-0.6}$
CDFS30557	$8.6^{+1.5}_{-1.2}$	128^{+6}_{-7}	55^{+8}_{-5}	$1.3^{+0.7}_{-0.5}$
CDFS29589	$4.1^{+0.2}_{-0.3}$	33^{+3}_{-3}	71^{+3}_{-3}	3^{+2}_{-1}
CDFS29831	$2.2^{+0.3}_{-0.3}$	8^{+14}_{-14}	45^{+17}_{-8}	$3.9^{+1.5}_{-1.3}$
CDFS29207	$2.55^{+0.12}_{-0.11}$	103^{+20}_{-22}	23^{+8}_{-6}	$1.6^{+0.4}_{-0.2}$
CDFS24904	$1.8^{+0.3}_{-0.3}$	128^{+14}_{-15}	49^{+16}_{-8}	$3.4^{+1.9}_{-1.6}$
CDFS30732	$3.20^{+0.19}_{-0.16}$	151^{+28}_{-22}	24^{+11}_{-7}	$0.8^{+0.2}_{-0.2}$
CDFS33014	$3.2^{+0.2}_{-0.2}$	119^{+4}_{-4}	58^{+3}_{-3}	$3.8^{+1.5}_{-1.1}$
CDFS30865	$3.6^{+0.2}_{-0.2}$	29^{+4}_{-4}	54^{+4}_{-3}	$1.5^{+0.7}_{-0.4}$
Median	$\mathbf{3.3}^{+0.9}_{-0.8}$	$\mathbf{55}^{+72}_{-41}$	$\mathbf{47}^{+13}_{-20}$	$\mathbf{1.7}^{+2.3}_{-0.7}$

where q_0 is the disk thickness, the ratio of scale length to scale height. The ratio typically ranges between $q_0 \sim 0.1$–0.6 for rotationally supported galaxies at low redshift (Law et al., 2012; Weijmans et al., 2014). We adopt q_0=0.2, for consistency with other high redshift surveys (Wisnioski et al., 2015; Harrison et al., 2017; Tiley et al., 2019). Overall, the galaxies in KURVS sample have a median effective radius of $R_e = 3.3^{+0.9}_{-0.8}$ kpc, Sérsic index of $n = 1.7^{+2.3}_{-0.7}$ and an inclination of $i = 47^{+13}_{-20}$ deg. We find that the Sérsic index is the least constrained parameter, thus we also run the fitting procedure with the Sérsic index fixed to n=1, finding that the derived properties are consistent with the full parameter modelling. This confirms that the uncertainties in the Sérsic index do not have a significant impact on the median values of the derived parameters for the sample.

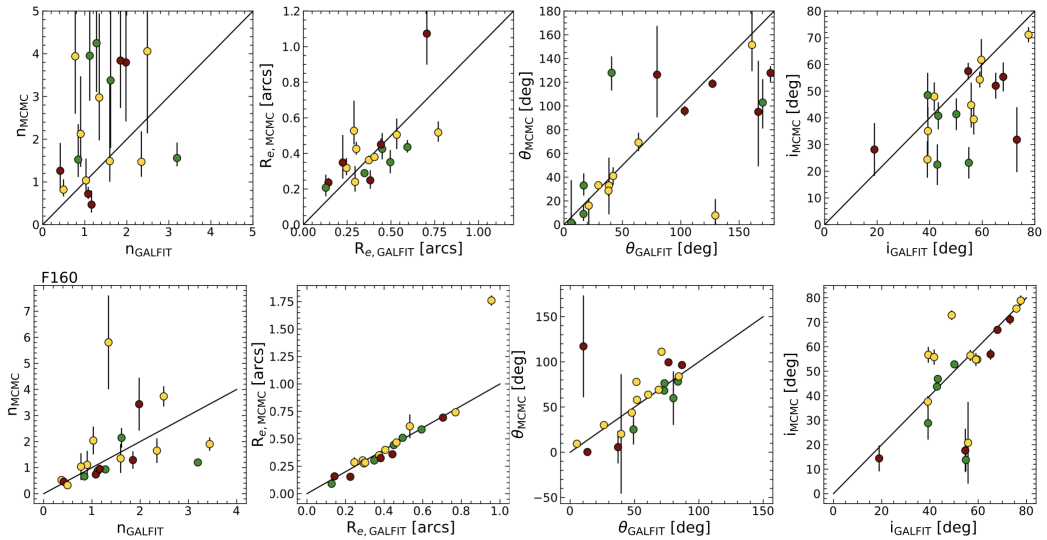

Figure 5.6: Comparison between different Sérsic profile fittings for KURVS galaxies. Green indicates morphologically regular systems, yellow shows slight disturbances, while red indicates morphologically disturbed galaxies. From left: Sérsic index, effective radius, positional angle and inclination. **Top row:** MCMC fitting to the stellar mass maps versus GALFIT fitting to the F160 photometry. **Bottom row:** MCMC fitting to the F160W photometry versus GALFIT fitting to the F160W photometry.

To further check our Sérsic profile modelling, we match our sample with the van der Wel et al. (2014) catalogue, who also derived the morphological properties of sources in the CDFS field by applying the GALFIT Sérsic modelling code (Peng et al., 2010) to the *HST* F160W image. Thus, we compare the fitting methods by running MCMC analysis on the F160W maps in Fig. 5.6. We note that there are a few differences in the methodology between us and van der Wel et al. (2014), such as different optimisation technique, pixel scale, and different mask maps, thus some differences are expected. Overall, as Fig.5.6 shows, we find good agreement in effective radii, positional angle and inclination results, with more scatter seen in the Sérsic index estimates. We also compare the published F160W results to the 2D stellar mass map best-fitting parameters in Fig. 5.6. As, on average, our methods are comparable to van der Wel et al. (2014) when running on the F160W images, any differences when run on stellar mass maps are likely not due to any systematic differences between the different fitting procedures. We see more scatter, especially in Sérsic index and inclination parameters. This is expected due to stellar mass maps providing more weight to evolved stellar populations and thus

is more sensitive to light from the bulge than F160W photometry alone, hence returning a systematically higher Sérsic index and potentially different inclination measurement. We also note that most of this scatter arises from galaxies that have disturbed morphologies from visual inspection (see Fig. 5.6).

The stellar mass maps and the median Sérsic model for each galaxy are shown in Fig. 5.7. For easier comparison, we also show the stellar mass surface brightness as a function of radius along the morphological kinematic axis extracted from stellar mass map and the median Sérsic model. Any differences seen for some galaxies (e.g. CDFS28138, CDFS30561) are not significant due to the errors in the stellar mass and the models, and this uncertainty is accounted for in further analysis. The final stellar mass map for each galaxy are shown in Fig. 5.7.

5.4.1.2 Gaseous component

To obtain the full baryonic contribution to the rotational velocity, the gas component has to be included. For this, we assume that the molecular gas is the main gas component in our high redshift galaxies, $M_{\rm gas} \approx M_{\rm mol}$, due to the steep evolution in H_2/HI ratio with redshift (Lagos et al., 2011; Tacconi et al., 2018). We note that the ionised gas contribution is only a small fraction of that of the molecular gas, therefore including the ionised component would not affect any of our conclusions while introducing additional uncertainties. The most robust way of including the gas contribution would be from direct CO measurements in the sub-millimetre wavelengths, however there are no available CO observations for the KURVS sources in the CDFS field. Therefore, we model the gas component assuming the same Sérsic profile (500 models) as the stellar component. The gas component is varied between $\mu_{\rm gas} = M_{\rm gas}/M_* = 0.3$–$0.5$. This is motivated by the empirical prediction from Tacconi et al. (2018) for the molecular gas evolution of main-sequence star-forming galaxies. The effective radius of the gas component is also allowed to vary between $R_{\rm e,*}$ and $2R_{\rm e,*}$, to allow for the possibility that the gas in a galaxy is more extended than the stellar component (e.g. Ivison et al., 2011). For each of the 500 Sérsic models, we calculate two gas components that

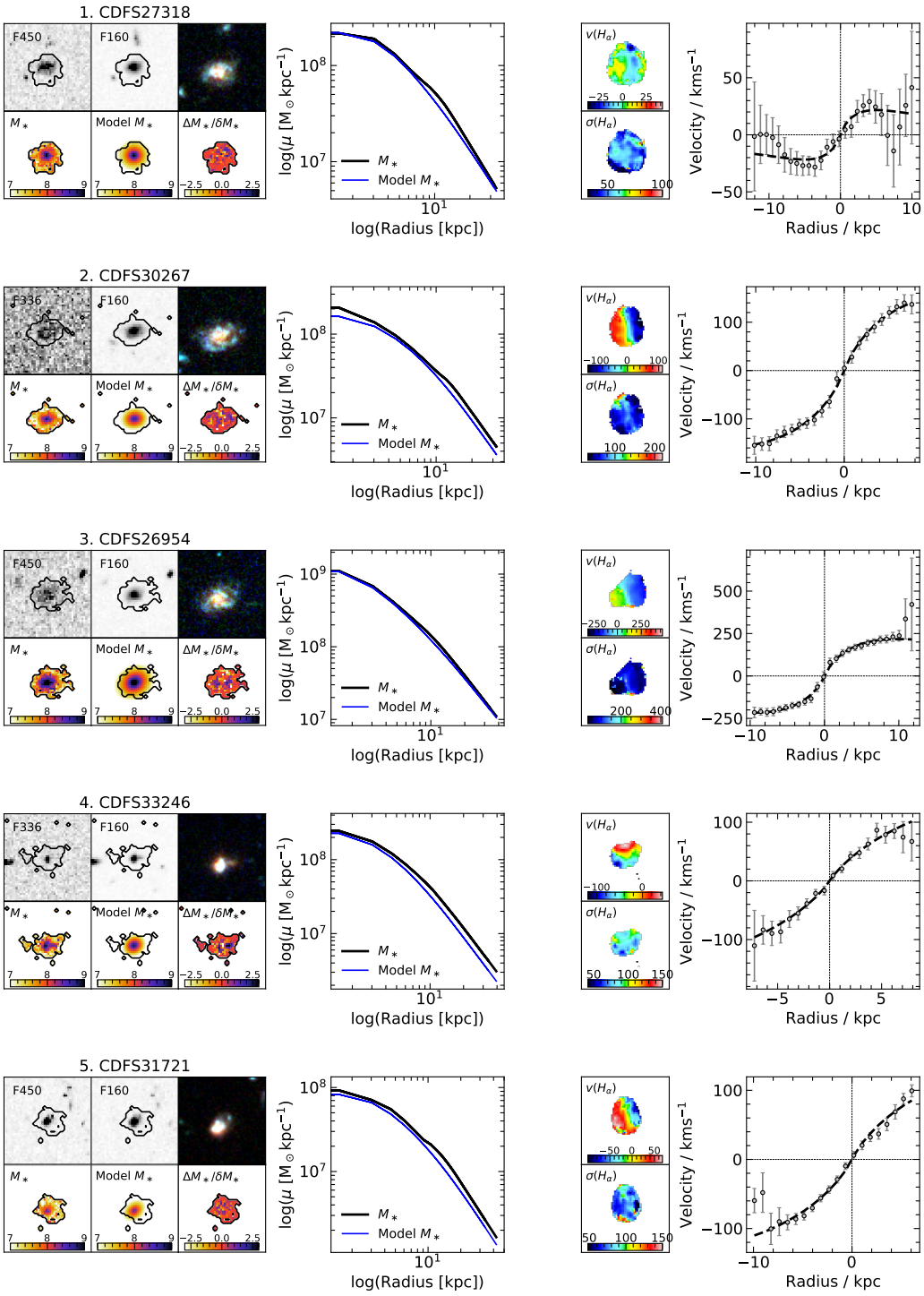
1. CDFS27318
F450
F160
M_*
Model M_*
$\Delta M_*/\delta M_*$
log(μ [M$_\odot$ kpc^{-1}])
log(Radius [kpc])
$v(H_\alpha)$
$\sigma(H_\alpha)$
Velocity / kms^{-1}
Radius / kpc
2. CDFS30267
F336
F160
3. CDFS26954
F450
F160
4. CDFS33246
F336
F160
5. CDFS31721
F450
F160

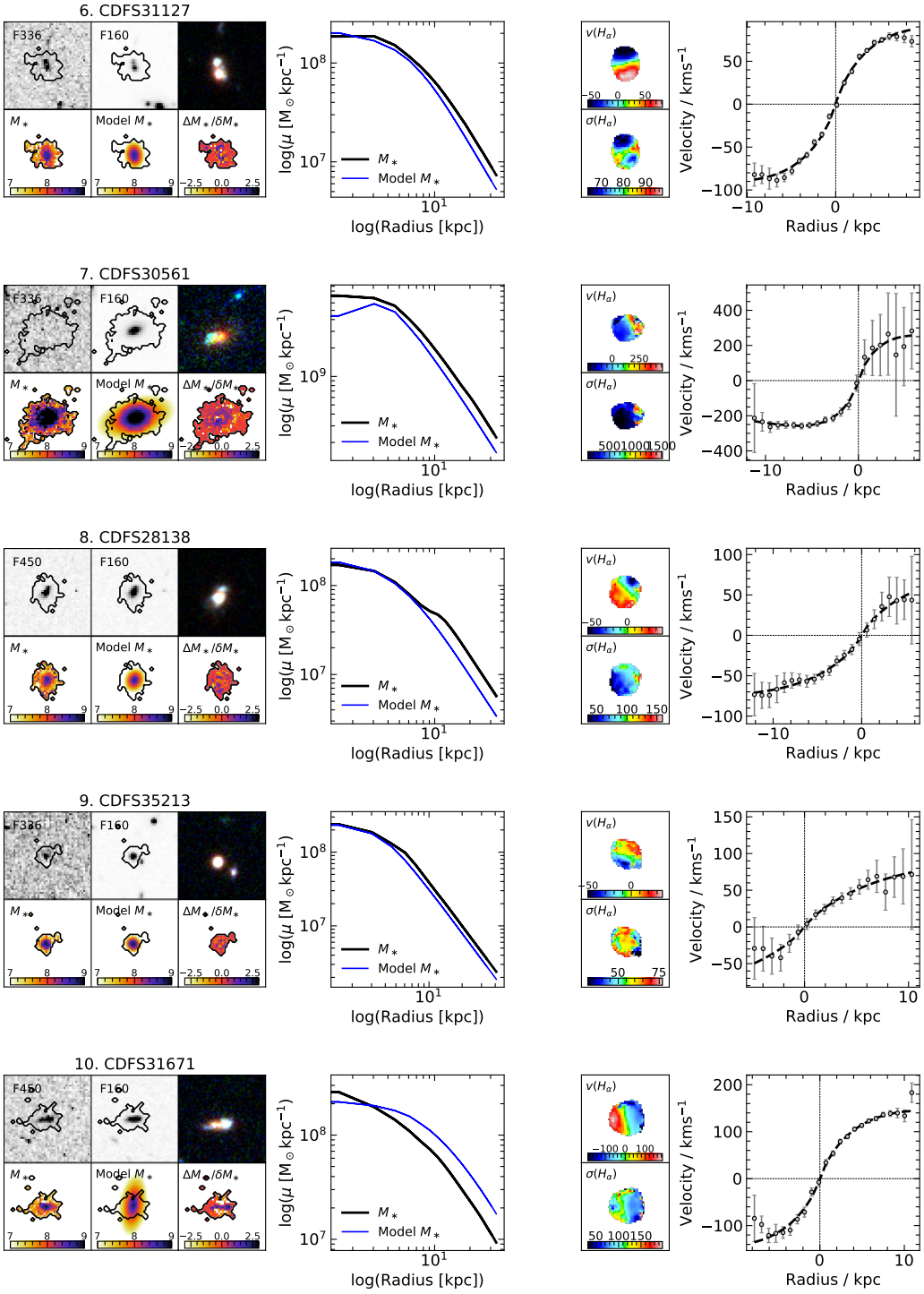
6. CDFS31127
F336
F160
M_*
Model M_*
$\Delta M_*/\delta M_*$
log(μ [$M_\odot$ kpc^{-1}])
log(Radius [kpc])
$v(H_\alpha)$
$\sigma(H_\alpha)$
Velocity / kms^{-1}
Radius / kpc
7. CDFS30561
8. CDFS28138
F450
9. CDFS35213
10. CDFS31671

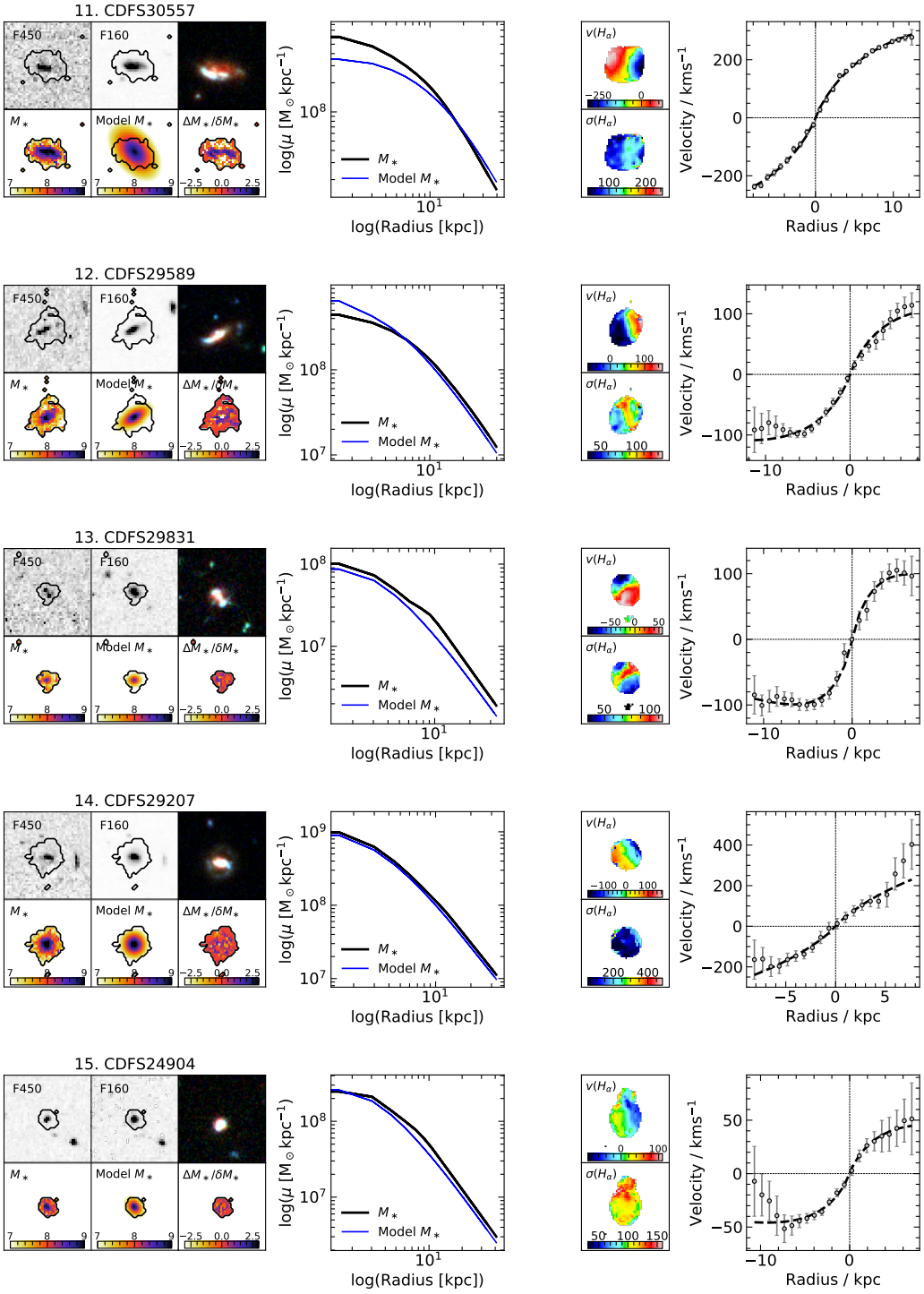
11. CDFS30557
12. CDFS29589
13. CDFS29831
14. CDFS29207
15. CDFS24904
F450
F160
M_*
Model M_*
$\Delta M_*/\delta M_*$
$\log(\mu\ [\mathrm{M_\odot\ kpc^{-1}}])$
log(Radius [kpc])
$v(H_\alpha)$
$\sigma(H_\alpha)$
Velocity / kms^{-1}
Radius / kpc

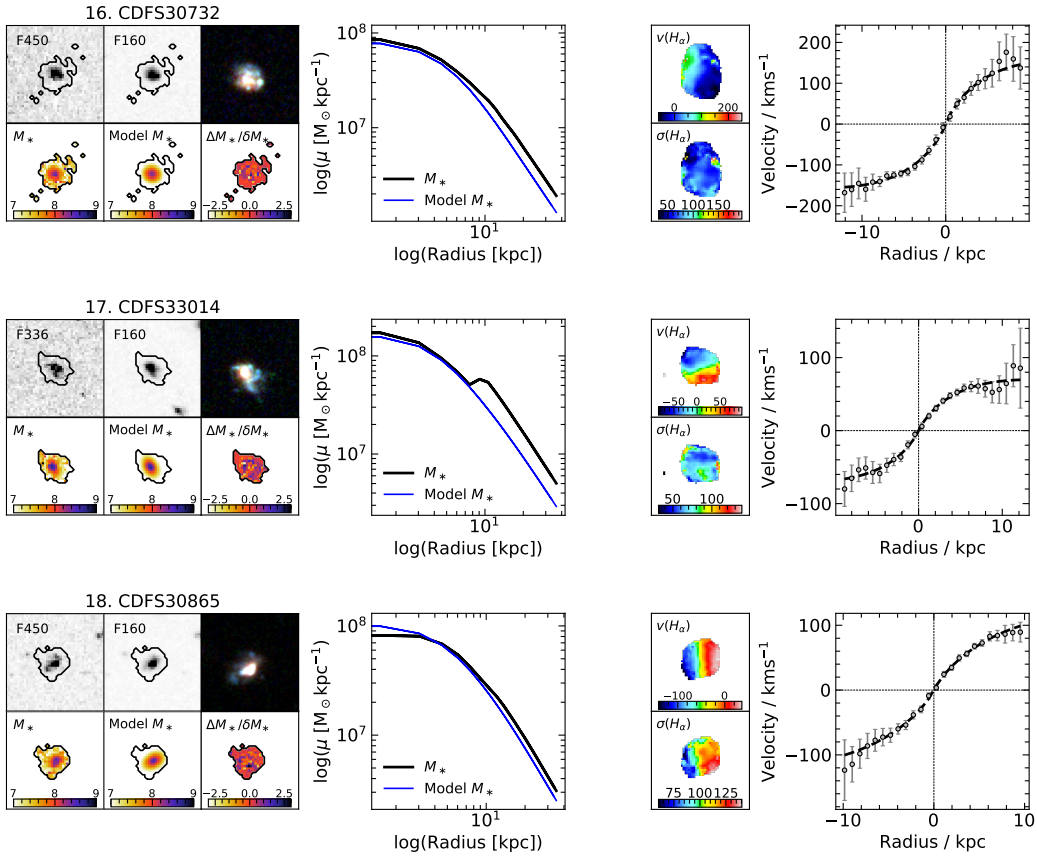

Figure 5.7: The morphological and kinematic properties of KURVS galaxies. **Left:** Top three panels show the bluest (F336W or F450W) and reddest (F160W) wavelength photometry thumbnails and the colour image for a given KURVS galaxy. The bottom three panels show the derived 2D stellar mass map from MAGPHYS fitting to individual pixels, best-fitting Sérsic model from MCMC analysis, and the fractional difference between them. Contours indicate the galaxy region obtained using SExtractor. The panel next to the thumbnails is showing the surface brightness as a function of radius obtained from the stellar mass map and the best-fit model. **Right:** The kinematic properties of KURVS galaxies from Puglisi et al. (in prep). Top panel is showing the Hα velocity field, and the bottom panel is showing the Hα velocity dispersion for a given galaxy. The extracted observed Hα rotation curve is shown on the right.

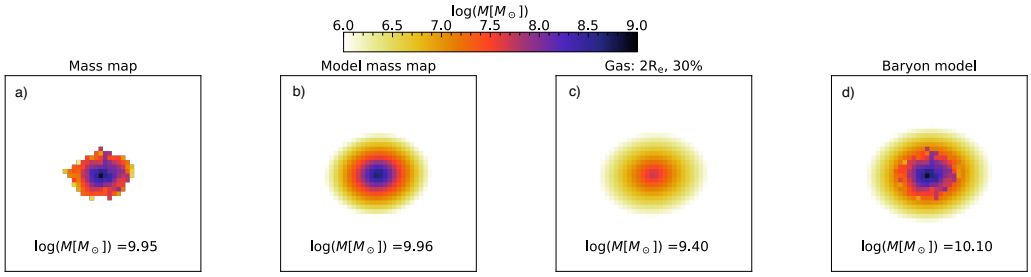

Figure 5.8: An example of the construction of a baryonic mass map. (a) the stellar mass map of CDFS30267 galaxy; (b) one of the 500 Sérsic models fitting this galaxy; (c) gas model assuming a gas fraction of 30 per cent and effective radius twice that of the stellar $R_{\rm e}$. The empty values in the stellar mass map are replaced by the Sérsic model values and this map is then combined with the gas map to produce the baryon mass model shown on in panel (d).

encompass the uncertainties in gas fraction and its scale length: one model with $R_{\rm e(}{\it gas}{\rm)} = R_{\rm e,*}$ and $\mu_{\rm gas} = 0.5$, which sets the upper limit of the mass profile at any given radius, and $R_{\rm e(gas)} = 2R_{\rm e,*}$ and $\mu_{\rm gas} = 0.3$, which sets the lower limit. An example of the gas component is shown in Fig. 5.8.

As an example, the construction of the final 2D baryonic mass map for CDFS30267 is shown in Fig. 5.8. We take the stellar mass map (panel a) and replace outer (empty) pixels with the model (panel b) values. We then add the gas map (panel c) to form the final baryonic mass map (panel d). This is repeated for all 500 model maps and the two maximal gas mass maps for each galaxy, resulting in 1000 baryonic mass maps for each galaxy. These 1000 models incorporate the uncertainties in the Sérsic model fitting as well as the assumptions for the gas component.

5.4.2 Dynamical component

In this section, we describe the derivation of the dynamical mass profile from the Hα maps of KURVS galaxies. The full description of Hα kinematics and extraction of the rotation curves is given in Puglisi et al. (in prep). Briefly, the Hα velocity fields were extracted from the KMOS cubes using an adaptive binning procedure (Stott et al., 2016; Tiley et al., 2019, 2021). For each spaxel, the flux is averaged in an increasing number of spaxels up to a 0.7×0.7" region, until $\rm S/N_{H\alpha} \geq 5$

is obtained, and the spectra fit with a combined Hα and [NII]$_{6548,6583}$ Gaussian profile. If a S/N$_{\mathrm{H}\alpha} \geq 5$ is not reached, that pixel is masked.

The Hα+[NII] spatially-resolved emission is modelled by applying the same procedure used to fit the one-dimensional spectra to each spatial pixel in the binned data-cube. The maps for the Hα line flux, observed line-of-sight velocity ($v_{\mathrm{pix}} - v_{\mathrm{sys}}$) and observed velocity dispersion (σ_{obs}) are constructed from the best-fit model. The velocity dispersion is corrected for the instrumental broadening as $\sigma_{\mathrm{int}} = \sqrt{\sigma^2_{\mathrm{obs}} - \sigma^2_{\mathrm{instr}}}$ where we measure the instrumental broadening, σ_{instr}, from the width of the sky lines. Error-bars on each map are the 1σ errors as obtained from the χ^2 minimisation routine. The velocity fields and velocity dispersion maps for each KURVS galaxy are shown in Fig. 5.7.

Using the 2D velocity field, the position angle of the kinematic major axis is calculated by rotating the observed velocity map in one degree steps and measuring the median velocity in a pseudo-slit with width of 5 pixels ($\sim 0.5''$) lying along the x-axis. The position angle is then the average between the angle that maximises the velocity gradient and the angle that minimises it at plus 90 deg. The rotation curve is extracted along the kinematic major axis by calculating the median velocity at each pixel within a pseudo-slit of 3 pixels radius, roughly corresponding to the width of the seeing in KURVS observations ($\sim 0.6''$). The same method is applied for extracting the velocity dispersion profile. Each rotation curve is fit with an exponential disc model (Freeman, 1970). The extracted observed Hα rotation curves are shown in Fig. 5.7.

In the CDFS field, the final extracted rotation curves extend out to $\gtrsim 3R_{\mathrm{e}}$ in 8/18 (44 per cent) of the sources, $\gtrsim 2R_{\mathrm{e}}$ in 16/18 (89 per cent) of the sources and $\gtrsim 1.5R_{\mathrm{e}}$ in 18/18 (100 per cent). Full data reduction and analysis of the shapes of the rotation curves is presented in Puglisi et al. (in prep).

The extracted observed velocity rotation curves are corrected for inclination (which was derived using using Eq. 5.2):

$$v_{rot} = v_{obs}/\sin(i) \tag{5.3}$$

The inclination-corrected rotation curve does not represent the intrinsic velocity curve, due to the effects of beam smearing and velocity dispersion. The former is an observational effect whereby the apparent velocity gradient at the galaxy centre is reduced, due to the convolution of the intrinsic velocity with the PSF (see Fig. 5.9), while the latter is an intrinsic effect. Star-forming galaxies at high redshift appear to have more turbulent disk structures (Förster Schreiber et al., 2009; Epinat et al., 2012; Wisnioski et al., 2015; Turner et al., 2017) than their local analogues as the velocity dispersion is increasing with redshift, and hence degree of the rotational support (as quantified by the v/σ ratio) decreases. Therefore, pressure support is a non-negligible part of their dynamics. This effect reduces the observed rotational velocity of the galaxy, hence pressure support needs to be taken into account in order to derive the dynamical mass of the system. As described in Burkert et al. (2010), the velocity rotation curve of a pressurised gas disk is:

$$v_0^2 = v_{\rm rot}^2 - 2\sigma^2 \frac{dln\Sigma}{dlnr} \tag{5.4}$$

where $v_{\rm rot}$ is the observed rotational velocity (which is corrected for inclination), σ is the intrinsic velocity dispersion, r is the galactocentric radius and Σ is the total mass surface density. For the latter term, we use a Sérsic profile derived from the 2D stellar mass fits, thus Eq. 5.4 can be expressed as:

$$v_0^2 = v_{\rm rot}^2 + 2\sigma^2 \frac{b_n}{n} \left(\frac{r}{r_{\rm e,conv}} \right)^{\frac{1}{n}} \tag{5.5}$$

Here, we use the convolved effective radius $r_{\rm e,conv}$, as we are adding the pressure-support term to the convolved dynamical component (see § 5.4.1.1 for more detail). Note that the pressure effects are increasingly significant for less rotationally supported systems ($v_{\rm rot}/\sigma \lesssim 3$) as well as at increasing radius from the centre of a given galaxy. Once the correction is applied to the observed inclination-corrected rotation curve (and the best-fitting exponential model of the rotation curve), the

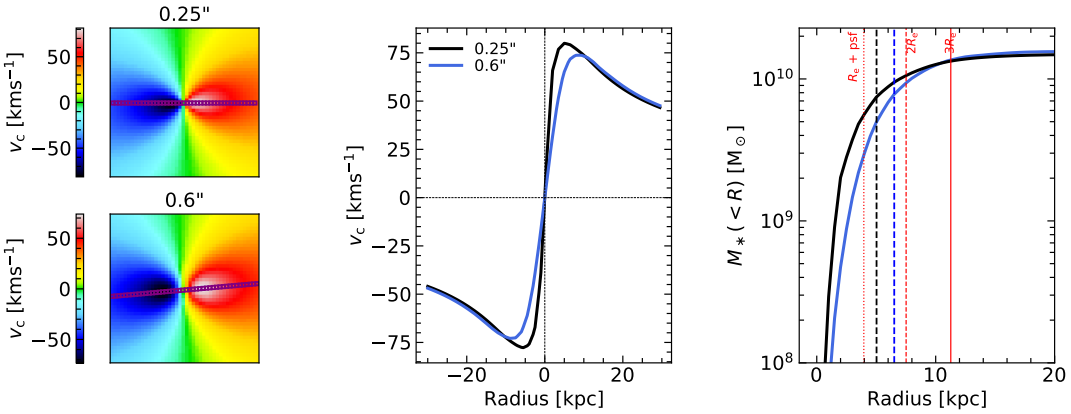

Figure 5.9: Example of the construction of stellar rotation curves and stellar mass profiles from the 2D velocity fields for a single model of KURVS CDFS30267 galaxy. **Left:** Top panel shows the velocity field constructed from the 2D stellar mass map (which is at *HST* seeing of 0.25″). To compare the baryonic rotation curve to the $H\alpha$ rotation curve, the velocity field has to be degraded to the KMOS seeing (0.6″). The 0.25″ velocity field is made into a cube (2D spatial + 1D spectral) and each slice is smoothed to 0.6″ seeing. The final, smoothed velocity field is shown at the bottom. Due to non-linear smoothing, the positional angle for some galaxies slightly changes and is therefore recalculated from the steepest gradient in the central region. **Middle:** The comparison between the baryonic rotation curve obtained from the morphological major-axis of the 0.25″ velocity field and the smoothed rotation curve from the 0.6″ velocity field. As expected, the 0.6″ velocity rotation curve peaks at a larger radii due to the beam smearing effect. **Right:** The baryonic mass profile extracted from the ∼0.25″ (black) and 0.6″ (blue) velocity rotation curves (shown in the middle panel). The effective radii of each profile is shown as the dashed vertical line in the respective colour. For comparison, the intrinsic radius combined with the 0.6″ seeing PSF ($\sqrt{R_e^2 + psf^2}$) is shown with red dotted line. This indicates that this simple 1D estimation cannot be applied, as it significantly underestimates the real convolved effective radius. However, the beam smearing effect at $2R_e$ and $3R_e$ is minimal, and thus these estimates can be further used without any correction factor.

resulting circular velocity can be used to calculate the enclosed dynamical mass as a function of radius using:

$$M(< r) = r v_c^2 / G \tag{5.6}$$

where G is the gravitational constant. The resulting dynamical mass profiles and their uncertainties are shown in Fig. 5.10. The error range encompasses the Sérsic modelling errors, in particular it accounts for the error in the inclination for the observed velocity term and the Sérsic index and the effective radius uncertainties for

the velocity dispersion term. We also include the error in the measurement of the intrinsic velocity dispersion. We note that some studies suggest that the ionised gas velocity dispersion might be systematically higher than that of atomic/molecular gas due to the expansion of HII regions from which the ionised emission originates (thermal broadening), and is also more strongly affected by stellar and AGN feedback (Übler et al., 2019; Girard et al., 2021). It is possible that some high values of velocity dispersion are due to undetected non-circular motions and/or outflows in the ionized gas component. Thus, intrinsic velocity dispersion might be ∼10–15 kms^{-1} lower (Übler et al., 2019). This would result, on average, in systematically lower dynamical masses by ~ 1.2 times for our sample galaxies.

5.4.3 Dynamical modelling of the baryonic component

The 2D baryonic mass maps (see Fig. 5.7 and Fig. 5.8) are at *HST* F160W seeing (∼0.2″), and thus cannot be directly compared to the dynamical mass obtained from the Hα observations (which are at KMOS seeing of $\sim 0.6\,''$). It is not trivial to degrade *HST* mass maps to the KMOS resolution. Specifically, KMOS IFU observations are in 3D (x, y, v) which yields an effective 3D resolution which is better than the quoted spatial resolution, therefore smoothing of the baryonic component also has to be carried out in 3D. This is due to two reasons, firstly smoothing the mass components is not the same as smoothing the velocity components ($M_* \propto rv^2$), thus the baryonic mass has to be converted to a velocity field to apply the smoothing. Secondly, the effects of beam smearing are further complicated by the shapes of the profiles being convolved, therefore we cannot just use a simplified Gaussian correction: $R_{\mathrm{e,conv}} = \sqrt{R_{\mathrm{e}}^2 + R_{\mathrm{PSF}}^2}$ to derive the convolved effective radius or the mass profile. This effect is shown in Fig. 5.9.

Therefore, we adopt a forward modelling technique and construct a 2D circular baryonic velocity profile for a given galaxy, as shown in Fig. 5.9. We use the 2D baryonic mass map constructed from the stellar mass map and a gas component that is then extended to a larger radii than the observed data using a Sérsic model to form a smooth profile and use:

$$v_c = \sqrt{GM_*(< r)/r} \times \cos(\theta) \tag{5.7}$$

where $M_*(< r)$ is the enclosed stellar mass within radius, r. The $\cos(\theta)$ term, where θ is the angle from the morphological major axis, is included to obtain the line of sight velocity. An example of the constructed velocity field is shown in Fig. 5.9. This is done for all 1000 baryonic mass maps of each galaxy, to carry the uncertainties forward.

These 2D velocity profiles are then converted to a 3D "model cube" ($v(x, y, z)$) by creating a Gaussian profile at each pixel spanning $v_c = \pm 500\,\mathrm{kms}^{-1}$ in $1\,\mathrm{kms}^{-1}$ steps. The mean of the Gaussian is set to the circular velocity of the given pixel, the FWHM is set by the intrinsic velocity dispersion of the KMOS observations and the intensity is set by the stellar mass at that given pixel. Each 2D slice is then convolved with a Gaussian profile, with a FWHM $= (0.6^2 - 0.25^2)$, to degrade the data to the KMOS seeing. The new smoothed velocity field for a given galaxy is extracted by taking the weighted mean circular velocity at each pixel. The circular velocity curve is extracted along the morphological major axis, in a 1 pixel ($0.18''$) wide aperture (see Fig. 5.9).

The effect of the smoothing is dependent on the stellar mass profile, therefore we recalculate the position angle of the resulting smoothed map by calculating the circular velocity curve at 1 deg increments and taking the angle with the largest gradient. We use these updated positional angle values for the rest of the analysis, though we note that for most galaxies the difference in the PA is minimal (median difference of 0.05 deg with a maximum of 3 deg). In Fig. 5.9, we see that, as expected, the raw ($0.25''$) rotation curve peaks at higher circular velocity and smaller radius, while the convolved ($0.6''$) rotation curve peaks at a larger radius with a lower maximum velocity. These differences are significant at small radii (including at the effective radius), however they are negligible above $2R_e$ where the beam smearing effect is no longer significant.

Working backwards from the rotation curve, we recalculate the mass profile of each

galaxy along the morphological major axis using Eq. 5.6. This method is repeated for all 1000 models and the final mass profile is taken to be the mean of all models at each radii. The final profiles and their uncertainties are shown in Fig. 5.10.

5.4.4 Dark matter component

Comparison of the smoothed baryonic mass profiles with the dynamical mass profiles, now allows us to extract the mass profile of the dark matter, $M_{\rm DM} = M_{\rm dyn} - M_{\rm bar}$. The uncertainties from the Sérsic modelling, gas modelling and Hα velocity and its' dispersion are all carried through. For the rest of the analysis, we only consider rotationally dominated ($v/\sigma \gtrsim 1.5$) KURVS galaxies since pressure support dominates galaxies with $v/\sigma \lesssim 1.5$ and uncertainties on the measurements implies that no meaningful results can be derived. Dark matter profiles for these galaxies are shown in Fig. 5.10. We also show the fraction of dark matter ($f_{\rm DM} = (M_{\rm dyn} - M_{\rm bar})/M_{\rm dyn}$) as a function of radius. Dashed lines in the mass profiles indicate regions below the convolved effective radius, where the effects of beam smearing are significant and thus, the true shape of the mass profiles of both components is uncertain. For full analysis of the dark matter profiles in these galaxies, full forward modelling of the intrinsic dark matter profile is required (similar to the baryonic modelling described in § 5.4.3). In the rest of this chapter we only focus on the parts of the profile where beam smearing is negligible, $R \gtrsim R_{\rm e,conv}$.

5.5 Results and Discussion

In this section we present the preliminary results of the decomposed galaxy rotation curves of KURVS galaxies and discuss the implications to the galaxy formation and evolution models. We also note the caveats in this study and consider future improvements. Throughout this section the results are for the 9 KURVS galaxies from the completed half of the survey that are rotation dominated ($v/\sigma \geq 1.5$).

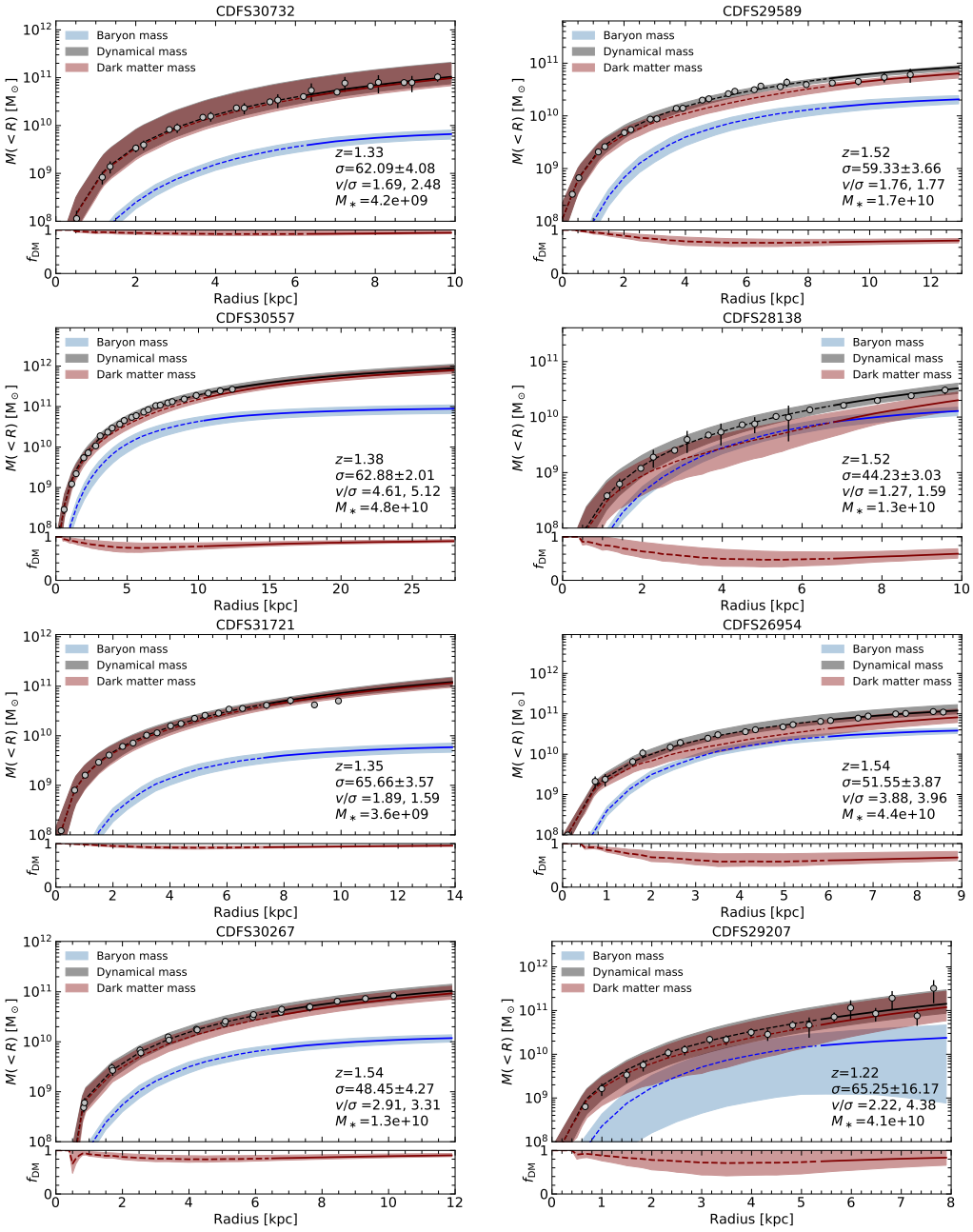

Figure 5.10: The decomposed mass profiles of KURVS galaxies that are rotationally dominated ($v/\sigma \gtrsim 1.5$). The baryonic component is shown in blue and consists of the combination of stellar and gas mass. The dynamical component is shown in grey and is derived from the model to the Hα velocity rotation curves (which are shown as grey circles). The dark matter component is calculated as the difference between the dynamical and baryonic components and is shown in red. All profiles are convolved to the KMOS seeing of 0.6″. Dashed lines in the mass profiles indicate regions below the effective radius where beam smearing effects are non-negligible and thus the gradients of the profiles are affected the most. In this study, we do not make conclusions about this region of the profiles, which is $\lesssim$6 kpc. The bottom panel shows the fraction of dark matter, $f_{\rm DM} = (M_{\rm dyn} - M_{\rm bar})/M_{\rm dyn}$ as a function of radius. We see that all galaxies have high fractions of dark matter, even close to the effective radius.

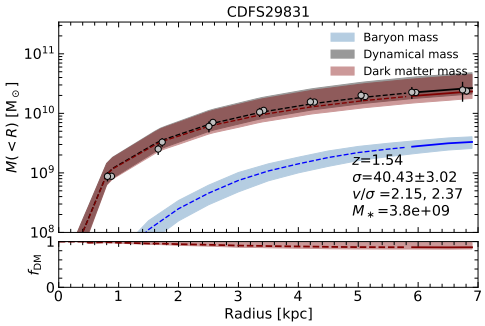

Figure 5.10: (*continued)*

5.5.1 Baryon profiles of KURVS galaxies

Before we discuss the dark matter profiles, we present the morphological properties of KURVS galaxies and compare them to similar studies of high redshift galaxies as well as those studied in the local Universe.

The sample selection of KURVS was not based on any morphological criteria, however the parent KGES sample was preferentially selected to be bright in the near-infrared ($K < 23$) and blue ($I - J < 1.7$) with priority given to galaxies previously detected in Hα emission and/or with an existing spectroscopic redshift. This means that KURVS sample galaxies are typically main-sequence star-forming galaxies with low-to-moderate dust attenuation. The median stellar mass of our sources is $M_* = 1.2{\times}10^{10}\,M_\odot$ (16-84th percentile of 0.6–$3.4{\times}10^{10}\,M_\odot$). For comparison, the DiskMass survey (Martinsson et al., 2013) of 30 local ($z < 0.01$) star-forming galaxies have a median stellar masses of $M_* \sim 2.3{\times}10^{10}\,M_\odot$, which is comparable to that of our sample. Throughout this section we also compare our results to a study of individual massive star-forming galaxies at $z = 1.2$–2.45 by Genzel et al. (2020), however their selection is biased towards the most massive systems at high redshift with a median stellar mass of $M_* \sim 4.0{\times}10^{10}\,M_\odot$ (for galaxies at $z \sim 1.2$-1.6 it is $M_* \sim 9.0{\times}10^{10}\,M_\odot$).

After taking into account the gas contribution, the total baryonic mass for the KURVS sample is $M_* = 1.6{\times}10^{10}\,M_\odot$ (16-84th percentile of 0.7-$4.8{\times}10^{10}\,M_\odot$). For comparison, the local DiskMass galaxies have a median of $M_* \sim 3.3{\times}10^{10}\,M_\odot$ and massive star-forming galaxies from Genzel et al. (2020) are estimated to have

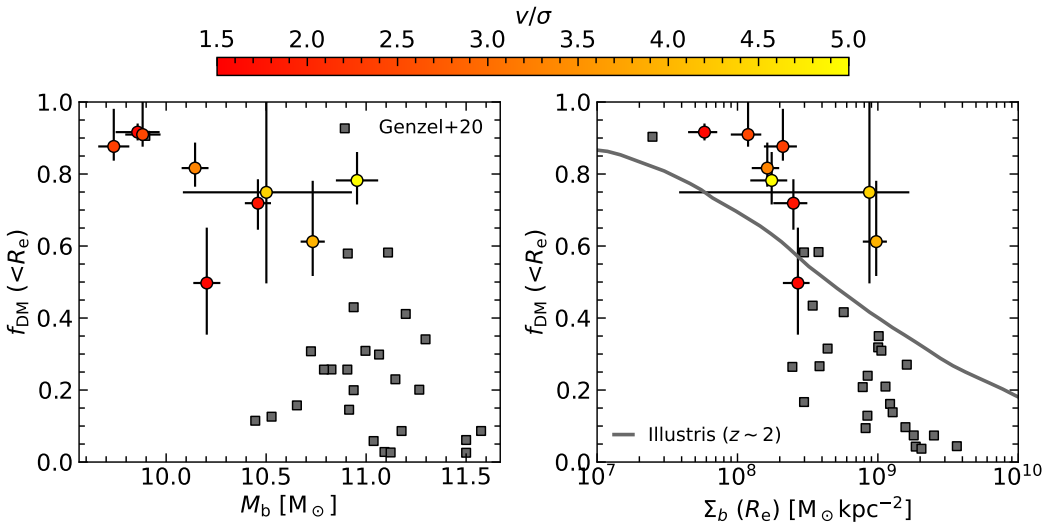

Figure 5.11: Dark matter fraction at the half mass (effective) radius as a function of the baryonic properties of KURVS galaxies that are rotationally dominated ($v/\sigma \gtrsim 1.5$), coloured by their respective v/σ values. **Left:** Dark matter fraction as a function of baryonic mass. For comparison, we show the results from the Genzel et al. (2020) study of star-forming galaxies at $z = 1.2$–2.5. Our sample has a significantly higher dark matter fraction, but they are also less massive compared to those in Genzel et al. (2020). **Right:** Dark matter fraction as a function of the baryonic surface density. There is a trend of galaxies with more concentrated baryons having a lower dark matter fraction. When compared with Genzel et al. (2020), we find that our sample has a higher dark matter fraction at a given baryonic surface density. We overlay results from Illustris-TNG100 hydro-dynamical simulations (Lovell et al., 2018) and see a trend of lower dark matter fractions at higher baryonic surface densities, but this is not as steep as seen in the observed data.

$M_* \sim 10 \times 10^{10}\,M_\odot$.

To understand how these galaxies compare structurally we calculate the central (at the effective radius) baryonic surface density for our galaxies and find a median of $\Sigma_{\rm bar} = 2 \times 10^8\,M_\odot kpc^{-2}$. This is systematically lower than that for the massive galaxies sampled by Genzel et al. (2020), as shown in Fig. 5.11.

5.5.2 Fraction of dark matter in $z \sim 1.5$ galaxies

In this section we investigate in more detail the fraction of dark matter in star-forming galaxies at high redshift. For this, we consider the fraction of dark matter at the convolved effective radius. The median fraction of dark matter within effective radius for our sample galaxies is $f_{\rm DM} = 0.78$ (16-84th percentile of 0.64–

0.90), suggesting that even at central galaxy regions our galaxies are dark matter dominated. The median within $3R_e$ is f_{DM} =0.88 (16-84th percentile of 0.70–0.92). The $z \sim 1.5$ results at $3R_e$ are higher than those found for local galaxies, $f_{DM} \sim 0.65$–0.70 for 19 galaxies from the THINGS survey (de Blok et al., 2008) and $f_{DM} = 0.68 \pm 0.08$ for DiskMass galaxies from (Martinsson et al., 2013; Courteau & Dutton, 2015). To probe the physical processes leading to these high dark matter fractions, we compare these dark matter fractions with the morphological and kinematic properties of the galaxies. As we will see, the behaviour of KURVS is well matched to that seen in DiskMass sample.

First, we compare the fraction of dark matter with the baryonic properties of the galaxies. Studies at low redshift have shown that the dark matter fraction at the disk effective radius decreases with increasing stellar, baryonic or halo mass (Courteau et al., 2014; Courteau & Dutton, 2015). Our results of individual star-forming galaxies at high redshift, combined with the 26 Genzel et al. (2020) massive star-forming galaxies shows a comparable trend, as shown in Fig. 5.11. A similar trend is also observed for the baryon surface densities, with galaxies where baryons are more centrally concentrated having lower dark matter fraction within the effective radius (Fig. 5.11).

We compare our results to the Illustris-TNG100 full hydro-dynamical simulation for $z \sim 2$ galaxies from Lovell et al. (2018), which includes baryon-dark matter interactions. The trend seen in the simulations is comparable to the observed trend, however is shallower: it underestimates dark matter fractions at lower surface densities and overestimates at higher surface densities.

Similarly, in Fig. 5.12, we see that the Illustris-TNG100 simulation underpredicts the fraction of dark matter for galaxies with lower circular velocities and overpredicts it in high velocity systems. KURVS galaxies have a median circular velocity at the effective radius of $v_c = 160^{+50}_{-40}\,\mathrm{kms}^{-1}$ and broadly cover a similar range in this parameter space as the low redshift late-type galaxies from the DiskMass survey. We see a very similar trend of decreasing dark matter fraction with increasing circular velocity as in DiskMass sample (see Fig. 5.12). However, we note

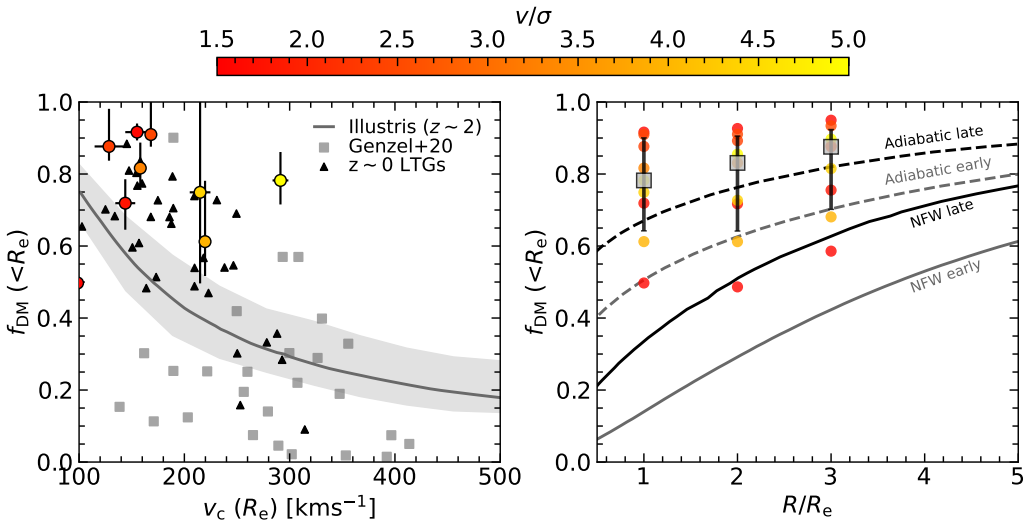

Figure 5.12: **Left:** Dark matter fraction as a function of circular velocity of the disk at half mass radius. For comparison, we show results from Genzel et al. (2020), as well as results from $z = 0$ late-type star-forming disks from Martinsson et al. (2013). Our results are comparable to the $z = 0$ estimates. **Right:** Dark matter fraction as a function of radius. For our sources we make measurements at the effective radius, R_e, as well as $2R_e$ and $3R_e$. This avoids the beam smearing effects and extends to the maximum radius we are able to trace with the $H\alpha$ rotation curves. For comparison, we overlay theoretical models from Courteau & Dutton (2015) for early- and late-type galaxies with $v_c(R_e) \simeq 230\,\mathrm{km\,s^{-1}}$. NFW models follow the concentration–mass relation from ΛCDM (Macciò et al., 2008). Dashed lines show adiabatically contracted NFW halos with correspondingly lighter IMFs.

that for the same velocity range as KURVS, the galaxies in Genzel et al. (2020) sample have lower dark matter fractions than either KURVS of DiskMass samples. Although, galaxies in the Genzel et al. (2020) sample have much higher baryon surface density, which may account for the offset.

As noted before, in Illustris-TNG100 the baryons and dark matter gravitationally interact, while a dark-matter only model would predict lower dark matter fraction at a given baryon mass, baryon surface density or circular velocity. Our observations at $z \sim 1.5$ support the scenario where baryon-dark matter interactions pull dark matter inward efficiently (and lead to higher dark matter fractions). This is the effect of adiabatic contraction, whereby haloes respond to galaxy formation by contracting (e.g. Blumenthal et al., 1986; Gnedin et al., 2004; Sellwood & McGaugh, 2005).

To analyse this further, in Fig. 5.12, we plot the fraction of dark matter as a

function of radius at R_e, $2R_e$ and $3R_e$ and compare to NFW (Navarro et al., 1997) halos (as well as adiabatically contracted NFW halos) of early and late type galaxies from Courteau & Dutton (2015). We show that KURVS sample galaxies follow the same trend of increasing dark matter fraction with increasing radius, and this is systematically higher (but within the uncertainties) than the adiabatically contracted NFW halo model. We note that the systematic offset is likely due to the model being for $v_c \sim 230\,\mathrm{km\,s^{-1}}$, while our sample galaxies have lower circular velocities.

5.6 Conclusions

In this chapter we presented our on-going study on the decomposition of individual high-redshift galaxy rotation curves from a very deep (∼80 h on-source integration) KMOS Ultra-deep Rotational Velocity Survey, KURVS. The Hα rotation curves extend to $\sim 3R_e$, allowing for comparison with studies of local galaxies. Using 2D stellar mass maps derived from *HST* photometry, we decompose the dynamical mass profile into the baryonic and dark matter components. The preliminary results are as follows:

- Galaxies in our sample have a median stellar mass of $M_* = 1.2^{+2.2}_{-0.6} \times 10^{10}\,\mathrm{M_\odot}$, and a median baryonic mass of $M_b = 1.6^{+3.2}_{-0.9} \times 10^{10}\,\mathrm{M_\odot}$ after accounting for the gas component (assuming $\mu_{\mathrm{gas}} = M_{\mathrm{gas}}/M_*$=0.3–0.5). In comparison, the median dynamical mass, calculated from the Hα emission, is $M_{\mathrm{dyn}} = 4.3^{+2.5}_{-1.6} \times 10^{10}\,\mathrm{M_\odot}$.

- We adopt a forward modelling technique to extract the baryonic mass profiles at 0.6″ seeing FWHM to match the dynamical constraints from the KMOS Hα observations. We find a median fraction of dark matter of $f_{\mathrm{DM}} = 0.78^{+0.12}_{-0.14}$ and $f_{\mathrm{DM}} = 0.88^{+0.05}_{-0.18}$ at R_e and $3R_e$, respectively. This indicates that these galaxies are dark matter dominated, even at the effective radius.

- We observe a trend in f_{DM} with Σ_{bar}, which is consistent with that seen in local galaxies from the DiskMass survey (Martinsson et al., 2013).

- The processes of galaxy formation are expected to modify the dark matter halo density profile that a galaxy resides in. Overall our results suggest that galaxy formation is a slow and smooth process for typical $z \sim 1.5$ main-sequence star-forming galaxies, where dark matter halo contracts and the central regions of these galaxies are sub-maximal (dark matter dominated at effective radius), consistent with theoretical models of adiabatic contraction. Some studies have claimed baryon dominated central regions of galaxies, both at low (Lelli et al., 2016) and high redshift (Genzel et al., 2017; Lelli et al., 2018; Genzel et al., 2020), however they sample the massive end of the star-forming main-sequence. In these sources mergers of and/or dynamical friction between the baryons and dark matter may lead to weak halo contraction or even halo expansion (e.g. El-Zant et al., 2001). Thus, for the most massive galaxies dark matter halos become gravitationally dominant at larger radii. This might indicate differences in the formation and evolution of typical main-sequence star-forming galaxies and the most massive galaxies at high redshift.

Chapter 6

Conclusions and future work

This thesis presented an analysis of the properties of star-forming galaxies across cosmic noon ($z \sim$1–4) spanning a wide range of stellar, gas and total masses, from strongly dust-obscured systems, to more typical 'main-sequence' galaxies. This chapter summarises the main results and discusses the ongoing studies, as well as future follow-up projects, to help better understand the formation and evolution of star-forming galaxies in the distant Universe.

6.1 Summary of presented work

6.1.1 SED fitting code: reliability of deriving the physical parameters of high redshift star-forming galaxies

The main focus of this thesis was the analysis of high redshift star-forming galaxies in order to gain a better understanding of their formation and evolution. In Chapter 2, we tested an SED fitting code, MAGPHYS (da Cunha et al., 2008, 2015; Battisti et al., 2019) for modelling high redshift galaxies, to better understand both its strengths and shortcomings when deriving photometric redshifts and the physical properties of the galaxies.

We tested the MAGPHYS code using ∼9000 simulated galaxies from the EAGLE simulations (Schaye et al., 2015). The predicted photometry from the simulated galaxies were modelled to derive the best-fitting SEDs and compare the predicted

physical properties with the 'true' values. This analysis revealed systematic offsets in some properties, such as star-formation rate, mass-weighted age, dust temperature and stellar mass. These differences are likely due to variations in the adopted star-formation histories, dust model and geometry in MAGPHYS compared to those in the radiative transfer code SKIRT (Baes et al., 2011; Camps & Baes, 2015) and the EAGLE simulation. Accounting for these differences was beyond the scope of this work, and instead we used their magnitude as a rough indicator of the scale of potential systematic errors in our analysis and thus, we used scatter around the best-fit trend lines, to estimate the minimum uncertainty on a given parameter in our analysis.

MAGPHYS was also tested and calibrated using the photometry for ∼300,000 star-forming 'main-sequence' galaxies from the UKIDSS UDS survey (Almaini et al. in prep), and on the ∼700 870μm-selected dust-obscured strongly star-forming galaxies from the AS2UDS survey (Stach et al., 2019). Comparison of the photometric redshifts with the available spectroscopic redshifts showed good agreement for both populations and our analysis confirms that the error due to the photometric redshift uncertainty on any given physical parameter from MAGPHYS is captured in the reported error range and is not affecting the posterior PDF. Importantly, MAGPHYS derived physical properties agree well with the photometric observables that they are empirically expected to correlate with (e.g. $M_{\rm d}$ with the observed-frame 870μm flux density, M_* with rest-frame ∼1.6μm luminosity). In particular, the strong positive correlation between the dust mass and observed-frame 870μm flux density indicates that the selection of the dust-obscured strongly star-forming population at 870μm is most sensitive to cold dust mass.

6.1.2 Dust-obscured strongly star-forming galaxies at high redshift

With the modelled SEDs from Chapter 2, in Chapter 3 we analysed 707 ALMA-identified sub-millimetre galaxies from the AS2UDS survey, with flux densities in the range $S_{870} = 0.6$–$13.6\,$mJy.

The 870μm-selected sample has a median redshift of $z = 2.61 \pm 0.08$ and our analysis suggests that such a redshift distribution can be reproduced by a simple model comprising of dark matter halo growth past a critical halo mass of $\sim 6{\times}10^{12}\,\mathrm{M}_{\odot}$ combined with a simple model of the evolution of gas fraction in the halos with redshift. The results indicate that SMGs may represent efficient collapse occurring in the most massive halos that can host such activity (see also Stach et al., 2021). Combining the far-infrared luminosity, dust mass and size measurements, we show that dust emission from our SMG sample is, on average, consistent with a homogeneous and homologous population, consistent with a centrally illuminated starburst (see also Gullberg et al., 2019).

The analysis of the build-up of stellar mass since the onset of the SMG phase (gas depletion analysis suggests $\sim$150 Myr) assuming a constant star-formation rate suggests that there is a substantial stellar component before the onset of the SMG phase ($M_{150\,\mathrm{Myr}}/M_{*} \sim 0.3$) and, by the end (after a further 150 Myr) these systems are likely to roughly double their pre-existing stellar masses to $\sim 1.6{\times}10^{11}\,\mathrm{M}_{\odot}$. By comparing to the stellar mass function of massive field galaxies, and accounting for the duty cycle of SMGs due to gas-depletion, we show that essentially all galaxies above a stellar mass of $M_{*} > 3 \times 10^{11}\mathrm{M}_{\odot}$ across $z \sim$1.8–3.4 (the 16–84$^{\mathrm{th}}$ percentile range of our sample) have gone through a sub-millimetre-luminous phase at some point in their evolution. This is in good agreement with the predictions of simulations (McAlpine et al., 2019).

Our analysis in Chapter 3 has shown that dust-obscured star-forming galaxies are a non-negligible part of the star-forming population at high redshift. We find that the contribution of 870-μm selected SMGs to the total star-formation rate density in the Universe increases steeply with redshift from $z \sim 1$, with the peak contribution being $\sim$15 per cent at $z \sim 3$ for the $S_{870} \gtrsim 3.6$ mJy (with typical $L_{\mathrm{IR}} \simeq 3.5{\times}10^{12}\,\mathrm{L}_{\odot}$) sub-sample and $\sim$60 per cent for SMGs brighter than $S_{870} = 1$ mJy (or $L_{\mathrm{IR}} \simeq 1{\times}10^{12}\,\mathrm{L}_{\odot}$). Thus, roughly half of the star- formation rate density at $z \sim 3$ arises in ULIRG-luminosity sources. In terms of the specific star-formation rate (SFR/M_{*}), we see that, at $z \sim 1$, typical SMGs lie a factor

of ∼6 above the 'main-sequence'. By $z \sim 4$ SMGs lie a factor of two above the 'main-sequence', due to the strong evolution of sSFR of the 'main-sequence'.

6.1.3 Relation between strongly star-forming galaxies to more typical dust-obscured galaxies

To investigate the differences in the dusty star-forming populations selected at different wavelengths, and probe the population closer to the star-forming 'main-sequence', in Chapter 4 we analysed the physical properties of a complete sample of 121 SMGs selected at 450μm from the SCUBA-2 Ultra Deep Imaging EAO Survey (STUDIES; Wang et al., 2017) in a consistent manner to the large 850-μm-selected survey from AS2UDS. The SEDs of 450μm-selected sources revealed that the selected population ranges from unobscured LBGs, through more typical $A_V \sim 1$ star-forming galaxies, to very obscured and completely optically undetected sources, with majority having far-infrared luminosities classing them as LIRGs ($\gtrsim 10^{11} L_\odot$). The 450μm selected sources lie at a significantly lower redshift than the more active sources selected at 850μm with SCUBA-2, with a median of $z = 1.85 \pm 0.12$, and only 9% at $z \gtrsim 3$, which can be explained by the evolution of the far-infrared luminosity function and the deeper 450-μm flux selection limit.

Comparison of the space densities revealed that the 450-μm sample has, on average, ∼14 times higher space density than the brighter 850-μm sample (of which, the vast majority are ULIRGs) out to $z \sim 2$, and a comparable space density at $z = 2$–3, before declining. Thus, ULIRGs are the dominant far-infrared luminous population at high redshifts, while LIRGs dominate at $z \lesssim 2$. Moreover, 450-μm sources have a lower dust-to-stellar mass ratio, suggesting more evolved systems with lower gas fractions.

We were able to investigate a uniform selection of dust-obscured galaxies across the cosmic noon $z \sim 1$–4, by constructing a rest-frame wavelength ($\lambda_{\rm rest} \sim 180\mu$m) and dust-mass matched ($M_d \geq 2 \times 10^8 M_\odot$) sample. The comparison of these samples indicated several potential differences in far-infrared luminous populations as a function of redshift. We observed a modest 3σ trend of increasing gas fraction with

increasing redshift in this population. Overall, the galaxies at $z \sim 1.5$, have three times lower star-formation efficiency at a given dust mass than the $z \sim 3.5$ sources. We suggest that $z \sim 1.5$ population has lower dust density (assuming similar geometry) as a result of their comparable inferred dust emission radii ($\sim$0.8 kpc), but lower dust masses compared to the $z \sim 3.5$ sources, leading to the lower dust attenuation in SMGs seen at $z \sim 1.5$. Finally, we find that the observed total dust mass density in galaxies across the cosmic noon is currently best reproduced by a model where dust content in galaxies is governed by a combination of both the variation of gas content and dust destruction timescale (Li et al., 2019).

6.1.4 The baryonic and dark matter components of star-forming 'main-sequence' galaxies

Finally, in Chapter 5 we analysed a sample of typical star-forming galaxies at $z \sim 1.5$ using spatially and spectroscopically resolved measurements. We have presented an on-going study on the decomposition of individual high-redshift galaxy rotation curves for which we used a very deep ($\sim$80 h on-source integration) sample from the KMOS Ultra-deep Rotational Velocity Survey, KURVS. These sources are representative of the star-forming 'main-sequence' at $z \sim 1.5$, and thus overlap with the 450μm population discussed in Chapter 4.

The extracted Hα maps extend out to $\sim$3 times the effective radius ($\sim$10–15 kpc) which allowed us to derive the dynamical mass profiles of these systems on scales comparable to those of local studies. Together with the 2D stellar mass maps derived using MAGPHYS SED fitting code modelling on the deep *HST* photometry, we decomposed the dynamical mass profiles into separate baryonic and dark matter components. Our analysis indicates that these 'main-sequence' star-forming galaxies are dark matter dominated, even at the effective radius with $f_{\rm DM} = 0.80^{+0.11}_{-0.14}$. We observe a trend in the fraction of dark matter with the baryonic surface density, which is consistent with that seen in local late-type galaxies from the DiskMass survey (Martinsson et al., 2013), indicating that these 'main-sequence' galaxies at high redshift have similar physical properties to the late-type galaxies observed

locally (in terms of stellar and dark matter mass). Overall, our results suggest that galaxy formation is a slow and smooth process for typical z ∼1.5 main-sequence star-forming galaxies, where dark matter halo contracts and the central regions of these galaxies are sub-maximal (dark matter dominated at effective radius), consistent with theoretical models of adiabatic contraction.

6.1.5 Overall summary: the evolution of star-forming galaxies across the 'main-sequence'

We have tested and checked the reliability of using an SED fitting code to derive photometric redshifts as well as key physical properties (such as stellar mass, far-infrared luminosity, star-formation rate) for high redshift star-forming galaxies in Chapter 2. Knowing the capabilities and shortcomings of the modelling code, in Chapters 3, 4 and 5 we modelled multi-wavelength photometric data to derive physical properties of galaxies across the 'main-sequence'. Consistent analysis and methodology allowed us to compare and contrast populations of different stellar/gas/dark matter masses free from systematic uncertainties which would arise from comparing results from different codes, and assess their evolutionary trends.

Our analysis in Chapter 3 underlines the fundamental connection between the population of gas-rich, strongly star-forming galaxies at high redshift (selected through 870μm) and the formation phase of the most massive galaxy populations over cosmic time. We suggest that the characteristics of these short-lived, but very active systems represent events where massive halos (with characteristic total masses of $\sim 6\times10^{12}\mathrm{M}_{\odot}$) with high gas fractions transform their large gas reservoirs into stars on a few dynamical times. Comparison with dust-obscured star-forming systems selected at 450μm revealed that the more typical star-forming galaxies, closer to the star-forming 'main-sequence', appear to have similar extent of the dust emission regions but lower dust densities. 450μm sources appear to be more evolved systems, with lower gas fractions, and thus, lower star-formation efficiencies than the most massive galaxies at high redshift. Thus, there appears to be physical differences between 'main-sequence' star-forming galaxies at $z \sim 1.5$ and the systems

on the 'main-sequence' at $z > 3$ (which includes 850μm sources).

A sample of star-forming galaxies at $z \sim 1.5$ were analysed using spatially and spectroscopically resolved measurements in Chapter 5. These sources are representative of the star-forming 'main-sequence' at $z \sim 1.5$. The source selection is based on Hα emission and availability of spectroscopic redshifts. In comparison to the dusty star-forming galaxies, they correspond to the lower stellar mass tail of the 450μm-selected population, residing at a similar redshift but having, on average, slightly lower stellar masses and dust attenuation. The decomposition of their dynamical mass profile, obtained from deep Hα observations, into the baryonic and dark matter components with the constraints from the 2D stellar mass maps, revealed high dark matter fractions ($\sim$0.8), even at effective radius, suggesting that the 'main-sequence' galaxies and more typical dust-obscured galaxies may reside in adiabatically contracted dark matter halos.

Therefore, through studying the most dust-obscured strongly star-forming systems, less extreme dust-obscured galaxies and the typical 'main-sequence' galaxies, we were able to probe the mass build up across the 'main-sequence'. We suggest that the most massive 870μm-selected SMGs reside in the most massive dark matter halos that can still support efficient cooling and collapse of gas (Dekel & Birnboim, 2006), which offers a description of why their massive galaxy descendants at $z \sim 0$ have the highest stellar baryonic to halo mass ratios of any collapsed systems (Gerhard et al., 2001; Stach et al., 2021). This suggests that these centrally-concentrated systems may be similar to the massive galaxies probed by Genzel et al. (2020) analysis, which indicated low dark matter fractions in the central regions of their sample galaxies. In comparison, we suggest that the 'main-sequence' galaxies and more typical dust-obscured galaxies, with lower stellar masses, show more evolved systems with much higher dark matter fractions in their central regions. Thus, our overall results suggest differences in the processes of mass build up and evolution in galaxies across the 'main-sequence'.

6.2 Ongoing and future work

In this thesis, we have addressed some of the questions regarding the physical properties of star-forming galaxies at high redshift, which helped us to assess the possible formation and evolution processes in these systems. In this section, we discuss a number of outstanding questions and follow-up projects that will allow detailed questions to be addressed about the role of high star-formation rate events in galaxies over a wide range of cosmic epochs.

6.2.1 Improving the photometric constraints of the SEDs of high redshift galaxies

Though significant progress in identifying counterparts (particularly using ALMA) has allowed measurements of many of the basic properties of SMGs from their rest-frame UV/optical emission, the dust spectral energy distributions (SEDs) are still relatively poorly constrained. SMGs emit the majority of their total bolometric luminosity in the far-infrared, therefore dust properties are an important tracer of the nature of this population. Prior to ALMA, *Herschel* provided the only means to sample their peak of the dust SED around $\sim$350μm for cool galaxies at $z \sim 2$–3, however the relatively bright confusion limit of *Herschel* means the constraints are relatively weak. Indeed, space-based studies using *Herschel* to constrain the dust SEDs of SMGs (e.g. Eales et al., 2010; Oliver et al., 2012; Symeonidis et al., 2013) are limited to the brightest sources, and even so, the coarse resolution ($\sim$ 20–30$''$ at 350–500μm) means that the maps are heavily confused and must be deblended using assumptions about the populations contributing to the emission (e.g. Roseboom et al., 2013; MacKenzie et al., 2016), which results in significant systematic uncertainties in their far-infrared luminosities.

Constraining the dust SEDs for individual galaxies using ALMA is crucial in order to derive reliable measures of $T_{\rm d}$ from the location of the peak of the far-infrared emission and hence estimate $L_{\rm FIR}$, and dust mass from the Rayleigh-Jeans slope of the SED and assess any evolutionary trends. For example, to test the trend

seen in Chapter 3 that SMGs are systematically cooler than comparably luminous local galaxies, direct measurement of the flux densities around the peak of the dust SED are needed. If SMGs are cooler, it would be an additional indication of more extended dust (and potentially molecular gas) reservoirs in high redshift galaxies compared to local ULIRGs, e.g. FWHM$\lesssim$1 kpc, compared to FWHM$\sim$2 kpc in high-redshift SMGs (Sakamoto et al., 2008; Simpson et al., 2015b; Ikarashi et al., 2015; Gullberg et al., 2019). Therefore, direct measurement of the flux densities around the peak of the dust SED are crucial in order to address this "evolution". The improved constraints in the dust SED would ultimately provide a fundamental test for the nature of SMGs, give insight into the mix of temperatures, dust masses and geometry within the population, to better understand this sub-mm bright evolutionary phase of most massive galaxies.

Moreover, the mid-infrared constraints for high redshift galaxies will be greatly improved with the launch of *James Webb Space Telescope* (*JWST* Gardner et al., 2006). The Mid-Infrared Instrument (MIRI) will allow us to probe the PAH contribution in these systems as well as constrain the hot dust component, thus improving constraints on the total far-infrared luminosity measurements. The mid-infrared coverage, as well as near-infrared coverage with Near-Infrared Camera (NIRCam), will also allow to identify possible AGN contamination, and thus improve the selection of the star formation dominant galaxies at high redshift.

6.2.2 Spectroscopic follow-up of dust-obscured star-forming galaxies

Though in Chapter 2 we have shown that MAGPHYS derived photometric redshifts are reliable for the AS2UDS population as a whole, this is not the case for any single source. Thus, for a detailed study of individual sources, spectroscopic redshifts are required. Due to the dusty nature of SMGs traditional optical/near-infrared methods are only possible for the less extreme sources where dust attenuation is lower. To get redshift confirmation for the more dust-obscured sources, facilities such as ALMA and NOEMA are particularly well suited through detection of low-

/mid-J CO emission lines.

Recently, we have been allocated a large KMOS programme, KAOSS (PI: I. Smail), to obtain spectroscopic redshifts of 545 ALMA-identified SMGs in the UDS, CDFS and COSMOS fields, which, when completed, will increase the number of SMGs with available spectroscopic redshift by a factor of three.

Moreover, spectroscopic redshifts are important to confirm the highly peaked redshift distribution of the 850μm-selected sources presented in Chapter 3 and potential differences between far-infrared luminous populations as a function of redshift suggested in Chapters 3 and 4. To test the trends uncovered in this thesis, spectroscopic redshifts based on reliable AS2UDS 850μm and 450-μm STUDIES 450-μm identifications will be necessary to confirm the redshift distribution differences between the 450- and 850-μm populations, as well as to improve the precision of the derived parameters from SED fitting.

As only small samples of these sources have been observed spectroscopically, identifying optical emission lines (Hα, Hβ, [OIII], [OII], [NII]) for large samples, such as the 450μ-selected STUDIES sources, is a crucial component in building a more complete picture of the star forming processes in these dusty galaxies and thus, serves as an important test for galaxy evolution models. Strong line methods, such as R23 (([OIII]+[OII])/Hβ) and N2 ([NII]/Hα), can be used to infer the metallicities and assess the SMGs place on the mass-metallicity relation. Any changes in the MZR slope can indicate changes in the physical processes that drive galaxy evolution as galaxies build up stellar mass (e.g. Peng et al., 2015). Multiple emission lines would also allow to assess the abundance ratios, such as [OIII]/Hβ ratio (which is correlated with sSFR of star-forming galaxies; Shimakawa et al., 2015; Holden et al., 2016). Moreover, [OIII] emission lines would help to assess the ionised component in these systems, since detecting strong [OIII] emission would indicate extreme ISM conditions, and a broad underlying [OIII] and Hα component would reveal outflows (e.g. Förster Schreiber et al., 2014; Carniani et al., 2015).

6.2.2.1 Dust and gas reservoirs of high-redshift star-forming galaxies

The analysis of the STUDIES survey in Chapter 4 has proposed that the 450μm-selected population represents a dominant dust-obscured star-forming population at $z \sim 1$–2. This raises a fundamental question of whether there is an evolutionary link between the dust-obscured half of the star formation seen in these high-redshift galaxies and the formation of galactic bulges and spheroids we see in the local Universe, which similarly account for around half of all stars in galaxies at $z \sim 0$. There does not yet seem to be a theoretical consensus for the trigger mechanisms driving the evolution of dusty star-forming galaxies, which would explain this proposed link. Theoretical studies have suggested that they can be driven by starbursts from major merger events (e.g. Narayanan et al. 2010, similar to what is believed to trigger local ULIRGs, e.g. Sanders et al. 1988; Farrah et al. 2001), or disc-instabilities (e.g. Lacey et al., 2016); they may simply be the most massive end of the star-forming secularly evolving disk galaxies (e.g. Davé et al., 2010); or possibly be a heterogenous population of both (e.g. McAlpine et al., 2019).

In contrast, a simple empirical view is that the least active (and least obscured) populations are driven by star formation in cold, marginally stable gas disks, while the more active and obscured systems have their star formation boosted by one or more of the processes listed above. However, this simple picture has been confused by recent claims that some of these compact starbursts may be hidden within the star-forming 'main-sequence' which is thought to represent a more smoothly evolving population driven by gas accretion from the surrounding CGM (Elbaz et al., 2018; Puglisi et al., 2019). Thus, to build a more complete picture of the evolutionary state of the population that produces the bulk of the far-infrared background, we need to assess the relative scale of obscured activity compared to their stellar extent. This would fill the gap between extreme SMGs and the 'main-sequence' in terms of star formation. Spatially-resolved sub-millimetre interferometry using ALMA will provide an empirical diagnostic into the evolutionary stage for the 450μm population (and possible connection to formation of bulges in massive galaxies); whether they are just scaled-down SMGs, or less extreme sources

with larger extent of the dust emission.

6.3 Spatially resolved analysis of star-forming galaxies at high redshift

In Chapter 5, we discussed the on-going analysis of the decomposition of individual galaxy rotation curves of star-forming galaxies at high-redshift. For this, we used the completed first half of the data from the KMOS Ultra-deep Rotational Velocity Survey, KURVS. Even though we are using the best observations currently available, there are improvements to be considered for future follow-up observations.

The analysis in Chapter 5 consists of the dynamical and baryonic components, both at $0.6''$ ($\sim$5 kpc) resolution. Therefore, the extracted dark matter profile is also obtained at similar spatial resolution and can only be assessed at large radii (above the effective radii). In order to derive properties of the dark matter halos on smaller scales within these galaxies and model each component consistently, our next step in this analysis is to forward model the dark matter profiles. For this we will be using a dark matter profile (e.g. NFW) and construct 3D model cubes which will then be convolved to $0.6''$ resolution in the same manner as the method explained in Chapter 5 for the baryonic component. This approach will allow us to assess the physical characteristics of the inner regions of the dark matter halos of the 'main-sequence' star-forming galaxies at $z \sim 1.5$.

The other unconstrained component in the analysis of galaxy rotation curves is the gas contribution. We used a range of possible gas-to-stellar mass ratios and radial extents to model the molecular gas distribution, which introduces large uncertainties in the derived baryonic profiles. We note that some galaxy integrated (or moderate resolution) CO measurements are available for a subset of the KURVS sample in the COSMOS field (which is not completed yet), which will allow us to estimate the average extent of the molecular gas distribution in these systems. However, future ALMA observations of spatially resolved CO emission will be needed

to construct reliable gas rotation curves as a function of radius, removing some of the remaining uncertainties from modelling of the cold molecular gas distribution.

As discussed and tested in Chapter 5, the current spatially resolved 2D mass maps are constructed using *HST* photometry which samples wavelengths up to 1.6μm in the observed frame (rest-frame R band). Therefore, there is no coverage around the 1.6μm stellar mass 'bump', which is at $\sim$4μm at the redshift of the sample. Both KURVS fields will be observed with *JWST* / NIRCam in the first cycle, thus we will be able to exploit the publicly available data to improve the stellar mass maps by including longer wavelength measurements.

6.4 Final remarks

Major technological advances in the last 20+ years, have allowed us to detect galaxies at increasingly high redshift to study their multi-wavelength properties, and also investigate their formation, evolutionary trends and understand their role in the evolution of massive galaxies we see today.

In particular, in the recent years, the commissioning of ALMA allowed detailed analysis of the far-infrared/sub-mm wavelengths of the dust-obscured populations at high redshift. With increasingly large, precisely located and complete, luminosity-limited samples of dust-obscured star-forming galaxies at high redshift, together with future observations covering emission across a wide range of wavelengths (e.g. *JWST*, SKA), a more detailed characterization of the obscured star-formation will be possible, shedding light on the intricacies of the processes involved in the formation and evolution of these starburst galaxies at high redshift.

The advances in the optical/near-infrared spectroscopy (e.g. SINFONI, MOSFIRE, OSIRIS), and especially in multi-object instruments (e.g. KMOS) which allow spatially resolved observations of multiple galaxies simultaneously, has allowed us to obtain large samples of sources at increasingly high redshifts. For example, the KMOS Large Programme, KAOSS (PI: I. Smail) of dust-mass-selected star-forming galaxies at $z \sim 2$ will not only provide spectroscopic identification of these massive

sources at high redshift, but also provide resolved Hα rotation curves of $\sim$150 sources. With resolved stellar mass maps for those sources in the *HST* and *JWST* fields, these observations will allow us to search for differences in the dark matter fraction as a function of stellar mass and star-formation rate and redshift, by comparing the high redshift dust-obscured massive systems to the more typical 'main-sequence' galaxies at $z \sim 1.5$ (such as KURVS). For comparison, the $z \sim 1.5$–2.5 KAOSS galaxies in the UDS region (a subset from the ALMA sample discussed in Chapter 3) has an order of magnitude higher median stellar mass and SFR compared to KURVS $z \sim 1.5$ sources.

The construction of the Enhanced Resolution Imager and Spectrograph (ERIS) on VLT (and the launch of *JWST*) will make the study of the dynamics of galaxies on sub-kpc scales possible. Future follow-up ERIS observations of galaxies across the 'main-sequence' would allow to obtain high–resolution adaptive optics spectra for KURVS and KAOSS sources at $z \sim 1.5$ and $z \sim 2.5$. The $0.1''$ resolution observations (compared to $0.6''$ from KMOS) match the resolution of *HST* and *JWST*, allowing for direct comparison between the total and stellar kinematics, without the need to degrade the data. This will vastly improve the constraints of the rotation curves in the central regions of galaxies (below the effective radius), allowing us to place tighter constraints on the dynamical, stellar and dark matter mass profiles. We also note that future ($\gtrsim$2025) observations with HARMONI on the ELT will improve the spatial resolution further by a factor of $\sim$5 than currently possible.

All these future observations will provide high-fidelity dynamical maps for gaseous and stellar components as well as the total rotation curve from the Hα kinematics. This direct decomposition, with minimal assumptions about the distributions, will allow us to directly constrain the mass contribution and dynamics of stars, gas and dark matter as a function of radius in these systems, which will allow to test the accepted cosmological models in greater detail than is currently possible and improve our understanding of gas cooling and subsequent star formation in massive high-redshift galaxies.

Bibliography

Abdalla F. B., et al., 2015, PoS, AASKA14, 017

Agladze N. I., Sievers A. J., Jones S. A., Burlitch J. M., Beckwith S. V. W., 1996, ApJ, 462, 1026

Aihara H., et al., 2019, PASJ, p. 106

Algera H. S. B., et al., 2020, ApJ, 903, 138

Álvarez-Márquez J., Burgarella D., Buat V., Ilbert O., Pérez-González P. G., 2019, A&A, 630, A153

An F. X., et al., 2018, ApJ, 862, 101

An F. X., et al., 2019, ApJ, 886, 48

Andrews B. H., Thompson T. A., 2011, ApJ, 727, 97

Aravena M., et al., 2019, arXiv e-prints, p. arXiv:1903.09162

Babcock H. W., 1939, Lick Observatory Bulletin, 498, 41

Baes M., Verstappen J., De Looze I., Fritz J., Saftly W., Vidal Pérez E., Stalevski M., Valcke S., 2011, ApJs, 196, 22

Barger A. J., Cowie L. L., Sanders D. B., Fulton E., Taniguchi Y., Sato Y., Kawara K., Okuda H., 1998, Nature, 394, 248

Battisti A. J., et al., 2019, ApJ, 882, 61

Baugh C. M., Lacey C. G., Frenk C. S., Granato G. L., Silva L., Bressan A., Benson A. J., Cole S., 2005, MNRAS, 356, 1191

Beckwith S. V. W., et al., 2006, AJ, 132, 1729

Beeston R. A., et al., 2018, MNRAS, 479, 1077

Begeman K. G., Broeils A. H., Sanders R. H., 1991, MNRAS, 249, 523

Behroozi P. S., Wechsler R. H., Conroy C., 2013, ApJ, 770, 57

Bell E. F., McIntosh D. H., Katz N., Weinberg M. D., 2003, ApJs, 149, 289

Bera A., Kanekar N., Chengalur J. N., Bagla J. S., 2019, ApJl, 882, L7

Bertelli G., Girardi L., Marigo P., Nasi E., 2008, A&A, 484, 815

Bertin E., Arnouts S., 1996, A&AS, 117, 393

Béthermin M., Dole H., Lagache G., Le Borgne D., Penin A., 2011, A&A, 529, A4

Béthermin M., De Breuck C., Sargent M., Daddi E., 2015, A&A, 576, L9

Béthermin M., et al., 2017, A&A, 607, A89

Biggs A. D., et al., 2011, MNRAS, 413, 2314

Birnboim Y., Dekel A., 2003, MNRAS, 345, 349

Blain A. W., Longair M. S., 1993, MNRAS, 264, 509

Blain A. W., Ivison R. J., Kneib J. P., Smail I., 1999, in Bunker A. J., van Breugel W. J. M., eds, Astronomical Society of the Pacific Conference Series Vol. 193, The Hy-Redshift Universe: Galaxy Formation and Evolution at High Redshift. p. 246

Blain A. W., Smail I., Ivison R. J., Kneib J. P., Frayer D. T., 2002, Phys. Rep., 369, 111

Bland-Hawthorn J., Gerhard O., 2016, ARA&A, 54, 529

Blumenthal G. R., Faber S. M., Primack J. R., Rees M. J., 1984, Nature, 311, 517

Blumenthal G. R., Faber S. M., Flores R., Primack J. R., 1986, ApJ, 301, 27

Bolatto A. D., Wolfire M., Leroy A. K., 2013, ARA&A, 51, 207

Boselli A., et al., 2010, PASP, 122, 261

Bosma A., 1978, PhD Thesis. University of Gronningen

Bothwell M. S., et al., 2013, MNRAS, 429, 3047

Bouché N., et al., 2007, ApJ, 671, 303

Boulade O., et al., 2003, MegaCam: the new Canada-France-Hawaii Telescope wide-field imaging camera. Proc. of the SPIE, pp 72–81

Bourne N., et al., 2016, MNRAS, 462, 1714

Bourne N., et al., 2017, MNRAS, 467, 1360

Bouwens R. J., et al., 2012, ApJ, 754, 83

Bouwens R. J., et al., 2016, ApJ, 833, 72

Bower R. G., Benson A. J., Malbon R., Helly J. C., Frenk C. S., Baugh C. M., Cole S., Lacey C. G., 2006, MNRAS, 370, 645

Braun R., 2012, ApJ, 749, 87

Brinchmann J., Charlot S., White S. D. M., Tremonti C., Kauffmann G., Heckman T., Brinkmann J., 2004, MNRAS, 351, 1151

Brisbin D., et al., 2017, A&A, 608, A15

Bruzual G., Charlot S., 2003, MNRAS, 344, 1000

Bruzual A. G., Charlot S., 1993, ApJ, 405, 538

Burgarella D., Nanni A., Hirashita H., Theule P., Inoue A. K., Takeuchi T. T., 2020, arXiv e-prints, p. arXiv:2002.01858

Burkert A., et al., 2010, ApJ, 725, 2324

Calura F., et al., 2017, MNRAS, 465, 54

Calzetti D., 2001, PASP, 113, 1449

Calzetti D., Armus L., Bohlin R. C., Kinney A. L., Koornneef J., Storchi-Bergmann T., 2000, ApJ, 533, 682

Camps P., Baes M., 2015, Astronomy and Computing, 9, 20

Camps P., et al., 2018, ApJs, 234, 20

Cappellari M., 2016, ARA&A, 54, 597

Carilli C. L., Walter F., 2013, ARA&A, 51, 105

Carniani S., et al., 2015, A&A, 580, A102

Casey C. M., et al., 2012, ApJ, 761, 140

Casey C. M., et al., 2013, MNRAS, 436, 1919

Casey C. M., Narayanan D., Cooray A., 2014, Phys. Rep., 541, 45

Catinella B., Giovanelli R., Haynes M. P., 2006, ApJ, 640, 751

Catinella B., Haynes M. P., Giovanelli R., 2007, AJ, 134, 334

Ceverino D., Dekel A., Bournaud F., 2010, MNRAS, 404, 2151

Chabrier G., 2003, PASP, 115, 763

Chang Y.-Y., et al., 2018, ApJ, 865, 103

Chapman S. C., Blain A. W., Smail I., Ivison R. J., 2005, ApJ, 622, 772

Charlot S., Fall S. M., 2000, ApJ, 539, 718

Chen C.-C., Cowie L. L., Barger A. J., Casey C. M., Lee N., Sanders D. B., Wang W.-H., Williams J. P., 2013, ApJ, 762, 81

Chen C.-C., et al., 2016, ApJ, 831, 91

Clemens M. S., et al., 2013, MNRAS, 433, 695

Clements D. L., et al., 2008, MNRAS, 387, 247

Clements D. L., et al., 2018, MNRAS, 475, 2097

Coelho P., Bruzual G., Charlot S., Weiss A., Barbuy B., Ferguson J. W., 2007, MNRAS, 382, 498

Condon J. J., 1992, ARA&A, 30, 575

Conroy C., 2013, ARA&A, 51, 393

Conselice C. J., Bluck A. F. L., Ravindranath S., Mortlock A., Koekemoer A. M., Buitrago F., Grützbauch R., Penny S. J., 2011, MNRAS, 417, 2770

Coppin K., et al., 2006, MNRAS, 372, 1621

Coppin K., et al., 2008, MNRAS, 384, 1597

Coppin K. E. K., et al., 2009, MNRAS, 395, 1905

Courteau S., Dutton A. A., 2015, ApJl, 801, L20

Courteau S., et al., 2014, Reviews of Modern Physics, 86, 47

Cowie L. L., Hu E. M., Songaila A., 1995, Nature, 377, 603

Cowie L. L., González-López J., Barger A. J., Bauer F. E., Hsu L. Y., Wang W. H., 2018, ApJ, 865, 106

Crain R. A., et al., 2015, MNRAS, 450, 1937

Daddi E., Cimatti A., Renzini A., Fontana A., Mignoli M., Pozzetti L., Tozzi P., Zamorani G., 2004, ApJ, 617, 746

Daddi E., et al., 2007, ApJ, 670, 156

Dale D. A., Helou G., Contursi A., Silbermann N. A., Kolhatkar S., 2001, ApJ, 549, 215

Danielson A. L. R., et al., 2011, MNRAS, 410, 1687

Danielson A. L. R., et al., 2017, ApJ, 840, 78

Davé R., Finlator K., Oppenheimer B. D., Fardal M., Katz N., Kereš D., Weinberg D. H., 2010, MNRAS, 404, 1355

Davé R., Anglés-Alcázar D., Narayanan D., Li Q., Rafieferantsoa M. H., Appleby S., 2019, MNRAS, 486, 2827

Davis M., Efstathiou G., Frenk C. S., White S. D. M., 1985, ApJ, 292, 371

Davis M., et al., 2007, ApJl, 660, L1

Decarli R., et al., 2016, ApJ, 833, 70

Decarli R., et al., 2019, arXiv e-prints, p. arXiv:1903.09164

Dekel A., Birnboim Y., 2006, MNRAS, 368, 2

Dekel A., et al., 2009, Nature, 457, 451

Delgado-Serrano R., Hammer F., Yang Y. B., Puech M., Flores H., Rodrigues M., 2010, A&A, 509, A78

Dickinson M., Giavalisco M., GOODS Team 2003, in Bender R., Renzini A., eds, The Mass of Galaxies at Low and High Redshift. p. 324 (arXiv:astro-ph/0204213), doi:10.1007/10899892_78

Dole H., et al., 2006, A&A, 451, 417

Donley J. L., et al., 2012, ApJ, 748, 142

Dopita M. A., et al., 2005, ApJ, 619, 755

Draine B. T., 2009, in Henning T., Grün E., Steinacker J., eds, ASP Conf. Ser. Vol. 414, Cosmic Dust - Near and Far. p. 453 (arXiv:0903.1658)

Draine B. T., Lee H. M., 1984, ApJ, 285, 89

Draine B. T., Li A., 2007, ApJ, 657, 810

Draine B. T., et al., 2007, ApJ, 663, 866

Driver S. P., et al., 2018, MNRAS, 475, 2891

Dubois Y., Peirani S., Pichon C., Devriendt J., Gavazzi R., Welker C., Volonteri M., 2016, MNRAS, 463, 3948

Dudzevičiūtė U., et al., 2020, MNRAS, 494, 3828

Dudzevičiūtė U., et al., 2021, MNRAS, 500, 942

Dunlop J. S., 2011, in Wang W., Lu J., Luo Z., Yang Z., Hua H., Chen Z., eds, ASP Conf. Ser. Vol. 446, Galaxy Evolution: Infrared to Millimeter Wavelength Perspective. p. 209

Dunlop J. S., et al., 2017, MNRAS, 466, 861

Dunne L., Eales S. A., Edmunds M. G., 2003, MNRAS, 341, 589

Dunne L., et al., 2009, MNRAS, 394, 1307

Dunne L., et al., 2011, MNRAS, 417, 1510

Eales S., Lilly S., Gear W., Dunne L., Bond J. R., Hammer F., Le Fèvre O., Crampton D., 1999, ApJ, 515, 518

Eales S., et al., 2010, PASP, 122, 499

Eales S., et al., 2012, ApJ, 761, 168

El-Zant A., Shlosman I., Hoffman Y., 2001, ApJ, 560, 636

Elbaz D., et al., 2018, A&A, 616, A110

Epinat B., et al., 2012, A&A, 539, A92

Faber S. M., Jackson R. E., 1976, ApJ, 204, 668

Farrah D., et al., 2001, MNRAS, 326, 1333

Farrah D., et al., 2006, Apjl, 641, L17

Farrah D., et al., 2008, ApJ, 677, 957

Feldmann R., et al., 2006, MNRAS, 372, 565

Ferrero I., et al., 2017, MNRAS, 464, 4736

Fitzpatrick E. L., 1999, PASP, 111, 63

Förster Schreiber N. M., Wuyts S., 2020, ARA&A, 58, 661

Förster Schreiber N. M., et al., 2009, ApJ, 706, 1364

Förster Schreiber N. M., et al., 2014, ApJ, 787, 38

Franceschini A., Toffolatti L., Mazzei P., Danese L., de Zotti G., 1991, A&As, 89, 285

Franco M., et al., 2018, A&A, 620, A152

Frayer D. T., Ivison R. J., Scoville N. Z., Yun M., Evans A. S., Smail I., Blain A. W., Kneib J. P., 1998, ApJl, 506, L7

Freedman W. L., Turner M. S., 2003, Reviews of Modern Physics, 75, 1433

Freeman K. C., 1970, ApJ, 160, 811

Frenk C. S., White S. D. M., Efstathiou G., Davis M., 1985, Nature, 317, 595

Furlong M., et al., 2015, MNRAS, 450, 4486

Furlong M., et al., 2017, MNRAS, 465, 722

Gardner J. P., et al., 2006, Space Sci. Rev., 123, 485

Geach J. E., Smail I., Moran S. M., MacArthur L. A., Lagos C. d. P., Edge A. C., 2011, ApJ, 730, L19

Geach J. E., et al., 2013, MNRAS, 432, 53

Geach J. E., et al., 2017, MNRAS, 465, 1789

Gehrz R., 1989, in Allamandola L. J., Tielens A. G. G. M., eds, IAU Symposium Vol. 135, Interstellar Dust. p. 445

Genel S., et al., 2014, MNRAS, 445, 175

Genzel R., et al., 2010, MNRAS, 407, 2091

Genzel R., et al., 2011, ApJ, 733, 101

Genzel R., et al., 2013, ApJ, 773, 68

Genzel R., et al., 2015, ApJ, 800, 20

Genzel R., et al., 2017, Nature, 543, 397

Genzel R., et al., 2020, ApJ, 902, 98

Gerhard O., Kronawitter A., Saglia R. P., Bender R., 2001, AJ, 121, 1936

Gillman S., et al., 2020, MNRAS, 492, 1492

Girard M., et al., 2021, ApJ, 909, 12

Gnedin O. Y., Kravtsov A. V., Klypin A. A., Nagai D., 2004, ApJ, 616, 16

Greve T. R., et al., 2005, MNRAS, 359, 1165

Griffin M. J., et al., 2010, A&A, 518, L3

Grogin N. A., et al., 2011, ApJs, 197, 35

Gruppioni C., Pozzi F., 2019, MNRAS, 483, 1993

Gruppioni C., et al., 2013, MNRAS, 432, 23

Gullberg B., et al., 2019, MNRAS, 490, 4956

Guo Y., et al., 2013, ApJs, 207, 24

Hainline L. J., Blain A. W., Smail I., Alexand er D. M., Armus L., Chapman S. C., Ivison R. J., 2011, ApJ, 740, 96

Hao C.-N., Kennicutt R. C., Johnson B. D., Calzetti D., Dale D. A., Moustakas J., 2011, ApJ, 741, 124

Harrison C. M., et al., 2017, MNRAS, 467, 1965

Harwit M., Pacini F., 1975, ApJ, 200, L127

Hatsukade B., et al., 2011, MNRAS, 411, 102

Hatsukade B., et al., 2016, PASJ, 68, 36

Hatsukade B., et al., 2018, PASJ, 70, 105

Hayward C. C., Kereš D., Jonsson P., Narayanan D., Cox T. J., Hernquist L., 2011, ApJ, 743, 159

Heinis S., et al., 2013, MNRAS, 429, 1113

Helou G., Soifer B. T., Rowan-Robinson M., 1985, ApJl, 298, L7

Herschel W., 1786, Philosophical Transactions of the Royal Society of London Series I, 76, 457

Hickox R. C., et al., 2012, MNRAS, 421, 284

Hodge J. A., et al., 2013, ApJ, 768, 91

Hodge J. A., et al., 2016, ApJ, 833, 103

Hodge J. A., et al., 2019, ApJ, 876, 130

Holden B. P., et al., 2016, ApJ, 820, 73

Holland W. S., et al., 2013, MNRAS, 430, 2513

Hopkins P. F., Kereš D., Murray N., Quataert E., Hernquist L., 2012, MNRAS, 427, 968

Hubble E. P., 1925, ApJ, 62, 409

Hubble E. P., 1926, ApJ, 64, 321

Hubble E., 1929, Proceedings of the National Academy of Science, 15, 168

Hubble E. P., 1936, Realm of the Nebulae

Huggins W., Miller W. A., 1864, Philosophical Transactions of the Royal Society of London Series I, 154, 437

Hughes D. H., et al., 1998, Nature, 394, 241

Ikarashi S., et al., 2011, MNRAS, 415, 3081

Ikarashi S., et al., 2015, ApJ, 810, 133

Ikarashi S., et al., 2017, ApJl, 849, L36

Ilbert O., et al., 2009, ApJ, 690, 1236

Iono D., et al., 2009, ApJ, 695, 1537

Ivison R. J., Smail I., Le Borgne J. F., Blain A. W., Kneib J. P., Bezecourt J., Kerr T. H., Davies J. K., 1998, MNRAS, 298, 583

Ivison R. J., et al., 2002, MNRAS, 337, 1

Ivison R. J., et al., 2007, MNRAS, 380, 199

Ivison R. J., et al., 2010, MNRAS, 402, 245

Ivison R. J., Papadopoulos P. P., Smail I., Greve T. R., Thomson A. P., Xilouris E. M., Chapman S. C., 2011, MNRAS, 412, 1913

Jin S., et al., 2018, ApJ, 864, 56

John T. L., 1988, A&A, 193, 189

Johnson H. L., et al., 2018, MNRAS, 474, 5076

Johnston R., Vaccari M., Jarvis M., Smith M., Giovannoli E., Häußler B., Prescott M., 2015, MNRAS, 453, 2540

Jones M. G., Haynes M. P., Giovanelli R., Moorman C., 2018, MNRAS, 477, 2

Jorgenson R. A., Wolfe A. M., Prochaska J. X., Lu L., Howk J. C., Cooke J., Gawiser E., Gelino D. M., 2006, ApJ, 646, 730

Kanekar N., Sethi S., Dwarakanath K. S., 2016, ApJl, 818, L28

Kant I., 1755, Allgemeine Naturgeschichte und Theorie des Himmels

Karim A., et al., 2013, MNRAS, 432, 2

Kawinwanichakij L., et al., 2020, arXiv e-prints, p. arXiv:2002.07189

Kennicutt Robert C. J., 1998, ARA&A, 36, 189

Kennicutt R. C., Evans N. J., 2012, ARA&A, 50, 531

Kennicutt Robert C. J., et al., 2009, ApJ, 703, 1672

Kereš D., Katz N., Weinberg D. H., Davé R., 2005, MNRAS, 363, 2

Khan S. A., et al., 2007, ApJ, 665, 973

Kirkpatrick A., Pope A., Sajina A., Roebuck E., Yan L., Armus L., Díaz-Santos T., Stierwalt S., 2015, ApJ, 814, 9

Koekemoer A. M., et al., 2011, ApJs, 197, 36

Koprowski M. P., et al., 2016, MNRAS, 458, 4321

Kormendy J., Richstone D., 1995, ARA&A, 33, 581

Kriek M., et al., 2015, ApJs, 218, 15

Krogager J.-K., Fynbo J. P. U., Møller P., Noterdaeme P., Heintz K. E., Pettini M., 2019, MNRAS, 486, 4377

Kroupa P., 2001, MNRAS, 322, 231

Lacey C. G., et al., 2016, MNRAS, 462, 3854

Lagache G., Puget J.-L., Dole H., 2005, ARA&A, 43, 727

Lagos C. D. P., Baugh C. M., Lacey C. G., Benson A. J., Kim H.-S., Power C., 2011, MNRAS, 418, 1649

Lagos C. d. P., et al., 2015, MNRAS, 452, 3815

Laigle C., et al., 2016, ApJs, 224, 24

Lang P., et al., 2017, ApJ, 840, 92

Lang P., et al., 2019, Apj, 879, 54

Law D. R., Steidel C. C., Shapley A. E., Nagy S. R., Reddy N. A., Erb D. K., 2012, ApJ, 759, 29

Lawrence A., et al., 2007, MNRAS, 379, 1599

Lee S.-K., Ferguson H. C., Somerville R. S., Wiklind T., Giavalisco M., 2010, ApJ, 725, 1644

Lelli F., McGaugh S. S., Schombert J. M., 2016, AJ, 152, 157

Lelli F., De Breuck C., Falkendal T., Fraternali F., Man A. W. S., Nesvadba N. P. H., Lehnert M. D., 2018, MNRAS, 479, 5440

Leroy A. K., et al., 2009, AJ, 137, 4670

Leroy A. K., et al., 2011, ApJ, 737, 12

Li Q., Narayanan D., Davé R., 2019, MNRAS, 490, 1425

Liang L., Feldmann R., Faucher-Giguère C.-A., Kereš D., Hopkins P. F., Hayward C. C., Quataert E., Scoville N. Z., 2018, MNRAS, 478, L83

Lilly S. J., Le Fevre O., Hammer F., Crampton D., 1996, ApJl, 460, L1

Lilly S. J., Eales S. A., Gear W. K. P., Hammer F., Le Fèvre O., Crampton D., Bond J. R., Dunne L., 1999, ApJ, 518, 641

Lim C.-F., et al., 2020, ApJ, 889, 80

Lindner R. R., et al., 2011, ApJ, 737, 83

Liu D., et al., 2018, ApJ, 853, 172

Lovell M. R., et al., 2018, MNRAS, 481, 1950

Lutz D., et al., 2011, A&A, 532, A90

MacKenzie T. P., Scott D., Swinbank M., 2016, MNRAS, 463, 10

Macciò A. V., Dutton A. A., van den Bosch F. C., 2008, MNRAS, 391, 1940

Madau P., 1995, ApJ, 441, 18

Madau P., Dickinson M., 2014, ARA&A, 52, 415

Madau P., Ferguson H. C., Dickinson M. E., Giavalisco M., Steidel C. C., Fruchter A., 1996, MNRAS, 283, 1388

Magdis G. E., et al., 2012, ApJ, 760, 6

Magnelli B., et al., 2010, A&A, 518, L28

Magnelli B., Elbaz D., Chary R. R., Dickinson M., Le Borgne D., Frayer D. T., Willmer C. N. A., 2011, A&A, 528, A35

Magnelli B., et al., 2012, A&A, 539, A155

Magnelli B., et al., 2013, A&A, 553, A132

Magnelli B., et al., 2020, ApJ, 892, 66

Magorrian J., et al., 1998, AJ, 115, 2285

Mannucci F., Cresci G., Maiolino R., Marconi A., Gnerucci A., 2010, MNRAS, 408, 2115

Maraston C., 2005, MNRAS, 362, 799

Martin D. C., et al., 2005, ApJl, 619, L1

Martinsson T. P. K., Verheijen M. A. W., Westfall K. B., Bershady M. A., Andersen D. R., Swaters R. A., 2013, A&A, 557, A131

McAlpine S., et al., 2019, MNRAS, p. 1653

McCracken H. J., et al., 2012, A&A, 544, A156

Menéndez-Delmestre K., et al., 2009, ApJ, 699, 667

Menéndez-Delmestre K., Blain A. W., Swinbank M., Smail I., Ivison R. J., Chapman S. C., Gonçalves T. S., 2013, ApJ, 767, 151

Messier C., 1781, Catalogue des Nébuleuses et des Amas d'Étoiles (Catalog of Nebulae and Star Clusters), Connoissance des Temps ou des Mouvements Célestes

Miettinen O., et al., 2017, A&A, 606, A17

Mocanu L. M., et al., 2013, ApJ, 779, 61

Muñoz Arancibia A. M., et al., 2018, A&A, 620, A125

Narayanan D., Hayward C. C., Cox T. J., Hernquist L., Jonsson P., Younger J. D., Groves B., 2010, MNRAS, 401, 1613

Narayanan D., et al., 2015, Nature, 525, 496

Navarro J. F., Frenk C. S., White S. D. M., 1997, ApJ, 490, 493

Novak M., et al., 2017, A&A, 602, A5

Oliver S. J., et al., 2012, MNRAS, 424, 1614

Oort J. H., 1927, Bull. Astron. Inst. Netherlands, 3, 275

Oort J. H., 1932, Bull. Astron. Inst. Netherlands, 6, 249

Oort J. H., 1940, ApJ, 91, 273

Osterbrock D. E., Ferland G. J., 2006, Astrophysics of gaseous nebulae and active galactic nuclei

Ostriker J. P., Peebles P. J. E., 1973, ApJ, 186, 467

Ostriker J. P., Peebles P. J. E., Yahil A., 1974, ApJl, 193, L1

Overzier R. A., Röttgering H. J. A., Rengelink R. B., Wilman R. J., 2003, A&A, 405, 53

Peebles P. J. E., 1982, ApJl, 263, L1

Peirani S., et al., 2017, MNRAS, 472, 2153

Peng C. Y., Ho L. C., Impey C. D., Rix H.-W., 2010, AJ, 139, 2097

Peng Y., Maiolino R., Cochrane R., 2015, Nature, 521, 192

Persic M., Salucci P., Stel F., 1996, MNRAS, 281, 27

Pettini M., Rix S. A., Steidel C. C., Adelberger K. L., Hunt M. P., Shapley A. E., 2002, ApJ, 569, 742

Planck Collaboration et al., 2011, A&A, 536, A19

Poglitsch A., et al., 2010, A&A, 518, L2

Pope A., et al., 2006, MNRAS, 370, 1185

Pope A., et al., 2008, ApJ, 689, 127

Popping G., Somerville R. S., Galametz M., 2017, MNRAS, 471, 3152

Pozzi F., Calura F., Zamorani G., Delvecchio I., Gruppioni C., Santini P., 2020, MNRAS, 491, 5073

Puget J. L., Abergel A., Bernard J. P., Boulanger F., Burton W. B., Desert F. X., Hartmann D., 1996, A&A, 308, L5

Puglisi A., et al., 2019, ApJl, 877, L23

Rangwala N., et al., 2011, ApJ, 743, 94

Rémy-Ruyer A., et al., 2014, A&A, 563, A31

Renzini A., 2016, MNRAS, 460, L45

Renzini A., Peng Y.-j., 2015, ApJl, 801, L29

Rho J., et al., 2008, ApJ, 673, 271

Riechers D. A., et al., 2013, Nature, 496, 329

Riechers D. A., et al., 2019, ApJ, 872, 7

Rieke G. H., Alonso-Herrero A., Weiner B. J., Pérez-González P. G., Blaylock M., Donley J. L., Marcillac D., 2009, ApJ, 692, 556

Rizzo F., Vegetti S., Fraternali F., Stacey H., Powell D., 2021, arXiv e-prints, p. arXiv:2102.05671

Rodighiero G., et al., 2011, ApJl, 739, L40

Rodighiero G., et al., 2014, MNRAS, 443, 19

Rodríguez-Merino L. H., Chavez M., Bertone E., Buzzoni A., 2005, ApJ, 626, 411

Roseboom I. G., et al., 2012, MNRAS, 419, 2758

Roseboom I. G., et al., 2013, MNRAS, 436, 430

Ross N. P., et al., 2009, ApJ, 697, 1634

Rubin V. C., Ford W. Kent J., 1970, ApJ, 159, 379

Rubin V. C., Ford W. K. J., Thonnard N., 1978, ApJl, 225, L107

Rubin V. C., Ford W. K. J., Thonnard N., 1980, ApJ, 238, 471

Rubin V. C., Ford W. K. J., Thonnard N., Burstein D., 1982, ApJ, 261, 439

Rubin V. C., Burstein D., Ford W. K. J., Thonnard N., 1985, ApJ, 289, 81

Sachdeva S., Gogoi R., Saha K., Kembhavi A., Raychaudhury S., 2019, MNRAS, 487, 1795

Sakamoto K., et al., 2008, ApJ, 684, 957

Salpeter E. E., 1955, ApJ, 121, 161

Sanders D. B., Mirabel I. F., 1996, ARA&A, 34, 749

Sanders D. B., Soifer B. T., Elias J. H., Neugebauer G., Matthews K., 1988, ApJl, 328, L35

Sanders D. B., et al., 2007, ApJs, 172, 86

Sargent B. A., et al., 2010, ApJ, 716, 878

Sawicki M., 2002, AJ, 124, 3050

Schaye J., et al., 2015, MNRAS, 446, 521

Schechter P., 1976, ApJ, 203, 297

Scheiner J., 1899, ApJ, 9, 149

Schinnerer E., et al., 2010, ApJs, 188, 384

Schlafly E. F., Finkbeiner D. P., 2011, ApJ, 737, 103

Schmidt M., 1957, Bull. Astron. Inst. Netherlands, 14, 17

Schreiber C., et al., 2015, A&A, 575, A74

Schreiber C., Pannella M., Leiton R., Elbaz D., Wang T., Okumura K., Labbé I., 2017, A&A, 599, A134

Scott K. S., et al., 2008, MNRAS, 385, 2225

Scoville N. Z., 2013, Evolution of star formation and gas, Eds J. Falcon-Barroso & J.H. Knapen, Cambridge University Press. Cambridge University Press, p. 491

Scoville N., et al., 2007, ApJs, 172, 1

Scoville N., et al., 2014, ApJ, 783, 84

Scoville N., et al., 2017, ApJ, 837, 150

Sellwood J. A., McGaugh S. S., 2005, ApJ, 634, 70

Shimakawa R., Kodama T., Tadaki K.-i., Hayashi M., Koyama Y., Tanaka I., 2015, MNRAS, 448, 666

Shu X. W., et al., 2016, ApJs, 222, 4

Shull J. M., Smith B. D., Danforth C. W., 2012, ApJ, 759, 23

Silva L., Granato G. L., Bressan A., Danese L., 1998, ApJ, 509, 103

Simpson J. M., et al., 2012, MNRAS, 426, 3201

Simpson C., Westoby P., Arumugam V., Ivison R., Hartley W., Almaini O., 2013, MNRAS, 433, 2647

Simpson J. M., et al., 2014, ApJ, 788, 125

Simpson J. M., et al., 2015a, ApJ, 799, 81

Simpson J. M., et al., 2015b, ApJ, 799, 81

Simpson J. M., et al., 2015c, ApJ, 807, 128

Simpson J. M., et al., 2017, ApJ, 839, 58

Simpson J. M., et al., 2020, MNRAS, 495, 3409

Skrutskie M. F., et al., 1997, in Garzon F., Epchtein N., Omont A., Burton B., Persi P., eds, Vol. 210, The Impact of Large Scale Near-IR Sky Surveys. p. 25, doi:10.1007/978-94-011-5784-1_4

Slipher V. M., 1914, Lowell Observatory Bulletin, 2, 66

Smail I., Ellis R. S., Aragon-Salamanca A., Soucail G., Mellier Y., Giraud E., 1993, MNRAS, 263, 628

Smail I., Ivison R. J., Blain A. W., 1997, ApJl, 490, L5

Smail I., Ivison R. J., Kneib J. P., Cowie L. L., Blain A. W., Barger A. J., Owen F. N., Morrison G., 1999, MNRAS, 308, 1061

Smail I., Chapman S. C., Blain A. W., Ivison R. J., 2004, ApJ, 616, 71

Smail I., Sharp R., Swinbank A. M., Akiyama M., Ueda Y., Foucaud S., Almaini O., Croom S., 2008, MNRAS, 389, 407

Smail I., et al., 2021, MNRAS, 502, 3426

Smith D. J. B., et al., 2013, MNRAS, 436, 2435

Smolčić V., et al., 2017, A&A, 602, A1

Sofue Y., Rubin V., 2001, ARA&A, 39, 137

Solimano M., et al., 2021, arXiv e-prints, p. arXiv:2107.09769

Soto K. T., Lilly S. J., Bacon R., Richard J., Conseil S., 2016, Monthly Notices of the Royal Astronomical Society, 458, 3210

Speagle J. S., Steinhardt C. L., Capak P. L., Silverman J. D., 2014, ApJs, 214, 15

Spergel D. N., et al., 2003, ApJs, 148, 175

Springel V., et al., 2005, Nature, 435, 629

Stach S. M., et al., 2018, ApJ, 860, 161

Stach S. M., et al., 2019, MNRAS, 487, 4648

Stach S. M., et al., 2021, MNRAS, 504, 172

Stott J. P., et al., 2013, MNRAS, 436, 1130

Stott J. P., et al., 2016, MNRAS, 457, 1888

Stoughton C., et al., 2002, AJ, 123, 485

Strandet M. L., et al., 2016, ApJ, 822, 80

Suess K. A., Kriek M., Price S. H., Barro G., 2019, ApJ, 877, 103

Swinbank A. M., Chapman S. C., Smail I., Lindner C., Borys C., Blain A. W., Ivison R. J., Lewis G. F., 2006, MNRAS, 371, 465

Swinbank A. M., et al., 2011, ApJ, 742, 11

Swinbank A. M., et al., 2012, MNRAS, 427, 1066

Swinbank A. M., et al., 2014, MNRAS, 438, 1267

Symeonidis M., Page M. J., Seymour N., 2011, MNRAS, 411, 983

Symeonidis M., et al., 2013, MNRAS, 431, 2317

Tacconi L. J., et al., 2018, ApJ, 853, 179

Tacconi L. J., Genzel R., Sternberg A., 2020, ARA&A, 58, 157

Taniguchi Y., et al., 2007, ApJs, 172, 9

Tasca L. A. M., et al., 2015, A&A, 581, A54

Tiley A. L., et al., 2019, MNRAS, 485, 934

Tiley A. L., et al., 2021, arXiv e-prints, p. arXiv:2106.05511

Toft S., et al., 2014, ApJ, 782, 68

Tomczak A. R., et al., 2016, ApJ, 817, 118

Tully R. B., Fisher J. R., 1977, A&A, 500, 105

Turner O. J., et al., 2017, MNRAS, 471, 1280

Übler H., et al., 2018, ApJl, 854, L24

Übler H., et al., 2019, ApJ, 880, 48

Umehata H., et al., 2014, MNRAS, 440, 3462

Umehata H., et al., 2018, PASJ, 70, 65

Umehata H., et al., 2020, A&A, 640, L8

Valiante E., et al., 2016, MNRAS, 462, 3146

Vazdekis A., 1999, ApJ, 513, 224

Vlahakis C., Dunne L., Eales S., 2005, MNRAS, 364, 1253

Vlahakis C., Eales S., Dunne L., 2007, MNRAS, 379, 1042

Vogelsberger M., et al., 2014a, MNRAS, 444, 1518

Vogelsberger M., et al., 2014b, Nature, 509, 177

Wall J. V., Pope A., Scott D., 2008, MNRAS, 383, 435

Walsh D., Carswell R. F., Weymann R. J., 1979, Nature, 279, 381

Walter F., Brinks E., de Blok W. J. G., Bigiel F., Kennicutt Robert C. J., Thornley M. D., Leroy A., 2008, AJ, 136, 2563

Walter F., et al., 2016, ApJ, 833, 67

Walter F., et al., 2020, ApJ, 902, 111

Wang W.-H., Cowie L. L., Barger A. J., Keenan R. C., Ting H.-C., 2010, ApJs, 187, 251

Wang S. X., et al., 2013, ApJ, 778, 179

Wang L., et al., 2014, MNRAS, 444, 2870

Wang W.-H., et al., 2017, ApJ, 850, 37

Wardlow J. L., et al., 2011, MNRAS, 415, 1479

Weijmans A.-M., et al., 2014, MNRAS, 444, 3340

Weiß A., et al., 2009, ApJ, 707, 1201

Weiß A., et al., 2013, ApJ, 767, 88

Whitaker K. E., Kriek M., van Dokkum P. G., Bezanson R., Brammer G., Franx M., Labbé I., 2012, ApJ, 745, 179

Whitaker K. E., et al., 2014, ApJ, 795, 104

White S. D. M., Frenk C. S., 1991, ApJ, 379, 52

White S. D. M., Rees M. J., 1978, MNRAS, 183, 341

Wilkinson A., et al., 2017, MNRAS, 464, 1380

Wilson C. D., Rangwala N., Glenn J., Maloney P. R., Spinoglio L., Pereira-Santaella M., 2014, ApJl, 789, L36

Wisnioski E., et al., 2015, ApJ, 799, 209

Wisnioski E., et al., 2019, ApJ, 886, 124

Wright T., 1750, An original theory or new hypothesis of the universe, doi:10.3931/e-rara-28672.

Younger J. D., et al., 2009, MNRAS, 394, 1685

Yun M. S., Reddy N. A., Condon J. J., 2001, ApJ, 554, 803

Zavala J. A., Aretxaga I., Hughes D. H., 2014, MNRAS, 443, 2384

Zavala J. A., et al., 2017, MNRAS, 464, 3369

Zavala J. A., et al., 2018, MNRAS, 475, 5585

Zehavi I., et al., 2011, ApJ, 736, 59

Zhang Z.-Y., Romano D., Ivison R. J., Papadopoulos P. P., Matteucci F., 2018, Nature, 558, 260

Zhukovska S., Henning T., Dobbs C., 2018, ApJ, 857, 94

Zwicky F., 1933, Helv. Phys. Acta, 6, 110

da Cunha E., Charlot S., Elbaz D., 2008, MNRAS, 388, 1595

da Cunha E., et al., 2015, ApJ, 806, 110

de Blok W. J. G., Walter F., Brinks E., Trachternach C., Oh S. H., Kennicutt R. C. J., 2008, AJ, 136, 2648

van de Hulst H. C., Raimond E., van Woerden H., 1957, Bull. Astron. Inst. Netherlands, 14, 1

van der Kruit P. C., 1971, A&A, 15, 110

van der Kruit P. C., 1973, A&A, 29, 263

van der Wel A., et al., 2014, ApJ, 788, 28